REPORT DOCUMENTATION PAGE

Form Approved OMB NO. 0704-0188

1. REPORT DATE (DD-MM-YYYY)	2. REPORT TYPE	3. DATES COVERED (From - To)
13-04-2017	Final Report	27-Sep-2010 - 26-Dec-2015

4. TITLE AND SUBTITLE
Final Report: Volume Bragg Gratings-Research, Testing and High Power Applications

5a. CONTRACT NUMBER
W911NF-10-1-0441

5b. GRANT NUMBER

5c. PROGRAM ELEMENT NUMBER

6. AUTHORS
Dr. Leonid Glebov, Ivan Divliansky, Larissa Glebova, Julien Lumeau, Axel Schulzgen, Christine Spiegelberg, George Venus, Boris Zeldovich

5d. PROJECT NUMBER

5e. TASK NUMBER

5f. WORK UNIT NUMBER

7. PERFORMING ORGANIZATION NAMES AND ADDRESSES
University of Central Florida
12201 Research Parkway, Suite 501

Orlando, FL 32826 -3246

8. PERFORMING ORGANIZATION REPORT NUMBER

9. SPONSORING/MONITORING AGENCY NAME(S) AND ADDRESS (ES)
U.S. Army Research Office
P.O. Box 12211
Research Triangle Park, NC 27709-2211

10. SPONSOR/MONITOR'S ACRONYM(S)
ARO

11. SPONSOR/MONITOR'S REPORT NUMBER(S)
58500-EL-HEL.42

12. DISTRIBUTION AVAILIBILITY STATEMENT
Approved for Public Release; Distribution Unlimited

13. SUPPLEMENTARY NOTES
The views, opinions and/or findings contained in this report are those of the author(s) and should not contrued as an official Department of the Army position, policy or decision, unless so designated by other documentation.

14. ABSTRACT
The project was dedicated to fundamental study of photoinduced structural transformations in photo-thermo-refractive glass, holographic optical elements recorded in this glass, and beam propagation in volume holograms, complex fibers and solid state lasers. Those studies enabled decrease of absorption and scattering in glasses and creation of comprehensive models for complex holographic elements precise fabrication. These data were used for development of numerous holographic optical elements that paves a way for unprecedented methods of laser beam control. These elements are reflecting volume Bragg gratings (VBGs) for spectral narrowing and stabilization of

15. SUBJECT TERMS

16. SECURITY CLASSIFICATION OF:			17. LIMITATION OF ABSTRACT	15. NUMBER OF PAGES	19a. NAME OF RESPONSIBLE PERSON
a. REPORT	b. ABSTRACT	c. THIS PAGE			Leonid Glebov
UU	UU	UU	UU		19b. TELEPHONE NUMBER 407-823-6983

Report Title

Final Report: Volume Bragg Gratings-Research, Testing and High Power Applications

ABSTRACT

The project was dedicated to fundamental study of photoinduced structural transformations in photo-thermo-refractive glass, holographic optical elements recorded in this glass, and beam propagation in volume holograms, complex fibers and solid state lasers. Those studies enabled decrease of absorption and scattering in glasses and creation of comprehensive models for complex holographic elements precise fabrication. These data were used for development of numerous holographic optical elements that paves a way for unprecedented methods of laser beam control. These elements are reflecting volume Bragg gratings (VBGs) for spectral narrowing and stabilization of semiconductor, fiber and solid state lasers, transmitting VBGs for angular selection of collimated beams for spatial brightness increase in all types of lasers, multiplexed VBGs recorded in the same volume of glass for coherent and spectral combining of laser beams, moiré VBGs providing narrowest spectral filtering, multipass VBGs providing ultimate contrast for spectral and angular filtering, chirped VBGs for ultrashort laser pulses stretching and compression, holographic phase masks enabling mode conversion in laser resonators and free space propagating beams, and achromatic phase masks that provide mode conversion and aberration correction for beams with high spectral width. With the use of these holographic elements such devices were created and studied as single transverse mode lasers with Fresnel numbers exceeding 100 (theoretical limit was considered as unit), spectral combiners of kilowatt fiber laser beams, spectral combiners of laser diode modules for dramatic increase of pumping brightness for fiber lasers, coherent beams combiners providing coherent emission of fiber laser arrays. Thus new horizons of diffractive optics based on photo-thermo-refractive glass are demonstrated.

Contents

Enter List of papers submitted or published that acknowledge ARO support from the start of the project to the date of this printing. List the papers, including journal references, in the following categories:

(a) Papers published in peer-reviewed journals (N/A for none)

Received		Paper
09/05/2013	1	Igor V. Ciapurin, Derrek R. Drachenberg, Vadim I. Smirnov, George B. Venus, Leonid B. Glebov. Modeling of phase volume diffractive gratings, part 2: reflecting sinusoidal uniform gratings, Bragg mirrors, Optical Engineering, (05 2012): 1. doi: 10.1117/1.OE.51.5.058001 304,968.00
09/05/2013	2	Marc SeGall, Vasile Rotar, Julien Lumeau, Sergiy Mokhov, Boris Zeldovich, Leonid B. Glebov. Binary Volume Phase Masks in Photo-Thermo-Refractive Glass, Optics Letters, (04 2012): 1190. doi: 304,969.00
09/05/2013	3	Peter Hofmann, Rodrigo Amezcua-Correa, Enrique Antonio-Lopez, Daniel Ott, Marc SeGall, Ivan Divliansky, Julien Lumeau, Larissa Glebova, Leonid Glebov, N. Peyghambarian, Axel Schulzgen. Strong Bragg Gratings in Highly Photosensitive Photo-Thermo-Refractive-Glass Optical Fiber, IEEE Photonics Technology Letters, (01 2013): 25. doi: 10.1109/LPT.2012.2227308 304,970.00
09/05/2013	4	Julien Lumeau, Leonid B. Glebov. Effect of the refractive index change kinetics of photosensitive materials on the diffraction efficiency of reflecting Bragg gratings, Applied Optics, (06 2013): 3993. doi: 10.1364/AO.52.003993 304,971.00
09/05/2013	5	Pankaj Kaswani, Clemence Jollivet, R. Andrew Sims, Axel Schulzgen, Lawrence Shah, Martin Richardson. Comparison of higher-order mode suppression and Q-switched laser performance in thulium-doped large mode area and photonic crystal fibers, Optics Express, (10 2012): 24295. doi: 304,972.00
10/03/2014	18	Clemence Jollivet, Daniel Flamm, Michael Duparre, Axel Schulzgen. Detailed Characterization of Optical Fibers byCombining S2 Imaging With CorrelationFilter Mode Analysis, Journal of Lightwave Technology, (03 2014): 1068. doi: 337,226.00
10/03/2014	19	Leonid Glebov. High-Performance Solid-State and Fiber LasersControlled by Volume Bragg Gratings, The Review of Laser Engineering, (09 2013): 684. doi: 337,227.00
10/03/2014	20	Marc SeGall, Daniel Ott, Ivan Divliansky, Leonid B. Glebov. Effect of aberrations in a holographic system on reflecting volume Bragg gratings, Applied Optics, (11 2013): 0. doi: 10.1364/AO.52.007826 337,228.00
10/03/2014	21	Daniel Ott, Ivan Divliansky, Brian Anderson, George Venus, Leonid Glebov. Scaling the spectral beam combining channels in a multiplexed volume Bragg grating, Optics Express, (11 2013): 0. doi: 10.1364/OE.21.029620 337,229.00
10/03/2014	22	Daniel B. Ott, Ivan B. Divliansky, Marc A. SeGall, Leonid B. Glebov. Stabilization system for holographic recording ofvolume Bragg gratings using a cornercube retroreflector, Applied Optics, (02 2014): 1039. doi: 337,230.00
11/03/2015	29	Clémence Jollivet, Bryce Samson, Lasse Leick, Lawrence Shah, Martin Richardson, Axel Schülzgen. Comparative study of light propagation and single-mode operation in large-mode area fibers designed for 2-?m laser applications, Optical Engineering, (08 2014): 0. doi: 10.1117/1.OE.54.1.011006 375,284.00
11/03/2015	30	Sergiy Kaim, Sergiy Mokhov, Boris Y. Zeldovich, Leonid B. Glebov. Stretching and compressing of short laser pulses by chirped volume Bragg gratings: analytic and numerical modeling, Optical Engineering, (12 2013): 0. doi: 10.1117/1.OE.53.5.051509 375,285.00

11/03/2015	31	Leonid Glebov, Vadim Smirnov, Eugeniu Rotari, Ion Cohanoschi, Larissa Glebova, Oleg Smolski, Julien Lumeau, Christopher Lantigua, Alexei Glebov. Volume-chirped Bragg gratings: monolithic components for stretching and compression of ultrashort laser pulses, Optical Engineering, (02 2014): 0. doi: 10.1117/1.OE.53.5.051514 375,286.00
11/03/2015	32	Sergiy Mokhov, Daniel Ott, Ivan Divliansky, Boris Zeldovich, Leonid Glebov. Moiré volume Bragg grating filter with tunable bandwidth, Optics Express, (08 2014): 0. doi: 10.1364/OE.22.020375 375,287.00
11/03/2015	28	Clémence Jollivet, Arash Mafi, Daniel Flamm, Michael Duparré, Kay Schuster, Stephan Grimm, Axel Schülzgen. Mode-resolved gain analysis and lasing in multi-supermode multi-core fiber laser, Optics Express, (11 2014): 0. doi: 10.1364/OE.22.030377 375,283.00
11/03/2015	33	Marc SeGall, Ivan Divliansky, Clémence Jollivet, Axel Schülzgen, Leonid B. Glebov. Holographically encoded volume phase masks, Optical Engineering, (07 2015): 0. doi: 10.1117/1.OE.54.7.076104 375,291.00
11/03/2015	37	Sergiy Kaim, Sergiy Mokhov, Ivan Divliansky, Vadim Smirnov, Julien Lumeau, Boris Y. Zeldovich, Leonid B. Glebov. Saturation of multiplexed volume Bragg grating recording, Journal of the Optical Society of America A, (12 2014): 0. doi: 10.1364/JOSAA.32.000022 375,349.00
11/03/2015	38	Leonid Glebov, Sergiy Kaim, Julien Lumeau, Vadim Smirnov, Boris Zeldovich. Metric for the measurement of the quality of complex beams: a theoretical study, Journal of the Optical Society of America A, (03 2015): 0. doi: 10.1364/JOSAA.32.000538 375,350.00
11/03/2015	39	Julien Lumeau, Leonid B. Glebov. Gradient of refractive index (GRIN) effect in photo-thermo-refractive glass, Applied Optics, (02 2015): 0. doi: 10.1364/AO.54.001587 375,351.00
11/03/2015	40	Ivan Divliansky, George Venus, Leonid Glebov, Daniel Ott, Marc SeGall. High-contrast filtering by multipass diffraction between paired volume Bragg gratings, Applied Optics, (10 2015): 0. doi: 10.1364/AO.54.009065 375,352.00
11/03/2015	36	B. Anderson, G. Venus, D. Ott, I. Divliansky, J. W. Dawson, D. R. Drachenberg, M. J. Messerly, P. H. Pax, J. B. Tassano, L. B. Glebov. Fundamental mode operation of a ribbon fiber laser by way of volume Bragg gratings, Optics Letters, (11 2014): 0. doi: 10.1364/OL.39.006498 375,348.00
TOTAL:	**21**	

Number of Papers published in peer-reviewed journals:

(b) Papers published in non-peer-reviewed journals (N/A for none)

Received	Paper

TOTAL:

Number of Papers published in non peer-reviewed journals:

(c) Presentations

Number of Presentations: 0.00

Non Peer-Reviewed Conference Proceeding publications (other than abstracts):

Received		Paper
09/12/2013	11	Daniel B. Ott, Ivan B. Divliansky, Marc A. SeGall, Leonid B. Glebov. Versatile phase stabilization technique for holographic recording oflarge aperture volume Bragg gratings, Practical Holography XXVII. 02-FEB-13, . : ,
09/12/2013	12	Brian Anderson, Sergiy Kaim, George Venus, Julien Lumeau, Vadim Smirnov, Boris Zeldovich, Leonid Glebov. Forced air cooling of volume Bragg gratings for spectral beam combination, Fiber Lasers X: Technology, Systems, and Applications. 08-APR-13, San Francisco, California, USA. : ,
09/18/2013	13	Axel Schülzgen, Peter Hofmann, Rodrigo Amezcua-Correa, Enrique Antonio-Lopez, Daniel Ott, Marc SeGall, Ivan Divliansky, Larissa Glebova, Leonid Glebov. Photo-Thermo-Refractive Glass Fibers, 3rd Workshop of Speciality Optical Fibers and Their Applications. 28-AUG-13, . : ,
09/18/2013	16	Peter Hofmann, Clémence Jollivet, Rodrigo Amezcua-Correa, Enrique Antonio-Lopez, Daniel Ott, Marc SeGall, Ivan Divliansky, Larissa Glebova, Leonid Glebov, Axel Schülzgen. Strong and Robust Bragg Gratings in Photo-Thermo-Refractive Glass Fiber, CLEO 2013. 09-JUN-13, . : ,
09/18/2013	15	C. Jollivet, K. Wei, B. Samson, A. Schülzgen. Low-Loss, Single-Mode Propagation in Large-Mode-Area Leakage Channel Fiber from 1 to 2 um, CLEO 2013. 09-JUN-13, . : ,
09/18/2013	14	C. Jollivet, D. Flamm, M. Duparré, A. Schülzgen. New Experimental Tool for Enhanced Fiber Mode Analysis, Frontiers in Optics/Laser Science XXIX. 06-OCT-13, . : ,
10/03/2014	25	Khawlah Al Yahyaei, Peter Hofmann, Rodrigo Amezcua-Correa, Enrique Antonio-Lopez, Daniel Ott, Marc SeGall, Ivan Divliansky, Larissa Glebova, Leonid Glebov, Alan Kost, Axel Schülzgen. HIGHTLY PHOTOSENSITIVE FIBER FABRICATED FROM PHOTO-THERMO-REFRACTIVE GLASS, International C onference & Expo on Advanced Ceramics & Composites (ICACC). 26-JAN-14, . : ,
TOTAL:	**7**	

Number of Non Peer-Reviewed Conference Proceeding publications (other than abstracts):

Peer-Reviewed Conference Proceeding publications (other than abstracts):

Received		Paper
09/05/2013	6.00	Ivan Divliansky, Daniel Ott, Brian Anderson, Derrek Drachenberg, Vasile Rotar, George Venus, Leonid Glebov. Multiplexed volume Bragg gratings for spectral beam combining of high power fiber lasers, Fiber Laser IX: Technology, Systems and Applications. 21-JAN-12, San Francisco, California, USA. : ,
09/05/2013	9.00	Marc SeGall, Daniel Ott, Ivan Divliansky, Leonid B. Glebov. The effect of aberrated recording beams on reflecting Bragg gratings, SPIE Photonics West: Practical Holography XXVII: Materials and Applications. 03-FEB-13, San Francisco, California, USA. : ,
09/05/2013	8.00	Derrek Drachenberg, Sergiy Mokhov, George Venus, Leonid Glebov, Vadim Laskin. Applying refractive beam shapers for spectral beam combining with volume Bragg gratings, SPIE Photonics West: Laser Sources adn Applications. 22-JAN-12, Brussels, Belgium. : ,
09/05/2013	7.00	Daniel Ott, Vasile Rotar, Julien Lumeau, Sergiy Mokhov, Ivan Divliansky, Aleksandr Ryasnyanskiy, Nikolai Vorobiev, Vadim Smirnov, Christine Spiegelberg, Leonid Glebov. Longitudinal mode selection in laser cavity by moirÃ© volume Bragg grating, SPIE Laser Resonators, Microresonators, and Beam Control XIV. 22-JAN-12, San Francisco, California. : ,
10/03/2014	23.00	Marc SeGall, Ivan Divliansky, Daniel Ott, Julien Lumeau, Sergiy Mokhov, Boris Zeldovich, Leonid B. Glebov, Andrew Forbes, Todd E. Lizotte. Beam shaping by volume phase structures in photo-thermo-refractive glass, SPIE Optical Engineering + Applications. 19-AUG-13, San Diego, California, United States. : ,
10/03/2014	24.00	W. Andrew Clarkson, Ramesh K. Shori, B. Anderson, G. Venus, D. Ott, I. Divliansky, L. Glebov. Compact cavity design in solid state resonators by way of volume Bragg gratings, SPIE LASE. 19-AUG-13, San Francisco, California, United States. : ,
11/03/2015	35.00	Alexis V. Kudryashov, Alan H. Paxton, Vladimir S. Ilchenko, Lutz Aschke, Kunihiko Washio, Ivan Divliansky, Clémence Jollivet, Axel Schülzgen, Leonid Glebov, Marc SeGall. Simultaneous laser beam combining and mode conversion using multiplexed volume phase elements, SPIE LASE. , San Francisco, California, United States. : ,
11/03/2015	41.00	Bahaa E. A. Saleh, Leonid B. Glebov, Alexei L. Glebov, Paul O. Leisher, Ivan Divliansky, Evan Hale, Marc SeGall, Daniel Ott, Boris Y. Zeldovich. Achromatic phase elements based on a combination of surface and volume diffractive gratings, SPIE LASE. , San Francisco, California, United States. : ,
TOTAL:	**8**	

Number of Peer-Reviewed Conference Proceeding publications (other than abstracts):

(d) Manuscripts

Received Paper

TOTAL:

Number of Manuscripts:

Books

Received Book

TOTAL:

Received Book Chapter

TOTAL:

Patents Submitted

Patents Awarded

Awards

Graduate Students

NAME	PERCENT_SUPPORTED

FTE Equivalent:
Total Number:

Names of Post Doctorates

NAME	PERCENT_SUPPORTED

FTE Equivalent:
Total Number:

Names of Faculty Supported

NAME	PERCENT_SUPPORTED

FTE Equivalent:
Total Number:

Names of Under Graduate students supported

NAME	PERCENT_SUPPORTED

FTE Equivalent:
Total Number:

Student Metrics

This section only applies to graduating undergraduates supported by this agreement in this reporting period

The number of undergraduates funded by this agreement who graduated during this period: 0.00
The number of undergraduates funded by this agreement who graduated during this period with a degree in science, mathematics, engineering, or technology fields:..... 0.00
The number of undergraduates funded by your agreement who graduated during this period and will continue to pursue a graduate or Ph.D. degree in science, mathematics, engineering, or technology fields:..... 0.00
Number of graduating undergraduates who achieved a 3.5 GPA to 4.0 (4.0 max scale):..... 0.00
Number of graduating undergraduates funded by a DoD funded Center of Excellence grant for Education, Research and Engineering:..... 0.00
The number of undergraduates funded by your agreement who graduated during this period and intend to work for the Department of Defense 0.00
The number of undergraduates funded by your agreement who graduated during this period and will receive scholarships or fellowships for further studies in science, mathematics, engineering or technology fields: 0.00

Names of Personnel receiving masters degrees

NAME

Total Number:

Names of personnel receiving PHDs

NAME

Total Number:

Names of other research staff

NAME PERCENT_SUPPORTED

FTE Equivalent:
Total Number:

Sub Contractors (DD882)

Inventions (DD882)

Scientific Progress

Technology Transfer

(1) Period covered by report: September 27 2010 – July 31, 2015

(2) Proposal Title: **Volume Bragg gratings– research, testing and high power applications**

(3) Contract/Grant number: W911NF-10-1-0441

(4) Author of report: Leonid Glebov (research groups leaders: Ivan Divliansky, Larissa Glebova, Julien Lumeau, Axel Schulzgen, Christine Spiegelberg, George Venus, and Boris Zeldovich)

(5) Performing Organization Name and Address: CREOL – the College of Optics and Photonics, University of Central Florida. 4304 Scorpius St. Orlando, FL 32816-2700

(7) Abstract

The project was dedicated to fundamental study of photoinduced structural transformations in photo-thermo-refractive glass, holographic optical elements recorded in this glass, and beam propagation in volume holograms, complex fibers and solid state lasers. Those studies enabled decrease of absorption and scattering in glasses and creation of comprehensive models for complex holographic elements precise fabrication. These data were used for development of numerous holographic optical elements that paves a way for unprecedented methods of laser beam control. These elements are reflecting volume Bragg gratings (VBGs) for spectral narrowing and stabilization of semiconductor, fiber and solid state lasers, transmitting VBGs for angular selection of collimated beams for spatial brightness increase in all types of lasers, multiplexed VBGs recorded in the same volume of glass for coherent and spectral combining of laser beams, moiré VBGs providing narrowest spectral filtering, multipass VBGs providing ultimate contrast for spectral and angular filtering, chirped VBGs for ultrashort laser pulses stretching and compression, holographic phase masks enabling mode conversion in laser resonators and free space propagating beams, and achromatic phase masks that provide mode conversion and aberration correction for beams with high spectral width. With the use of these holographic elements such devices were created and studied as single transverse mode lasers with Fresnel numbers exceeding 100 (theoretical limit was considered as unit), spectral combiners of kilowatt fiber laser beams, spectral combiners of laser diode modules for dramatic increase of pumping brightness for fiber lasers, coherent beams combiners providing coherent emission of fiber laser arrays. Thus new horizons of diffractive optics based on photo-thermo-refractive glass are demonstrated.

Contents

Volume 1

Volume 2

Scientific Progress and Accomplishments

1. Introduction

The main objective of this research project is to push forward the technology and applications of volume Bragg gratings (VBGs) to provide operations with laser beams at the level required for 100 kW class laser systems. The general approach is to explore opportunities for power scaling of CW and pulsed fiber lasers with the utilization of such new components as VBGs and more complex holographic optical elements. This approach brings together research activities in different but adjacent research fields: materials science (minimizing losses while maximizing refractive index change in PTR glass, development of complex medium combining properties of a photosensitive holographic material and a laser medium, development of PTR glass pairs for fiber drawing, and shift of a photosensitivity spectrum to longer wavelengths), holography (recording technology to improve efficiency and uniformity of volume Bragg gratings and to develop a technology of grating multiplexing, creation of new phase optical elements which are combinations of gratings and phase masks, and development of a new approach for temperature control of volume Bragg gratings), semiconductor lasers (mode control and spectral beam combining to achieve high brightness pumping), fiber lasers (modal analysis and selection of transverse and longitudinal modes to achieve larger single mode area and minimize Brillouin scattering, fibers and fiber lasers in PTR glass), and laser beam combining (coherent and spectral).

The main areas of utilization of volume Bragg gratings (VBGs) recorded in photo-thermo-refractive (PTR) glass are following – diode lasers spectrally narrowed by VBGs are spectrally combined by a stack of VBGs to provide the highest brightness with the minimum quantum deficit in the gain fiber; a large area multimode fiber in an external resonator with a VBG mode selector provides single-transverse mode operation at higher powers; coherent combining of several lasers by means of passive radiation exchange by means of multiplexed VBGs provides coherent beam combining within a single aperture; and spectral beam combining by a stack of VBGs provides the final power scaling to the 100 kW level through a single aperture.

2. Photo-thermo-refractive (PTR) glass

2.1. Absorption

One of the main goals of the project is to decrease absorption of PTR glass in regions of high power lasers emission in vicinity of 1 μm. We have investigated the origin of absorption in pristine PTR glass by combining the multi-wavelengths measurements of absorption performed using a laser calorimetry system developed at CREOL. This method measures heating of a sample by laser radiation. It is based on transmission monitoring of the intrinsic Fabry-Perot interferometer produced by the plane-parallel surfaces of the measured sample when it is heated by high power laser radiation. Repeatability of the measurements is better than 10% while detection limit is below 10^{-5} cm^{-1}. Using this system, absorption was measured in several glass melts at different wavelengths: 808, 976 and 1085 nm. It was found (Tab. 1) that in most of the melts, absorption is the highest at 976 nm. Up to now, the only known sources of absorption

Table 1. Absorption measured at three wavelengths in several different glass melts

Melt ID#	A(808 nm)	A(976 nm)	A(1085 nm)
C43	8.89E-05	1.46E-04	1.02E-04
C44	9.96E-05	1.33E-04	8.91E-05
C45	6.73E-05	1.12E-04	8.84E-05
N47	1.21E-04	1.13E-04	1.03E-04

were associated with ferric iron having an absorption band with maximum at 1075 nm and silver containing particles having an absorption band with maximum around 450 nm. It is obvious that combining these two sources of absorption cannot explain higher absorption at 976 nm than at 808 or 1085 nm.

To investigate the source of this additional absorption, we developed a specific method that would allow measuring the absorption spectra in pristine PTR glass with high accuracy using a commercial spectrophotometer. Actually, the relative precision on any spectrum measurement performed on the last generation of spectrophotometers (in our case a Perkin Elmer Lambda 950) is between 0.01 and 0.1%. This corresponds to optical density between 4×10^{-5} and 4×10^{-4}. We are trying to reveal changes of absorption of a few 10^{-5} cm^{-1} and we know that the optical density (*OD*) is proportional to the sample's thickness (*t*).

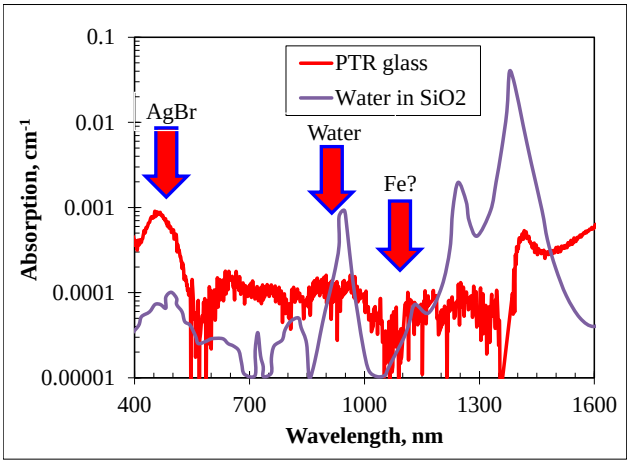

Fig. 1. Absorption spectrum measured in a 42-mm-thick PTR glass sample.

To be able to detect fluctuations of the optical density of at least 4×10^{-5}, sample's thickness must be larger than 40 mm. We therefore prepared thick homogeneous PTR glass samples (t~42 mm), in order to be able to detect small fluctuations of the PTR glass absorption. We also developed the metrology and signal processing to allow such losses measurement in divergent beams and tested the repeatability and the possible source of measurement error of this technique. Figure 1 shows a typical absorption spectrum measured in such a regular PTR glass. It is very noisy because of very low level of absorption. This spectrum is overlapped with the spectrum of hydroxyl groups as measured in fused silica by Heraeus Company. One can see some correlation between the hydroxyl groups absorption spectrum of fused silica and the absorption spectrum of PTR glass. This correlation is not strong because of high level of noise in the spectrum of

hydroxyl in multicomponent silicate glass. It is still very hard to extract a very accurate absorption spectrum of PTR glass. However, it becomes quite clear that the higher absorption as measured at 976 nm in pristine PTR glass can reasonably be associated with the third harmonic of the hydroxyl groups absorption band. This absorption is very low (a few 10^{-5} cm^{-1}) due to the low level of water in PTR glass (less than 30 ppm). We therefore see that dehydration of PTR glasses will be one of the next challenges to solve in order to further decrease absorption in near-IR range.

It is important to study the effect of UV-exposure (as needed to trigger the PTR glass photosensitivity) on absorption in near IR region to enable PTR glass element operation in high power IR laser beams. We studied a pristine high purity PTR glass and exposed this glass to UV-radiation from a He-Cd laser (4 mW) at 325 nm. Dosage of UV-exposure was incrementally increased up to 10 J/cm^2, and bulk absorption was measured at 808 and 1085 nm for different dosages of UV exposure (Fig. 2), using a custom calorimetric setup for low absorption measurement [1]. One can see that increasing the dosage of UV-exposure tends to increase the absorption at both 808 and 1085 nm. Similar experiment performed with a PTR glass sample doped with a 15 ppm of iron resulted in an increase of the absorption at 1085 nm more than one order of magnitude higher. It was shown that concentration of iron impurities in high purity PTR glass being within 1 ppm. Therefore, this result tends to prove that one of the main mechanisms at the origin of an increase of absorption in near-IR region after UV-exposure is the photoinduced reduction of iron:

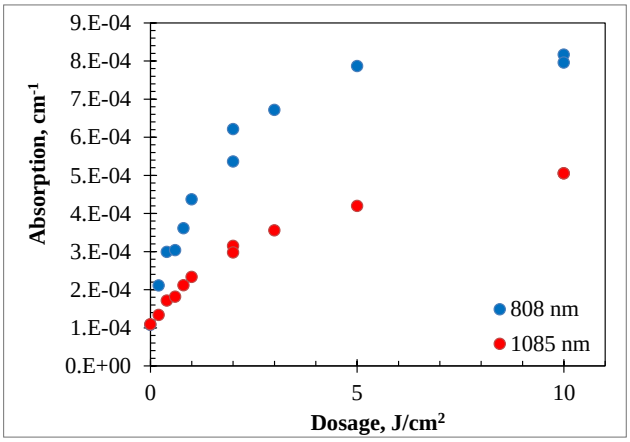

Fig. 2. Dependence of absorption measured at 808 and 1085 nm on dosage of UV-exposure at 325 nm before thermal treatment.

However, this model is not exhaustive. Actually, absorption increases both at 808 and 1085 nm. However, due to the spectral dependence of the specific absorption of Fe^{2+}, the increase of absorption is expected to be smaller at 808 nm than at 1085 nm. Hence, data of Fig.2 cannot be explained by such a simple model. To further understand the origin of this absorption, we performed high accuracy spectroscopic measurement of absorption with a thick (50 mm) PTR glass sample using a Perkin Elmer Lambda 950 spectrophotometer. We developed the methods and procedures that allow treating and interpreting the data when thick samples are measured.

[1] J. Lumeau, L. Glebova and L. B. Glebov, Applied Optics 50(30), 5905–5911 (2011)

Then we measured absorption in thick pristine high purity PTR glass and after exposing this glass to 1 J/cm^2 at 325 nm (Fig. 3). One can see that after UV-exposure, new absorption bands with maximum in UV and visible regions tend to extend to near-IR region, contributing to an increase of absorption at 808 nm and probably 1085 nm (but with smaller contribution). These induced absorption band can be modeled using most of the electron and hole centers absorption bands that were discovered when studying the generation of color centers in PTR glass matrix [2]. It is important to note that these centers are thermally stable, even when temperature is increased to 300-400^{o}C, in contrary to color centers in soda-lime silicate glass that tend to fade quickly at temperature of 150^{o}C. Therefore, one can expect that these centers still might contribute to absorption in near-IR region after thermal treatment.

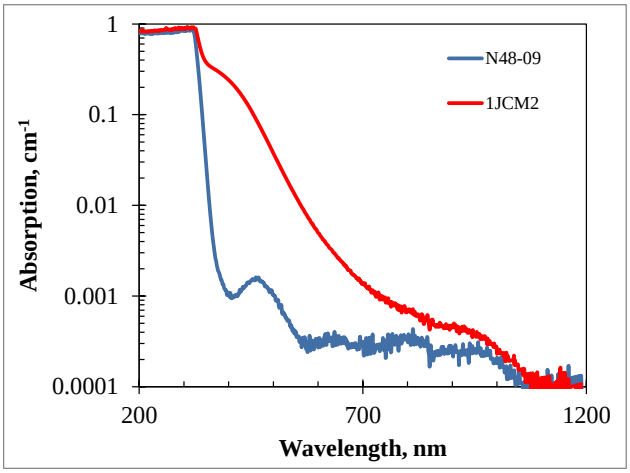

Fig. 3. Absorption spectrum measured in a 50-mm thick regular PTR glass in UV-VIS-NIR-regions. Blue curve corresponds to pristine PTR glass, red curve corresponds to PTR glass exposed to 1 J/cm^2 at 325 nm.

To further understand absorptio9n in PTR glass, an accurate method for the measurement of small absorption in PTR glass and VBGs was presented.[3] It is based on laser induced heating and the measurement of the temperature increase using an interferometric method. It was shown that absorption in pristine PTR glass is between 5×10^{-5} and 10^{-4} cm^{-1}, while the lowest absorption achieved in VBGs is 10^{-4} cm^{-1}. Absorption coefficient in this report is $= -log_{10}T_i/t$, where T_i is internal transmission of the sample and t is the thickness.

Regular photosensitive PTR glass containing $15Na_2O–5ZnO–4Al_2O_3–70SiO_2–5NaF–1KBr–0.01Ag_2O–0.01CeO_2$ (mol.%) and minor amounts of Sn and Sb was used. Polished 25×25×5 mm^3 samples were prepared for these experiments. The chemical homogeneity of the

[2] K. Chamma, J. Lumeau, L. Glebova, and L. B. Glebov, Journal of Non Crystalline Solids 356 (44-49), 2363–2368 (2010)

[3] J. Lumeau, L. Glebova and L. B. Glebov, "Near-IR absorption in high purity photo-thermo-refractive glass and holographic optical elements: measurement and application for high energy lasers", Applied Optics 50(30), 5905–5911 (2011).

samples is a critical parameter affecting PTR glass properties,[4] thus homogeneity was tested by the shadow method in a divergent beam of a He–Ne laser and was quantified by measurements using a Fizeau interferometer (GPI Zygo). The samples selected for this study had refractive index fluctuations of less than 40 ppm (peak-to-valley) across the aperture.

UV-exposure of samples was performed by scanning a He-Cd laser (4 mW, 325 nm) over the glass aperture. Dosage was controlled with the scanning speed.[5] Some of the samples were then nucleated at 485^{o}C for 100 minutes and heat-treated for one hour at temperature 515°C. After heat-treatment, the samples were re-ground and polished in order to remove any incipient silver precipitation or NaF crystallization on the surfaces that would contribute to an increase of the measured absorption. Testing performed on samples with different thicknesses showed that surface absorption contribution is no more than a few percent of the bulk absorption and therefore can be neglected.

Absorption was analyzed by combining two different techniques. First of all we used a custom absorption measurement setup combining calorimetry and interferometry.[6] This setup uses three different lasers with respective wavelengths of 808, 976 and 1085 nm. Accuracy of these measurements was within a few percent of the measured absorption whatever the measured absorption value was. We also carried out transmission spectra measurements in the 200-3000 nm range using a Perkin Elmer Lambda 950 spectrophotometer and transmission spectra measurements in the 2500-5000 nm range using a Perkin Elmer Spectrum 100 Optica FTIR system. As spectrophotometers measured overall losses, i.e. the sum of absorption and scattering losses, the models that were developed in order to separate the contributions of absorption and scattering described in the previous report were applied to each measured spectrum. Also it is important to note that while the relative precision of spectrophotometric measurements is between 0.01 and 0.1%, the absolute precision on one order magnitude worse, i.e. between 0.1 and 1%. To overcome this difference, we developed a custom laser photometer that allows the measurement of the reflection and the transmission at 1085 nm without any interference problem and an absolute precision of 0.01%. In this case, this measurement was used to calibrate the spectrophotometric measurements and therefore achieve a relative and an absolute precision on losses both between 0.01 and 0.1%.

[4] J. Lumeau, A. Sinitskiy, L. N. Glebova, L. B. Glebov and E. D. Zanotto, "Method to assess the homogeneity of photosensitive glasses: application to photo-thermo-refractive glass", Journal of Non Crystalline Solids 355, 1760–1768 (2009).
[5] O.M. Efimov, L.B. Glebov and H.P. Andre, “Measurement of the induced refractive index in a photo-thermo-refractive glass by a liquid-cell shearing interferometer”. Appl. Optics, 41 (2002) 1864-1871
[6] J. Lumeau, L. Glebova and L. B. Glebov, "Near-IR absorption in high purity photo-thermo-refractive glass and holographic optical elements: measurement and application for high energy lasers", Applied Optics 50(30), 5905–5911 (2011).

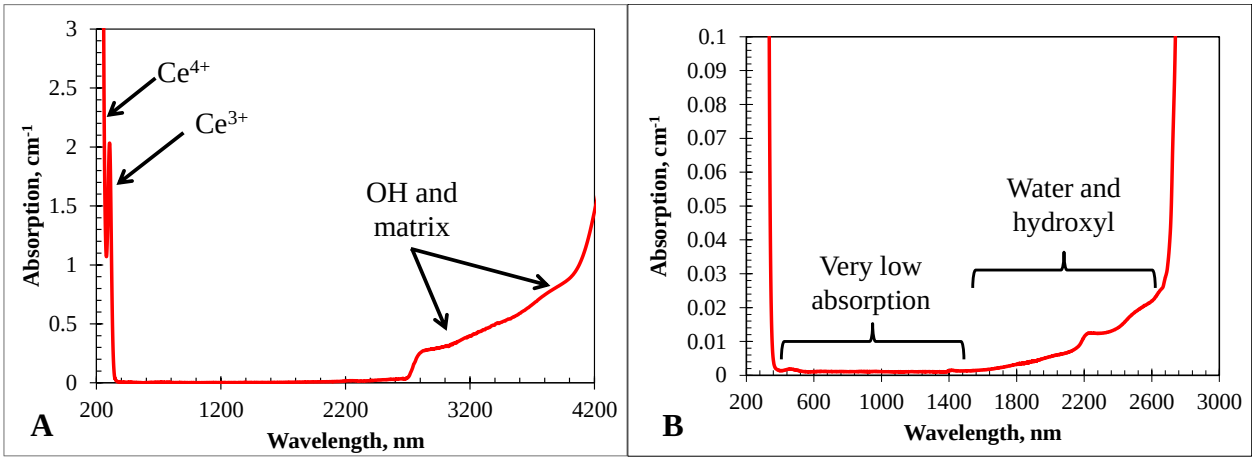

Fig. 4. Absorption spectrum of pristine PTR glass. A – absorption coefficient range 0-3 cm^{-1}, B – absorption coefficient range 0-0.1 cm^{-1}.

Figure 4A shows the typical absorption spectrum measured in a regular PTR glass sample in the range from 200 to 4200 nm. One can see that, in first approximation, the typical transparency range of PTR glass lies in between 350 and 2500 nm. The lower limit is due to the presence of cerium ions in the glass which are mandatory elements for having photosensitivity of the PTR glasses at 325 nm. The recent studies have shown that this absorption is the combination of the overlapped absorption bands of Ce^{3+} and Ce^{4+} ions.[7] Regarding the longer wavelength transmission limit, this one is associated with two different contributions. The first one is the presence of hydroxyl groups. It was shown that absorption spectrum of water extracted from experimental spectra of soda-lime silicate glass[8,9] contains well known absorption bands at 2300, 2800, and 3500 cm^{-1} and their multiphonon repetitions in the short wavelength region. Recent studies have shown that the same bands apply to PTR glasses,[10] therefore limiting transparency range of PTR glass to 2700 nm. Within the same study, it was also shown that the dehydration of PTR glass is not enough to provide a longer wavelength limit up to 3500 nm. A new absorption band of the silicate glass matrix with maximum at 3.2 μm and going down to 2.8 μm was retrieved. It was assigned to the three-phonon absorption of the asymmetric stretch vibration transition of sodium silicate glass at 10.6 μm.

Zooming on the transmission spectra of PTR glass (Fig. 4B) shows that defining such a large transmission range is not completely accurate. In the range from 1600 to 2600 nm, one can see that absorption ranges 0.001 and 0.025 cm^{-1}. This absorption can be associated with harmonics of the water and hydroxyl group absorption bands. While such level of absorption is tolerable for low power applications, it becomes unacceptable as soon as power reaches the watt or tens of

[7] M. Anne, J. Lumeau, L. Glebova and L.B. Glebov, "Specific absorption spectra of cerium in multicomponent silicate glasses", Journal of Non Crystalline Solids 356 (44-49), 2337–2343 (2010).
[8] E.N Boulos, L.B Glebov, T.V Smirnova, "Absorption of iron and water in the Na2O–CaO–MgO–SiO2 glasses. I. Separation of ferrous and hydroxyl spectra in the near IR region", Journal of Non-Crystalline Solids 221(2–3), 213–221 (1997).
[9] L.B. Glebov, E.N. Boulos, "Absorption of iron and water in the Na2O-CaO-MgO-SiO2 glasses. II. Selection of intrinsic, ferric, and ferrous spectra in the visible and UV regions", Journal of Non-Crystalline Solids 242, 49-62 (1998).
[10] M. Anne, L. Glebova, J. Lumeau and L. B. Glebov, "IR absorption edge of multicomponent silicate glasses", 8th Pacific Rim Conference on Ceramic and Glass Technology (PACRIM 8) (Vancouver, British Columbia, Canada), paper PACRIM8-S25-005-2009, June 2009.

watts level. Therefore, high transparency range of PTR glass can be narrowed down to wavelengths between 400 and 1600 nm where absorption appears to be below 10^{-3} cm^{-1}.

The fabrication of volume Bragg gratings (VBGs) in PTR glass requires a multi-step processing of the glass. First of all the glass is exposed to UV-radiation producing an oxidation of Ce^{3+} and the formation of atomic silver ($Ag^{+} + Ce^{3+} + h\nu \rightarrow Ag^{0} + Ce^{4+}$). Then, heat-treating the glass at temperatures above the glass transition temperature triggers silver clustering during a first high temperature thermal treatment, and then heterogeneous nucleation and growth of NaF nano-crystals on further heating. The appearance of these NaF nano-crystals correlates with the appearance of a refractive index change of the UV-exposed areas.[11] In this section, we study the impact of each of these steps on absorption in visible and near-IR ranges.

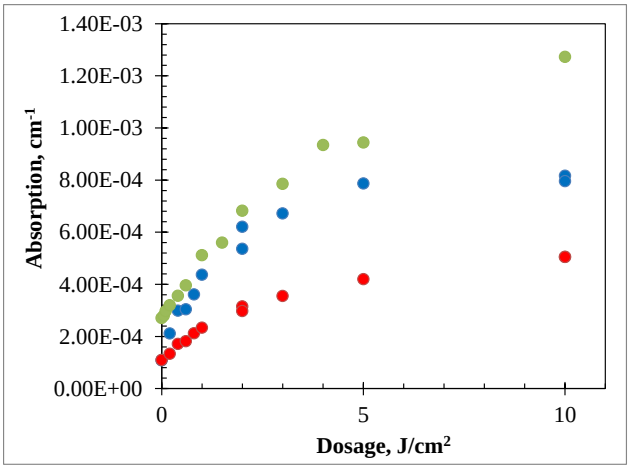

Fig. 5. Dependence of the absorption in PTR glass on dosage of UV-exposure. Red dots: high purity glass at 1085 nm, blue dots: in high purity glass at 808 nm, green dots: in low grade glass at 1085 nm.

The recording of volume Bragg gratings first requires the exposure of PTR glass to UV-laser. We investigated the impact of UV-exposure on absorption. We considered a pristine PTR glass and measured its absorption at 808 and 1085 nm using the calorimetric setup, equal at both wavelength to ~10^{-4} cm^{-1}. We then exposed this glass to the radiation from a He-Cd laser at 325 nm incrementally increasing the dosage of UV-exposure up 10 J/cm^2 and measuring absorption at dual wavelength after each increment (Fig. 5). One can see that increasing the dosage of UV-exposure increases the absorption in near-IR range. Experiments performed on glasses melted with chemicals with lower purity resulted in a higher absorption increase at 1085 nm, proving that UV-exposure tends to effect the absorption level of these impurities. As we have seen in the previous section, one of the most critical impurities is iron. While Fe^{3+} does not present any absorption band in near-IR range, Fe^{2+} has a very broad one with maximum at ~1100 nm. Therefore, one might expect that exposure changes the valence state of iron converting Fe^{3+} into Fe^{2+}.

[11] T. Cardinal, O.M. Efimov, H.G. Francois-Saint-Cyr, L.B. Glebov, L.N. Glebova and V.I. Smirnov, "Comparative study of photo-induced variations of X-ray diffraction and refractive index in photo-thermo-refractive glass", Journal of Non-Crystalline Solids 325 (2003) 275–281.

Table 2. Gaussian functions parameters and assigned charges for absorption bands of photoinduced color centers in PTR glass.

Gaussian	Central wavelength, nm	Charge	Width, cm^{-1}
G1	214	hole	1886
G2	232	electron	1534
G3	262	Unknown	3100
G4	300	hole	2507
G5	344	electron	2740
G6	381	electron	3357
G7	434	hole	3313
G8	-	hole	-
G9	680	hole	2850

To further understand the origin of this absorption after UV-exposure, we combined the calorimetric data with high accuracy spectroscopic measurement of absorption on thick (42 mm) PTR glass using the Perkin Elmer Lambda 950 spectrophotometer. We plotted in Fig. 3 the absorption spectrum measured in a thick pristine high purity PTR glass and after exposing this glass to 1 J/cm^2 at 325 nm. One can see that after UV-exposure, new absorption bands with maxima in UV and visible regions that tend to extend to near-IR region, contributing to an increase of absorption at 808 nm and probably 1085 nm (but with smaller contribution). To understand the origin of these absorption bands we modeled the induced absorption (difference between the absorption spectra measured on the same PTR glass after and before UV-exposure) using the electron and hole centers absorption bands that were discovered when studying the generation of color centers in PTR glass matrix.[12] Parameters of each band are summarized in Table 2.

One can see in Fig. 6 that a linear combination of some of these bands allows an accurate description of the PTR glass induced absorption spectrum, proving that color centers are most probably at the origin of the additional induced absorption after PTR glass UV-exposure. Moreover, it is important to stress that these centers are thermally very stable, even when temperature is increased to 300-400^{o}C, in contrary to color centers in soda-lime silicate glass that tend to fade quickly at temperature of 150^{o}C.[13] Therefore, one can expect that these centers still might contribute to absorption in near-IR region after thermal treatment. However, as it will be seen later, such a conclusion is hard to make due to the appearance of new absorption species with maximum in the blue/green region.

[12] K. Chamma, J. Lumeau, L. Glebova, and L. B. Glebov, "Generation and bleaching of intrinsic color centers in photo-thermo-refractive glass matrix", Journal of Non Crystalline Solids 356 (44-49), 2363–2368 (2010).
[13] A.V. Dotsenko, L.B. Glebov, V.A. Tsekhomsky, Physics and Chemistry of Photochromic Glasses. CRC Press, Boca Raton, NY, 1997.

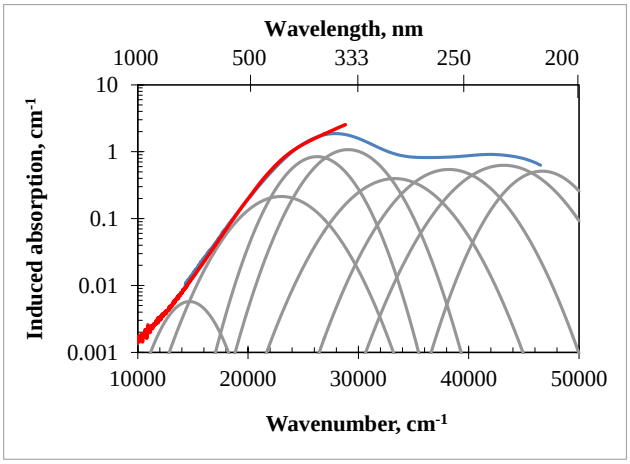

Fig. 6. Absorption spectra of a 42 mm thick high purity PTR glass. Red curve - induced absorption spectrum – difference between blue and red curves in Fig. 3 and its modeling using the sum of the Gaussian bands of color centers generated in PTR glass matrix (blue curve - sum of the bands, grey curves - individual Gaussian bands).

The second processing step of PTR glass consists in heat-treating the glass at high temperature using a two-step process: first nucleating the glass at a temperature around 485°C and then developing the glass at a temperature around 515°C in order to promote the growth of NaF crystals. While nucleation does not produce any measurable change of the absorption of VBGs in PTR glass, this step is one of the most critical steps in term of increasing the PTR glass absorption. The nucleation of PTR glass relies on the creation of silver containing particles with a plasmon resonance generating an absorption band in the 400-500 nm region. It was shown that this absorption band is not an elementary absorption band but the sum of several elementary absorption bands corresponding to particles combining silver and bromine. Table 3 summarizes each of the absorption band parameters and origin that were used to model silver containing particles absorption band at any stage of the thermal treatment process.

Table 3. Parameters of the Gaussian bands (G_i) and exponential tails (E_i) used for the fitting of silver containing particles absorption band. σ_i^0 is the central wavenumber in cm^{-1}, $\Delta\sigma_i$ is the half width at $1/e^2$ and λ_i^0 the central wavelength in nm.

	G4	G3	G2	G1	E2	E1
σ_i^0	26575	24275	22000	19500	8	7.2
$\Delta\sigma_i$	3465	2055	3200	2800	20000	18000
λ_i^0	376	412	455	513	4.E-04	4.E-04
Origin	Hole	Ag	AgBr	Ag/AgBr	G2	G1

The silver containing nanoparticles of AgBr and AgBr:Ag have particular properties as they have a long-wavelength tail following an Urbach rule,[14] therefore contributing to near-IR region absorption. Figure 7 presents an example of the structure of the silver containing particles produced in PTR glass after nucleation. It is important to note that this structure evolves in the process of PTR glass heat-treatment.[15] Precise calorimetric characterization of absorption at 1085 nm performed on PTR glasses after UV-exposure and thermal treatment showed that absorption increases by more than one order of magnitude reaching a level between 5×10^{-3} and 10^{-2} cm^{-1}.

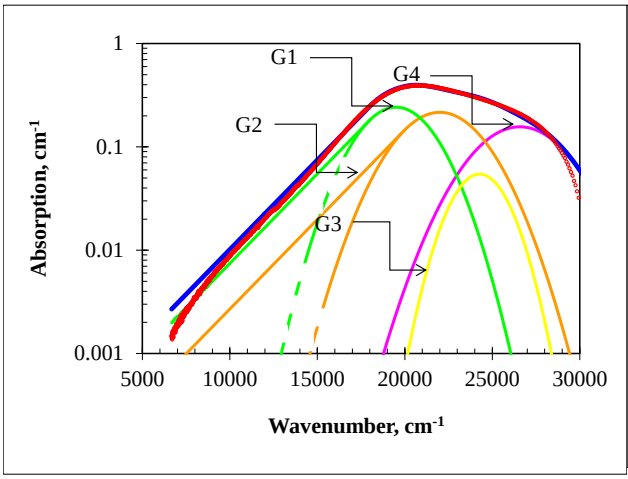

Fig. 7. Typical decomposition of silver containing particles absorption spectrum using Gaussian and exponential functions. G1 and E1 are in green, G2 and E2 in orange, G3 in yellow and G4 in pink, the sum of the bands id in blue. Experimental data are in red, the sum of modeling functions is in blue.

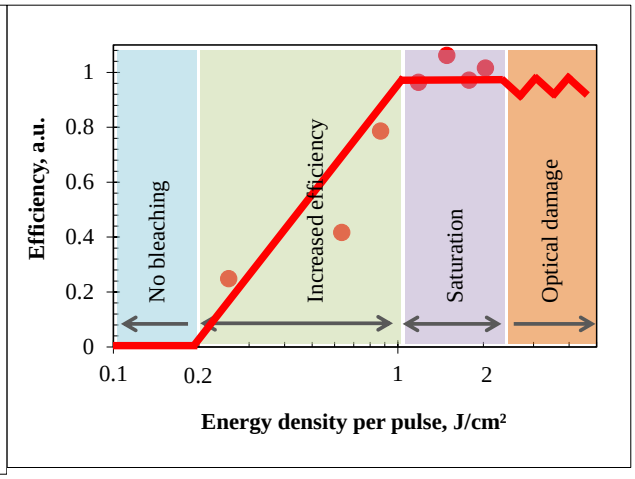

Fig. 8. Dependence of bleaching efficiency of Ag containing particles on 10 ns pulse energy density at 532 nm.

To overcome this problem of high absorption in the final VBG, methods for mitigating this absorption were developed. It was shown that absorption band of the silver containing particles can be bleached using the second harmonic of a Nd:YAG laser. It was shown that it is therefore possible to severely decrease the absorption in VBGs used in high power beams and that intense bleaching can permit to bleach not only the visible part of absorption but also the long wavelength tail. Bleaching mechanisms were also studied and shown to rely on a more complex interaction than simple two-photon absorption process. In Fig. 8, we show the dependence of bleaching efficiency on energy per pulse. One can see that below 0.1 J/cm^2, no or un-measurable bleaching occurs while above 1 J/cm^2, efficiency saturates and above 2 J/cm^2, damage threshold of platinum particles is achieved. This atypical behavior was explained by the fact that optical bleaching of silver containing nano-particles is not an optical process but a thermal process based on the gradual dissipation of these particles as the number of pulses is increased. Therefore, silver containing particles are destroyed by thermal destruction of those one and diffusion of the components in the cold glass matrix. Using this technique, it was possible to achieve absorption

[14] F. Moser and F. Urbach, "Optical absorption of pure silver halides", Phys. Rev. 102 (6), 1519 – 1523 (1956).
[15] J. Lumeau, L. Glebova and L. B. Glebov, "Evolution of Absorption Spectra in the Process of Nucleation in Photo-Thermo-Refractive Glass", Advanced Materials Research, 39-40, 395–398 (2008).

at 1 µm in a UV-exposed and developed VBG of 1×10^{-4} cm^{-1}. However, it was shown that the destruction of the silver containing particles cannot be performed with only one pulse, whatever its energy, but requires several tens, even hundreds, of pulses in order to achieve complete destruction of those particles, the absorption coefficient decreasing exponentially with the number of incident pulses. The reached level of absorption is very important because, as it was shown in Ref. [16], it allows using these VBGs for application involving lasers with more than 10 kW power at 1 µm without severe heating and consequently thermal distortions.

Up to now we have discussed the different sources of bulk absorption in PTR glass and VBGs and the methods to mitigate it. While absorption in final VBGs kept in normal condition is ultra-stable, as no change could be measured after several years; there are several parameters that can influence the absorption of the VBGs. One is very obvious and concerns the environmental conditions of the VBGs. As we have seen previously, glass is sensitive to UV light with wavelengths below 360 nm and exposing the glass to such radiation induces an increase of the absorption of the glass through reduction of iron but also the creation of very stable color centers. Therefore, it is very important to pay attention to the emission spectrum of the environmental light sources.

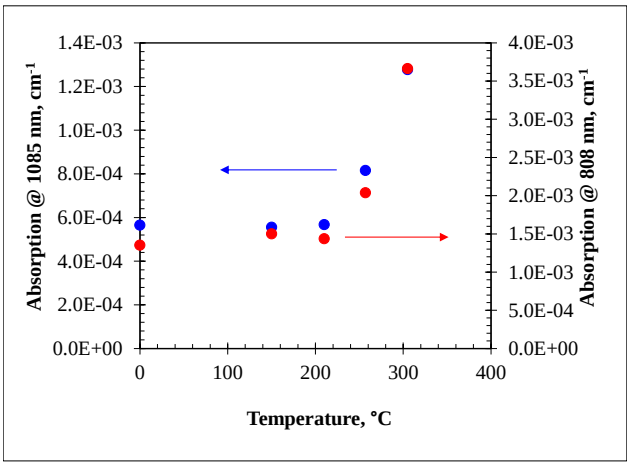

Fig. 9. Evolution of absorption at 808 and 1085 nm in bleached VBGs as a function of aging temperature (isothermal heat-treatment for 30 minutes).

But there is another parameter even more critical which is the temperature stability of the fabricated VBGs. In order to investigate this stability we considered a VBG for 1064 nm region after full processing but that was only partially bleached to an absorption of 1.5×10^{-3} cm^{-1} at 808 nm and 0.5×10^{-3} cm^{-1} at 1085 nm. Then we heated this VBG to a given temperature in a temperature-controlled furnace for 30 minutes. Temperature varied between 150 and 300°C. After each heat-treatment, absorption was measured in this VBG at dual wavelengths (Fig. 9). One can see that below 200°C, heating the glass for 30 minutes at high temperature does not deteriorate the VBG's absorption, while a significant increase of the absorption is measured when VBG is heated at temperature above 200°C. Additional experiments aiming to understand

[16] J. Lumeau, L. Glebova and L. B. Glebov, "Near-IR absorption in high purity photo-thermo-refractive glass and holographic optical elements: measurement and application for high energy lasers", Applied Optics 50(30), 5905–5911 (2011).

the effect of the thermal treatment duration have shown that the critical temperature for re-increasing absorption lies in between 180 and 200°C. Origin of this absorption was also investigated by measuring absorption spectra after each 30 minute heat-treatment.

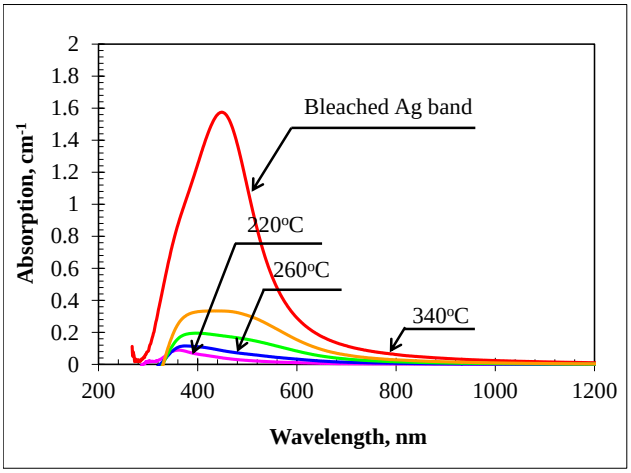

Fig. 10. Induced absorption spectra of silver containing particles after isothermal heat-treatment for 30 minutes at different temperatures from 220 to 340°C and the induced absorption band of silver containing particles before bleaching.

Figure 10 shows the induced absorption spectra obtained by differentiating the absorption spectra measured after and before each heat-treatment. One can see that heat-treatment generates an absorption band with maximum in blue/green region similar to the silver containing absorption band, but with a shape that cannot be modeled using the Gaussian bands that were defined in Table 3. Therefore, heat-treatments trigger the creation of some new silver containing particles with parameters different from that were previously destroyed. Such result is not surprising as it was shown that mobility of silver starts at temperature around 150°C such as the formation of silver containing particles could be revealed in UV-exposed PTR glasses. Moreover, we have shown that bleaching is a thermal process and that destruction rate is most probably limited by the ability of silver to diffuse away from the particle site. Therefore one can see that all these parameters tend to limit the thermal stability of bleached VBGs. This result is critical for high power applications because it shows that the critical temperature that must not be reached is not the glass transition temperature (T_g = 460°C) but ~180°C.

In parallel with study of mechanisms of photosensitivity we conducted experiments directed to optimization of glass composition with the goal to increase RIC and to decrease losses. It was found that increase of photosensitizers' concentration causes generation of larger concentration of nucleation centers and therefore increases concentration of crystals and decreases size of crystals for the same volume fraction of crystalline phase. This means that scattering for the same RIC should be lower. It was good fortune that in some range of concentrations of photosensitizers we were able to find concurrent increasing RIC for 30%, decreasing scattering by 30% and decreasing induced absorption by 30% (Fig. 11). This optimization resulted in doubling figure of merit (ratio of RIC to induced losses) for new PTR glasses by two times. This success enables fabrication of complex gratings that were beyond technological limits.

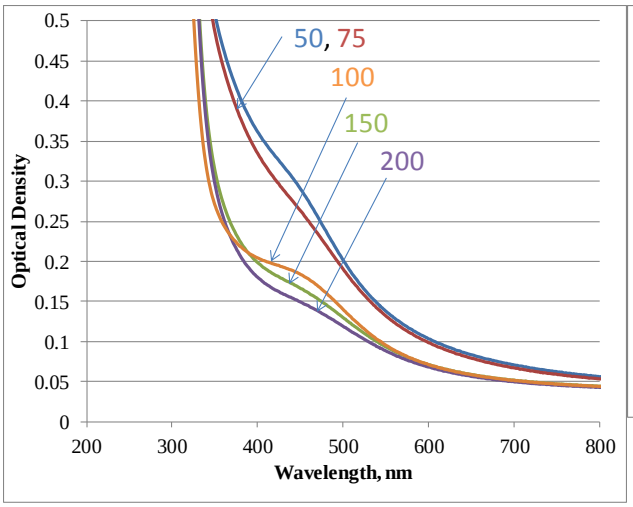

Fig. 11. Absorption spectra of PTR glasses with different concentration of photosensitizer. The sample was exposed to 0.9 J/cm2 at 325 nm and developed for 1 hour at 515ºC. The samples thickness is 1.98 mm.

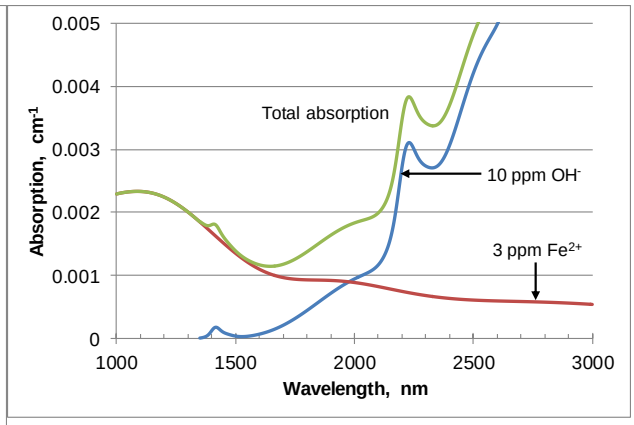

Fig. 12. Absorption spectra of typical contaminations in high purity multicomponent silicate glass.

It should be noted that last achievements in increasing power of Tm and Ho doped fiber and solid state lasers have required more attention to longer wavelength absorption, particularly in 2 μm region. This absorption in high purity glasses was studied in multiple works (see for example Ref. [17, 18, 19]). It was found that to well-known absorption bands of iron at 1.1 μm and water (more exactly hydroxyl ions OH^-) at 2.8 μm, there are several other absorption bands that are difficult to distinguish because of mutual masking (Fig. 12). This figure shows estimated absorption spectra for small concentration of iron and water in multicomponent silicate glasses. One can see that while in the range of 1 μm the dominant absorption is determined by iron, at longer wavelengths absorption of water dominates. The results for this estimation were observed in Ref. [20]. While we have demonstrated homogeneous multicomponent glasses with iron concentration at the level of 1 ppm[21], no positive results were achieved in the technology of a photosensitive glass with low level of water contamination along with high optical homogeneity.

We started a development of a glass fabrication setup which allows effective dehydration of silicate, germanate and tellurite glasses while keeping high optical homogeneity. This technology would enable fabrication of optical glass with low admixture of hydroxyl and identification of residual sources of losses that are currently masked by hydroxyl absorption. This study should

[17] E. N. Boulos, L. B. Glebov, T. V. Smirnova. Absorption of Iron and Water in the Na2O-CaO-MgO-SiO2 Glasses. Part 1. Separation of Ferrous and Hydroxyl Spectra in the Near IR Region. Journal of Non-Crystalline Solids, 221, 213-221 (1997).

[18] L.B. Glebov, E.N. Boulos. Absorption of iron and water in the Na2O-CaO-MgO-SiO2 glasses. II. Selection of intrinsic, ferric, and ferrous spectra in the visible and UV regions. Journal of Non-Crystalline Solids, 242, (1998) 49-62.

[19] L. Glebov, E. Boulos. Absorption Spectra of Iron and Water in Silicate Glasses. Proc. of International Commission on Glass Conference "Glass in the New Millenium." S4-2, Amsterdam 2001.

[20] M.L. Anne, L. Glebova, J. Lumeau and L. B. Glebov. IR absorption edge of multicomponent silicate glasses. 8th Pacific Rim Conference – 2009 PACRIM8-S23-004-2009.

[21] High brightness multiwavelength laser architecture based on volume diffractive gratings in PTR glass. Final report. DARPA / ADHELS program, Contract HR0011-09-C-0089.May 17, 2011.

provide data on the theoretical limit of transparency of these glass matrices between 1.5 and 5 µm. These efforts will give us understanding of what would be practical limits of the transparency for silicate, germanate and tellurite glasses in the 1.5-5 µm spectral region.

The first version of the experimental setup for glass melting in isolated atmosphere is shown in Fig. 13. The basic idea of the setup is to provide isolated atmosphere in the glass melting volume concurrently with an opportunity to produce stirring. To realize this approach, a fused silica cover with a hole in the roof having a diameter a bit larger than that of Pt stirrer was placed on the top of Pt crucible used for glass melting. Dry air was purged under the cover through a hole in the furnace sole. Small difference in diameters of the hole in the cover's roof and the stirrer's rod provided positive pressure under the cover and prevented penetration of atmospheric air to the crucible. For initial experiments we used standard pressed air and a commercial air drier. Air flow was measured and controlled.

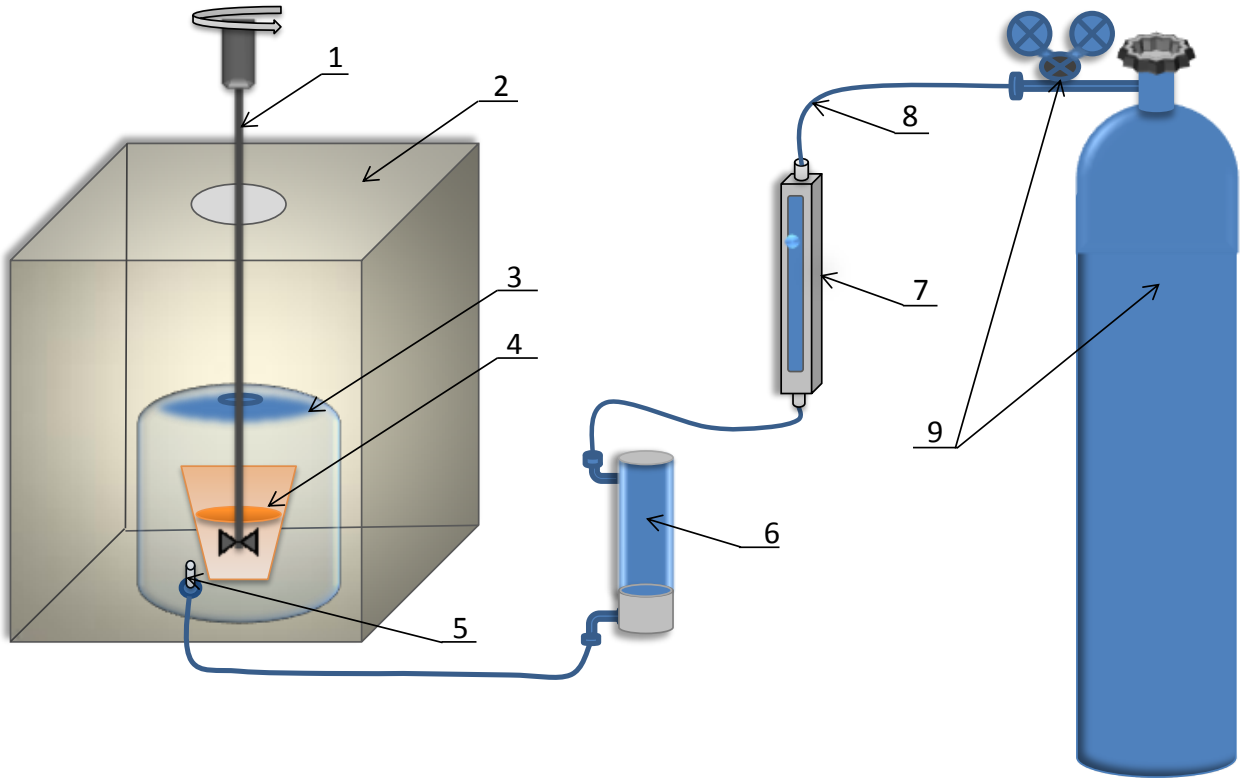

Fig. 13. Experimental setup for glass melting in isolated atmosphere.

1. Rotating Pt Stirrer
2. Glass melting furnace
3. Fused silica cover tight the Pt crucible
4. P crucible with the batch for dry glass melt
5. Ceramic tube supplying the dry gas which is pumped inside the fused silica crucible
6. Drying agent cylinder for drying the compressed air
7. Gas flowmeter
8. Plastic piping system
9. Compressed air cylinder with the gas flow regulators

The first experiment was made with photo-thermo-refractive (PTR) glass. High purity raw materials were used without additional dehydration procedures (they will be applied in future experiments). IR fractions of absorption spectra of glasses prepared by a conventional technology and by melting in isolated volume are shown in Fig. 14. One can see that IR absorption was mitigated for more than two times. We consider this result as a proof of concept for a technology providing both mitigation of hydroxyl contamination and high optical homogeneity by stirring in the isolated volume.

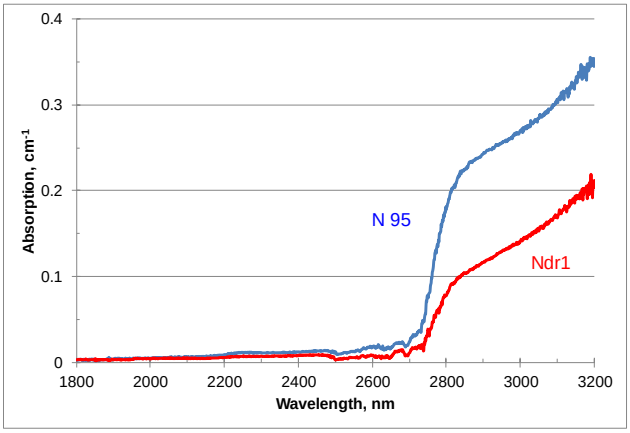

Fig. 14. IR absorption spectra of a multicomponent photo-thermo-refractive glass conventionally melted in open atmosphere (blue) and in isolated volume with dry air purging (red).

It is known that hydroxyl groups can efficiently affect process of crystalline phase precipitation in glasses. Therefore, one of the tasks in those experiments was to study refractive index change and losses after UV exposure followed by thermal development that resulted from crystalline phase of NaF precipitation in exposed areas. It is important to note that refractive index change in dehydrated glass was the same as in a conventional PTR glass and no additional scattering was observed. These results pave the way to effective use of holographic optical elements in high power laser systems operating in 2 μm spectral range.

2.2. Crystalline phase precipitation and scattering

Preliminary observations have shown that the presence of scattering from the surface or/and the bulk of pristine PTR glass will have a deep impact on the scattering losses measured after UV-exposure and thermal treatment. It was shown that this scattered light will interfere with the incoming beam forming a new type of scattering loss (so-called holographic scattering) that will result in a ring of scattered light that will have very specific spectral and angular selectivity. However, no specific study aiming to understand clearly how surface and bulk scattering separately contribute to holographic scattering was performed.

To study the influence of surface scattering of optically polished PTR glass samples on scattering in UV and thermally treated PTR glass, a 5 mm thick sample of PTR glass was cut into two 25×12 mm^2 samples. Back side of each sample was covered with a blackened matching liquid to diminish as much as possible the back reflection and scattering. Then one part was UV-exposed

by scanning a He-Cd laser at 325 nm with dosage of 0.9 J/cm^2 while the beam directly hit the front surface. The other part was UV-exposed through a 20 mm thick high quality fused silica flat. The contact between the two glasses was performed using a drop of matching liquid. This second type of exposure permitted to decrease the intensity of the scattered light that will interfere with the specular beam transmitting in the volume of the PTR glass sample. Finally, both glasses were thermally developed for 100 minutes at 485^{o}C followed by 1 hour at 515^{o}C to induce refractive index change. After processing, both samples were shined using a green He-Ne laser at 543 nm and aligned such as holographic scattering results in rings with comparable diameters (Figs. 15-a and 15-b). Intensity of scattering rings appears larger in samples UV-exposed directly than in samples UV-exposed through the fused silica flat. Therefore, this experiment tends to confirm that surface scattering in pristine PTR glass results in a non-negligible fraction of holographic scattering.

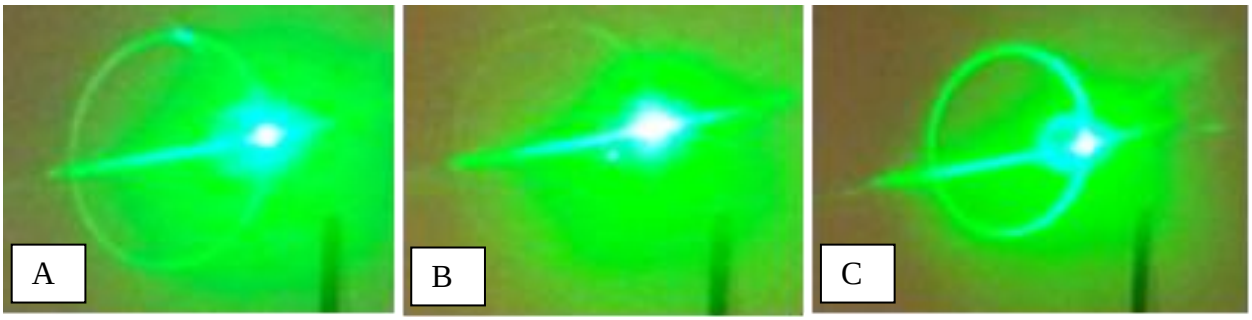

Fig. 15. Holographic scattering as revealed by shining a green He-Ne laser through PTR glasses after UV-exposure and thermal treatment. A - was obtained after UV-exposure of a regular PTR glass, B - was obtained after UV-exposure of a regular PTR glass through a fused silica window and C - was obtained after UV-exposure of PTR glass with a high number of bubbles.

We then studied the influence of bulk scattering on holographic scattering and more precisely the effect of bubbles and inclusions. Another 5 mm thick pristine PTR glass was UV-exposed by scanning a He-Cd laser at 325 nm with dosage of 0.9 J/cm^2. But the chosen sample had a large number of large and small bubbles that would result in significant bulk scattering. This sample was thermally developed for 100 minutes at 485^{o}C followed by 1 hour at 515^{o}C to induce refractive index change. After processing, this sample was finally shined using a green He-Ne laser at 543 nm and aligned such as holographic scattering results in rings with diameter comparable to the previous one (Fig. 2-c). Very bright scattering rings can be observed, proving the severe consequences of bubbles and inclusions on holographic scattering.

The effect of dosage of UV-exposure on the losses in regular PTR glass and effect of co-doping of PTR glass with rare earth ions was studied. Regular PTR glass samples were UV-exposed at 325 nm with dosages of 0.5, 1, 2 and 4 J/cm^2, then nucleated for 100 minutes at 485^{o}C and heat treated at 515^{o}C for 40, 70 and 130 minutes. Samples were finally bleached and re-polished and refractive index change and losses at 750 nm were measured in each glass. It was found that after bleaching the induced absorption in visible and near IR regions, losses near 750 nm are mainly determined by scattering. Dependence of scattering coefficient on refractive index change is plotted in Fig. 16. One can see that for different thermal treatment duration, dependence of losses on refractive index change is dramatically different. Such evolution can be explained by the nature of the scattering losses. Scattering is due to the appearance of nano-crystals of NaF with a smaller refractive index than that in the glass matrix. Because of small size on NaF crystals

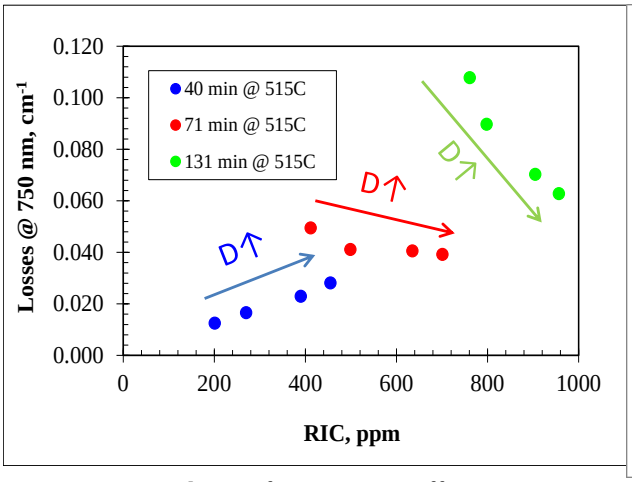

Fig. 16. Dependence of scattering coefficient at 750 nm on refractive index change measured in PTR glass exposed with different dosages 0.5, 1, 2 and 4 J/cm^2 followed by a thermal treatment for 40, 70 and 130 minutes at 515^{o}C.

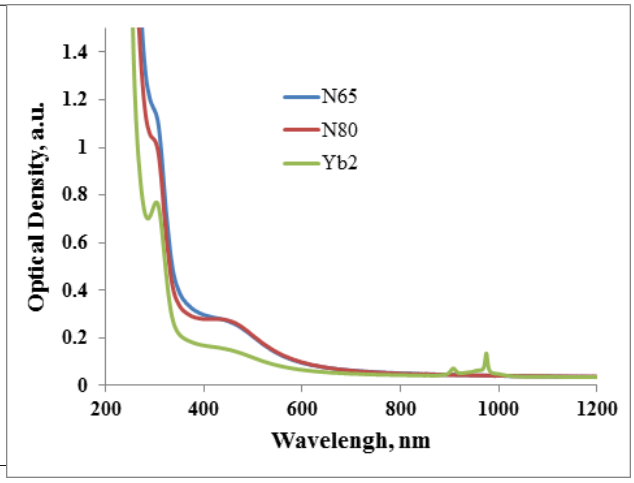

Fig. 17. Absorption spectra of irradiated and developed regular PTR glasses (N65 and N80) and Yb doped PTR glass.

(about 15 nm), scattering follows the Rayleigh regime. Its amplitude is therefore linearly dependent on the volume fraction of crystals and has a fourth power dependence on the crystal diameter which explains why changing the dosage of UV-exposure changes the scattering losses level [22]. However, one general trend is that, for a given refractive index change, increasing the dosage of UV-exposure appears as a good way to decrease losses. However, one should remember that increasing the dosage will also tend to increase the effect of refractive index change saturation on dosage. Actually, it was shown that the refractive index change saturation on dosage induces a distortion of the refractive index modulation of volume Bragg gratings. This effect is equivalent to a decrease of the effective refractive index modulation. Thus, while changing the dosage of UV-exposure appears as a possible way to decrease scattering losses; its usage could be restricted due to its indirect consequences on Bragg gratings diffraction efficiency.

Working on development of new types of PTR glasses for the monolithic laser, which have doped regular glass with rare earth (RE) elements, such as Nd, Yb and Er [23]. It was found that PTR glasses containing RE elements as a rule have lower scattering after the hologram recording and the thermal development. In Fig. 17, it clearly can be seen that Yb doped PTR glass has lower scattering than two regular PTR glasses. All these glasses have very close refractive index change after the thermal development, which is the measure of the photosensitivity of PTR glass. It is not easy to make the final conclusion about this effect since Nd and Yb, which were used in our study, have absorption bands in the spectral region of our interest. So, we expect to continue this study using La, because this element does not have any absorption in UV-Vis-NIR region.

[22] J. Lumeau, L. Glebova and L. B. Glebov, Journal of Non Crystalline Solids, 354, 425–430 (2008)
[23] Larissa Glebova, Julien Lumeau, Leonid B. Glebov. Photo-thermo-refractive glass co-doped with Nd3+ as a new laser medium. Optical Materials 33 (2011) 1970–1974.

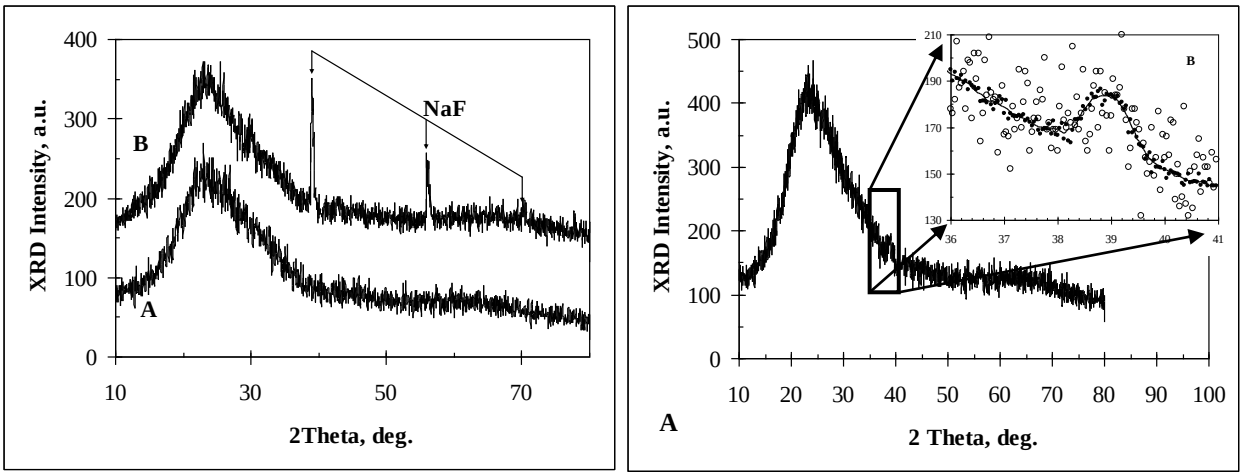

Fig. 18. X-ray diffraction patterns for PTR glass samples: left – unexposed and developed at 600ºC for 15 hours; right – exposed for 2 J/cm^2 at 325 nm and developed at 520ºC for 1 hour.

As was discussed, RIC in PTR glass is considered as a result of photoinduced thermal precipitation of crystalline phase of NaF in areas exposed to UV radiation. Stresses in vicinity of NaF crystals of about 15 nm resulted from great difference in coefficients of thermal expansion of crystals and glass matrix cause the RIC in this two-phase system[24]. However, definitive understanding of the mechanism (or mechanisms) of RIC is far from completion. Figure 18 shows X-ray diffraction patterns for PTR glass samples developed for different times at different temperatures. One can see that while spontaneous crystallization at high temperature provides

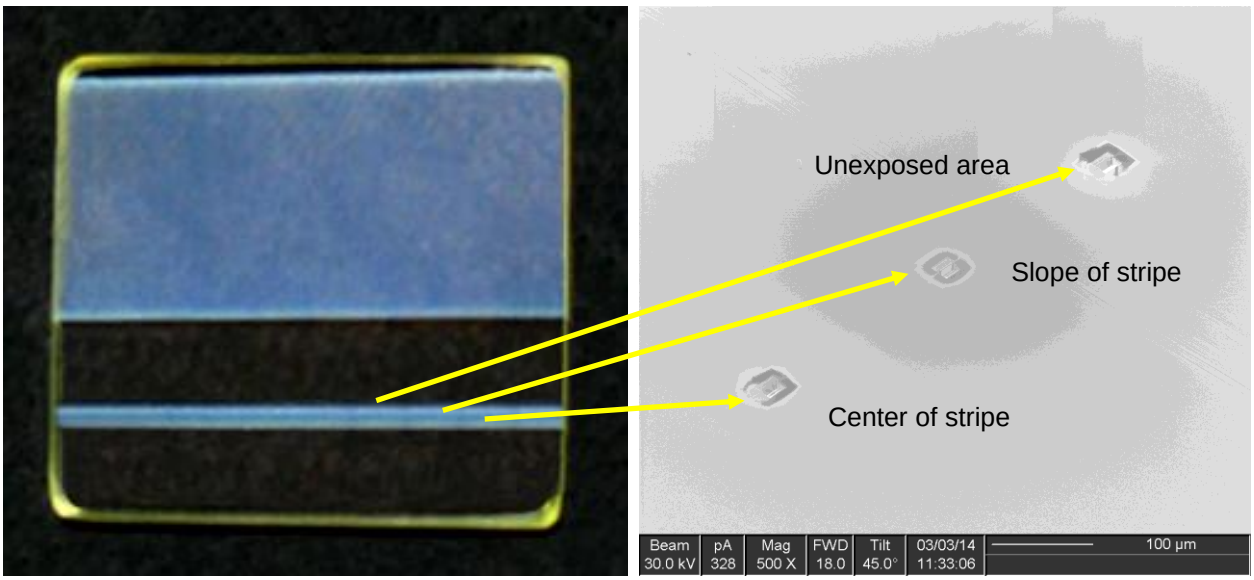

Fig. 19. Left: photo of a PTR glass sample exposed to UV radiation at 325 nm with a rectangular pattern (top) and a stripe having lateral Gaussian dosage profile (bottom). Maximum dosage in the center 0.9 J/cm^2, stripe width (FWHM) 1 mm. developed at 515ºC for 1 hour. Right: photo of the sample areas taken to prepare slides for transmission electron microscopy (TEM).

[24] Julien Lumeau, Larissa Glebova, Valerii Golubkov, Edgar D. Zanotto, Leonid B. Glebov. Origin of crystallization-induced refractive index changes in photo-thermo-refractive glass. Optical Materials 32 (2009) 139–146.

undoubtable evidence of precipitation of cubic NaF, identification of crystalline phase for the sample developed at conditions used for hologram recording requires specific treatment to can see even the main peak of NaF in vicinity of 39º. Multiple attempts to make photos of crystals produced at such regime by electron microscope were not successful for many years because electron beams cause alteration of crystals. Finally Dr. M. Klimov at AMPAC/UCF developed a method that excludes alteration while enabling to detect crystalline phase of few nanometers at early stages of thermal development.

To confirm the role of photoinduced crystallization the following experiment was performed. A sample of PTR glass ($15\times15\times2mm^3$) was exposed to UV radiation at 325 nm with two patterns (Fig. 19). The first one is rectangular with a dosage of 0.9 J/cm^2. The second one is a stripe with a Gaussian lateral profile of dosage. Dosage in the center of the stripe was 0.9 J/cm^2, stripe width (FWHM) 1 mm. The sample was developed at 515ºC for 1 hour. Measurements in the shearing interferometer [25] have shown usual RIC with the shape close to Gaussian one. X-ray diffraction showed the presence of a single crystalline phase of cubic NaF. Three samples were taken by a focused ion beam from different positions in the stripe area (Fig. 12, right). One sample was taken from the center of the stripe, another – next to the visible edge of the stripe and the third from an unexposed area next to the stripe.

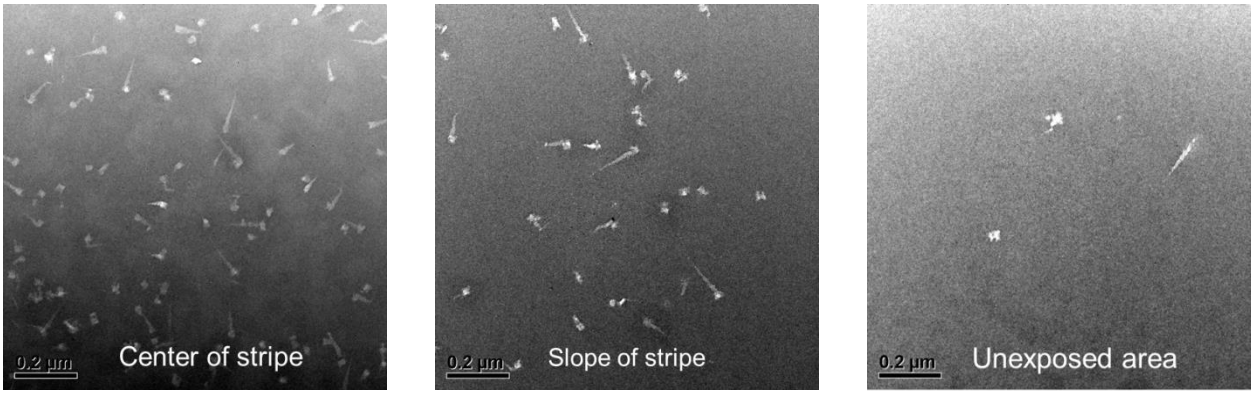

Fig. 20. Transmission electron micrographs of the different areas of the exposed stripe on the sample depicted in Fig. 19.

One can see in Fig. 20 that in the center of the stripe there are a number of crystals having complex shape of cubes about 15 nm with pyramids at one of the cube's sides about 100 nm. Average distance between crystals is about 100 nm. There is no anisotropy in the spatial distribution of these crystals. This micrograph with highest concentration of crystals corresponds to maximum of RIC in the exposed stripe. The first impression from this micrograph is that there are two different crystals grown next to each other. However, X-ray diffractometry does not show the second crystalline phase. Therefore, we need to expect that by some reason NaF crystals in PTR glass grow in such a complex shape. This phenomenon requires additional study. The next micrograph is taken from the stripe area with smaller dosage. One can see that while the shape of crystals is the same (cube with pyramid), the size of crystals is larger and their concentration is smaller. This is naturally explained by smaller concentration of nucleation

[25] O.M. Efimov, L.B. Glebov, H.P. Andre. Measurement of the induced refractive index in a photothermorefractive glass by a liquid-cell shearing interferometer. Appl. Optics, 41 (2002) 1864-1871.

centers produced by smaller dosage of UV radiation. The third micrograph taken from the unexposed area shows a few large crystals. These crystals have complex shape (dendrites) which is typical for spontaneous crystallization. Thus we have the first demonstration of a crystalline phase shape in PTR glass treated with a regime similar to hologram recording.

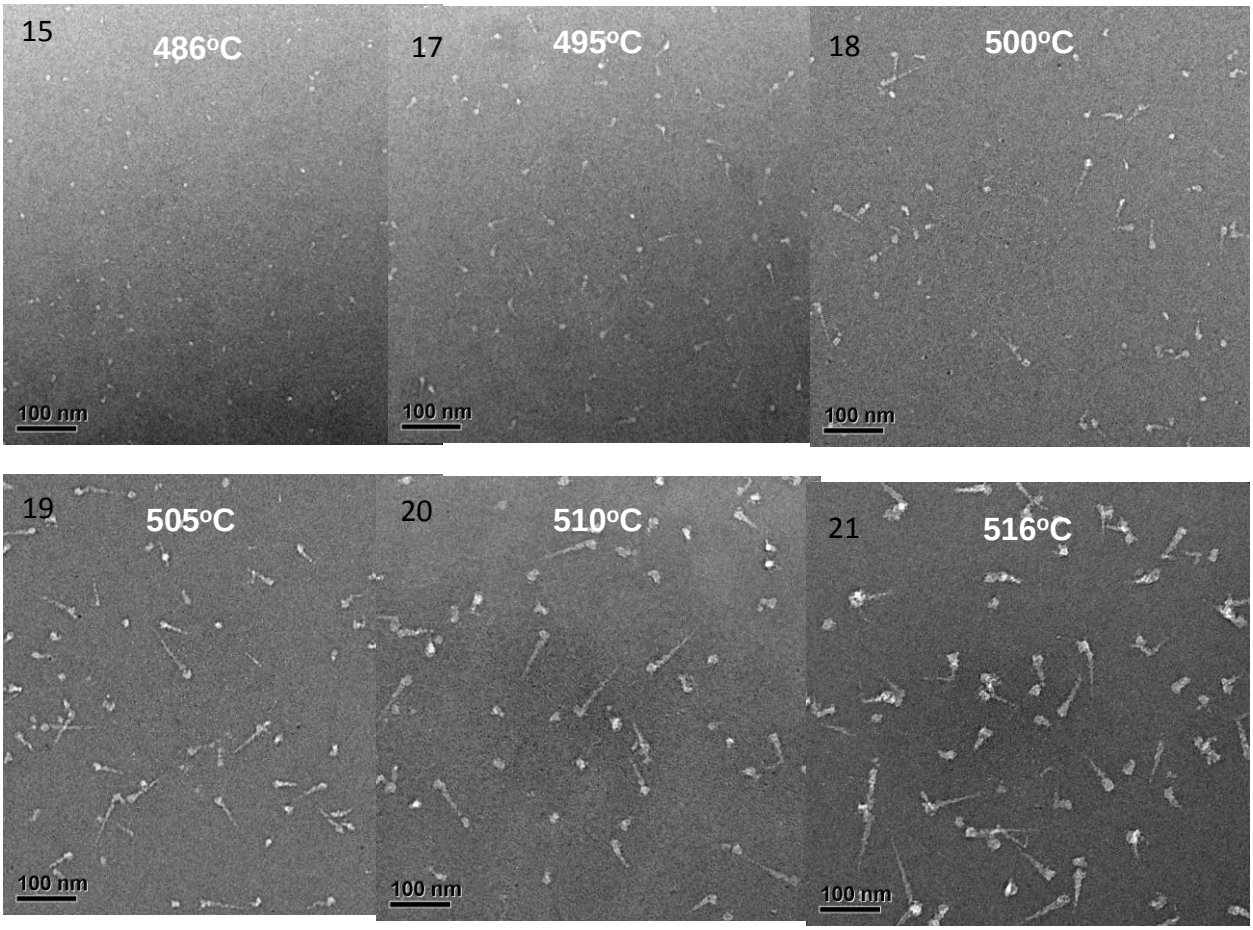

Fig. 21. Transmission electron micrographs of the PTR glass sample exposed to a uniform laser radiation for 1 J/cm^2 at 325 nm, nucleated at 485°C for 1 hour and developed at different temperatures for 1 hour.

The next experiment was to study dependence of features of the crystalline phase on temperature of thermal development. The samples of PTR glass were exposed in the same manner as shown in Fig. 19. Then they were nucleated at 485ºC for one hour and then developed for one hour at different temperatures. The stripes were used to measure RIC. A few slides were taken from the uniformly exposed area of each sample for TEM study. The micrographs are shown in Fig. 21. One can see that there is dramatic dependence of size of crystals on temperature of thermal development. It is important that the shape of crystals is the same for different temperatures of development.

Image treatment of micrographs in Fig. 21 has shown that length and width of crystals exposed to UV radiation and nucleated at 485ºC linearly increased with the temperature of development (Fig. 22). At the same time concentration of crystals is the same for all studied conditions of thermal development. This means that concentration of crystals is determined by concentration

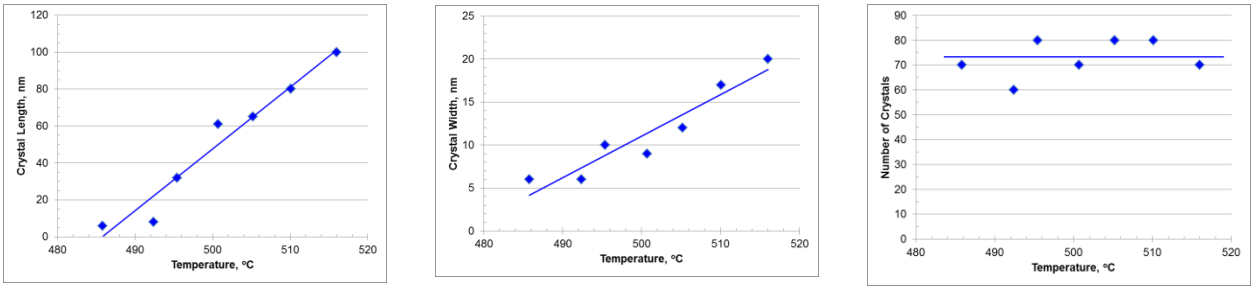

Fig. 22. Dependence of crystal length (left), width (center) and concentration (right) on temperature of development. PTR glass samples exposed to a uniform laser radiation for 1 J/cm^2 at 325 nm, nucleated at 485^{o}C for 1 hour and developed at different temperatures for 1 hour.

of nucleation centers produced by UV radiation and the first thermal treatment (nucleation). These features are in agreement with crystal growth models discussed in the previous section for conditions when crystalline components are far from depletion. Linear increase of width and length of crystals with increasing development temperature means cubic increase of the crystalline phase volume. Figure 23 shows dependence of RIC on temperature of development. One can see that the increase of RIC with increased development temperature is well described by a fit with cubic function. This means that RIC is proportional to the volume of crystalline phase precipitated in PTR glass. This result produced with transmission electron microscopy confirms our old results produced with comparison of intensity of X-ray diffraction with RIC while it brings new important information about size and concentration of crystals.

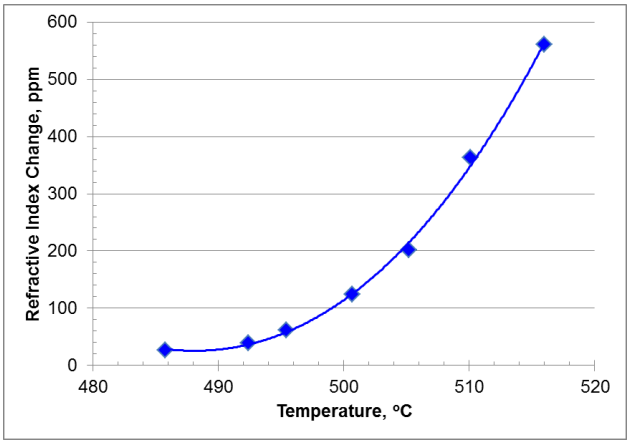

Fig. 23. Dependence of refractive index change (RIC) on temperature of development for the samples exposed to a uniform laser radiation for 1 J/cm^2 at 325 nm, nucleated at 485^{o}C for 1 hour and developed at different temperatures for 1 hour. Solid line is a fit by a cubic function.

It must be noted that the new results obtained with TEM show that while there is a very good correlation between concentration of crystalline phase and RIC, the distance between adjacent crystals is about 100 nm. The most common Bragg mirror for 1.06 μm radiation has period about 300 nm. The shortest wavelength for Bragg mirror was produced by recording in counter propagating beams at 325 nm.[26] This grating has a period about 100 nm. Relative diffraction efficiency in high frequency VBGs was close to 100%. This means that high quality spatial patterns with periods down to 100nm were recorded. However, it is not possible to draw high quality sinusoidal pattern with period of 100 nm in a recording medium with the same grain size. Therefore it is necessary to look for additional mechanisms of RIC in PTR glass.

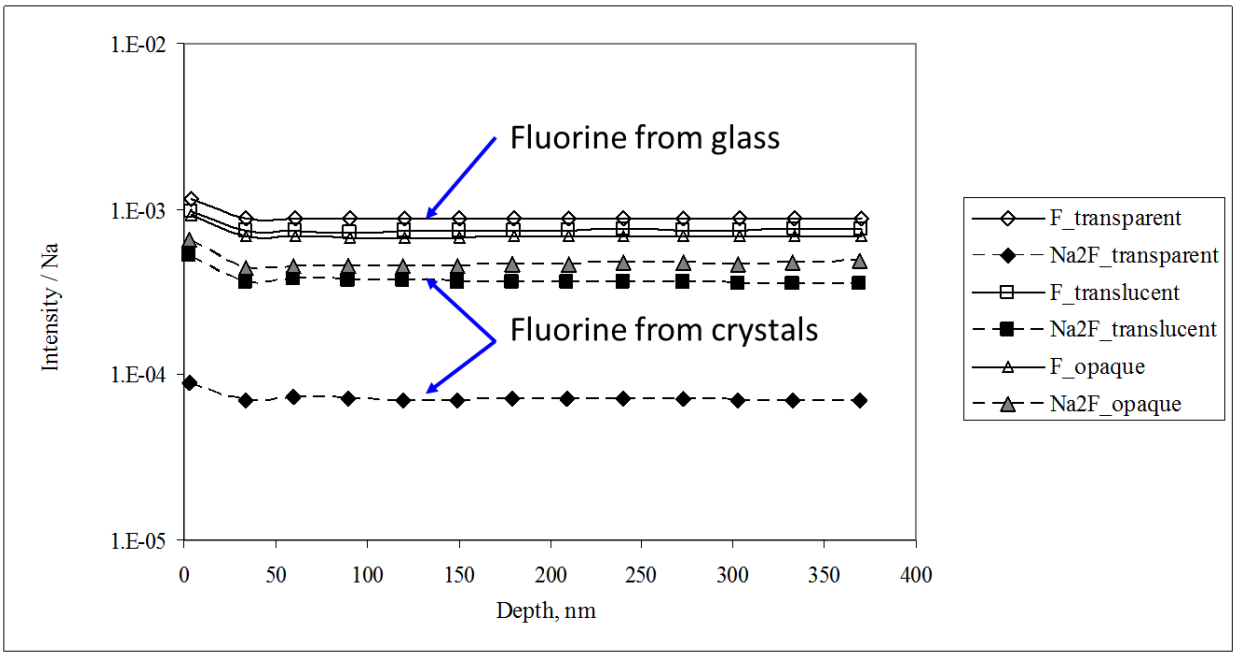

Fig. 24. Vertical profiles of SIMS signal for F^- and $(NaF)Na^+$ ions in virgin PTR glass (transparent), partially crystallized (translucent) and completely crystallized (opaque).

To study distribution of crystals in PTR glass, a new method with high spatial resolution was developed. This Secondary Ion Mass Spectroscopy (SIMS) where the sample is exposed to ion beam that slowly etches the surface of the sample while the emitted ions are analyzed with a mass spectrometer. This method allows analysis of composition with vertical resolution of several nanometers. This method is widely used for chemical analysis of thin films and nano-devices. We used SIMS for analysis of PTR glass composition for a long time. Some time ago, it was found that fluorine produces several different ions which are F^-, $(NaF)Na^+$ and $2(NaF)Na^+$. It was found that for virgin PTR glass F^- signal about order of magnitude larger that $(NaF)Na^+$ one (Fig. 24). However, after crystallization, F^- signal drops by about two times while $(NaF)Na^+$ signal increases by 5 times. This result enables an important conclusion that under ion exposure of fluorine containing glass mainly single fluorine ions are emitted. The same exposure of glass containing NaF crystals significant part of emitted ions is $(NaF)Na^+$. This phenomenon was used

[26] O.M. Efimov, L.B. Glebov, V.I. Smirnov. High-frequency Bragg gratings in photothermorefractive glass. Optics Letters, 23 (2000) 1693-1695.

for analysis of spatial distribution of NaF crystals in PTR glass after different regimes of UV exposure and thermal development.

A sample of PTR glass was exposed to uniform UV radiation at 325 nm and developed for one hour at 650ºC to grow large NaF crystals that could be detected in optical microscope. A slice was cut from this sample in direction perpendicular to the front surface exposed to UV radiation. The micrograph of this slice is shown in Fig. 25, left. One can see that crystals could be observed only in deep layers of glass sample but the surface layer of 8 μm is free from crystals. This phenomenon is explained by effusion of fluorine from the surface layer during thermal development. The right figure shows SIMS profiles for F^- and $(NaF)Na^+$ ions. One can see that while in the bulk of the sample both ions have similar signals with difference in magnitude about 2, the surface layer with thickness of 8 μm shows dramatic decrease of $(NaF)Na^+$ signal. It is important that SIMS can detect this signal from nano-sized crystals that could not be observed in optical microscope.

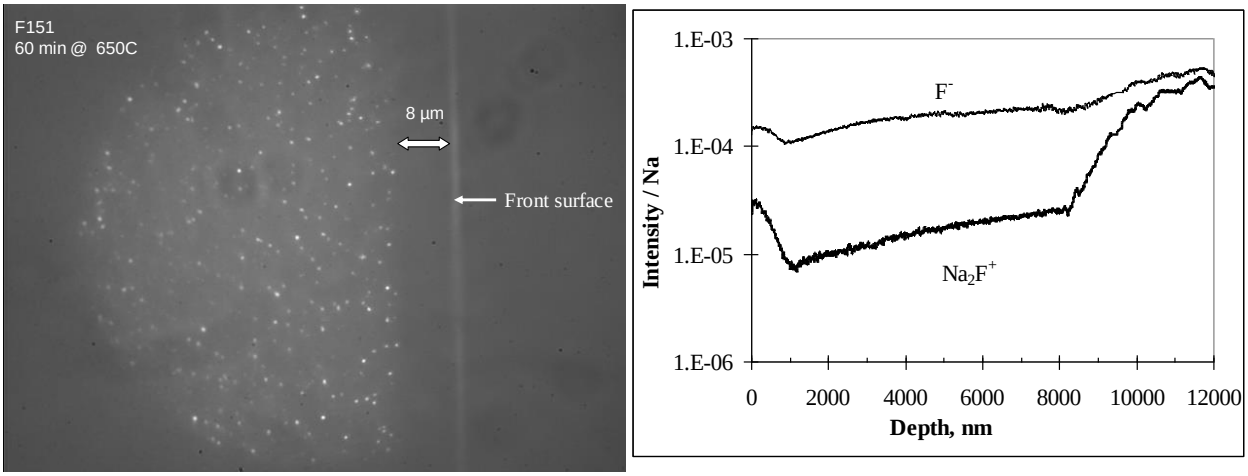

Fig. 25. PTR glass sample exposed to 1 J/cm^2 at 325 nm and developed at 650ºC for one hour. Left: Micrograph of the slice of the sample cut perpendicularly to the exposed front surface. Right: Profiles in depth of SIMS signals F^- and $(NaF)Na^+$.

Thus we can state that uniform UV exposure of PTR glass follower by thermal development produces nanocrystals of NaF with a typical size of 15×15×60 nm^3. These crystals are detected by TEM, SIMS and X-ray diffraction. All methods show that there is high contrast between exposed area with a distance between crystals about 100 nm and unexposed area where a small number of large crystals are produced.

While a description of photosensitivity of PTR glass exposed to uniform pattern of UV radiation is obvious, difference between refractive indices in exposed and unexposed areas (RIC), such a description for a periodical UV pattern requires introducing some definitions. They are depicted in Fig. 26. Refractive index of original virgin PTR glass is n. After thermal treatment of virgin PTR glass at a temperature of development, which is higher than glass transition temperature T_g, its refractive index changes resulting from structural relaxation and possible chemical reactions and becomes n_{td}. An exposed part of the glass plate shows refractive index n_{ed}. Difference between these indices is RIC $\Delta n = n_{td} - n_{ed}$. If a glass plate is exposed to a periodical UV pattern with 100% visibility of fringes and dosage in fringes equal to that for a uniform pattern, the

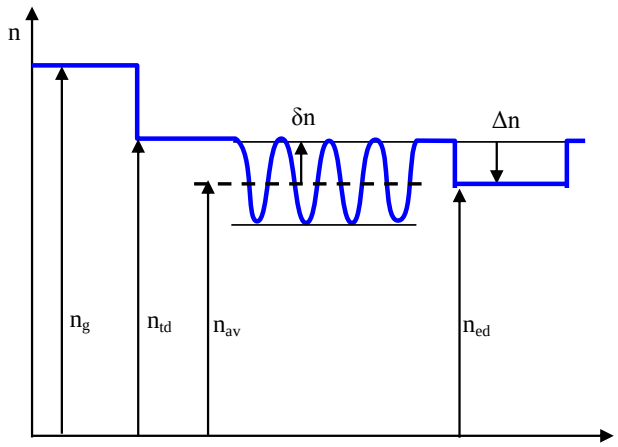

Fig. 26. Definitions of refractive index (n) in virgin annealed PTR glass (n_g) and after thermal development: n_{td} – virgin glass, n_{ed} – glass exposed to uniform UV radiation, n_{av} – average refractive index in glass exposed to periodical UV pattern. Δn – refractive index change (RIC) in uniformly irradiated area, δn – refractive index modulation (RIM) in periodically irradiated area.

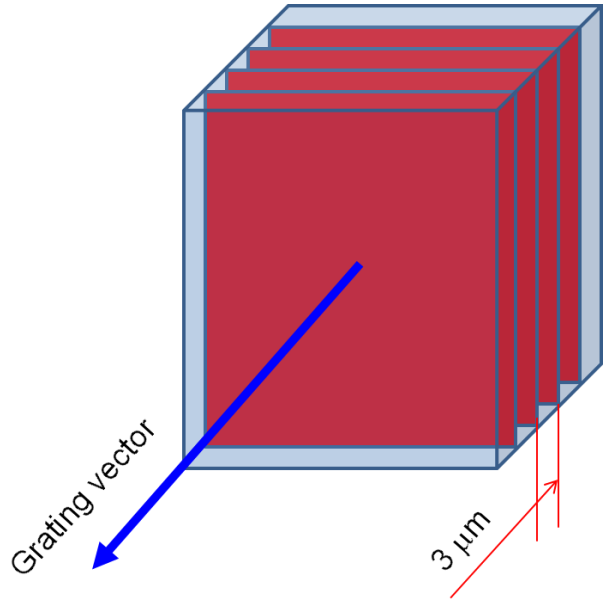

Fig. 27. Volume Bragg grating with period of 3 μm for studying distribution of crystals.

average refractive index of an exposed area would be n_{av} with spatial refractive index modulation of δn. If all processes are linear and there is no interaction between fringes $\Delta n=2\delta n$. In reality this ratio could be different for different conditions of exposure and development and the coefficient could vary from 1 to 2.

To study distribution of crystals in gratings, a sample was prepared by exposure to a UV pattern with period of 3 μm (Fig. 27). Diffraction at this grating in transmitting geometry was tested, period of 3 nm was confirmed and refractive index modulation of δn=250 ppm was measured. This grating studied with SIMS to check spatial distribution of fluorine. Figure 28 shows a fraction of the total profile chart that presents dependence of concentration of emitted $(NaF)Na^+$ and $2(NaF)Na^+$ ions on distance in the direction perpendicular to grating vector (parallel to planes of constant refractive index). One can see that there are no detectable fluctuations. Similar measurements in direction collinear to grating vector show periodical variations of the signals

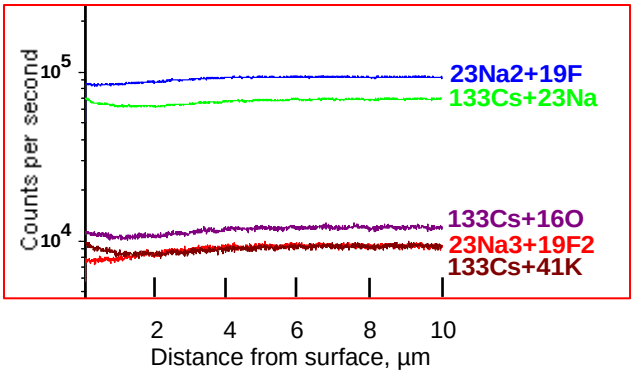

Fig. 28. SIMS profiles for $(NaF)Na^+$ (blue) and for $2(NaF)Na^+$ (red) in direction perpendicular to the grating vector in Fig. 27.

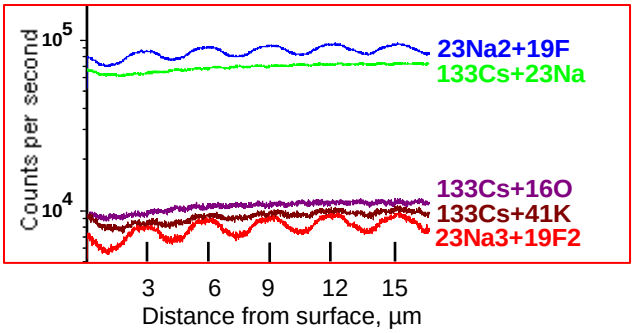

Fig. 29. SIMS profiles for $(NaF)Na^+$ (blue) and for $2(NaF)Na^+$ (red) in direction collinear to the grating vector in Fig. 20.

with period of 3 μm (Fig. 29). As it was discussed earlier, this means that concentration of NaF crystals has periodical variations. This result confirms that volume Bragg gratings in PTR glass are produced by refractive index change resulted from precipitation of NaF crystals. However, there is an interesting peculiarity in this case. One can see in Fig. 25 that "crystalline" signal in glass area with no crystals is about order of magnitude less than that in crystallized area. Figure 29 shows that difference in signals produced by exposed and unexposed areas is less than two times. This effect could be a result of low visibility of fringes (background illumination in dark stripes) or a reason to think about additional, unknown for us mechanism of refractive index change. This phenomenon needs additional study.

One of the problems with comparison of different exposure patterns is effect of inequality of different samples, fluctuations in exposing power temperature regimes in development furnaces, etc. Therefore, to extend our study to periodical structures with smaller periods, we have prepared a sample with a complex grating recorded in the volume. This is a moiré grating produced by sequential recording of two collinear gratings with slightly different periods. In this case an average exposing dosage is the same across the aperture but uniform exposure patterns

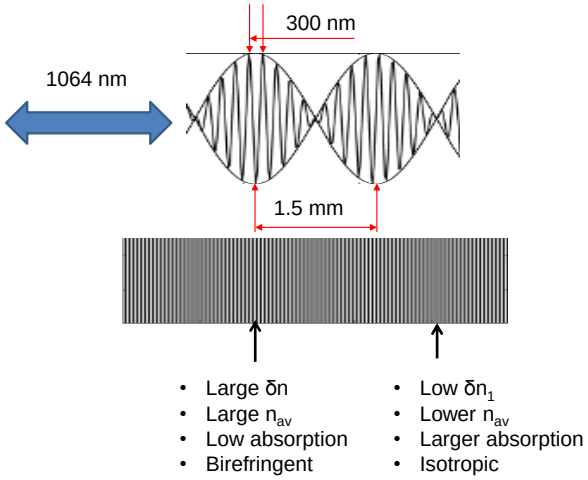

Fig. 30. Moiré grating in PTR glass produced by sequential recording of two collinear gratings with slightly different periods. Resonant wavelength 1064 nm, period 300 nm, period of envelope 1.5 mm.

alternate with periodical patterns (Fig. 30). In our case periodical pattern has period of 300 nm, and long envelopes have period of 1.5 mm. Thus, in the same sample we have both periodic and uniform patterns produced in the same conditions in the same sample.

This study has revealed a number of new phenomena that forces us to reconsider a number of results obtained in early times. The first important feature of PTR glass is its linearity for exposure to low power radiation at 325 nm. The reciprocity law (independence of RIC and induced absorption on power of irradiation) for PTR glass [27]was demonstrated a lot of years ago and no effect of size of the exciting beam was detected in any experiments. However, it was found that the sample with moiré grating inside demonstrates dark and light stripes and sinusoidal profile of average refractive index (Fig. 31). The areas with high refractive index modulation (δn), where strong diffraction grating is recorded, show larger average refractive index (n_{av}) and smaller additional absorption while the areas with no refractive index modulation show smaller average refractive index and larger additional absorption. This feature is confirmed by SIMS measurements that have shown lower concentration of NaF crystals in areas with uniform illumination.

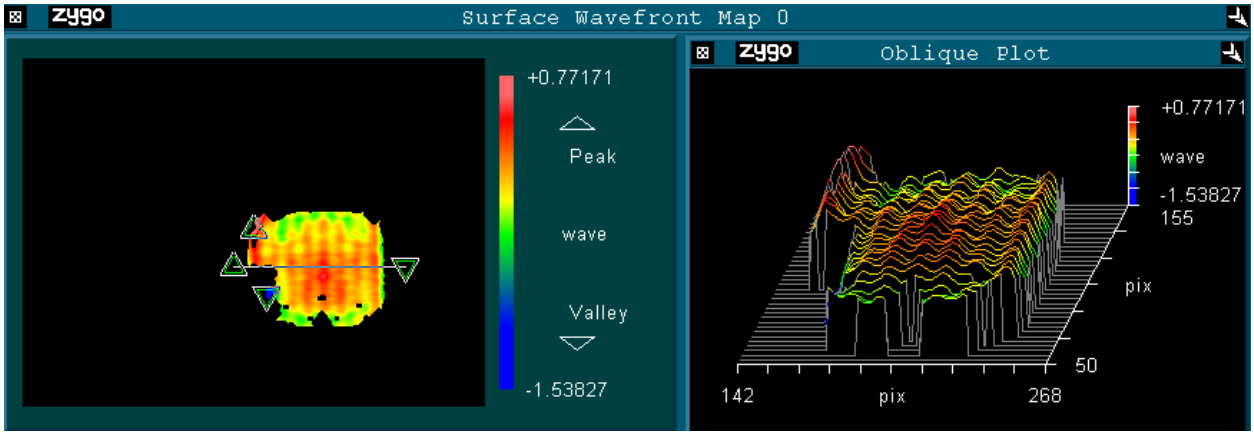

Fig. 31. Refractive index profile in a PTR glass sample with moiré grating. Long period refractive index modulation is 15 ppm.

It should be noted that for conventional uniform gratings, where refractive index modulation is determined by dosage, the situation is opposite: the larger refractive index modulation, the smaller average refractive index and larger additional absorption. It is clear that higher dosage causes higher level of photoionization, which causes larger induced absorption and larger number of nucleation centers, which causes larger refractive index modulation and correspondingly smaller average refractive index (as could be seen in Fig. 26). If one can use this logic for moiré gratings, lighter coloration and higher average refractive index in areas with high refractive index modulation should correspond to lower dosage. However, dosage is the same in all areas. Thus this important result cannot be explained within existing knowledge about PTR glass and requires additional study.

[27] O.M. Efimov, L.B. Glebov, H.P. Andre. Measurement of the induced refractive index in a photothermorefractive glass by a liquid-cell shearing interferometer. Appl. Optics, 41 (2002) 1864-1871.

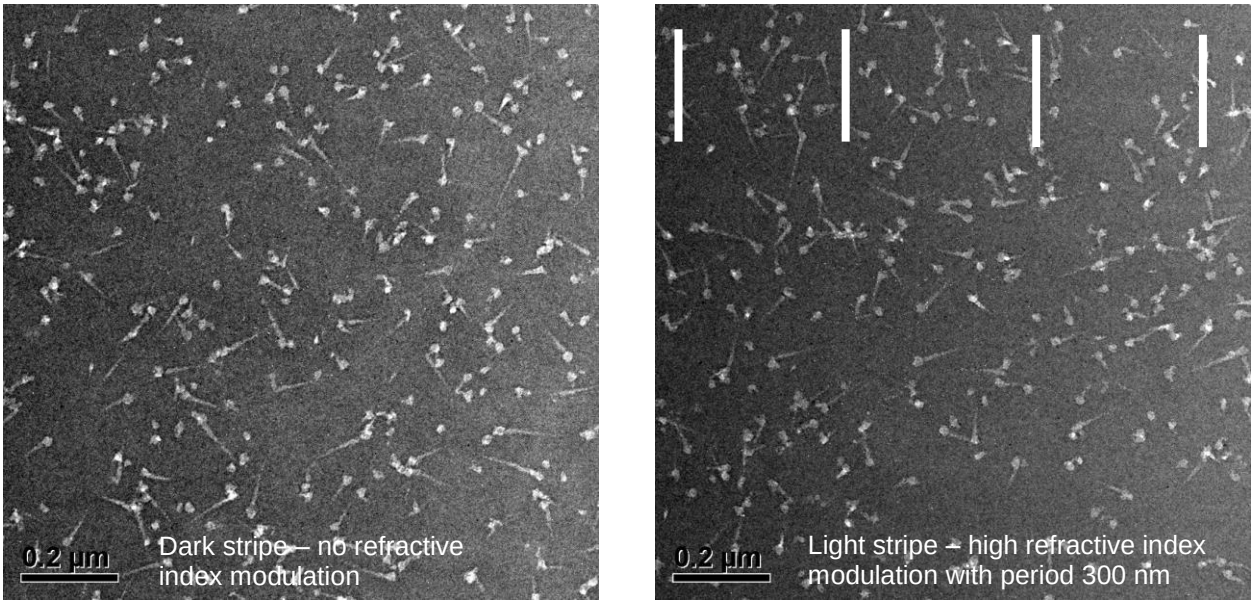

Fig. 32. Transmission electron micrographs of moiré grating in PTR glass. The sample was taken from dark stripe (left) and from the light stripe (right). Direction of the micrograph is perpendicular to grating vector. White lines shows the period of grating.

TEM study of moiré grating revealed even more unpredictable data. Two samples were cut from the sample from dark stripe with no refractive index modulation and from light stripe with high refractive index modulation (Fig. 32). It was found that size of crystals is the same in both stripes. The concentration of crystals in dark stripe is a bit higher than that in light stripe that support data produced by optical measurements and SIMS discussed above. This concentration corresponds to that in high efficiency uniform gratings. However one cannot see any periodicity in concentration of crystals in light stripe. White lines in the right micrograph shows a period of the grating recorded in this area. To exclude any mistakes in sample orientation, two more samples with orthogonal orientations were cut from the sample and studied. No periodicity in crystal concentration anywhere! This result forces us to state that refractive index modulation in high spatial frequency gratings is not produced by precipitation of NaF crystals!!! This is flabbergasting result which requires further study to understand mechanism of high spatial frequency gratings recording.

2.3. Photo-ionization and photo-thermal refractive index change

Refractive index change in PTR glass is obtained only after a very complex series of chemical and physical process. Moreover, refractive index change is controlled by three interconnected parameters: the dosage of UV-exposure, the thermal treatment temperature and thermal treatment duration. Controlling the final refractive index change in volume Bragg grating is a key point in order to obtain an optimized holographic element. An accurate model predicting the refractive index change after exposure to any UV-dosage and thermal development at any temperature and for any duration is under development. A set of PTR glass samples exposed with a Gaussian profile stripe with dosage at maximum of 0.9 J/cm^2 and then developed for different duration at different temperatures between 485 and 535°C was prepared. Dependence of the refractive index on time of thermal treatment for different temperatures is shown in Fig. 33 for UV dosage of

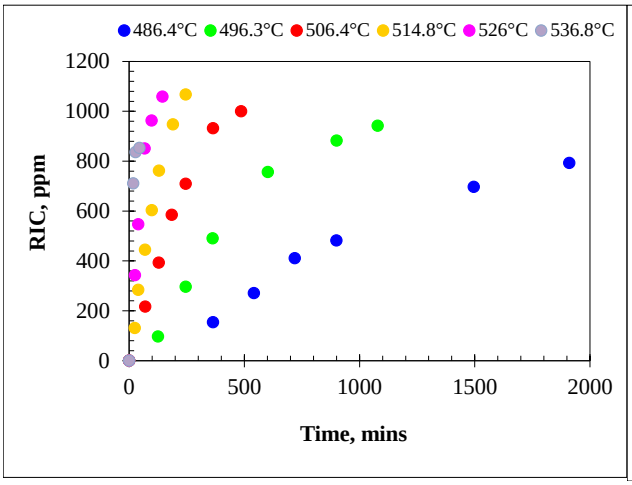

Fig.33. Dependence of the refractive index change on thermal treatment duration measured in PTR glass UV-exposed with dosage of 0.9 J/cm^2 and developed at different thermal treatment temperatures.

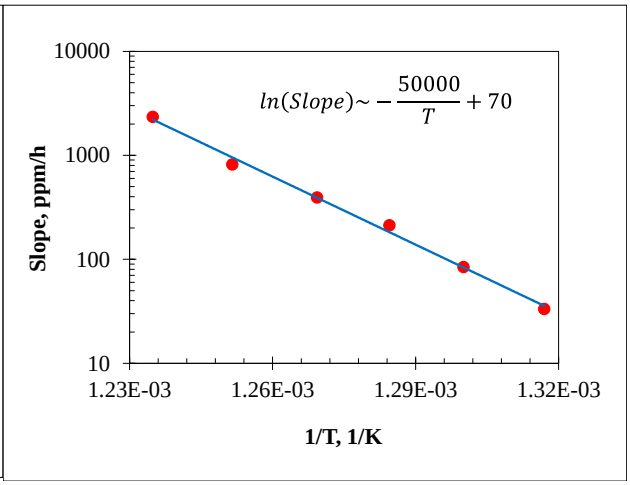

Fig. 34. Dependence of the refractive index decrement slope at t = 0 on temperature of thermal treatment.

0.9 J/cm^2. At development temperature of 485^{o}C, the refractive index change increases very slow. In this case, 40+ hours are required to reach refractive index of 600 ppm which is about ½ of the saturation level. In contrary, when developing at 535^{o}C, approaching the saturation level is obtained after less than one hour, such as the precise control of the refractive index requires extremely precise control on the thermal treatment procedure; therefore using temperatures above than 535^{o}C is also out of any commercial application. In conclusion, we see that the range of useful temperatures for developing PTR glass is equal to only 50^{o}C. From the curves in Fig. 33, we could extract one basic parameter defining the refractive index change kinetics, i.e. the slope of refractive index decrement at t = 0. Figure 34 shows the dependence of this slope (in ppm/hour) on inverted temperature 1/T (in K^{-1}). One can see that the slope at t = 0 follows a Boltzmann law and that the refractive index change kinetics change by 2 orders within 50^{o}C change of the development temperature!! This result demonstrates that any small change of the thermal treatment temperature will induce significantly different refractive index change kinetics and justifies the high interest of being able to perfectly model and predict the refractive index change for any given dosage of UV-exposure and thermal treatment temperature and duration.

One more important parameter could be extracted which is a saturation level of the refractive index change. It is clear from Fig. 33 that there is a dependence of the maximum refractive index change ($\Delta n_{max}(0.9\ J/cm^2, T)$) that can be achieved and the thermal treatment temperature. Maximum refractive index change was calculated on the basis of hyperbolic approximation of kinetics curves. The temperature dependence of the maximum refractive index change is shown in Fig. 35. One can see that, with good approximation, the maximum refractive index change appears to be, within our temperature range, almost a linearly dependent function of the thermal treatment temperature and can be described with the equation:

$$\Delta n_{max}(0.9J/cm^2, T) = \Delta n(0.9J/cm^2, \infty, T) = 5.22(T^oC - 460) + 777 \quad (3)$$

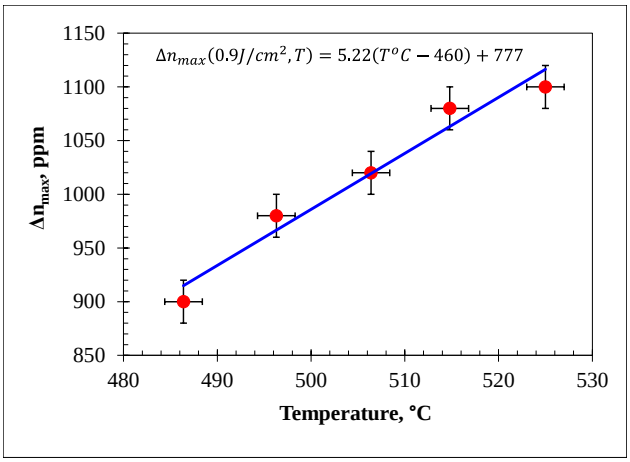

Fig. 35. Dependence of the refractive index change at saturation versus thermal treatment temperature.

As stress is supposed to be one of the main effect causing the refractive index change[28], this linear dependence can be explained by the change of the stress level surrounding the crystal while cooling from thermal treatment temperature down to T_g. Actually, despite the fact that thermal treatment is performed at a temperature above Tg (460°C), and that one would expect that only plastic deformation would occur, the situation is different. It was shown[29] that due to the depletion of NaF, the glass surrounding crystal has a T_g higher than the development temperature resulting in an elastic deformation of the glass that generates larger stress in the crystal and larger refractive index change when higher temperature is used. Therefore higher stresses result in higher the refractive index change.

To generate proper data for modeling, a set of PTR glass samples exposed with a Gaussian profile stripe with dosage at maximum of 0.9 J/cm^2 and then developed for different duration at different temperatures between 485 and 535°C was prepared and characterized. All dependences of refractive index change on dosage of UV-exposure and thermal treatment duration were presented in the last report. The first part of our modeling consisted in analyzing the isothermal refractive index change versus time at constant dosage of 0.9 J/cm^2. We used the Johnson-Mehl-Avrami-Kolmogorov (JMAK) equation [30] to model the refractive index change. This model is generally used to model the crystallization kinetics (i.e. the evolution of the volume fraction of crystals versus time and temperature of thermal treatment) of ceramics. In case of JMAK, the refractive index change kinetics ($\Delta n(0.9\ J/cm^2, t, T)$) is:

$$\Delta n(0.9J/cm^2, t, T) = \Delta n_{max}(0.9J/cm^2, T)\left(1 - exp(-K(T)t^n)\right) \quad (1)$$

Where $\Delta n_{max}(0.9\ J/cm^2, T)$ is the refractive index at saturation with a linear temperature dependence that was presented in the previous report, $K(T)$ is a thermodynamic parameter (with Boltzmann law) describing the slope at t = 0 versus temperature and n is the Avrami coefficient

[28] J. Lumeau, L. Glebova, L. B. Glebov, V. Golubkov and E. D. Zanotto, Optical Materials 32, 139–146 (2009).
[29] G.P. Souza, V.M. Fokin, E.D. Zanotto, J. Lumeau, L. Glebova, L.B. Glebov, Physics and Chemistry of Glasses: European Journal of Glass Science and Technology Part B 50 (5), 311–320 (2009)
[30] A.N. Kolmogorov, Izv. Akad. Nauk USSR, Ser. Mathem. 3, 355 (1937)

describing the type of crystallization. One common method for extracting each of the three unknown parameters consists in re-writing the equation (1) to linearize it:

$$ln\left(-ln\left(1-\frac{\Delta n(0.9J/cm^2,t,T)}{\Delta n_{max}(0.9J/cm^2,T)}\right)\right)=ln\big(K(T)\big)+nln(t) \quad (2)$$

That way, by plotting the left term of the equation (2) as a function of *ln(t)*, we can obtain so-called Avrami plots. By fitting each curve with a linear function, we can extract the Avrami coefficient *n* from the slope while the intercept gives *ln(K(t))*. We plotted in Fig. 36 the left term of the equation (2) as a function of *ln(t)*. One can see that we obtain parallel linear curves with slope equal to 1.5 ± 0.2, this slope depending also on the extracted $\Delta n_{max}(0.9\ J/cm^2, T)$. The coefficient *n* is a parameter describing the crystallization mechanisms. When it equals to ~1.5, it can be associated from the point of view of a crystallization process, with a diffusion-controlled growth of spherical particles from pre-existing nuclei [31]. NaF crystals are expected to grow isotropic into a cubic shape, which is close to the situation predicted by n = 1.5. Therefore equation (1) can be used to model the dependence of $\Delta n(0.9\ J/cm^2, t,T)$ on any thermal treatment temperature and duration.

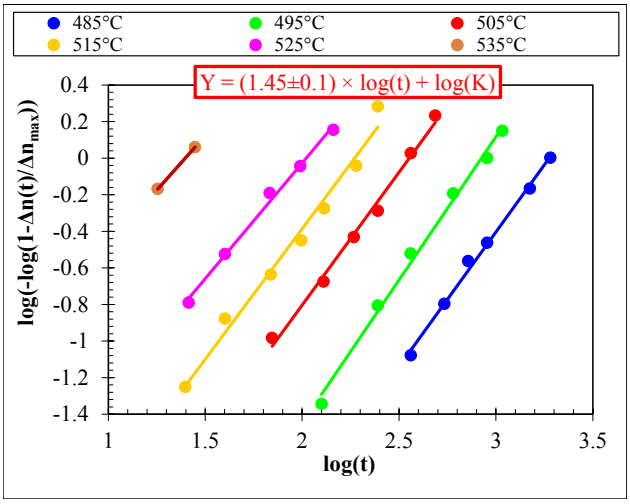

Fig. 36. Avrami plots calculated from the curves of refractive index change dependence on thermal treatment duration for different temperatures.

We also studied the dependence of refractive index change versus dosage for any thermal treatment duration and temperature. It was shown [32] that by writing balance equations associated with the photochemistry of PTR glass and supposing that trapping of electrons by silver and holes have the same probability, the dependence of the refractive index change (Δn) on dosage (D) follows an hyperbolic function:

[31] M. Avrami, J. Chem. Phys. 7, 1103 (1939)
[32] L.B. Glebov, Optical Materials 25(4), 413-418 (2004)

$$\Delta n(D) = \frac{n_S D}{D + \varepsilon} \tag{3}$$

where n_S is the refractive change at saturation and n_S/ε is the inverse of the slope at $D = 0$. Using the refractive index change at 0.9 J/cm^2 ($\Delta n(0.9\ J/cm^2, t, T)$) that can be predicted using JMAK theory (Equation (1)), the equation (3) becomes:

$$\Delta n(D, t, T) = \frac{\Delta n(0.9 J/cm^2, t, T)\big(0.9 + \varepsilon(t, T)\big)D}{0.9\big(D + \varepsilon(t, T)\big)} \tag{4}$$

In our case $\varepsilon(t,T)$ is a thermodynamic parameter following an exponential law. Combining the data of the equations (1) and (4) thus allows fitting each of the curves of the refractive index change dependence on dosage for any thermal treatment temperature and duration (Fig. 37).

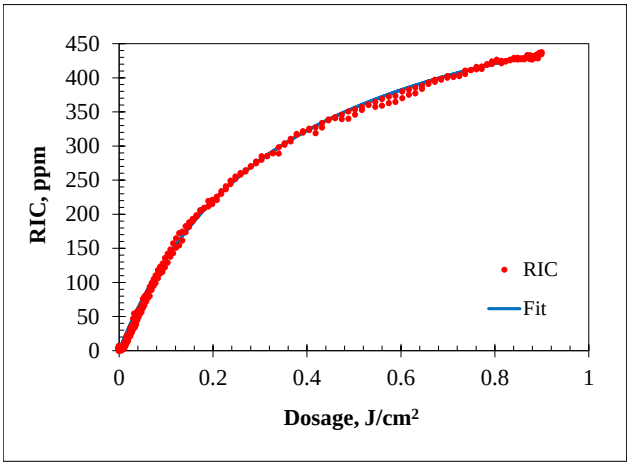

Fig. 37. Dependence of the refractive index change (RIC) in PTR glass on the dosage of UV-exposure at 325 nm after thermal development at ~515°C for ~60 minutes.

Refractive index of glasses depends on thermal history. The highest refractive index is observed after aging at glass transition temperature (T_g) and cooling to room temperature with low rate. The T_g for PTR glass is 460ºC. Fine annealing is usually required cooling rate below 0.1º/min. Refractive index of this glass is shown in Fig. 26 as n_g. Thermal development of PTR glass includes aging in temperature range 480-500ºC (nucleation), further aging in the temperature range 500-520ºC (crystalline phase precipitation) and cooling with rate about 1º/min. No crystalline phase precipitation was observed in unexposed PTR glass. However, a faster cooling rate results in lower refractive index (n_{td}) of a glass sample after thermal development even this sample was not exposed to UV radiation. Exposure to UV radiation triggers a chain of structural transformations that occur in PTR glass during thermal treatments. These transformations that include precipitation of crystalline phase of NaF cause decrease of refractive index to n_{ed}. Difference between refractive indices in virgin and exposed glasses after thermal development is refractive index change (RIC) and is denoted as Δn.

Exposure of a glass sample to a periodic pattern produced by an interference pattern resulted from splitting and recombining the same UV beam causes a periodic variations of refractive index. While a dosage averaged across the aperture of exposure is the same as for uniform irradiation, the dosage in areas of negative interference of the recording beams is zero and dosage in areas of positive interference is doubled. This means that refractive index in unexposed areas would be equal to n_{td}. Not to overburden this consideration of definitions, it is supposed that Δn is proportional to dosage of UV exposure. In this case an average refractive index n_{av} would be the same as n_{ed} as it is depicted in Fig. 26. Refractive index change in maxima of an interference pattern would be twice larger than Δn. It should be noted that mathematical models describe diffraction of light on such periodic phase structures with sinusoidal functions. They use spatial refractive index modulation (RIM) δn which is a coefficient before a sinusoidal function. In case of linear dependence of Δn on dosage, δn=Δn. However, it is clear that no photosensitive materials have exactly linear dependence of refractive index on dosage.

Let us look to refractive index change (RIC) in PTR glass produced by exposure to UV radiation with uniform or periodic pattern if a real photo-sensitometric function is taken into account. Suppositions are: refractive index of the original glass is n_g, no RIC occurs in an unexposed area after thermal development (it is not correct but it is not important for this consideration), no attenuation of UV radiation is in the glass plate and, therefore, distribution of RIC along normal to the surface is uniform, no scattering or any optical nonuniformity exists in the glass sample that could smear a periodic pattern. In this case a RIC in an exposed area is described by a hyperbolic function[33]:

$$\Delta n = \frac{\Delta n_s D_0}{k + D_0}, \quad (1)$$

where Δn is absolute value of RIC, Δn_s is saturation level at infinite dosage, k is half saturation dosage, D_0 is dosage (exposing dosage at 325 nm). Figure 38 (blue curve) shows dependence of RIC on dosage for parameters typical for PTR glass - $\Delta n_s = 10^{-3}$ (1000 ppm), k=0.2 J/cm^2.The

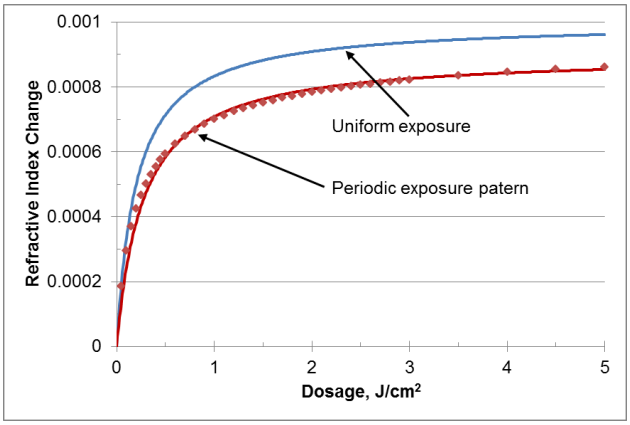

Fig. 38. Dependence of refractive index change on UV dosage (blue) and average refractive index change in a periodic pattern (red).

[33] Leonid B. Glebov. Kinetics modeling in photosensitive glass. Optical Materials 25 (2004) 413–418.

One can see that for D_0=2 J/cm^2 RIC is about 90% from the saturation level. The highest photosensitivity is observed at initial stage of exposure $\Delta n_s/k$=5000 ppm/(J/cm^2). In the process of exposure photosensitivity decreases and finally RIC comes to the saturation level. Typical exposures from 0.7 to 2 J/cm^2 correspond to RIC within 80-90% from the saturation level (1000 ppm).

Spatial distribution of dosage produced by irradiation of a PTR glass plate with an interference pattern of UV radiation having the same wavelength and the same average dosage, which means that the beam was split and recombined with no losses:

$$D(x) = D_0\left(1 + Sin2\pi\frac{x}{d}\right), \quad (2)$$

where x is a spatial coordinate, d is a period of an interference pattern. Figure 39 (top) shows spatial profiles for three different dosages of UV irradiation for 0.1, 0.5 and 0.9 J/cm^2 that have uniform and periodic areas. The absolute refractive index of PTR glass after exposure and thermal development is:

$$n = n_0 - \frac{\Delta n_n D_0\left(1+Sin2\pi\frac{x}{d}\right)}{k+D_0\left(1+Sin2\pi\frac{x}{d}\right)}, \quad (3)$$

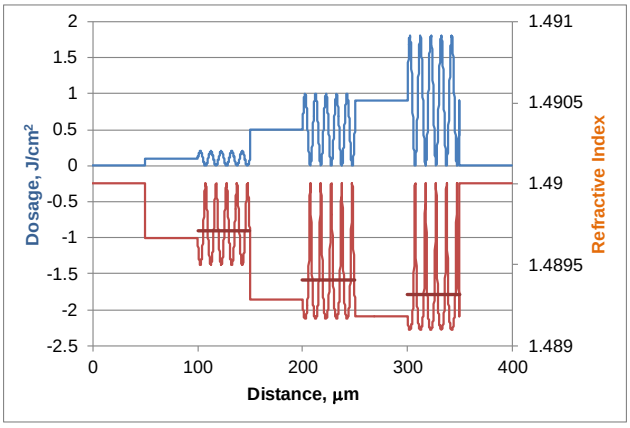

Fig. 39. Spatial profiles of dosage (top) and refractive index in PTR glass for uniform and periodic irradiation patterns. Strait lines in refractive index profiles exposed to periodic patterns correspond to average refractive index.

It is clear that for a medium with linear dependence of RIC versus dosage, an exposure to sinusoidal and uniform patterns of actinic radiation would result in sinusoidal and flat top profiles of refractive index. The average refractive index would be the same in both areas. Figure 6 (bottom) shows spatial profiles in the different areas of the glass plate. It is important that even for relatively small dosage of 0.1 J/cm^2, where dependence of RIC on dosage is almost still linear (Fig. 38), one can see in a periodic profile some distortions for the sinusoidal shape and difference in average refractive indices in uniform and periodical areas. This phenomenon is caused by the feature of interference pattern where dosage in light fringes is twice higher comparing to uniform illumination. One can see in Fig. 39 that deviations from sinusoidal shape

become larger when dosage increases and RIC approaches the saturation level. The average refractive index in the areas exposed to periodic pattern is higher that corresponds to lower effective dosage. This feature is illustrated in Fig. 38. One can see that average RIC in the areas exposed to periodic patterns is smaller comparing to that in uniformly illuminated areas. Modeling of this curve with hyperbolic function showed that for the periodic pattern saturation level n_s is about 90% of that in the uniform area, while dosage of half saturation (k) is larger for 30%.

Let us model effect of refractive index saturation on more complex periodical structures as moiré gratings (they were described in the previous report) produced by sequential recording of two collinear volume Bragg gratings with slightly different periods. Total profile of dosage after two exposures is:

$$D(x) = 0.5\, D_0 \left(2 + Sin2\pi \frac{x}{d_1} + Sin2\pi \frac{x}{d_2}\right) \qquad (4)$$

In this case a spatial profile of dosage has a high frequency component with a period, which is average between the periods of two patterns, and a slow changing envelope that has a period determined by a difference between the periods of the patterns. Such devices are used as extremely narrow band transmitting filters (moiré volume Bragg gratings). Figure 40 (top) shows a spatial profile of dosage produced by two sequential exposures to periodic patterns with periods of 10 and 10.2 μm. A moiré period for such a pattern is 500 μm. The bottom curve shows a refractive index profile. It is clear that this profile is far from the original moiré pattern.

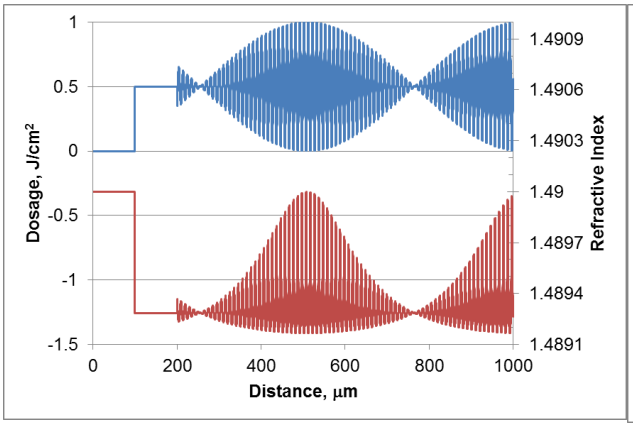

Fig. 40. Spatial profiles of dosage (top) and refractive index (bottom) for two sequential illuminations with dosages of 0.25 J/cm^2 and periods of 10.0 and 10.2 μm. Moiré period is 500 μm.

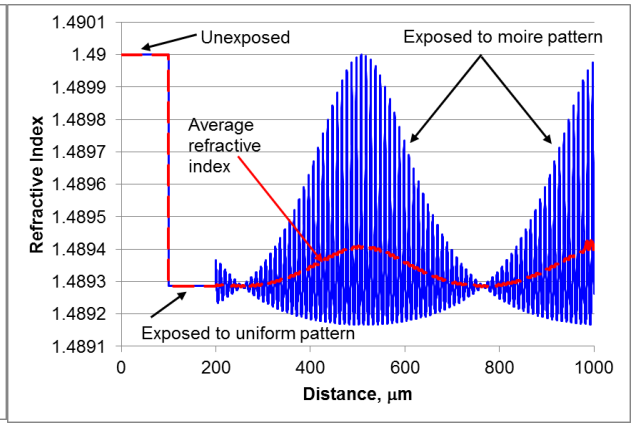

Fig. 41. Refractive index and average refractive profiles in a glass plate exposed to a uniform and moiré patterns.

Figure 41 shows the same refractive index profile combined with a profile of average refractive index. One can see that average refractive index in areas with no refractive index modulation is lower than that in the areas with strong gratings. This means that while an average dosage is constant along the moiré pattern, an equivalent dosage is higher in areas with no high frequency spatial modulation. These periodic fluctuations of an average refractive index could cause corresponding fluctuations of Bragg wavelength and result in broadening of the filter width.

There are several applications of holographic optical elements in PTR glass that require very thick (up to several centimeters) reflecting volume Bragg gratings (VBGs). One of these applications is spectral locking and narrowing of high power semiconductor lasers for pumping low pressure alkali vapor lasers (DPALs)[34, 35, 36]. To achieve spectral width of high power laser systems in the range of 20 pm, which corresponds to spectral width of absorption lines of Rb and Cs at subatmospheric pressures, thickness of reflecting VBGs used as output couplers should be about 2 cm. Another important application is ultrashort pulse stretching and compression by means of chirped volume Bragg gratings (CBGs)[37]. These gratings have a period that is linearly chirped along the beam propagation direction. Due to this variation in period, different spectral components of a pulse incident on the grating along the z direction are reflected by different parts of the grating along its thickness. The optical path length difference between the different spectral components leads to a wavelength-dependent group delay. A stretched pulse being launched to the same grating from the opposite direction would be compressed to its original state. Using this technology, stretching of ultrashort pulses with widths exceeding 100 fs to 1000 ps and high-efficiency re-compression to near-transform-limited pulse duration has been demonstrated.

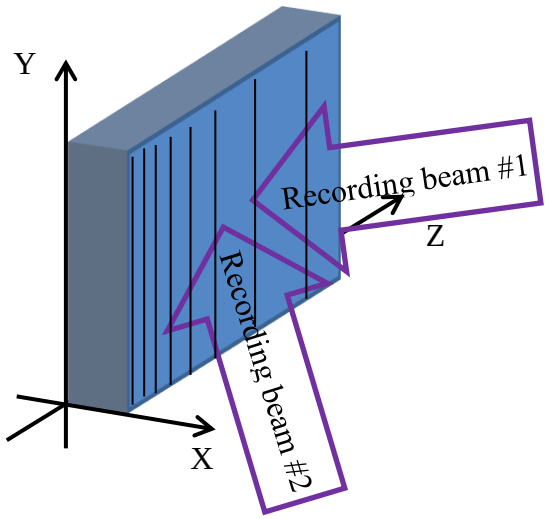

Fig. 42. Geometrical configuration of a holographically recorded thick reflecting VBG.

[34] A. Gourevitch, G. Venus, V. Smirnov, and L. Glebov. Efficient pumping of Rb vapor by high-power volume Bragg diode laser. Opt. Lett. 32 (2007) 2611-2613.
[35] A. Gourevitch, G. Venus, V. Smirnov, D. A. Hostutler, and L. Glebov. Continuous wave, 30 W laser-diode bar with 10 GHz linewidth for Rb laser pumping. Opt. Lett. 33 (2008) 702-704.
[36] A. Podvyaznyy, G. Venus, V. Smirnov, O. Mokhun, V. Koulechov, D. Hostutler, L. Glebov. 250W diode laser for low pressure Rb vapor pumping. , Proc. of SPIE 7583 (2010) High-Power Diode Laser Technology and Applications VIII, ed. M.S. Zediker. 758313, 1-6.
[37] L. Glebov, E. Flecher, V. Smirnov, A. Galvanauskas, and K.-H. Liao, "Stretching and compression of laser pulses by means of high efficiency volume diffractive gratings with variable periods in photo-thermo-refractive glass," U.S. patent 7,424,185 B2 (9 September 2008).

There are multiple parameters that will influence the quality of the beam diffracted by thick reflecting VBGs. One of these effects is the gradient of refractive index or GRIN. Actually, CBGs are fabricated by holographic recording of plane parallel fringes (Fig. 42). The angle between the recording beams in plane X-Z determines the average period of the grating. The photosensitive process is triggered by absorption of UV radiation by cerium ions incorporated in PTR glass. Therefore, it appears a gradient of absorbed dosage that will be converted into a gradient of refractive index (GRIN) along the X-direction of the VBGs. This GRIN then produces a mirage effect. Due to the different beam paths of each spectral component, each of them will be deflected to a different place, finally impacting the quality of the diffracted beam. More precisely, people have shown that GRIN will result in the elongation of the beam in vertical direction after diffracting on a CBG[38]. Authors have also shown that it is however possible to compensate this effect by pressing the CBG and deforming it. Actually, GRIN results in a vertical tilt of the grating vector along the CBG's thickness that can be expressed in a term of a radius of curvature (R_{GRIN}) that is equal to:

$$R_{GRIN} \approx \frac{1}{GRIN} \qquad (1)$$

Therefore, by pressing it is possible to mechanically deform the glass and create a physical deformation of the glass which equivalent radius of curvature will compensate the one of the GRIN.

To experimentally study GRIN, we recorded in a 6 mm thick PTR glass plate five Gaussian stripes with increasing dosages of 0.3, 0.6, 0.9, 1.2 and 1.5 J/cm^2. Exposure was carried out using a He-Cd laser at 325 nm, 4 mW, FW1/e^2 of 0.55 mm. The stripes were obtained by scanning the PTR glass sample in the laser beam at constant speed, this speed controlling the dosage of UV-exposure. The used PTR glass samples were doped with 0.01 mol.% of cerium oxide. Due to absorption of cerium at 325 nm, these samples exhibited a gradient of refractive index through

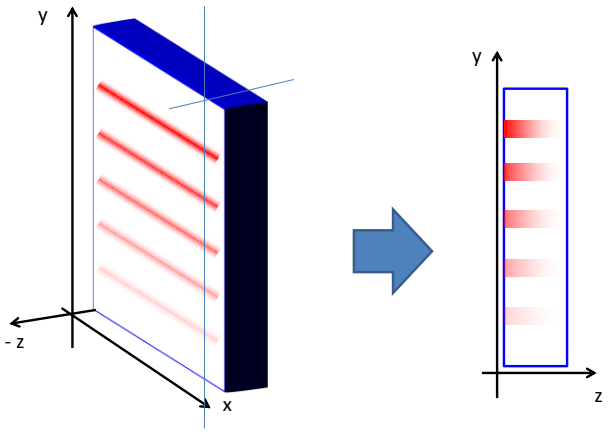

Fig. 43. Scheme of the geometry of the samples exposed to UV stripes in Z direction with different dosage that is used for studying gradient of average refractive index (GRIN) in PTR glass

[38] Christophe Moser and Frank Havermeyer, "Distortion free pulse stretching and compression by chirped volume holographic gratings", Proc. SPIE 75810E (2010).

the thickness of the glass that could be detected and measured after thermal development. These glass samples were then heat-treated using a standard heat treatment schedule that allows achieving high refractive index change with low losses, i.e. for 100 minutes at 485°C (nucleation) followed by a second heat treatment at 515°C for 30, 60 and 90 minutes.

To characterize the lateral gradient of average refractive index (GRIN) in these samples we developed a specific procedure, based on a custom liquid-cell shearing interferometer that was developed a few years ago[39]. We first cut the sample to pencil-like geometries with thickness of ~2 mm (Fig. 2, right) and double-side polished them to flatness of λ/2 at 633 nm. These samples thus have a laterally varying refractive index (GRIN) resulted from gradual attenuation of actinic radiation in the glass plate (Fig. 43). We developed specific programs that allowed a local analysis of the fringe shift and therefore a local extraction of the refractive index change dependence versus dosage as defined by the Gaussian profile. Then, by extracting the dependence of the maximum refractive index change versus sample position and knowing the aperture size, we were able to plot the curve of the refractive index change versus the glass depth. .

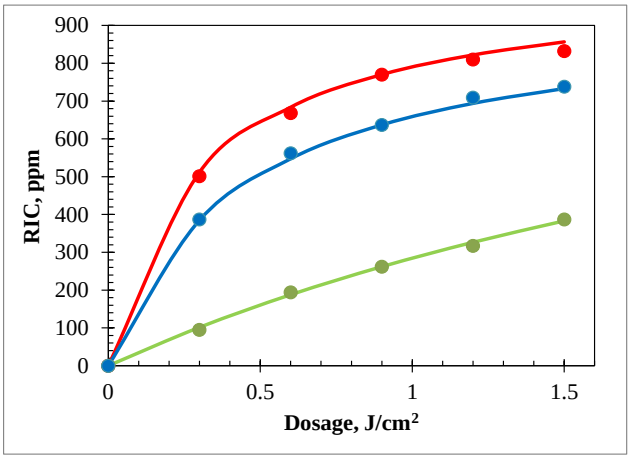

Fig. 44-a. Refractive index change dependence on dosage of UV-exposure at 325 nm. Points refer to experimental data and continuous curves to the hyperbolic fit. The samples were developed at 515°C for 30 min. (green), 60 min. (blue) and 90 min. (red).

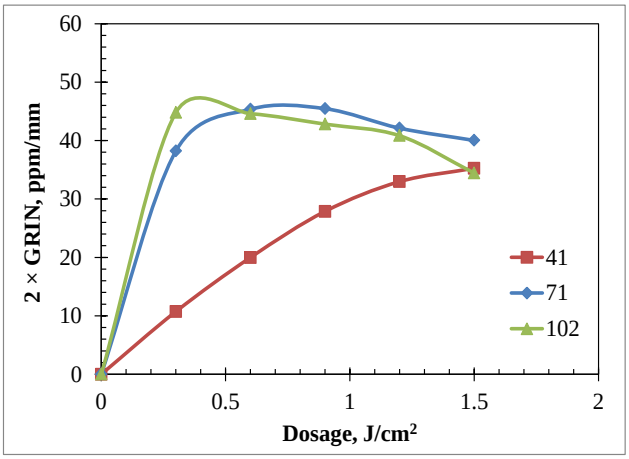

Fig. 44-b. Dependence of the GRIN on the dosage of UV-exposure for different durations (in minutes) of thermal treatment at 515°C.

We have studied GRIN versus dosage of UV exposure and thermal treatment duration in glasses containing 0.01 mol.% of cerium oxide. We plotted in Fig. 44a and 44b, the evolution of the maximum refractive index at the front face of the exposed sample and the GRIN versus dosage of UV-exposure for different thermal treatment durations at 515°C. One can see that while maximum refractive index change monotonously increases with an increase of either the dosage of UV-exposure or the thermal treatment duration, GRIN shows a maximum for a dosage between 0.5 and 1 J/cm^2 when the thermal treatment duration is longer than 60 minutes at 515°C. It is also seen that the curves of GRIN versus dosage after 71 and 102 minutes at 515°C intercept at 0.6 J/cm^2, proving that GRIN is a complex function of dosage of UV-exposure and thermal

[39] Oleg M. Efimov, Leonid B. Glebov, and Hervé P. Andre, "Measurement of the Induced Refractive Index in a Photothermorefractive Glass by a Liquid-Cell Shearing Interferometer," Appl. Opt. 41, 1864-1871 (2002)

treatment duration. Another way to present these data consists in combining the Fig. 44a and 44b and plot GRIN versus maximum refractive index change (Fig. 45). In first approximation, GRIN appears not to be an independent function of dosage and thermal treatment duration, but more generally a function of the maximum refractive index change. For maximum refractive index change below 500 ppm, GRIN is linearly increasing with an increase of the maximum refractive index change. Then GRIN reaches a maximum in the 500-700 ppm region before quickly decreasing when maximum refractive index change saturates. Moreover, for a given refractive index change, GRIN cannot be severely modified by changing the dosage or the thermal treatment procedure. In order to understand if this process is a deterministic one, we developed a model of GRIN based on the measured photosensitivity curve. For each GRIN measurement, the refractive index change measured at the front face of the glass corresponds to the refractive index change that can be achieved for a given dosage of UV-exposure and thermal treatment temperature and duration. Using this data, we could extract the dependence of the refractive index change (RIC) versus the dosage of UV-exposure for each thermal treatment (Fig. 44a). Then we modeled these curves using a hyperbolic function (Fig. 44a), as it was shown that such function perfectly describes the dosage-dependence of refractive index change in PTR glasses[40]:

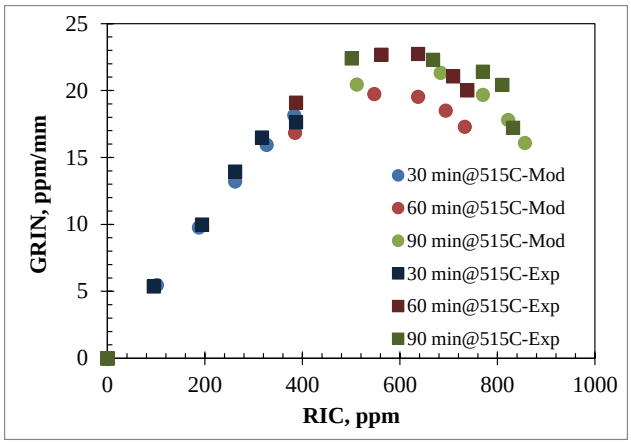

Fig. 45. Evolution of the GRIN versus maximum refractive index change in PTR glass. Circles refer to measured data and squares to modeled data.

$$\Delta n(D,t,T) = \frac{\Delta n(0.9J/cm^2,t,T)(0.9+\varepsilon(t,T))D}{0.9(D+\varepsilon(t,T))} \quad (2)$$

The two controlling parameters $\Delta n(0.9J/cm^2,t,T)$ and $\varepsilon(t,T)$ were then extracted for further modeling (Tab. 4).

Table 4. Parameters extracted from the fit of the refractive index change versus dosage using a hyperbolic function.

Parameters	30 minutes	60 minutes	90 minutes
$\Delta n(0.9J/cm^2,t,T)$	262	637	770
$\varepsilon(t,T)$	3.39	0.44	0.30

Absorption at 325 nm in the characterized glass is equal to $\alpha = 0.74$ cm^{-1}. It is therefore possible to calculate the distribution of dosage ($D(z)$) through the glass thickness z:

[40] Julien Lumeau and Leonid B. Glebov. Modeling of the induced refractive index kinetics in photo-thermo-refractive glass. Opt. Mat. Express 3, No. 1 (2013) 95-104.

$$D(z) = 0.9 \cdot 10^{-\alpha z} \quad (3)$$

Combining the equations (2) and (3) allows calculating the dependence of the refractive index throughout the glass sample and therefore to model the GRIN. The measured and calculated GRINs are overlapped in Fig. 45. Agreement between theory and experiment is fair, proving that GRIN is not only determined the glass absorption but by a combination of the glass absorption and photosensitivity curve.

Due to the high impact of GRIN on volume Bragg gratings properties; we developed a model that allows predicting GRIN for any dosage of UV-exposure followed by any thermal treatment temperature and duration. Previously we have shown that the refractive index change versus dosage and thermal treatment duration and temperature can be fully modeled using simple equations. First we have shown that the refractive index dependence ($\Delta n(D,t,T)$) on dosage (D) follows an hyperbolic function:

$$\Delta n(D,t,T) = \frac{\Delta n(0.9J/cm^2,t,T)(0.9+\varepsilon(t,T))D}{0.9(D+\varepsilon(t,T))} \quad (4)$$

Where $\Delta n(0.9J/cm^2,t,T)$ and $\varepsilon(t,T)$ are two parameters that are time and temperature dependent. We have shown that the first parameter follows the KJMA equation [12]:

$$\Delta n(0.9J/cm^2,t,T) = \Delta n_{max}(0.9J/cm^2,T)\left(1 - exp(-K(T)t^{1.5})\right) \quad (5)$$

Where $\Delta n_{max}\left(0.9J/cm^2,\ T\right)$ is the refractive index change at saturation and follows a linear dependence on temperature:

$$\Delta n_{max}\left(0.9J/cm^2,\ T\right) = 5.22(T^oC - 460) + 777 \quad (6)$$

And $K(T)$ is a thermodynamic parameter that follows a Boltzmann law:

$$K(T) = K_0 \times exp\left(-\frac{E_K}{RT}\right) \quad (7)$$

The second parameter $\varepsilon(t,T)$ follows an exponential function:

$$\frac{1}{\varepsilon(t,T)} = exp(\beta(T)t) \quad (8)$$

While $\beta(T)$ is a thermodynamic parameter that follows a Boltzmann law:

$$\beta(T) = \beta_0 \times exp\left(-\frac{E_\beta}{RT}\right) \quad (9)$$

To perform our modeling, we supposed that all these dependences are the same for all glass melts as it was modeled in Ref. [12]. Finally, all simulations were done for a 6 mm thick glass. Using this set of equations we could extract simple equations that describe the dependence of GRIN on PTR glass and processing parameters. First, we can show that at constant dosage (0.9 J/cm^2) and temperature (515^{o}C) of development, GRIN can be expressed as:

$$GRIN(\alpha, t) = \frac{\Delta n(0.9,t)}{L}\left(\frac{\varepsilon(t)(1-10^{-\alpha L})}{0.9\times10^{-\alpha L}+\varepsilon(t)}\right) \quad (10)$$

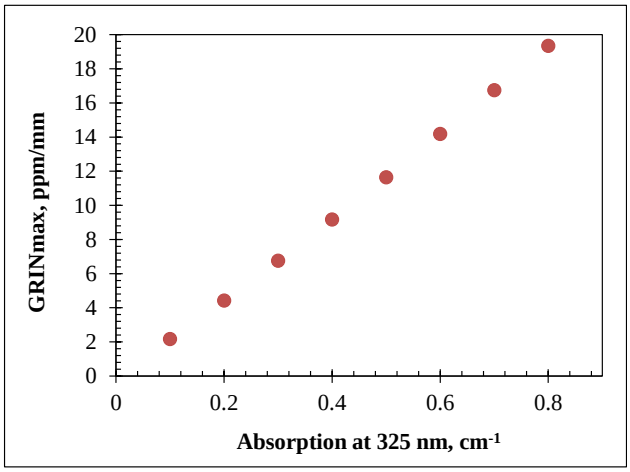

Fig. 46. Dependence of GRIN amplitude on the absorption coefficient at 325 nm.

We plotted in Fig. 46 the dependence of GRIN amplitude at maximum on the absorption coefficient at 325 nm which is proportional to cerium concentration. One can see that GRIN is linearly increasing with the cerium concentration. Dosage of UV-exposure is another way to control the GRIN. At constant absorption (0.73 cm^{-1} at 325 nm) and temperature of development (515^{o}C), the dependence of GRIN on dosage can be expressed as:

$$GRIN(D, t) = \frac{\Delta n(D,t)}{L}\left(\frac{\varepsilon(t)(1-10^{-\alpha L})}{D\times10^{-\alpha L}+\varepsilon(t)}\right) \quad (11)$$

From this equation, it can again be shown that the shape of the dependence of GRIN on refractive index change has no dependence on the dosage of UV-exposure, the only changing parameter being the amplitude of the GRIN. We plotted in Fig. 47 the dependence of GRIN amplitude at maximum on the dosage of UV-exposure. One can see that GRIN is decreasing with an increase of the dosage of UV-exposure. This result is easily explained by the fact that increasing the dosage results in a higher saturation of the dependence of refractive index change on dosage that minimizes the refractive index decrease through the glass thickness. Finally, the third controlling parameter is the temperature of thermal treatment. At constant absorption (0.73 cm^{-1} at 325 nm) and dosage of UV-exposure (0.9 J/cm^2), the dependence of GRIN on temperature of thermal treatment can be expressed as:

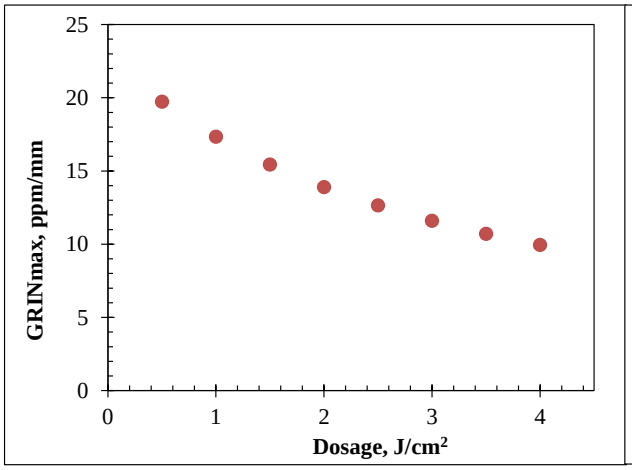

Fig. 47. Dependence of GRIN amplitude at maximum on the dosage of UV-exposure.

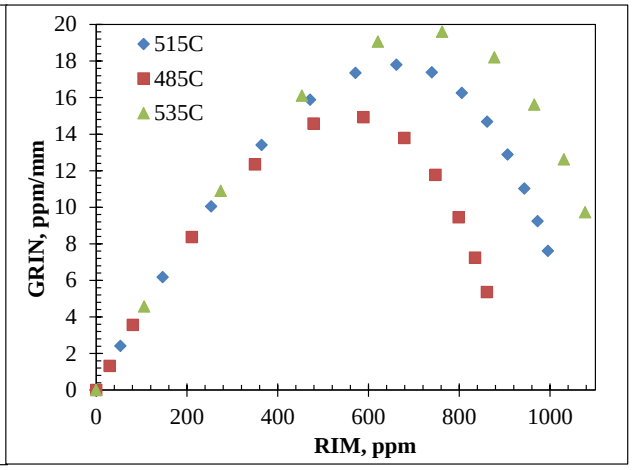

Fig. 48. Dependence of GRIN on refractive index change for different temperatures of thermal treatment.

$$GRIN(T,t) = \frac{\Delta n(0.9,T,t)}{L}\left(\frac{\varepsilon(t,T)(1-10^{-\alpha L})}{D\times 10^{-\alpha L}+\varepsilon(t,T)}\right) \qquad (12)$$

From this equation, it can again be shown that both the shape and the amplitude of the dependence of GRIN on refractive index change will depend on the temperature of thermal treatment. We plotted in Fig. 48 the dependence of GRIN on refractive index change for different temperatures of thermal treatment. One can see that GRIN amplitude is decreasing with a decrease of the thermal treatment temperature and that saturation and decrease of GRIN on refractive index change appears faster. This can be explained by the fact that maximum refractive index at saturation that can be achieved in PTR glass depends linearly (in first approximation) on the temperature of thermal treatment, the lower the thermal treatment temperature, the lower the refractive index change at saturation.

In conclusion, we have seen that four main parameters will influence the level of GRIN, i.e. the cerium concentration and its associated absorption at 325 nm, the dosage of UV-exposure, the temperature of thermal treatment and the thermal treatment duration.

2.3. Long wavelength photosensitivity

It was commonly accepted that photosensitivity of PTR glass is determined by Ce^{3+} absorption band that does not extend beyond 351 nm [41]. Therefore, recently discovered photosensitivity of PTR glass to the third harmonic radiation from a Nd:YAG laser at 355 nm was explained with a non-linear mechanism [42]. With the development of the method and procedures to measure the spectral dependence of the transmission in very thick PTR glass, we were able to re-investigate this effect. Figure 49 shows the spectral dependence of absorption coefficient of pristine PTR glass doped with regular cerium concentration. One can see that cerium appears to contribute to absorption beyond 360 nm. One can see that absorption coefficient at 355 nm is about 60 times smaller than that at 325 nm. However, it was not clear if excitation at longer wavelengths would provide photoionization.

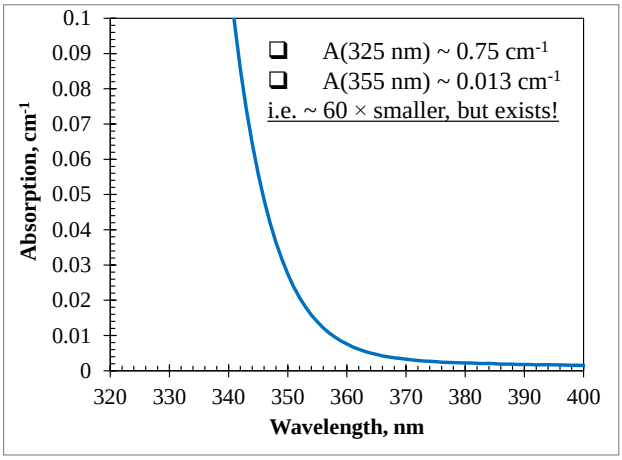

Fig. 49. UV absorption spectrum measured in a 50-mm-thick regular PTR glass.

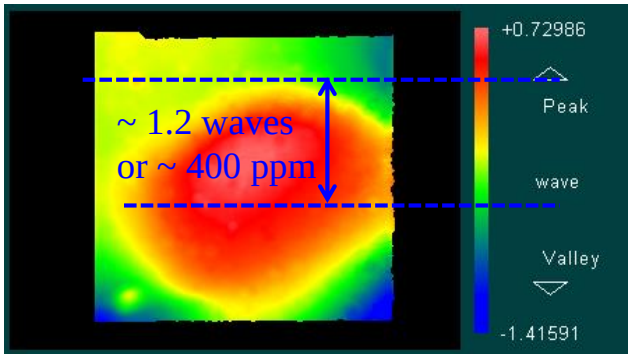

Fig. 50. Fizeau interferogram measured after propagating through a PTR glass plate exposed to ~60 J/cm^2 at 355 nm and thermally developed.

We therefore tested again the photosensitivity of PTR glass to 355 nm radiation. It is obvious that non-linear photosensitivity regime of PTR at 355 nm exists and it is hard to avoid it when nano-second pulses from a tripled frequency Nd:YAG laser are used. To minimize nonlinear effects, we increased a beam diameter up to 20 mm. A virgin PTR glass was exposed in this beam until reaching an approximate dosage of 60 J/cm^2. This sample was finally developed and placed in a Fizeau interferometer (Zygo Corp.) that allowed analyzing the wavefront distortions after propagating through this plate (Fig. 50). One can see that the exposed area of the PTR glass exhibits wavefront distortions corresponding to a peak-to-valley change of the refractive index equal to about 400 ppm. Power density could be estimated to be about 100 kW/cm^2. At such level, the probability to have two-photon absorption is very low and therefore, it is very likely that this result proves that PTR glass presents linear photosensitivity at 355 nm. This result is crucial because it paves a way to the development of new recording techniques that will allow:

- Decreasing the recording time due to the availability of Nd:YAG lasers with high energy.

[41] M. Anne, J. Lumeau, L. Glebova and L.B. Glebov, Journal of Non Crystalline Solids 356 (44-49), 2337–2343 (2010)
[42] L. Siiman, J. Lumeau, and L. B. Glebov, Journal of Non Crystalline Solids, 354, 4070–4074 (2008)

- Further decreasing this recording time if cerium concentration is optimized in order to get an absorption coefficient at 355 nm comparable to the one at 325 nm using the current cerium concentration.
- High energy of Nd:YAG laser will also allow the recording of even larger aperture volume Bragg gratings.
- Actual concentration of cerium combined with 355 nm radiation will allow the recording of more homogeneous volume Bragg gratings.

Photo-thermo-refractive (PTR) glass is a sodium-zink-aluminum silicate glass doped with several cations (Ce, Ag, Sn, and Sb) and anions (F and Br). The hologram recording process consists of two main stages, exposure to UV radiation and thermal development. Photo-structural transformations of PTR glass[43] are triggered by excitation of trivalent cerium ions (Ce^{3+}), having an absorption band in near UV region between 280 nm and 350 nm that corresponds to transition from a ground state to the $5d^1$ band. In PTR glass, this band is placed above the mobility threshold for electrons in the glass matrix. As a result of such an excitation, Ce^{3+} ion converts to Ce^{4+} ion, releasing an electron. The electron is then captured by the silver ion Ag^+, converting it to a neutral Ag^0 atom. Spatial distribution of silver atoms does not produce noticeable refractive index change and presents a latent image of the interference pattern. The thermal treatment comprises two steps. At the first step glass is heated to the temperatures above 480°C, causing silver atoms to diffuse, creating silver containing clusters. Those clusters serve as nucleation centers for consequent growth of sodium fluoride nanocrystals that takes place at the second step, at the temperatures above 500°C. Upon that, refractive index decreases in the exposed areas of the glass sample. As a result, spatial modulation of refractive index in accordance with the latent image can reach 10^{-3} (1000 ppm) or more. Spatial frequency of recorded VBGs can be higher than 9000/mm.

One of the basic features of holograms is necessity to use the same wavelength for reconstruction as was used for recording. As it was mentioned above, photosensitivity range of PTR glass is limited by the UV absorption band of Ce^{3+}, located in the 280-340 nm spectral region. As a result, only trivial planar holographic elements, such as volume Bragg gratings, can be recorded in PTR glass for applications in visible and IR spectral regions. In this case change of incidence angle for a beam at a different wavelength provides coincidence with the Bragg angle for this wavelength. Contrary, complex holographic elements, e.g. curved Bragg mirrors, could be used only within the photosensitivity range in near UV. It would be very beneficial to find a way for recording complex holograms for visible and near IR regions in material similar to PTR glass, which can provide imaging combined with fine filtering and be stable and reliable for high-power laser applications. Because a complex hologram could be completely restored only at the wavelength of recording, a new material similar to PTR glass has to have photosensitivity in visible and near IR regions while be stable under exposure to such radiation. The first step in this direction has been demonstrated in this section.

The long history of dielectric photosensitive glasses development has shown that Ce^{3+} used as a photosensitizer in PTR glasses provides the longest wavelengths of photoionization and no ways for further long wavelength shift of photosensitivity were described. To utilize long wavelength

[43] L.B. Glebov. Photochromic and photo-thermo-refractive (PTR) glasses. In Encyclopedia of Smart Materials, Volume 2. John Wiley & Sons, NY, 2002, 770-780.

excitation one should use a nonlinear excitation with participation of several photons. The use of multiphoton excitation usually requires high power pulsed irradiation (power density should exceed 1 MW/cm^2) that is difficult realize in a reliable holographic setup. This is why we studied an excited state absorption (ESA) mechanism to populate an electron level, which is situated above the mobility threshold of electrons in a glass matrix. In this case concurrent exposure to two optical beams with longer wavelengths can provide excitation from a ground state to one of the upper levels with a reasonably long lifetime and then excitation from this level to the desirable one. Such a two-step excitation should provide generation of mobile electrons that are necessary for triggering the chain of photo-structural transformations. In some cases such a mechanism can be realized at reasonably low power in the recording beams.

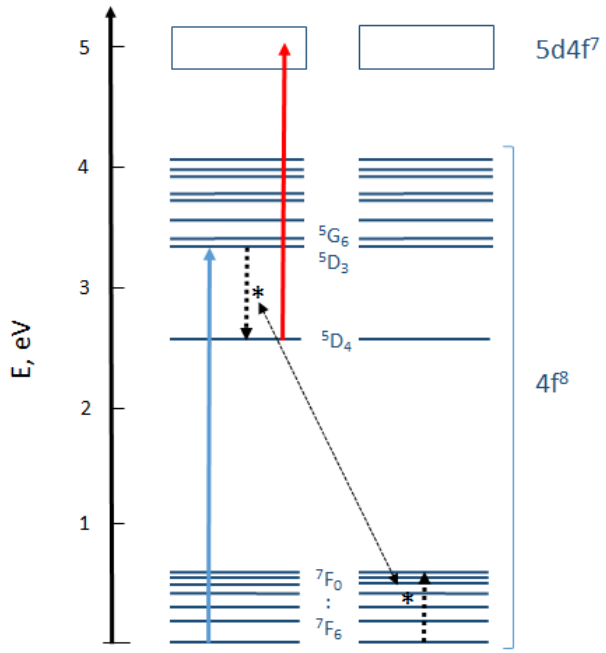

Fig. 51. Energy diagram for Tb^{3+} ions in silicate glass. Blue arrow – absorption from the ground state to $^5D_3$ level. Dotted arrows with * – cross relaxation from $^5D_3$ to $^5D_4$ with concurrent excitation to upper ground sublevels in a neighboring ion, red arrow – excited state absorption from $^5D_4$ to $5d4f^7$ level.

To realize such a mechanism, a photosensitizer with a complex structure of upper electron states that should be used. For the first experiments, a Tb^{3+} ion was chosen. The diagram of its electron levels is shown in Fig. 51. The broad group of levels that produces wide $5d^14f^7$ band is placed about 5 eV above the ground level $7F^6$ while it is beyond electron mobility threshold for a number of wide bandgap inorganic compounds[44, 45]. A metastable level of terbium ions $^5D_4$ in $4f^8$

[44] P. Dorenbos. "The 5d level positions of the trivalent lanthanides in inorganic compounds", Journal of Luminescence 91, 155 (2000).
[45] C. W. Thiel, Y. Sun, R. L. Cone. "Progress in Relating Rare Earth Ion 4f and 5d Energy Levels to Host Bands in Optical Materials for Hole Burning, Quantum Information, and Phosphors", Journal of Modern Optics 49, 2399 (2002).

shell is placed 2.6 eV above the ground state. It shows a long millisecond lifetime in different crystals or glass matrices[46]. Long lifetime of this excited state is one of the key parameters to influence the efficiency of the ESA process. The ESA is an upconversion process, which allows exciting higher energy level via intermediate level by consecutive absorption of two photons. It should be noted that no absorption increase in the range of 400-1500 nm with an exception of the small area around 480 nm was reported in Tb doped glasses after exposure to UV radiation[47]. This feature could be useful to avoid induced losses in holograms recorded for longer wavelengths.

A PTR glass containing 2 mol.% Tb_2O_3 instead of CeO_2 (Tb:PTRG) was melted in an electrical furnace in a platinum crucible at the temperature of 1460 °C for 5 hours. Platinum stirrer was used to provide high optical homogeneity. The glass boule was annealed at the temperature of 460°C for 6 hours and then was slowly cooled down to room temperature for 24 hours. Polished wafers of 25×8×2 mm^3 were fabricated. Surface flatness was better than $\lambda/4$ at 633 nm and refractive index uniformity across the aperture was of 30 ppm or better. Thermal development was produced by in two steps aging the samples sequentially at temperatures of 480 and 515°C for periods from a few of minutes to several hours.

Absorption spectra in UV-vis-IR regions were measured with a Perkin Elmer Lambda 950 spectrophotometer. Luminescence and excitation of luminescence spectra were measured with a Perkin Elmer LS45 fluorimeter in reflecting geometry. Surface flatness and optical homogeneity were measured with a Fizeau interferometer (Zygo GPI). Refractive index difference between an exposed stripe of about 1 mm thick and an unexposed area at the sample (Δn) was measured with a shearing interferometer which provided precision of better than 5 ppm[48]. Irradiation of the Tb:PTRG samples was produced with the following sources. Emission from an LED at 375 nm (3.30 eV) was projected to a sample in a square spot of 7.5×7.5 mm^2 with power density up to 1 W/cm^2. Multimode broad area blue and green laser diodes were used for ESA in Tb:PTRG. A blue LD emitted 1.5 W CW power at 449 nm (2.76 eV). A green LD had 1 W CW power at 522 nm (2.37 eV). The beams from LDs were projected to the samples in such way that they provided a stripe with a close to Gaussian lateral profile of intensity. This stripe had a width of 0.9 mm (FWHM) and a length of 5 mm with a flat top intensity profile. Maximum intensity in stipes was 59 W/cm^2 for 449 nm LD and 39 W/cm^2 for 522 nm LD. 2-mm-thick glass samples were placed at the intersection of square and stripe shaped beams. Beam alignment was performed so that a stripe shaped LD beam was imposed upon the center of a square shaped 375 nm LED beam.

[46] M.D. Chambers, D.R. Clarke "Doped Oxides for High-Temperature Luminescence and Lifetime Thermometry", Annu. Rev. Mater. Res. 39, 325 (2009).
[47] A. Hoaksey, J. Wood, K. Taylor "Luminescence of Tb3+-ions in silicate glasses." Journal of Luminescence 17, 385 (1978).
[48] O.M. Efimov, L.B. Glebov, H.P. Andre. "Measurement of the induced refractive index in a photo-thermo-refractive glass by a liquid-cell shearing interferometer" Appl. Optics, 41, 1864-1871, (2002).

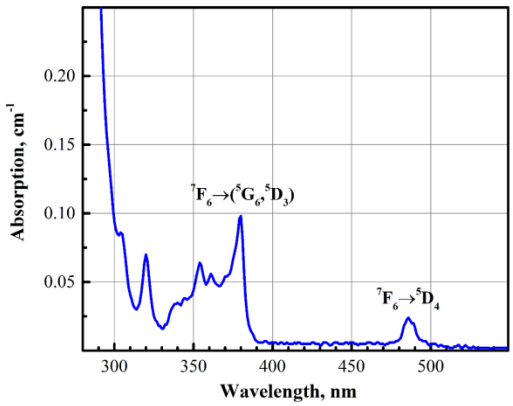

Fig. 52. Absorbtion spectrum of PTR glass doped with 2 mol.%Tb_2O_3.

Absorption spectrum of a Tb:PTRG for near UV and visible spectral regions is presented in Fig. 52. This absorption spectrum consists of a band with maximum at 486 nm (2.55 eV), a group of overlapped bands from 310 to 390 nm (4.00-3.18 eV) with the most intense line at 379 nm (3.27 eV) and a sharp absorption edge at 290 nm (4.28 eV). The longest wavelength band at 486 nm could be ascribed to a transition from a ground level $^7F_6$ to a first metastable level $^5D_4$ (Fig. 51). The group of lines at shorter wavelengths corresponds to the transitions from a ground state $^7F_6$ to $^5G_0$-$^5G_6$ and $^5D_3$ levels (Fig. 51). According to Ref.[19, 49], the second metastable $^5D_3$ level cannot be clearly separated from the lowest in the G group $^5G_6$ level in silicate glass due to inhomogeneous line broadening in glass and small ~26 meV energy gap between the levels. Therefore one can suppose that they both contribute to the absorption band with maximum at 379 nm.

An absorption band corresponding to the transition from the ground state $^7F_6$ to $5d^14f^7$ state of Tb^{3+} could not be defined directly in the absorption spectrum of Tb^{3+}-doped PTR glass. According to studies in different glasses and crystals[50, 51], an absorption band corresponding to a $^7F_6$-$5d^14f^7$ transition should be placed in the range of 220-260 nm (4.77-5.16eV). However, this band in PTR glass should overlap with absorption bands of Sb^{5+} and Ag^+ dopants and could not be distinguished within sharp absorption edge near 290 nm (Fig. 17). To clarify absorption of Tb^{3+} in the short wavelength region, a PTR glass matrix without conventional dopants (Ce, Ag, Sb) but with 2 mol.%Tb_2O_3 was melted and a number of samples with different thickness were prepared to enable measurements in vicinity of PTR glass matrix intrinsic absorption edge which is placed near 210 nm[52]. An absorption spectrum of this glass in a logarithmic scale is shown in

[49] A.D.Sontakke, K.Biswas, K.Annapurna "Concentration-dependent luminescence of Tb3+ ions in high calcium alumino silicate glasses", Journal of Luminescence 129, 1347 (2009).
[50] H. Ebendorf-Heidepriem, D. Ehrt "Formation and UV absorption of cerium, europium and terbium ions in different valences in glasses", Optical Materials 15, 7 (2000).
[51] E. Nakazawa "The lowest 4f-to-5d transition and charge transfer transitions of rare earth ions in YPO4 hosts." Journal of Luminescence 100, 89 (2002).
[52] Leonid Glebov, Larissa Glebova, Eugeniu Rotari, Andrei Gusarov, and Francis Berghmans. Radiation-induced absorption in a photo-thermo-refractive glass. Photonics for Space Environments X, ed. E.W. Taylor, Proceedings of SPIE 5897 (2005) 58970J-1 – 58970J-6.

Fig. 53. One can see small absorption bands of Tb^{3+} described earlier and placed between 290 and 550 nm. The sharp absorption edge in vicinity of 210 nm could be mainly ascribed to intrinsic absorption of a PTR glass matrix. A high intensity absorption band with maximum at 230 nm and a shoulder near 260 nm could be ascribed to transitions from the ground state of Tb^{3+} to different components of $5d^14f^7$ band or higher excited states.

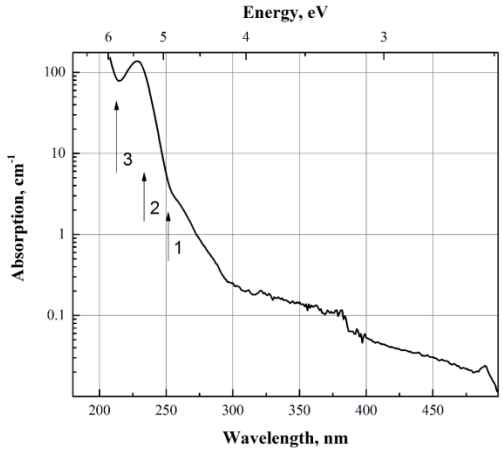

Fig. 53. Absorption spectrum (logarithmic scale) of PTR glass matrix doped with 2 mol.%Tb_2O_3. Arrows correspond to positions in the absorption spectrum for excitation from $^5D_4$ level with wavelengths of 522 nm (1), 449 nm (2) and 375 nm (3).

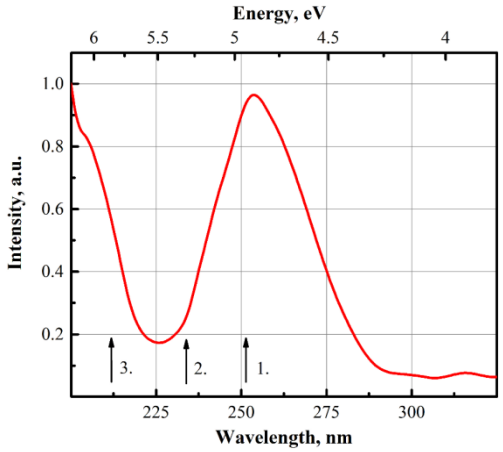

Fig. 54. Spectrum of luminescence excitation in PTR glass matrix doped with 2 mol.%Tb_2O_3. Arrows correspond to positions in the luminescence excitation spectrum for excitation from $^5D_4$ level with wavelengths of 522 nm (1), 449 nm (2) and 375 nm (3).

To understand features of excitation to these upper states of Tb^{3+}, its luminescence was studied. It was found that luminescence spectra of PTR glass and PTR glass matrix doped with Tb^{3+} look similar to that in different silicate glasses. They consist of two separated groups of lines. Groups in spectral 380-440 nm range (blue luminescence) are related with $^5D_3$-^7F_j transitions, and those in spectral region 485-620 nm (green luminescence) correspond to $^5D_4$-^7F_j transitions. The second group shows intensity of luminescence by an order of magnitude higher than the first one. The same proportion describes the relationship between lifetimes of the excited $^5D_4$, which is 3.9 ms, and $^5D_3$ levels, which is less than 0.3 ms. Such quenching of $^5D_3$-^7F_j blue luminesce is well known for Tb^{3+}-ions in different glasses where it was explained by a cross-relaxation process with a nonradiative energy transfer where a down transition from $^5D_3$ to $^5D_4$ causes an up transition from $^7F_6$ to $^7F_0$ at the neighboring ion. This process becomes effective for terbium concentration higher than 1%[53].

We studied excitation spectra for blue ($^5D_3$-^7F_i) and green ($^5D_4$-^7F_i) luminescence over the short wavelength range of 200- 340nm (Fig. 54). It was found that short wavelength excitation spectra were identical for both types of luminescence. One can see a small maximum at 330 nm, a main maximum at 253 nm (4.90 eV) with spectral width of ~35 nm (0.66 eV) and a tail of a short wavelength band. There is a problem to describe this spectrum because an excitation maximum

[53] W.F. van der Weg, Th. J. A. Popma, A. T. Vink. “Concentration dependence of UV and electron-excited Tb3+ luminescence in Y3Al5O12”

at 330 nm corresponds to a minimum in the absorption spectrum of Tb (Fig. 52). The band with maximum at 253 nm in the excitation spectrum corresponds to the shoulder in vicinity of 260 nm in the absorption spectrum of Tb^{3+} (Fig. 53). This band could be associated with transition from the ground $^7F_6$ state to $5d^14f^7$ band. This assignment is in close agreement with the literature data for such transition in different type of glasses. The increase of efficiency of luminescence excitation in a short wavelength region could correspond to transitions to higher levels of Tb^{3+} or to glass matrix states with further energy transfer to Tb^{3+} levels.

Thus the study of absorption and luminescence in Tb^{3+} doped PTR glass has shown that similar to other silicate glasses it has a weak absorption band at 486 nm and a group of overlapped weak bands between 310 and 390 nm that correspond to excitation for ground state to $^5G_4$ and $^5D_3$ levels correspondingly. Relaxation from these levels to the ground state results in green and blue luminescence. Strong absorption at wavelengths shorter 300 nm includes a band with maximum at 230 nm and a shoulder at 260 nm that could be assigned to transitions from the ground state to $5d^14f^7$ band, which appears as a shoulder, and to higher levels of Tb^{3+} and glass matrix. Excitation to this UV bands results in further relaxation to $^5D_3$ and $^5D_4$ levels and both blue and green luminescence.

It was found in Ref.[54, 55, 56] that excitation of Tb-doped calcium aluminate and borosilicate glasses in short wavelength absorption bands (λ<300 nm) of Tb^{3+} caused not only luminescence but induced absorption band with maximum in vicinity of 350 nm. Comparison of this band with absorption spectra of Tb doped glasses melted in strong oxidizing conditions has proved that this

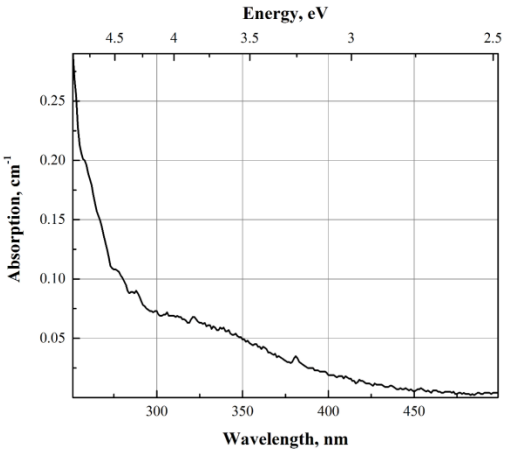

Fig. 55. Spectrum of additional absorption in Tb-doped PTR glass after exposure to 375 nm radiation at power density of 0.84 W/cm^2 for 15 kJ/cm^2 exposing dosage.

[54] H. Hosonoyx, T. Kinoshitay, H. Kawazoey, M. Yamazakiz, Y. Yamamotoz, N. Sawanoboriz "Long lasting phosphorescence properties of Tb3+-activated reduced calcium aluminate glasses", J. Phys.: Condens. Matter 10, 9541 (1998).
[55] R.K. Verma, K. Kumar, S.B. Rai "Inter-conversion of Tb3+ and Tb4+ states and its fluorescence properties in MO-Al2O3:Tb (M - Mg, Ca, Sr, Ba) phosphor materials.", Solid State Sciences 12, 1146, (2010).
[56] Q. Liu, B. F. Johnston, S. Gross, M. J. Withford, M. J. Steel "A parametric study of laser induced-effects in terbium-dope borosilicate glasses: prospects for compact magneto-optic devices", Optical materials express 3, 2096 (2013).

is absorption of Tb^{4+}. Therefore excitation to the short wavelength absorption bands of Tb^{3+} results in its photoionization and conversion to Tb^{4+}. This means that for those glasses the $5d^14f^7$ band associated with absorption short wavelength absorption (λ<300 nm) is placed above the mobility threshold of electrons in glass matrix.

To study long wavelength excitation and photoionization in Tb:PTRG, we produced irradiation of the samples with an LED emitting at 375 nm (3.30 eV). The LED provided up to 1 W/cm^2 power density in a spot of 7.5×7.5 mm. According to the energy diagram of Tb^{3+} (Fig. 51), absorption of a 3.30 eV photon should result in excitation from the ground level to a $^5D_3$ level of Tb^{3+} with further fast relaxation to a metastable $^5D_4$ level placed at 2.55 eV above the ground state. Absorption of the second photon of 3.30 eV should result in excitation from the metastable $^5D_4$ level to upper states of $5d^14f^7$ band and in photoionization of Tb^{3+}. It was found that while Tb:PTRG is not sensitive to low power irradiation at 375 nm, power density in the range of 1 W/cm^2 is enough to produce additional absorption. Figure 55 shows an additional absorption spectrum of the sample, which was irradiated by LED emission at 375 nm with power density of 0.84 W/cm^2 for 5 hours. The wide absorption band with a maximum at 340-350 nm corresponds to the absorption band of Tb^{4+} and confirms the supposition that Tb:PTRG can be ionized by two photon ESA at 375 nm. The natural supposition would be that similar to photoionization of Ce^{3+}, the photoionization of Tb^{3+} should trigger a chain of structural transformations in PTR glass and cause refractive index change.

To confirm this supposition, difference in refractive index between irradiated and non-irradiated areas in Tb:PTRG, the samples were exposed to different dosages at 375 nm using the same LED source. The exposed samples were treated using the two-step thermal development procedure, which is used for conventional PTR glass. After the treatment, difference in refractive index up to 220 ppm between exposed and unexposed areas was observed. The obtained result verifies that the upconversion processes (ESA in Tb^{3+} ions) provides a refractive index change (Δn) in Tb:PTRG. It should be noted that the effect of refractive index change by a single source of incoherent radiation is unwanted from the point of view of hologram recording with the use of an LED emitting in near UV and lasers emitting at visible wavelengths. It is clear photoionization produced by ESA of incoherent near UV radiation would cause some undesired background refractive index change and, therefore, decrease the dynamic range for two-beam hologram recording. To mitigate this effect, one should decrease power density and dosage of incoherent UV irradiation. For our two-beam experiments irradiation at 375 nm provided power density of 0.84 W/cm^2. Exposure for 120 min corresponded to an absorbed dosage of 139 J/cm^2 for a 2 mm thick sample. It was found that such irradiation by a single source resulted in refractive index change of only 50-60 ppm that provided enough dynamic range for two-wavelength experiments.

Multimode broad area blue and green laser diodes emitting 449 and 522 nm were used for two-wavelength experiments for the study of the ESA process in Tb:PTRG. Parameters of lasers and conditions of illuminations were described above. The PTR glass samples of 2 mm thickness were placed at the intersection of UV and visible beam paths. A beam alignment was performed so that a stripe-shaped beam from LD was imposed upon the center of a uniform 7.5×7.5 mm^2 square-shaped LED beam at 375 nm.

To prove that there is not nonlinear photoionization of Tb^{3+} by blue or green light the samples were exposed to radiation of LDs at maximum power for several hours. No refractive index change were observed after such illumination followed by thermal development. Concurrent irradiation of the samples by two wavelengths (375 and 522 nm) for 120 min. followed by thermal development resulted in refractive index change of 223 ppm. Concurrent irradiation of the samples by 375 and 449 nm for 240 min. followed by thermal development resulted in refractive index change of 190 ppm. Spatial modulation of refractive index about 200 ppm in a 2 mm thick sample enables π phase incursion for visible wavelengths and therefore allows recording of any type of holograms with high diffraction efficiency working in the blue/green spectral region.

The surprising result is that photosensitivity for longer wavelength of 522 nm is ~3.5 times higher than that for 449 nm while the simplest supposition should be that higher excitation should provide more efficient ionization. This surprising result could be explained by a complex structure of high electronic states of Tb^{3+} and their interaction with electronic states of glass matrix. Supposing that excitation with 375 nm delivers an electron to $^5D_4$ level placed at 2.55 eV above the ground state (absorption band at 486 nm) and then excitation with visible photons delivers it to some upper levels of Tb^{3+}. In this case, irradiation at 522 nm delivers an electron to a position at 4.93 eV while irradiation at 449 nm elevates it to 5.31 eV. One can see in Fig. 53 and Fig. 54 that energy of 4.93 eV corresponds to positions of a shoulder at 260 nm in the absorption spectrum and a maximum in the luminescence excitation spectrum. One can suppose that excitation to these states near 4.9 eV provides both relaxation to lower levels responsible for luminescence and photoionization. It looks that the short wavelength absorption band at 230 nm (5.5 eV) corresponds to some localized states that prevents both relaxation to lowers levels of Tb^{3+} (it corresponds to the minimum in the luminescence excitation spectrum) and electron release to glass matrix. An interesting correlation is observed: the ratio of intensity of luminescence for 4.9 and 5.3 eV is 3.8 that close to the ratio of values of photosensitivity for 522 and 449 nm. Thus, the band at 260 nm in absorption and luminescence excitation spectra could correspond to $5d^14f^7$ band of Tb^{3+} in PTR glass.

It is clear that the used visible LDs were not suitable for complex hologram recording in conventional two-beam geometry due to their short coherence length resulted from poor spectral and spatial characteristics. To demonstrate a visible complex hologram in Tb:PTRG, we decided to record a reference-free hologram where interference is produced by diffracted and transmitted fractions of the same beam[57]. The similar hologram was demonstrated in the first publication on hologram recording in PTR glass[58]. Such

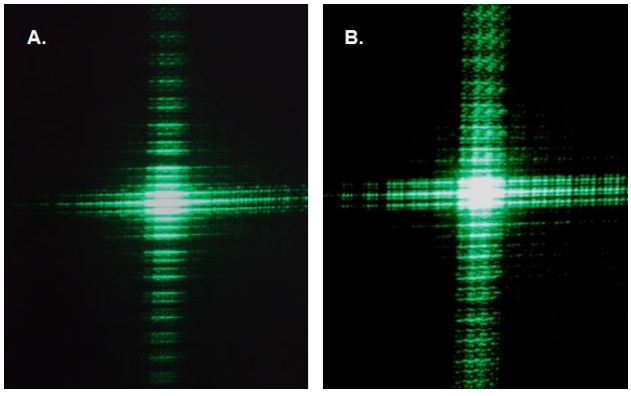

Fig. 56. Diffraction on a metal grid (A) and reference-free complex hologram of "difraction on a metal grid" (B).

[57] B.Y. Zeldovich, A.V Mamaev, V.V. Shkunov "Speckle-wave interaction in application to holography and nonlinier optics", CRC Press, (1994).

[58] V.A. Borgman, L.B. Glebov, N.V. Nikonorov, G.T. Petrovskii, V.V. Savvin, A.D. Tsvetkov. Photothermal refractive effect in silicate glasses. Sov. Phys. Dokl., 34, No 11 (1989) 1011-1013.

holograms do not require long coherence length and high beam quality of the laser. A thin metal grid with 100 μm cells was chosen as an object. A diffraction pattern at the metal grid produced by a 1 mm beam of an LD emitting at 522 nm is shown in Fig. 56A. Then the grid was set against a Tb:PTRG blank and illuminated by the beam at 522 nm. At the same time, the glass blank was illuminated from the backside by the 375 nm LED. Parameters and time of exposure were kept the same as the previous experiments. After thermal development, the sample was returned to the same place and illuminated by the same 522 nm beam. Figure 65B shows a pattern of complex green hologram reconstruction. Resemblance of the two images can be clearly seen. A similar hologram was created using the blue LD. We can state that the first complex visible holograms are recorded in Tb doped PTR-glass.

Thus, a new phase holographic material with sensitivity to visible radiation is demonstrated. It is photo-thermo-refractive glass doped with Tb^{3+}. Volume holograms recorded in this material are not sensitive to visible radiation and cannot be bleached. The mechanism of photosensitivity is photoionization of Tb^{3+} ions by means of excited state absorption resulted from concurrent exposure to near UV and visible radiation. As the first step, UV radiation with power density below 1 W/cm^2 excites electron to a $^5D_3$ level with further relaxation to $^5D_4$ level. As the second step, visible radiation excites electron to $5d^14f^7$ band placed above the electron mobility threshold of PTR glass. The released electron triggers a chain of structural transformation in glass resulted in permanent refractive index change. Complex reference-free holograms in blue and green regions are demonstrated.

2.4. Fiber PTR glass

Three types of PTR glass have been melted for drawing of the PTR fibers (Table 5). It was a regular glass #CR8 that was used for a bare core fiber drawing, PTR glass matrix with no photosensitizers #0 that was used for insensitive fiber cladding, and #Yb2-2 glass doped with Yb that have higher refractive index that the regular PTR glass and, therefore, was used for core in a core/clad fiber. In the first attempt of the drawing the only regular photosensitive PTR glass has been used. Such bare core glass fiber was successfully used for initial measurements of losses and reflecting fiber Bragg grating was recording in that fiber. A fiber with both core and cladding made of the photosensitive glasses was drawn. However it was not possible to record a grating because of different crystallization rates in regular and Yb doped PTR glasses. This is

Table 5. Glasses developed for fiber drawing.

#	Glass ID	Photosensitive dopants Wt.%	Lasing dopants Wt.%	Application
1	#CR8	Ce - 0.01% Ag - 0.02%	none	Core, cladding
2	#0	none	none	Cladding
3	#Yb2-2	Ce - 0.01% Ag - 0.02%	Yb - 2%	Core

why we prepared a new pair of glasses – insensitive matrix of the regular PTR glass with lower refractive index for cladding and the PTR glass with photosensitive components doped with Yb, which has higher refractive index and can be used for fiber core. This Yb doped glass allows for obtaining the emission along with the possibility of the hologram recording. The glass slabs prepared for preforms fabrication are shown in Fig. 57.

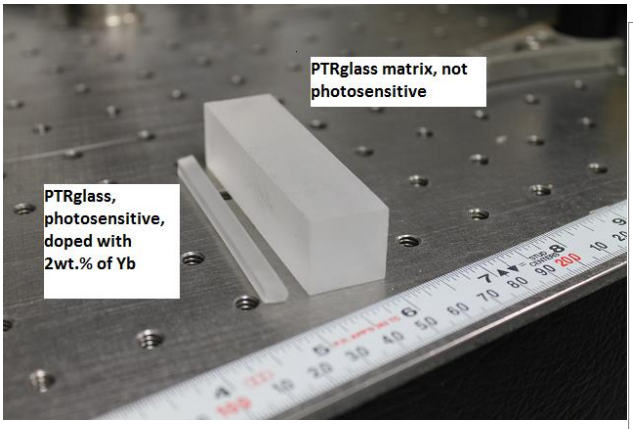

Fig. 57. Two glass slabs prepared for fiber preforms fabrication. Glass for the core – photosensitive PTR glass, doped with 2 wt.% of Yb; glass for the cladding –PTR glass-matrix with no photosensitizers.

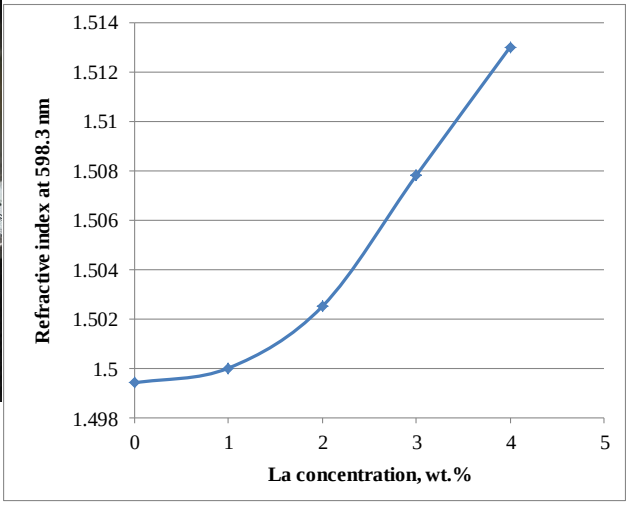

Fig. 58. Dependence of refractive index of PTR glass on La concentration.

These encouraging results enabled further activity in development of optical fibers based on PTR glasses. We have focused on studying the optical and mechanical properties of glasses which we propose to use as a cladding and a core in the fiber drawing. The main attention has been paid to the development of a pair of glasses with refractive index difference between a core and a cladding in the range 1000 - 3000 ppm that enable a numerical aperture (NA) required for single mode optical fibers operating near 1 µm. To enable drawing with proper diameters of core and cladding, the viscosity of those glasses must be taken in account and thoroughly studied. Those glasses should not induce crystallization during and after the drawing process and they should have relatively small difference in coefficients of thermal expansion to avoid cracking.

In the fiber which is intended for the recording of VBGs, the cladding must be done using non-photosensitive glass which has the viscosity matching or close to the viscosity of the core glass. Also, the refractive index of the cladding glass must be circa 2000 ppm lower than the core glass. To elaborate the main tools for managing the composition of both glasses, we have melted a series of PTR glasses with different concentration of fluorine and lanthanum and then studied their influence on viscosity and refractive index. Lanthanum has been chosen because this element does not affect absorption of PTR glass in studied regions (from UV to near IR), but at the same time can slightly change the refractive index and viscosity of PTR glass. So, it can be a flexible tool for creating required properties of glass. In Fig. 58 one can see that increasing of concentration of La in PTR glass definitely increases refractive index of glass.

One can see that required difference between refractive indices of original and modified glass (about 2000 ppm) could be achieved by adding about 1.5% of La in the basic PTR glass. As it was shown earlier, additions of rare earth components could result in a decrease of photosensitivity. However, it was found that photosensitivity of such glass was at the acceptable level (600 ppm of RIC after the second development). Absorption spectra of the La doped glass are shown in Fig. 59. One can see that absorption spectra of PTR glass were not affected significantly by co-doping with lanthanum. Slight difference in absorption spectrum of La:PTR glass can be explained by slightly lover photosensitivity of this glass and, therefore, lower level of scattering which is mainly responsible for additional losses in this spectral region.

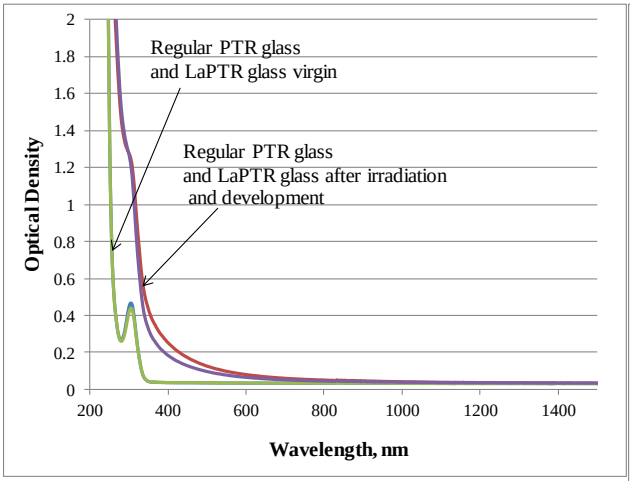

Fig. 59. Absorption spectra of regular PTR glass and PTR glass doped with La before and after the irradiation and thermal development. Glass thickness is 0.198 cm.

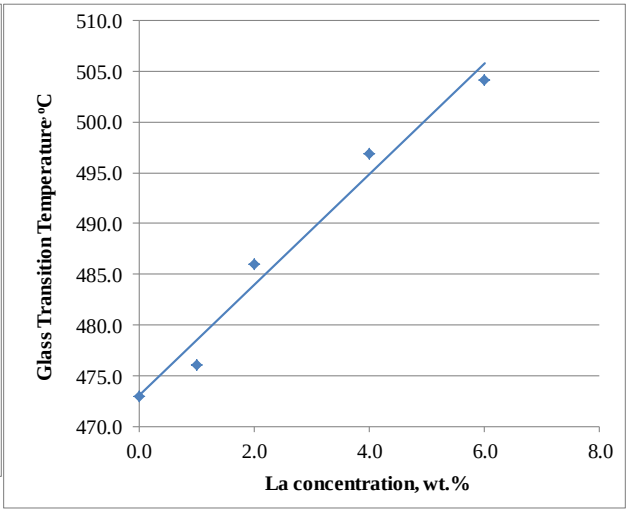

Fig. 60. Dependence of glass transition temperature T_g on La concentration.

We also studied a dependence of viscosity of PTR glass on La concentration in PTR glass. In Fig. 60 it can be seen that increasing of La concentration in PTR glass increases T_g, which is a measure of a glass viscosity since T_g is the temperature when $\log_{10}$ of glass viscosity equal to 12 Pa s. It could be seen in Fig. 60 that doping of PTR glass with La at the level of 1.5% would increase T_g for about 6 K. This difference is not dangerous from the point of view of fiber drawing.

Thus, we can state that the pair of glasses with refractive index required for single mode fiber operating at 1 μm is developed. The core glass is a photosensitive La:PTR glass. The cladding glass is the PTR glass matrix with no photosensitizers which would not be crystallized after UV exposure and thermal development required for hologram recording in the core.

2.5. Laser PTR glass

The Photo-Thermo-Refractive (PTR) glass is composed of eight main components: cations Si, Na, K, Zn, and Al and anions O, F, and Br. This glass is usually doped with four more components added in small concentrations: Sb, Sn, Ce, and Ag. The two last elements are responsible for the photosensitivity of the glass and enable VBGs recording. As it was demonstrated in our earlier studies, additional doping with such elements as Yb, Nd, and Er

allows fabricating gain elements for lasers with external and internal Bragg resonators. All melts were done in a 1 liter Pt crucible with continuous stirring for the satisfactory homogenizing of the glass melt. After annealing the melt, it was sliced and diced to the required dimensions and then polished. The polished glass samples were undergone characterization according to specifications.

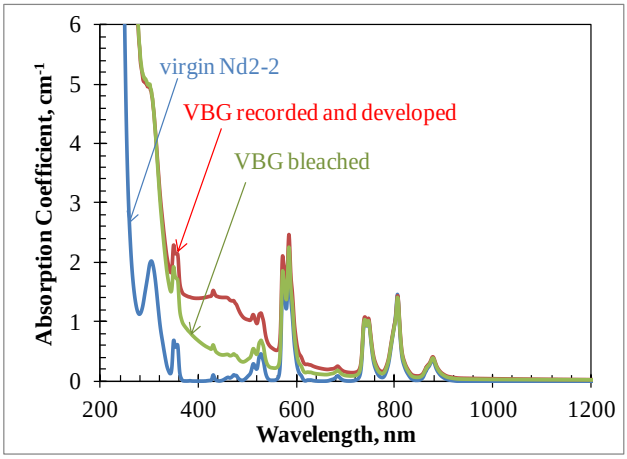

Fig. 61. Absorption spectra of a virgin Nd doped PTR glass sample and the same glass sample after recording a VBG and subsequent bleaching.

The main concern of incorporating of lasing elements in PTR glass was the undesirable possibility of the competing interaction between a photosensitizer Ce and Nd or Yb luminescent agents. Nevertheless, Nd and Yb doped PTR glasses with 2 wt. % of Yb and Nd ions have been prepared and the influence of UV irradiation and thermal treatment (similar to conditions of VBG recording and development) was studied. The absorption spectra of virgin and developed glasses doped with Nd ions are presented in Fig. 61. It clearly can be seen that absorption bands, which are relevant to emission of Nd, are not affected by the process of recording and development of VBGs. Similar results were obtained for Yb doped PTR glasses. These results clearly demonstrate that PTR glass doped with Nd and Yb ions can be used as the gain media emitting light at different wavelengths and at the same time can bare the holograms recorded in the same volume of glass.

Measurements of emission spectra were also carried out in these glasses using an Ocean Optics spectrometer when glass is excited with diode laser emitting at 808 nm (in case of Nd ions) and 915 nm (for Yb ones) (Fig. 62.). One can see that this glass presents broadband emission spectra demonstrating the possibility for wide range tunability. The luminescence lifetime was measured using a photodiode when glass was excited with a modulated diode laser emitting at 808 nm and 915 nm. It was found that decay exhibits a uniform feature that could be described by a single exponential function. The extracted lifetime of Nd and Yb doped PTR glasses with 2 wt. % of Nd and Yb ions were found to be ~ 0.8 ms and ~3 ms respectively.

The photosensitivity of these glasses was measured using the standard procedure developed for the conventional PTR glass, which is provided by exposure of a sample with an UV stripe having a Gaussian lateral profile of intensity followed by fringe shift measurements in a liquid cell

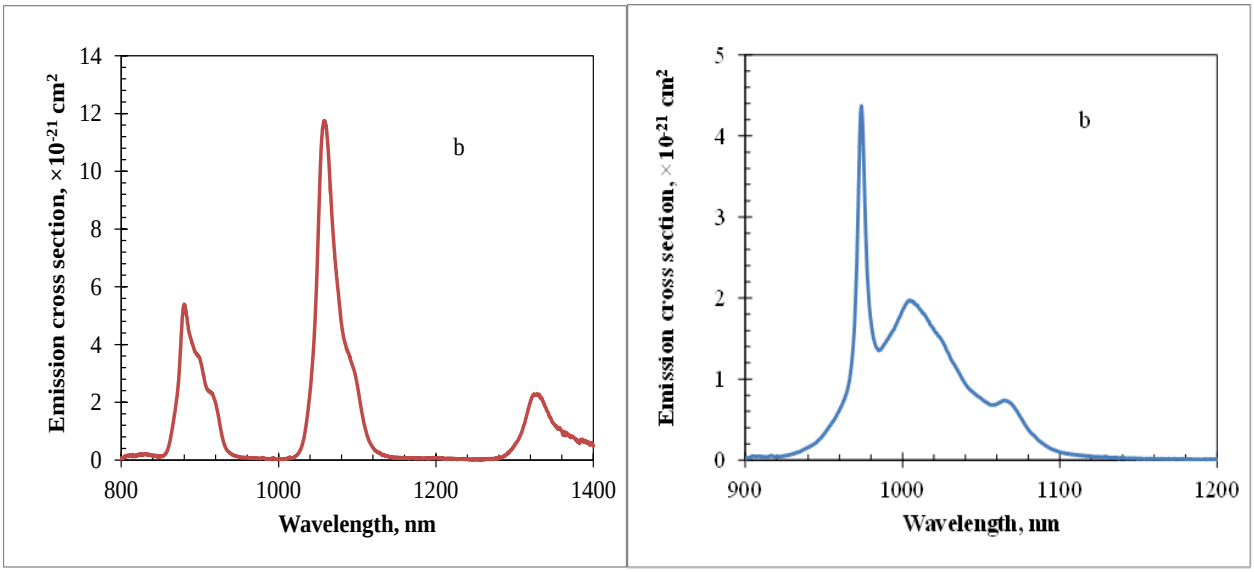

Fig. 62. Luminescence spectra of PTR glasses doped with 2% of Nd ions (a) and 2% of Yb ions (b.)

shearing interferometer. It was found that, in order to get an acceptable refractive index change after an irradiation and a thermal development, the time and temperature had to be increased. For example, a glass sample developed by the standard procedure gave us refractive index change for only 134 ppm. Additional development for one hour at the temperature elevated for 20 K resulted in total 340 ppm of refractive index change. Such phenomenon – smaller Δn after the hologram development in PTR glasses co-doped with luminescent rare earth elements if compared with conventional PTR glass, was explained after studying of the thermal properties of those glasses. It was shown (Fig. 63) that the incorporation of Nd, Yb,and Er ions elevates their glass transition temperature (T_g). Since T_g is a measure of glass viscosity, it is clear that increasing the viscosity at the temperature of the hologram development results in decreasing the mobility of ions participating in photo-thermo-induced structural transformations. This can be taken into account by increasing the time and the temperature or/and the glass composition.

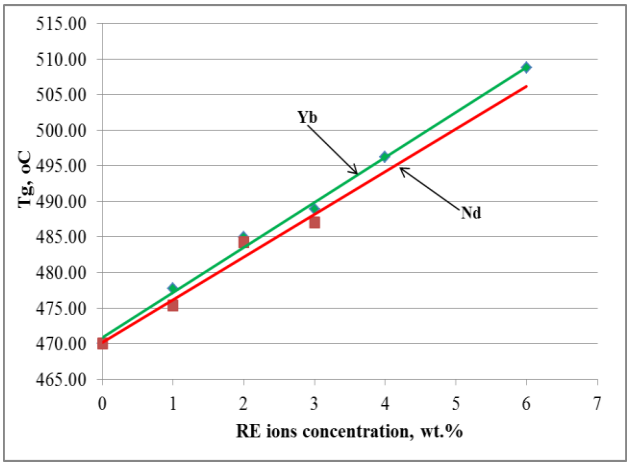

Fig. 63. Dependence of glass transition temperature of PTR glass on luminescent rare earth ions concentration

It is known that viscosity of glasses can be decreased by increasing the concentration of fluorine. To study such a phenomenon in PTR glass, we have melted a series of glasses with different amount of fluorine and measured T_g of those glasses. As it can be seen in Fig. 64, increasing of fluorine concentration in PTR glass decreases the glass transition temperature. Following this study, we have melted two Yb doped PTR glasses with 6 wt.% of Yb and one of them with the increased concentration of fluorine. It was shown that glass with 4 mol.% of F did not demonstrated any photo-chemical reactions at the temperature of conventional thermal development (520ºC). After increasing the fluorine concentration up to 5 mol.%, the photo-induced crystallization at the same temperature was possible and resulted in the refractive index change up to 230 ppm. Temperature of glass transition of this glass decreased down to 484^{o}C compared to T_g=508^{o}C in the glass with 4 mol.% of F.

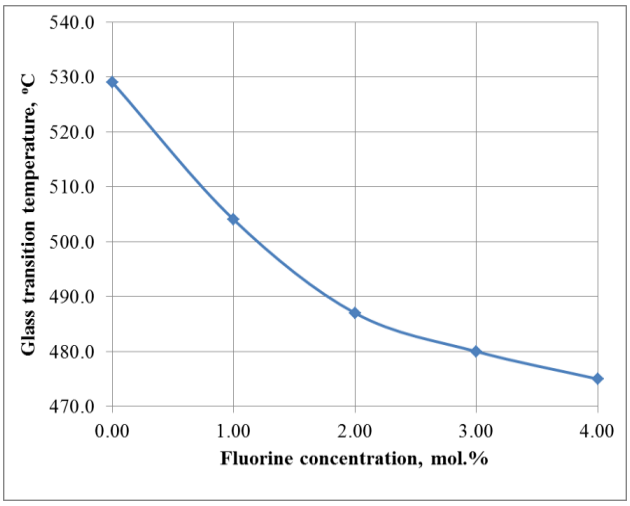

Fig. 64. Dependence of glass transition temperature (T_g) on fluorine concentration in PTR glasses.

Thus, the observed results enable fabrication of PTR like glasses with different concentration of rare earth ions. Those ions could be used for fitting refractive index in pairs of glasses required for achievement of necessary numerical aperture in fibers and for luminescence and amplification required for lasing. Combination of co-doping with rare earth ions and fluorine allows manipulating with glass viscosity and, therefore, with rate of diffusion which controls crystalline phase precipitation and photosensitivity of PTR glass. These results pave a way for both fiber and bulk monolithic solid state lasers.

3. Volume holographic elements

3.1. Theory of beam propagation in complex volume Bragg gratings

3.1.1. Multiplexed gratings for beam combining

One of the important developments in beam combining is the use of multiplexed VBGs that enable splitting and combining of several laser beams in the same volume of such an element. Therefore, multiplexed VBGs were studied, when the same hologram contains several gratings, satisfying Bragg conditions for simultaneous coherent energy transfer from *N* individual waves

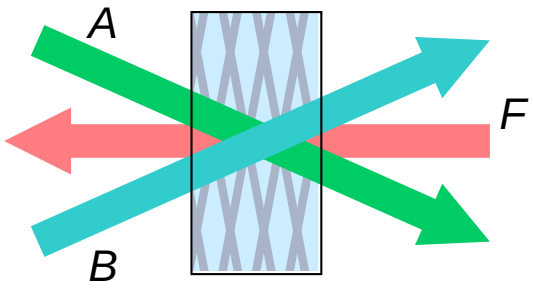

Fig. 65. Scheme of a multiplexed VBG coherently coupling two channels *A* and *B* into a common channel *F*.

A, *B*,…, *D* into one reflected wave *F*, and inverse process $F \to A, B, \ldots, D$, see illustration on Fig. 65.

Coupled wave equations at exact Bragg resonance for slowly varying envelopes (SVE) were taken as

$$\frac{dA}{dz} = i\kappa F(z), \quad \frac{dB}{dz} = i\kappa F(z), \quad ..., \quad \frac{d}{dz}F(z) = -i\kappa[A(z) + B(z) + ... + D(z)]. \qquad (4)$$

Here $\kappa = \pi n_1/\lambda_0$ [m^{-1}], coupling coefficient, $S_1 = \kappa L$ is the strength of individual grating with zero-to-top modulation amplitude of refractive index n_1. To simplify the notations, we have assumed all coupling coefficients κ to be real positive numbers. Then an explicit solution of equation (4) at $z = L$ can be represented in transfer matrix form

$$\begin{pmatrix} A(L) \\ B(L) \\ ... \\ D(L) \\ F(L) \end{pmatrix} = \hat{\mathrm{M}} \begin{pmatrix} A(0) \\ B(0) \\ ... \\ D(0) \\ F(0) \end{pmatrix}, \quad \hat{\mathrm{M}} = \begin{pmatrix} 1+\frac{-1+\cosh S}{N} & \frac{-1+\cosh S}{N} & ... & \frac{-1+\cosh S}{N} & \frac{i\sinh S}{\sqrt{N}} \\ \frac{-1+\cosh S}{N} & 1+\frac{-1+\cosh S}{N} & ... & \frac{-1+\cosh S}{N} & \frac{i\sinh S}{\sqrt{N}} \\ ... & ... & ... & ... & ... \\ \frac{-1+\cosh S}{N} & \frac{-1+\cosh S}{N} & ... & 1+\frac{-1+\cosh S}{N} & \frac{i\sinh S}{\sqrt{N}} \\ -\frac{i\sinh S}{\sqrt{N}} & -\frac{i\sinh S}{\sqrt{N}} & ... & -\frac{i\sinh S}{\sqrt{N}} & \cosh S \end{pmatrix}, \quad S = \sqrt{N}\kappa L. \qquad (5)$$

Here $S = S_1\sqrt{N}$ is the strength of MVBG with *N* gratings of identical strengths S_1.

Appropriate boundary conditions allow finding all the necessary reflection and transmission coefficients. For example, if only *F*-wave is incident, so that corresponding boundary conditions are $F(0) = 1$, while $A(L), B(L), \ldots, D(L) = 0$, then almost all the power P_F is diffracted in equal portions into reflected powers $P_A, P_B, \ldots, P_D$:

$$P_A = P_B = ... = P_D = \eta(A \leftarrow F)P_F, \quad \eta(A \leftarrow F) = \frac{\tanh^2 S}{N} \approx \frac{1}{N}, \quad \tau(F \leftarrow F) \approx 0. \qquad (6)$$

If only *A*-wave is incident upon the MVBG with interaction of all $N + 1$ waves, then boundary conditions are $A(L) = 1$, $B,\ldots,D(L) = 0$, $F(0) = 0$, and the efficiencies of diffraction and transmission are

$$\eta(F \leftarrow A) = \frac{\tanh^2 S}{N} \approx \frac{1}{N}, \quad \eta(B,...,D \leftarrow A) = \frac{1}{N^2}\left(\frac{1}{\cosh S} - 1\right)^2 \approx \frac{1}{N^2},$$
$$\tau(A(L) \leftarrow A(0)) = \left(1 + \frac{1}{N}\left(\frac{1}{\cosh S} - 1\right)\right)^2 \approx \left(\frac{N-1}{N}\right)^2. \qquad (7)$$

The sum of all those reflection coefficients, η, and transmission ones, τ, is equal 1 for both exact expressions and (for $S \geq 3$) for approximate ones.

Important consequence of those solutions is that high efficiency of energy exchange ($\eta \approx 99\%$), which requires $S \approx 3$, may be achieved with relatively small value of strength of individual gratings, $S_1 = 3/\sqrt{N}$. That allows using the PTR glass even in conditions of limitation on the dynamic range of PTR response n_1 in recording.

The system of coupled equations was also derived for general case of spectral detuning from Bragg resonance, and it was solved numerically. Corresponding coherent spectral profiles are presented on Figure 66a and 66b for 2 + 1 wave coupling MVBG, consisted of two gratings with separate diffraction efficiency 99% at resonance, and with FWHM spectral bandwidth about 210 pm.

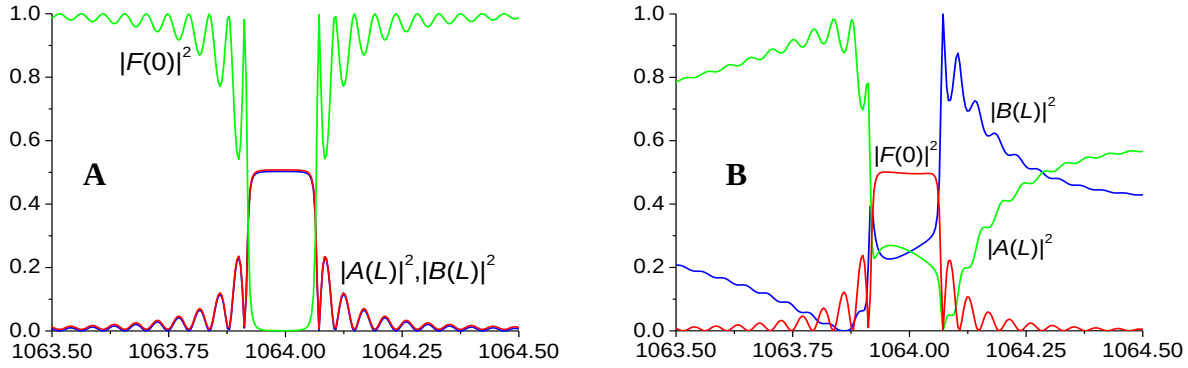

Fig. 66. Spectral properties of double MVBG with 2 + 1 wave coherent coupling: a) incident wave *F*; b) incident wave *A*.

Diffraction efficiencies of several waves incident to MVBG simultaneously can be calculated as well with use of transfer matrix $\hat{M}$ from (5), and results will strongly depend on their mutual phases at boundaries.

It should be emphasized that coherent operation of MVBG cannot be represented by sequence of regular beam splitters; therefore this optical element gives new possibilities for laser system design.

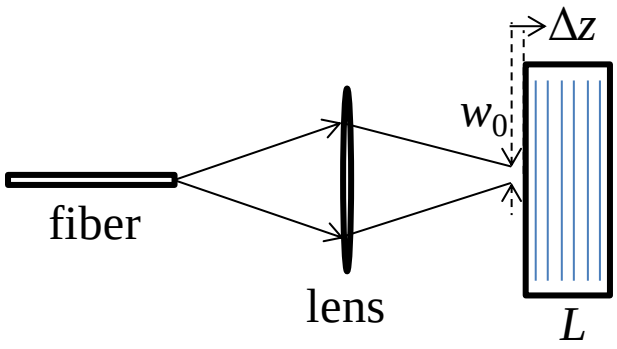

Fig. 67. Scheme of angular and spectral selection of converging fiber radiation by RBG.

3.1.2. Mode selection by reflecting VBGs in converging beams

During the reporting period, we studied theoretically the process of transverse mode selection of a fiber laser radiation by reflecting VBGs in the scheme presented in Fig. 67 where the VBG working as an output coupler in an external resonator of a fiber laser supporting a number of transverse modes. This VBG is placed in a focused beam. Since most lenses and fibers possess axial symmetry, we used system of Laguerre-Gaussian functions of radial coordinate $r=\sqrt{x^2+y^2}$ and azimuthal angle φ: $x=r\cos\varphi, \quad y=r\sin\varphi$. Here are those functions:

$$\psi_{nm}(r,\varphi)=(-1)^n\sqrt{\frac{n!}{\pi(n+|m|)!}}\left(\frac{\sqrt{2}r}{w_0}\right)^{|m|}L_n^{|m|}\left(\frac{2r^2}{w_0^2}\right)e^{-\frac{r^2}{w_0^2}}e^{im\varphi}\frac{\sqrt{2}}{w_0}, \quad \int_0^{2\pi}d\varphi\int_0^{\infty}rdr\psi^*_{n'm'}\psi_{nm}=\delta_{n'n}\delta_{m'm}. \tag{1}$$

These functions are mutually orthogonal at different *m*, *n*, and normalized. The problem of reflection by RBG is facilitated by the fact, that these functions preserve their exact structure under transformation to angular space $(u\equiv\theta_x,\ v\equiv\theta_y)$ with $u=s\cos\varphi, \quad v=s\sin\varphi$:

$$\tilde{\psi}_{nm}(s,\varphi)=\frac{1}{\lambda}\int\psi_{nm}(r,\varphi)e^{-ik(ux+vy)}dxdy=$$

$$=kw_0\sqrt{\frac{n!}{2\pi(n+|m|)!}}\left(-i\frac{kw_0s}{\sqrt{2}}\right)^{|m|}L_n^{|m|}\left(\frac{k^2w_0^2s^2}{2}\right)e^{-\frac{k^2w_0^2s^2}{4}}e^{im\varphi},$$

$$\int_0^{2\pi}d\varphi\int_0^{\infty}sds\tilde{\psi}^*_{n'm'}\tilde{\psi}_{nm}=\delta_{n'n}\delta_{m'm}. \tag{2}$$

This property allowed us to compile the user-friendly program of modal decomposition of the Laguerre-Gaussian mode of laser beam reflected by a VBG with particular parameters. Figure 68 shows screenshot of the user's interface of this program. The particular example shown in Fig. 68 corresponds to a RBG with thickness L = 2 mm and maximum reflection efficiency R = 65% at Bragg resonance wavelength λ_0 = 1.064 μm. The black curve shows an angular profile of

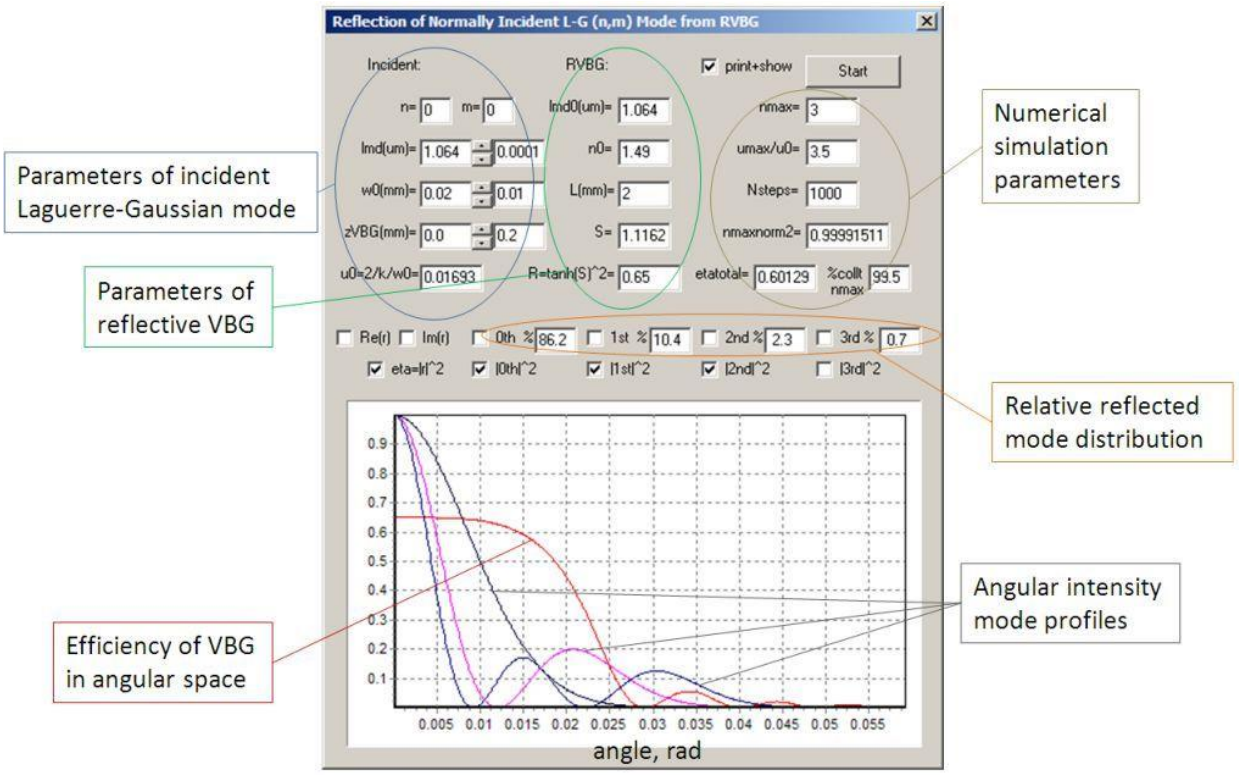

Fig. 68. Screen-shot of interface of program for modeling mode-selective reflectivity of RBG.

intensity of an incident 00-th Laguerre-Gaussian mode with the radius (HWe^{-2}IM) w_0 = 20 μm at the same wavelength $\lambda = \lambda_0$. The waist of the focused beam is located at the front surface of the reflecting VBG, $\Delta z = 0$. The horizontal axis at the plot in the bottom part of the screenshot shows the angle s in air is measured in radians. The red curve depicts angular dependence of diffraction efficiency $\eta = |\rho|^2$ of the VBG under consideration:

$$\rho = \frac{i\,S/G \cdot \sinh(G = \sqrt{S^2 - X^2})}{\cosh G - i\,X/G \cdot \sinh G}, \quad X = \left(k_{\text{in}} - \frac{Q}{2}\right)L, \quad Q = \frac{4\pi n_0}{\lambda_0},$$
$$k_{\text{in}} = \frac{2\pi n_0}{\lambda}\cos\theta_{\text{in}}, \quad \cos\theta_{\text{in}} = \sqrt{1 - s^2/n_0^2}. \qquad (3)$$

The total reflectivity is equal η_{tot} = 60.1% for a particular small size w_0 of the beam waist, while for a wide beam at resonance it should be equal $R = \tanh^2 S$ = 65% for a corresponding grating strength $S = \pi/\lambda_0 \cdot n_1 L$ = 1.12 where n_1 is amplitude of refractive index modulation. Particular numbers, $\eta_{(0\to0)}$ = 86.2%, $\eta_{(0\to1)}$ = 10.4%, $\eta_{(0\to2)}$ = 2.3%, $\eta_{(0\to3)}$ = 0.7%, yield the relative efficiencies of reflection of an incident 00-mode into higher radial n0-modes presented by other colors. These numbers are based on the expressions:

$$\eta_{(0\to n)} = \left|\langle 0|\rho|n\rangle\right|^2 / \eta_{tot}, \quad \eta_{tot} = 2\pi\int \left|\rho(s)\tilde{\psi}_{00}(s,\varphi)\right|^2 s\,ds,$$
$$\langle 0|\rho|n\rangle = 2\pi\int \tilde{\psi}^*_{00}(s,\varphi)\rho(s)\tilde{\psi}_{n0}(s,\varphi)s\,ds. \qquad (4)$$

In general case the redistribution of reflected radiation with the same efficiency η_{tot} into higher-order *n*0-modes depends on relative distance Δz between the waist of the incident beam and the front surface of a VBG. In order to calculate such dependence, the corresponding spherical divergence phase factor $\exp(iku^2\Delta z)$ should be included under integral in ‹0|ρ|*n*›. The black curve in Fig. 69 shows how relative efficiency $\eta_{(0\to0)}$ for lowest mode depends on shift Δz of a beam waist from a 2-mm-thick VBG for numerical parameters discussed above and the grey curve corresponds to a twice thicker VBG with the same maximum reflection efficiency *R*. One can see that maximum relative reflection efficiency of the lowest mode into itself is achieved when beam waist is located inside of volume of the VBG at the distance which is a fraction of grating thickness.

This compiled program with user-friendly interface calculates each variant almost momentarily which allows efficient numerical modeling of angular mode selection in low-mode fiber lasers with the use of VBG providing selective feedback in external fiber resonators.

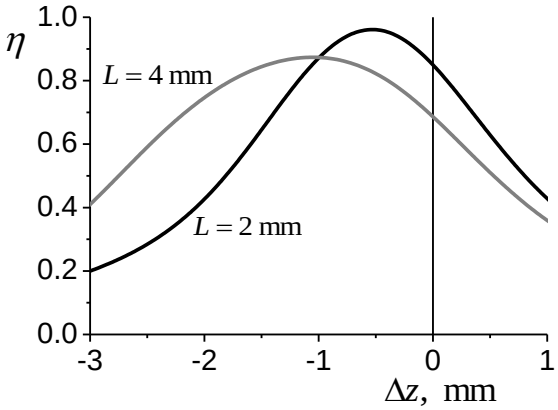

Fig. 69. Dependence of relative efficiency $\eta_{(0\to0)}$ for lowest mode on shift of beam waist from RBG.

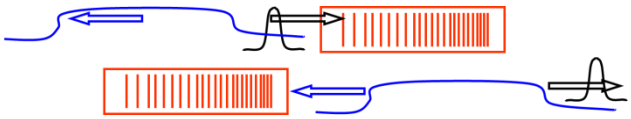

Fig. 70. Stretcher-compressor scheme using CBG.

3.1.3. Stretching and compression of ultrashort laser pulses

We continued working on the modeling of Chirped Bragg Gratings (CBG, reflective) in the scheme Stretcher-Compressor (Fig. 70). The following modifications (in comparison with previous variants of the program) were introduced.

1. With the aim of consideration of CBG composed of two separate pieces, we modeled the problem of two CBGs separated by immersive inert (i.e. without grating) piece of the same glass. Squeezing extra piece of glass between two CBGs resulted in creation of effective Fabry-Perot cavity. The effect of suppressed reflection at the resonant frequencies of the cavity resulted in excitation of long-lived modes of the cavity and lead to spikes in the stretched pulse, Fig. 71.

However, if the phases of two pieces were adjusted (i.e. their distance is tuned with the accuracy of the small fraction of wavelength), then insertion of relatively small piece of inert material, of thickness about 0.4 mm or less, did not hinder the performance of Stretcher-Compressor scheme,

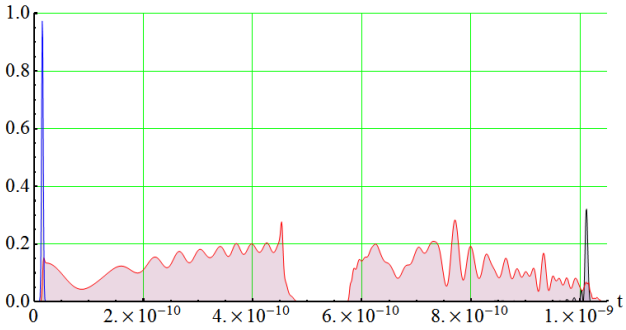

Fig. 71. Input pulse (blue, with unit peak intensity); stretched pulse (red, intensity is scaled by factor 40); re-compressed pulse (black), for the case of CBG with L = 0.1 m and inert insertion ΔL = 0.0125 m, but perfect matching of the phase.

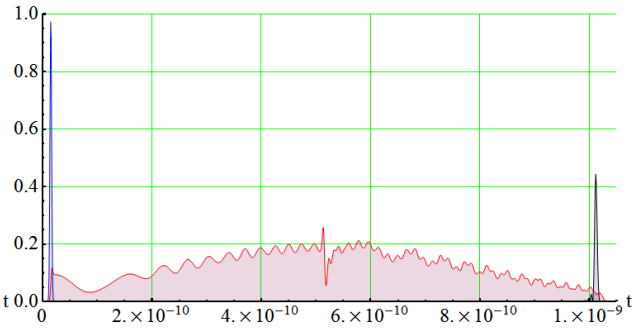

Fig. 72. Input pulse (blue, with unit peak intensity); stretched pulse (red, intensity is scaled by factor 40); re-compressed pulse (black), for the case of CBG with L = 0.1 m and inert insertion ΔL = 0.0004 m, but perfect matching of the phase.

see Fig. 72. On the contrary, detuning from the exact phase matching of two pieces turned to be harmful for the temporal profile of the stretched pulse, and lead also to increase of precursors in the recompressed pulse.

2. We were able to modify the CBG modeling program in such a way, that it completely accounts now for 2a) difference between phase and group velocities; 2b) spread of the input pulse due to Group Velocity Dispersion (GVD); 2c) dispersion of actual glass in all orders of GVD, as described by Sellmeier formula.

Group refractive index of PTR Glass at λ = 1.06 μm turns to be n_{gr} = 1.5017, while phase refractive index is n = 1.4901. GVD parameter, $d^2k / d\omega^2$, turns to be relatively small, $d^2k / d\omega^2 = 1.6 \cdot 10^{-28}$ sec^2 / m. As a result, the length of dispersion spread $z_{disp} = \tau^2 / (2\, d^2k / d\omega^2)$ of a Gaussian pulse with τ(HWe^{-2}IM) = $3 \cdot 10^{-12}$ sec is z_{disp} = 28 km, i.e. much larger than any reasonable length of CBG. However, GVD spread of the pulse may have crucial influence on the stretching-compression of femtosecond pulses.

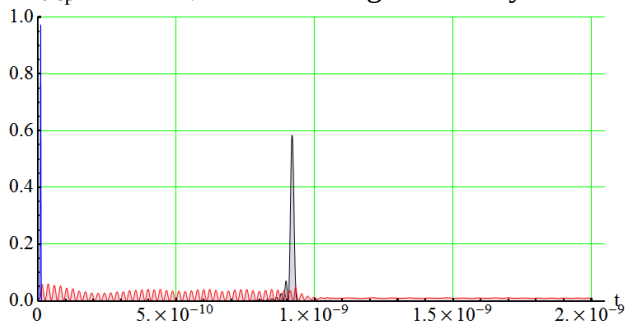

Fig. 73. Input pulse (blue, with unit peak intensity); stretched pulse (red, intensity is scaled by factor 40); re-compressed pulse (black, intensity is scaled by factor 16), for the case of fictitious glass with extremely high dispersion.

Figure 73 shows modeling of stretcher-compressor scheme for a fictitious glass with extremely large dispersion: n = 1.81, n_{gr} = 4.38, $d^2k / d\omega^2 = 5.5 \cdot 10^{-23}$ sec^2 / m, just to demonstrate the performance of modeling program. This variant of program may be important for modeling of stretching and compression of femtosecond pulses, where the dispersion in actual PTR Glass may play important role.

3.1.4. Scheme ASADOG for stretching or compressing short optical pulses

A new type of optical element is proposed for stretching and compression of short laser pulses. Angular Selective Achromatic Diffraction Optical Grating (ASADOG) scheme is evaluated theoretically in application for stretching of short optical pulses. Compromise between polarization-sensitivity, broadband operation and Time Delay Dispersion (TDD) is discussed.

Optical schemes for introduction of wavelength-dependent time delay into a short pulse are used in numerous devices of laser technology. Among them are lasers generating phase-locked combs with spectrum broader then octave and with non-zero value of time-averaged $\langle E^3(t)\rangle$. Laser schemes based on time-stretching of a weak input pulse into a longer chirped pulse, amplification of that chirped pulse and final compression of it back into almost transform-limited short high-energy pulse are actually widely used. Recently fiber Chirped Bragg Gratings (CBGs) were used for considerate stretching of short pulses and their subsequent compression. Important idea was suggested to exploit the same CBG for both, stretching in one direction and compressing in other direction; it helps in overcoming imperfections of CBG.

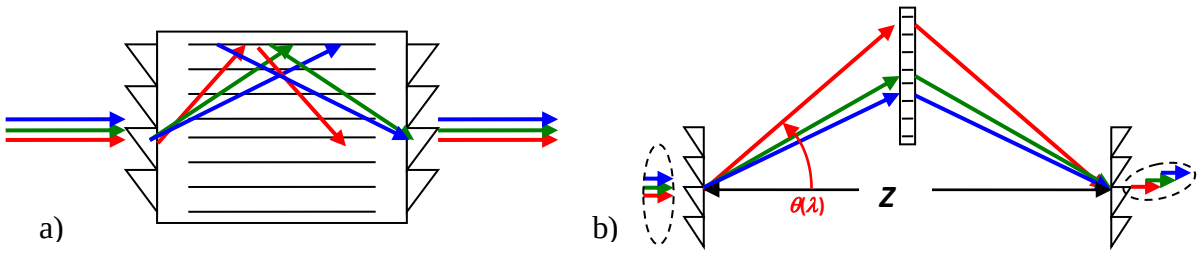

Fig. 74. a) Basic ASADOG scheme: normally incident waves of different wavelengths satisfy Bragg condition inside VBG, if Λ(Surface) $=$ 2Λ(VBG). b) Use of ASADOG configuration as a device for wavelength-dependent time delay.

Here we evaluate the parameters of ASADOG device. It consists of combination of 3 diffraction gratings: Transmission Volume Bragg Grating (TVBG) and two Surface Diffraction Optical Gratings (SDOG), Fig. 74a. Normally incident waves with different wavelength λ are diffracted by first SDOG at different angles:

$$\sin\theta(\lambda) = \lambda/n\Lambda(\mathrm{SDOG}) \qquad (1)$$

where n is the refractive index in the space after SDOG. If the input and output faces of TVBG are provided with SDOG, then the waves incident normally (i.e. along z-axis) upon SDOG all acquire the same x-component of wave vector $q_x = 2\pi/\Lambda(\mathrm{SDOG})$ (for 1-st diffraction order). Under the condition

$$\Lambda(\mathrm{SDOG}) = 2\Lambda(\mathrm{TVBG}) \qquad (2)$$

all those A-waves automatically satisfy Bragg condition for the diffraction $A \rightarrow B$ into the wave B symmetrically situated with respect to z-axis. Functioning of ASADOG is based on well-known Angular Selectivity of TVBG.

Let us evaluate ASADOG scheme as a stretcher or compressor device. The work of such scheme is based on the different time delay

$$t(\lambda) = Z \cdot \left[\cos\theta(\lambda) \cdot v_{\mathrm{gr}}(\lambda)\right]^{-1} \qquad (3)$$

where Z is total distance passed along the orientation of TVBG fringes. Possible variant of using ASADOG configuration for stretching (or compression) shown on Fig. 74b. The scheme presented there (or it's equivalents) also may be implemented with TVBG substituted by SDOG–Mid, with $\Lambda(\mathrm{SDOG}-\mathrm{Mid}) = 0.5 \cdot \Lambda(\mathrm{SDOG1,2})$. However, large required change of propagation direction at SDOG-Mid would make it difficult to achieve high diffraction efficiency for it.

Fig. 75 shows the results of modeling the propagation of 3 beams: with $\lambda = 450$ nm, $\lambda = 550$ nm, and $\lambda = 650$ nm, with the transverse Gaussian profiles $E_0(x) = \exp(-x^2/w^2)$ at the input. The period was chosen as $\Lambda(\mathrm{SDOG1,2}) = 1.0$ μm . For air as medium of intermediate propagation, $n = 1$, $\theta(\lambda = 0.55) = 33.4°$, and the graph of Time Delay Dispersion (TDD) $T(\lambda)$ for total length $Z = 2$ m is presented on Fig. 76.

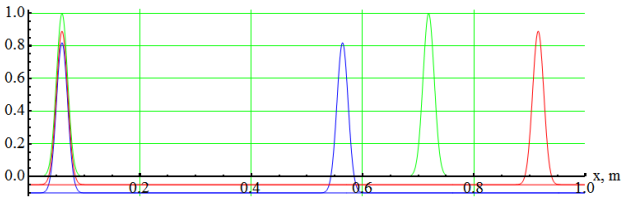

Fig. 75. Transverse profiles of intensity of beams: right, diffracted by sequence of SDOG1 and TVBG; left, finally diffracted by SDOG2. Red lines for $\lambda = 650$ nm; green lines for $\lambda = 550$ nm, blue lines for $\lambda = 450$ nm.

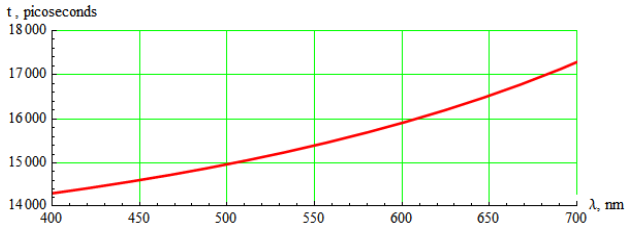

Fig. 76. Time Delay Dispersion (TDD) curve for the scheme Fig. 70 b, with $Z = 2$ m.

We assumed realistic parameters of Transmission VBG: $\Lambda(\mathrm{TVBG}) = 0.5$ μm, $n(x) = n_0 + n_1 \cos(2\pi x/\Lambda_{\mathrm{VBG}})$, $n_1 = 1.3 \cdot 10^{-4}$, thickness of VBG was chosen as $d = 0.002$ m. This resulted in rather modest angular selectivity, $\Delta\theta(\mathrm{FW\O M}) = 0.6 \cdot 10^{-3}$ rad at $\lambda = 0.55$ μm, which in turn resulted in the possibility to handle the beams with w as small as $\Delta x(\mathrm{HWe^{-2}IM}) = w = 0.02$ m, and for any larger values of w. Diffraction efficiency of VBG was $\eta(\lambda = 0.45\ \mu\mathrm{m}) = 0.91$, $\eta(\lambda = 0.55\ \mu\mathrm{m}) = 0.995$, $\eta(\lambda = 0.65\ \mu\mathrm{m}) = 0.93$ for s-polarization; for p-polarization they were 0.99, 0.78 and 0.49 respectively. Steepness of TDD curve, $dT/d\lambda$, is directly proportional to total distance Z along z-direction, and for $Z = 2$ m it was $dT/d\lambda\ (\lambda = 0.65\ \mu\mathrm{m}) = 9.3\,\frac{\mathrm{ps}}{\mathrm{nm}}$. As of now, ASADOG scheme allows for positive $dT/d\lambda$ only.

To conclude, we suggested and modeled theoretically the use of Surface Grating – Volume Gratings – Surface Gratings in ASADOG configuration for wavelength-dependent time delay, with potentially of use as a stretcher or compressor device.

3.1.5. Self-Fourier-Transform Beams and Their Quality Characterization

We introduced new axially-symmetric optical beams, which are Self-Fourier-Transformed and are close to waveguide modes. Quality characteristics for those and other beam types were found: M_x^2, Power-in-the-Bucket product $r\cdot\theta/\lambda$ etc.

Fourier-Transformation is an excellent tool for the study of beam propagation in linear homogeneous medium:

$$\widetilde{E}_{1D}(q_x)=\frac{1}{\sqrt{2\pi}}\int_{-\infty}^{\infty}E_{1D}(x)e^{ix\cdot q_x}dx,\quad \widetilde{E}(q_x,q_y)=\frac{1}{2\pi}\int_{-\infty}^{\infty}\int_{-\infty}^{\infty}E(x,y)e^{ix\cdot q_x+iy\cdot q_y}dxdy \quad . \quad (4)$$

To discuss functions, which do (or do not) possess the property of being Self-Fourier-Transforms (SFT), we need to identify $E_{1D}(x)$ and $\widetilde{E}_{1D}(q_x)$ as belonging to the same space of functions, thus making both x and q_x dimensionless: $q_x=x'$. Corresponding Mathematical Fourier-Transform Operator (MFTO) is defined by

$$\hat{\mathrm{F}}[E](x)=\frac{1}{\sqrt{2\pi}}\int_{-\infty}^{\infty}E(x')e^{ix\cdot x'}dx',\quad \hat{\mathrm{F}}[E](x,y)=\frac{1}{2\pi}\int_{-\infty}^{\infty}\int_{-\infty}^{\infty}E(x',y')e^{ix\cdot x'+iy\cdot y'}dx'dy' \quad . \quad (5)$$

Parseval's theorem guarantees that this is a unitary operator for any number of dimensions. Double application of this operator is, essentially, inverse Fourier transformation, where one has "forgotten" to change the sign in the exponential. Thus the fourth power of MFTO equals to identity operator. Therefore any eigenvalue Λ satisfies $\Lambda^4=1$, and so one gets only four possible (but degenerate) eigenvalues Λ_k of MFTO:

$$\hat{\mathrm{F}}^4=\hat{1},\quad \text{for}\quad \hat{\mathrm{F}}[g(x)]=\Lambda g(x)\quad\rightarrow\quad \Lambda_0=+1,\ \Lambda_1=i,\ \Lambda_2=-1,\ \Lambda_3=-i. \quad (6)$$

Here are two examples of eigenfunctions of one-dimensional MFTO, both with eigenvalue $\Lambda = +1$:

$$g_0(x)=\exp(-x^2/2),\quad c_0(x)=1/\cosh(x\sqrt{\pi/2}) \quad . \quad (7)$$

Important for SFT property is the particular transverse scale of those functions, as in (7). It is convenient to introduce operators U ("up") and D ("down"), which allow generating new eigenfunctions of MFT:

$$\hat{U}=x-d/dx,\ \hat{D}=x+d/dx;\ \text{for}\ \hat{\mathrm{F}}[g_\Lambda(x)]=\Lambda g_\Lambda(x),\quad h(x)=\hat{U}g_\Lambda(x)\rightarrow\hat{\mathrm{F}}[h](x)=i\Lambda h(x) \quad , \quad (8)$$

so that operator U multiplies eigenvalue by $+i$. Similarly, operator D multiplies eigenvalue by $-i$. Well-known system of Hermite-Gaussian (1D) functions,

$$g_n(x) = \left(\sqrt{\pi}\,2^n n!\right)^{-1/2} H_n(x)\exp(-x^2/2), \qquad (9)$$

may be generated by the application of necessary power n of U-operator to the original function $g_0(x)$ from (7).

Generalization of Gaussian SFT to two-dimensional case is trivial: product of two Gaussians, $\exp(-x^2/2)\cdot\exp(-y^2/2) \equiv \exp(-\rho^2/2)$ is automatically axially-symmetric function, and the products $g_n(x)\cdot g_m(y)$ are SFT functions with $\Lambda = i^{m+n}$. Certain disadvantage of Hermite-Gaussian functions (including $g_0(x)$), or their combinations, Laguerre-Gaussian functions, is that their exponent of decrease at large values of x is proportional to $-x^2$ (1D), or to $-\rho^2$ in (2D). Meanwhile, the modes of an optical waveguide have their exponent of decrease at large values of $|x|$ is proportional to $-|x|$ (1D), or to $-\rho$ in (2D). This is exactly the property of hyperbolic secant function $c_0(x)$ from (7). The product $c_0(x)\cdot c_0(y)$ definitely is SFT-function in 2D, but it is not axially-symmetric.

In this work we study a new type of axially-symmetric 2D SFT-function of dimensionless radius ρ:

$$C_{00}(\rho) = (1/2\pi)\int_0^{2\pi} c_0(\rho\cos\varphi)c_0(\rho\sin\varphi)d\varphi; \quad C_{00}(\rho) \cong (4/\rho\sqrt{\pi/2})\exp(-\rho\sqrt{\pi/2}) \text{ at } \rho\to\infty. \qquad (10)$$

The graph of the function $C_{00}(\rho)$ is given in Fig. 77. In actual work with this function, we have calculated the values of the integral for large number of points with small steps $\Delta\rho$ once and forever, and then used the standard spline interpolation procedure, resulting in high speed of calculations.

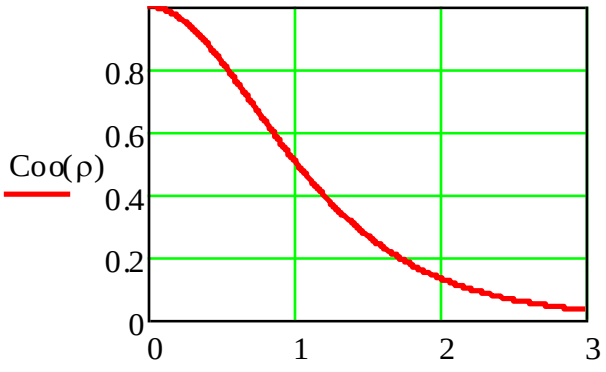

Fig. 77. Self-Fourier-Transform function $C_{00}(\rho)$.

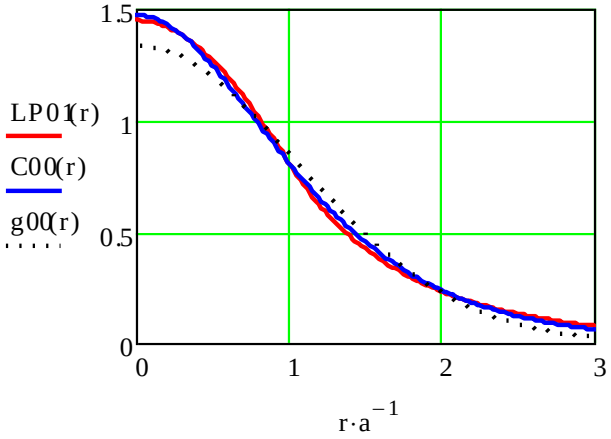

Fig. 78. Profile of the total-power-normalized modal field $LP_{01}(r)$ (red curve); its approximation by $C_{00}(\rho\cdot w)$ (blue) and by $G_{00}(\rho\cdot w)$ (dotted); $w = 1.07a$, where a is core radius.

This axially symmetric field is pretty good approximation for the lowest mode $LP_{01}(r)$ of optical fiber with circular step-index profile of refractive index (core radius a), if appropriate size w is chosen for $LP_{01}(r) \approx C_{00}(\rho \cdot w)$. Figure 78 shows an example of a fiber mode $LP_{01}(r)$ for a fiber with V-parameter $V = 1.7$, and $C_{00}(\rho \cdot w)$ function with $w = 1.07a$.

Square of normalized overlapping integral for the mode profile $LP_{01}(r)$ with normalized $C_{00}(\rho \cdot w)$, for V-parameter $V = 1.7$, and $w = 1.07a$ was equal to $1–1.76 \cdot 10^{-3}$, while similar square of overlapping for Gaussian function was $1–1.7 \cdot 10^{-2}$. Here M_x^2 is well-known quality parameter of the beam quality. This parameter has been calculated for step-index fiber modes analytically.

To conclude, we have introduced new Self-Fourier-Transform axially symmetric amplitude profile $C_{00}(\rho)$ from (10), which has the property of linear-exponential decrease at large radius. This SFT profile approximates LP_{01} fiber mode with much better accuracy than Gaussian profile.

3.1.6. Spectral dependence of optical absorption in VBGs

Coefficients of absorption and scattering in PTR glass are key characteristics which define the total optical losses in VBG. In high-power laser applications such as spectral beam combining realized with VBGs[59], the heating due to absorption is the main limiting factor of the whole system performance. The amount of power loss per unit thickness in an optical element is proportional to the loss coefficient and the local intensity. Depending on resonant conditions, the intensity distribution along a thickness of a Bragg grating changes dramatically. Thus for a VBG operated at some power level the absorption heating as a part of optical losses will be different for different wavelength detuning from the Bragg resonance. In other words, the effective thickness of the Bragg grating depends on wavelength detuning and therefore at the same incident power the amount of absorbed and scattered power varies correspondently with changing the effective thickness.

In this part of report we present a study of the dependence of absorption inside uniform reflective VBGs on detuning from an exact Bragg resonance condition. Our results and conclusions are based on a theoretical analytical approach to the problem of a uniform reflective VBG. We assume that the loss coefficient $\alpha[m^{-1}]$ responsible for effects of absorption and scattering is relatively small and it is uniform along a thickness of the grating L, so $\alpha L \ll 1$. Also we assume that transverse profile of propagating beam inside reflective Bragg grating does not change its shape which is typically Gaussian one, so we will discuss longitudinal profiles of intensity along beam axis which is equivalent to discussing of longitudinal profiles of total beam power.

In considered case of small α, we can use the following approach. First we will find the intensity profile $I(z)$ along the grating thickness without any losses and then we will calculate an total drop of intensity as a product of α by integrated $I(z)$ along the grating. This integral of intensity is nothing else as a product of incident intensity by effective thickness of grating. For an incident beam with intensity I_0 and with a wavelength far from Bragg resonance the propagating intensity is very slowly decreasing along grating thickness by simple exponential law $I(z) = I_0 \cdot e^{-\alpha z}$, and it

[59] O. Andrusyak, V. Smirnov, G. Venus, V. Rotar, and L. Glebov, "Spectral Combining and Coherent Coupling of Lasers by Volume Bragg Gratings," IEEE J. Sel. Top. Quantum Electron. 15, 344–353 (2009).

can be assumed as uniform equal I_0 for $\alpha L \ll 1$. The lost intensity after propagation is just a simple product $\alpha L I_0 \approx I_0 - I_0 \cdot e^{-\alpha L}$. So αL is the fraction of intensity lost in PTR glass plate. Goal of our analysis is to study the relative variation of this fraction in the vicinity of the Bragg resonance in uniform gratings with modulated refractive index $n_0 + n_1\cos(Qz)$, $Q = 4\pi n_0/\lambda_0$, where λ_0 is the resonant Bragg wavelength.

Propagation of electromagnetic waves inside Bragg gratings is typically represented in terms of counter-propagating waves $A(z)\exp(-i\omega t + ikz)$ and $B(z)\exp(-i\omega t - ikz)$ with $k = n_0\omega/c = 2\pi n_0/\lambda$. Coupled equations for slowly varying envelopes $A(\zeta)$ and $B(\zeta)$, where we introduced normalized dimensionless coordinate $0 \le \zeta = z/L \le 1$, are the following

$$\frac{dA}{d\zeta} = iS \cdot B(\zeta)e^{-2iX\zeta}, \quad \frac{dB}{d\zeta} = -iS \cdot A(\zeta)e^{2iX\zeta}, \quad S = \frac{\pi n_1}{\lambda_0}L, \quad X = (k - \tfrac{1}{2}Q)L \approx -2\pi n_0 \frac{\Delta\lambda}{\lambda_0^2}L \quad , \quad (11)$$

Here the dimensionless coupling parameter S is so-called Strength of Reflection[60], and X is the dimensionless wavelength detuning. Because we will be interested in the detuning dependence of relative values, let us make for convenience the amplitude of incident beam $A(0) = 1$, and another standard boundary condition for the reflection problem is $B(\zeta{=}1) = 0$.

According to mentioned boundary conditions and based on the well-known analytical solution of the system (11) for uniform Bragg gratings we can write down explicit expressions for the wave amplitudes along the ζ-coordinate inside the grating in the following form

$$A(\zeta) = e^{-iX\zeta}\frac{\cosh[G(1-\zeta)] - iX/G \cdot \sinh[G(1-\zeta)]}{\cosh G - iX/G \cdot \sinh G}, \; B(\zeta) = e^{iX\zeta}\frac{iS/G \cdot \sinh[G(1-\zeta)]}{\cosh G - iX/G \cdot \sinh G}, \; G = \sqrt{S^2 - X^2} \quad .(12)$$

The second expression in (12) agrees with the well-known formula for spectral reflectivity of a uniform Bragg grating $R = |B(0)|^2 = \sinh^2 G/(\cosh^2 G - X^2/S^2)$, which gives $R_0 = \tanh^2 S$ at the exact Bragg resonance. This theoretical spectral behavior of reflectivity is shown in Fig. 79 together with experimental spectrum of actual VBG recorded for 99% resonant reflectivity in PTR glass with the following parameters: L = 3.6 mm, λ_0 = 1066.14 nm, n_0 = 1.49, $n_1 = 265 \cdot 10^{-6}$.

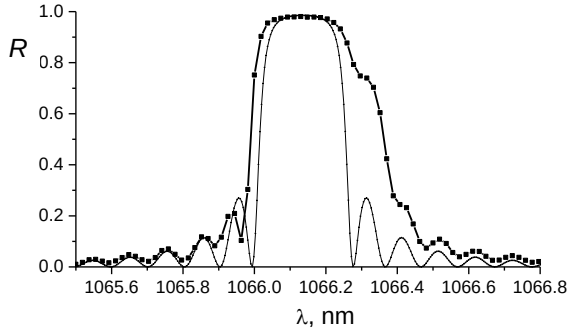

Fig. 79. Experimental reflection spectrum of a VBG with a simulated profile (thin line).

[60] S. Mokhov and B. Zeldovich, "Strength of electromagnetic, acoustic and Schrödinger reflections," Proc. R. Soc. A 464, 3071-3080 (2008).

The corresponding reflection strength is $S = 2.81$. Asymmetry of the experimental reflection profile and washing out of its zeros can be explained by longitudinal non-uniformities of fabricated VBG [29].

Intensity profiles of two counter-propagating waves $|A|^2$ and $|B|^2$ occurring at two different resonant conditions are presented in Fig. 80 according to explicit expressions (12). Total intensity inside a VBG is equal to sum of them, $I(\zeta) = |A|^2 + |B|^2$. Plots in Fig 80a show longitudinal intensity distribution profiles at exact Bragg resonance, $X = 0$, when incident intensity $|A|^2$ and reflected intensity $|B|^2$ are exponential decrease with propagation along the thickness inside the grating. As a consequence of lossless coupled wave equations (12) the Poynting vector $|A|^2 - |B|^2$ will be conserved for any wavelength detuning. Plots on Fig 80b show longitudinal intensity distribution profiles at wavelength detuning corresponding to 1st reflection zero and as result to total transmission, $B(0) = 0$ leads to $X_{1st} = (S^2 + \pi^2)^{1/2}$. These plots demonstrate an accumulation of intensity inside VBG which is very similar to effect of increasing a resonant intensity capacity in Fabry-Perot cavities.

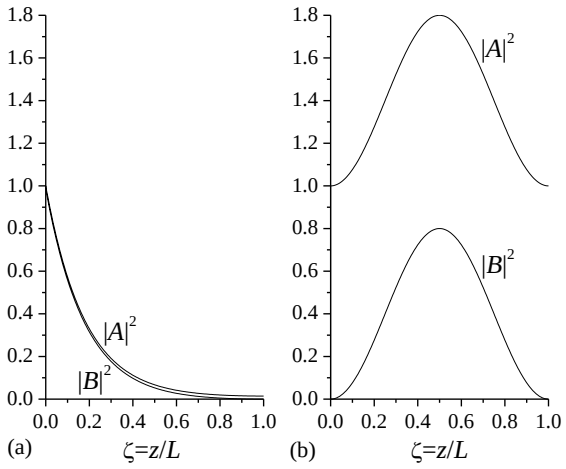

Fig. 80. Intensity distributions: a) at exact Bragg resonance; b) at wavelength detuning to the 1st reflection zero.

The next step in determination of the variation of losses with detuning is the calculation of the intensity profile $I(\zeta)$ inside the Bragg grating with the use of (12) and integrating this profile along whole length:

$$I(\zeta) = |A|^2 + |B|^2 = \frac{\cosh[2G(1-\zeta)] - X^2/S_0^2}{\cosh^2 G - X^2/S_0^2}, \quad f(S,X) = \int_0^1 I(\zeta)d\zeta = \frac{\sinh(2G)/(2G) - X^2/S^2}{\cosh^2 G - X^2/S^2} \quad . \quad (13)$$

Because we are using a normalized incident intensity $|A(0)|^2 = 1$, the last integral gives us the necessary relative function $f(S,X)$ of the variation of total losses in the Bragg grating with wavelength detuning; far from resonance $f|_{X\to\infty} = 1$.

We made experimental measurements of the variation of losses in a VBG at a small incidence angle. In this case the incident and reflected beams can be resolved and the power balance can be precisely measured with beam sampler for incident power calibration in the experimental setup presented in Fig. 81. The absolute value of losses was less than 10^{-2}.

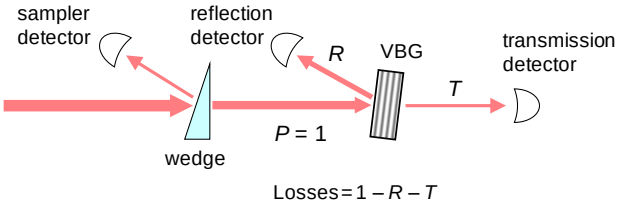

Fig. 81. Experimental setup for measurement of losses in VBG.

Figure 82 represents the experimental relative variation of losses versus wavelength detuning from Bragg resonance and corresponding theoretical curve of this loss ratio variation $f(S,X(\lambda))$ (13) with particular value of the grating strength S mentioned before. Despite some systematic errors of measurements and previously mentioned non-homogeneities inside the VBG, both curves in Fig. 24 clearly demonstrate the common spectral behavior.

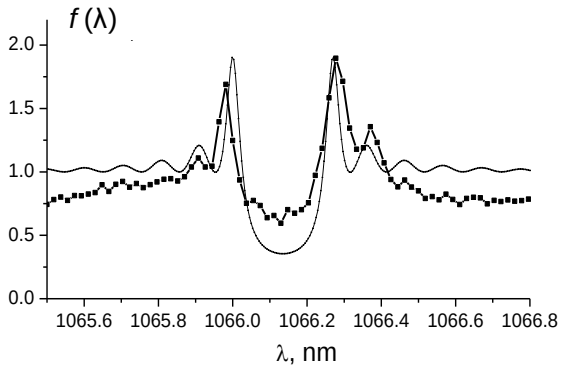

Fig. 82. Experimental variation of absorption ratio versus detuning and corresponding numerical simulation (thin line).

The lowest value of theoretical function (13) is $f_{min} = f(S,0) = 1/S \approx 0.35$ at the exact Bragg resonance for the used parameters of grating. Lowering of absorption in this case is explained by the exponential decrease of the reflected and transmitted power inside the grating, see Fig. 22a. The highest value $f_{max} \approx 1.91$ occurs near the first zero of the reflection spectrum due to increased resonant capacity of the grating, similar to a Fabry-Perot resonator, Fig. 22b. We see that relative variation of loses can differ up to 6 times for the same grating with the reflectivity about 99%.

Obtained results show the importance of taking into account the possibility of varying of absorption in VBGs used in different beam combining schemes because scattering and

absorption in high-power applications could cause significant thermal heating and distortion of VBGs themselves or their mounting elements.

3.1.7. Effect of refractive index kinetics on optical properties of gratings

Recording of Volume Bragg Gratings (VBG) in Photo-Thermo-Refractive glass is limited to maximum refractive index change about 0.002 (2000 ppm). We discuss various saturation curves and their influence on amplitudes of recorded gratins. Special attention is given to multiplex VBGs aimed at recording of several gratings in the same volume. The best shape of saturation curve for production of strongest gratings is the threshold-type curve. Two photon absorption as mechanism of recording also allows increasing the strength of multiplexed VBG.

Volume Bragg Gratings (VBG) recorded in Photo-Thermo-Refractive (PTR) glass constitute new set of optical elements. Many of these elements are multiplexed VBGs, i.e. they contain several gratings with different spatial frequencies. Amplitudes of recorded gratings, both single and multiplexed ones, i.e. spatial Fourier-components of recorded $\delta n(\mathbf{r})$, are limited due to the fact of saturation of refractive index change by value $\Delta n_{\max}$. In the case of PTR glass the value of $|\Delta n_{\max}|$ in the best condition of recording and thermal development of VGB is about $|\Delta n_{\max}| \approx 0.002$.

Recording several volume holograms in the same volume has been studied theoretically and experimentally in Ref. [61], [62] and numerous other works, with the purpose of data storage. Those studies were aimed to maximize the number of recorded holograms. The requirements to diffraction efficiency of each individual grating were not very stringent: diffracted wave had to be detectable at the level of rather weak noise. Most of those data-storage works were discussing and implementing multiplexed recording in electro-optic photorefractive crystals. Those crystals do not have strong response to the pedestal of recording beam intensity [63], [64], therefore only small spatial period (spatial AC) components of illumination at recording were accounted for. As a result, the mean square average amplitude of spatial AC-modulation grows as $\sqrt{N}$, where N is the number of gratings with independent periods and independent phases.

The main application of PTR glass-based VBGs, both single and multiplexed ones, is handling high-power beams, be they inside the laser cavity or outside it. Therefore the achievement of large diffraction efficiency via generating strong spatial Fourier-component of refractive index modulation (RIM) is of essence. Exposure of the medium via single-photon absorption of interference patterns is assumed to be:

$$U(\mathbf{r}) = U_1[1 + \cos(\mathbf{q}_i\mathbf{r} + \varphi_1)]$$

---

[61] D.Psaltis, D. Brady, K.Wagner, "Adaptive optical networks using photorefractive crystals", Applied Optics V. 27, No. 9, 1752-1759 (1988).
[62] J.R.Wullert II, Y.Lu, "Limits of the capacity and density of holographic storage", Applied Optics V. 33, No. 11, 2192-2196 (1994).
[63] P. Günter, J. P. Huignard, "Photorefractive Materials and Their Applications 1: Basic Effects" (v.2), Springer (2005)
[64] P. Günter, J. P. Huignard, "Photorefractive Materials and Their Applications 2" (v.2), Springer (2006)

The main feature of PTR-VBG is that the pedestal part, $U_1 \cdot 1$, of the exposure, counts with the same coefficient as the grating part, $U_1 \cos(\mathbf{q}_i\mathbf{r} + \varphi_1)$. For large degree of multiplexing, $N \gtrsim 4$ it is the saturation of recording response by sum of pedestals $\sum_j U_j \sim U_1 N$, that is the crucial factor. Meanwhile, individual gratings, $U_j \cos\big(\mathbf{q}_j\mathbf{r} + \varphi_j\big)$, have random phases, and their r.m.s. amplitude grows as $U_1\sqrt{N}$.

We study theoretically in this work the influence of saturation on recorded VBG with account of the following factors:
1) Shape $\rho(U)$ of the saturation curve, i.e. dependence of refractive index change upon total exposure $U(\mathbf{r})$: $\Delta n(\mathbf{r}) = \Delta n_{\max} \cdot \rho\big(U(\mathbf{r})\big)$
2) Number N of individual gratings aimed to be recorded.
3) Spatially-average exposure $\langle U \rangle \approx U_1 N$ due to pedestal.

All 7 shapes $\rho(U)$ studied by us are normalized in such a way that $\rho(U \to \infty) = 1$. Besides that, first 5 curves under consideration have the property $\rho(U \to \infty) = 1 \cdot U$. The latter condition just means the choice of units of exposure. Here are 7 different shapes that we have considered:

$$\rho_{\text{th}}(U) = \tanh(U) \tag{3.1}$$

$$\rho_{\text{at}}(U) = (2/\pi)\arctan(\pi U/2) \tag{3.2}$$

$$\rho_{\text{pw}}(U) = U/(1+U) \tag{3.3}$$

$$\rho_{\text{ex}}(U) = 1 - \exp(-U) \tag{3.4}$$

$$\rho_{45}(U) = U \ \text{ at } \ 0 < \text{U} < 1, \ \ \rho_{45}(U) = 1 \ \text{ at } \ \text{U} > 1 \tag{3.5}$$

$$\rho_{60}(U) = 0 \ \text{ at } \ 0 < \ \text{U} < 0.5, \ \ \rho_{60}(U) = 2(U - 0.5) \ \text{ at } \ 0.5 < \text{U} < 1, \ \ \rho_{60}(U > 1) = 1 \tag{3.6}$$

$$\rho_{st}(U) = 0 \ \text{ at } \ 0 < \text{U} < 1, \ \ \rho_{st}(U) = 1 \ \text{ at } \ \text{U} > 1. \tag{3.7}$$

These 7 curves of saturation are presented in Fig. 83. By saturation curve $\rho(U)$ we denote function $\rho(U)$ in the relationship, that we assume in our model:

$$\Delta n(\mathbf{r}) = \Delta n_{\max} \cdot \rho(U). \tag{3.8}$$

We assume that an individual grating is recoded via interference pattern of 2 coherent waves. Intensity in such interference pattern is

$$U_j\big(1 + \cos\big(\mathbf{q}_j\mathbf{r} + \varphi_j\big)\big). \tag{3.9}$$

For single-photon absorption, the exposure by N sequential interference patterns is

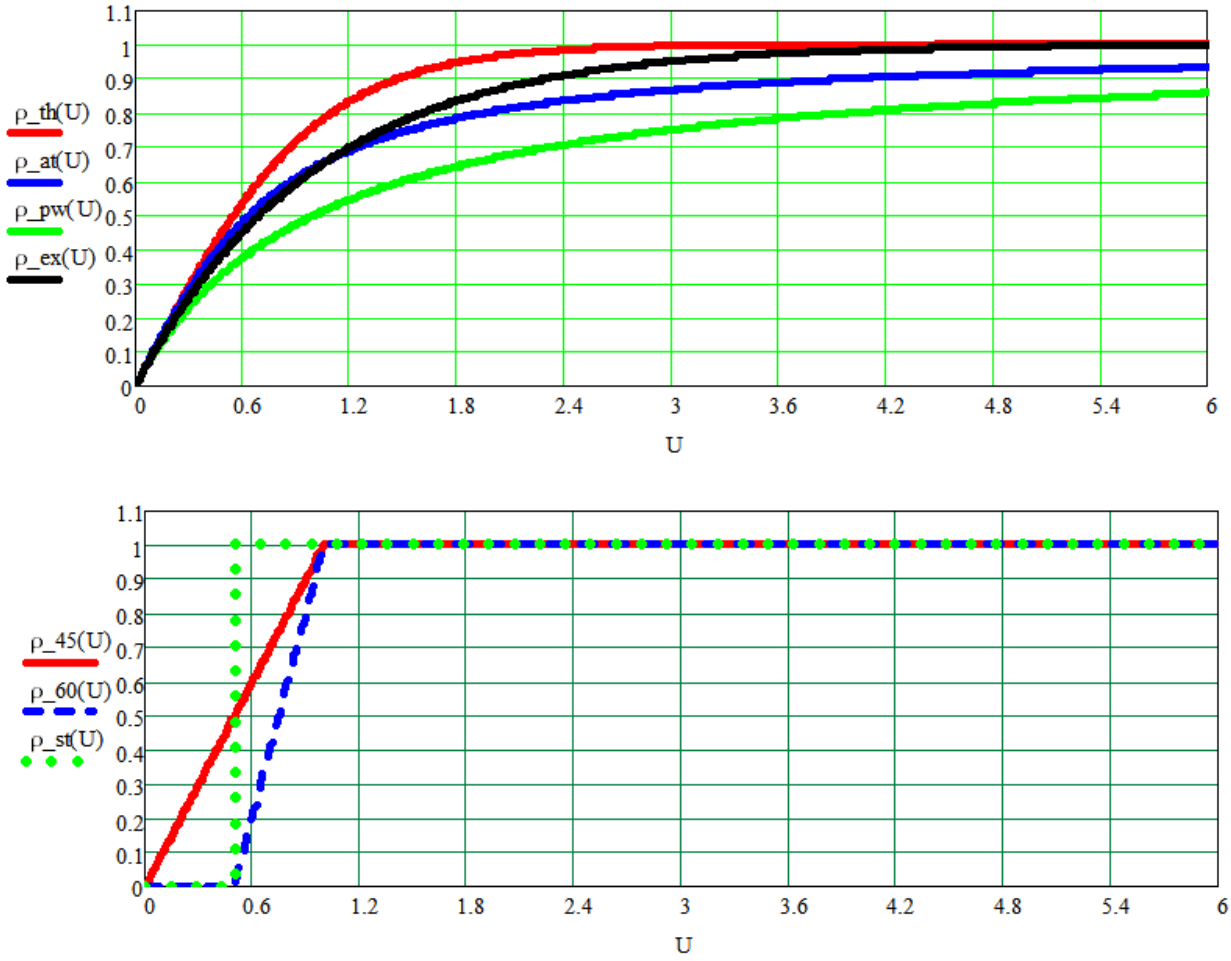

Fig. 83. Seven curves of saturation: refractive index change vs. exposure dose U. Here $\rho_{\text{th}}(U) = \tanh(U)$, $\rho_{\text{at}}(U) = (2/\pi)\arctan(\pi U/2)$, $\rho_{\text{pw}}(U) = U/(1+U)$, $\rho_{\text{ex}}(U) = 1 - \exp(-U)$, $\rho_{45}(U) = U$ at $0 < \text{U} < 1$, $\rho_{45}(U) = 1$ at $\text{U} > 1$, $\rho_{60}(U) = 0$ at $\text{U} < 0.5$, $\rho_{60}(U) = 2(U - 0.5)$ at $0.5 < \text{U} < 1$, $\rho_{60}(U > 1) = 1$, $\rho_{st}(U) = 0$ at $0 < \text{U} < 0.5$, $\rho_{st}(U) = 1$ at $\text{U} > 0.5$.

$$U(\mathbf{r}) = \sum_{j=1}^{N} U_j\left[1 + \cos\left(\mathbf{q}_j\mathbf{r} + \varphi_j\right)\right]. \tag{3.10}$$

Figure 84 shows the processes of recording of single interference pattern in condition of saturation according to arctangent law, Eq. (3.2).

For definiteness we consider all N intensities U_j to be the same at multiplexed recording: $U_j = U_1$. Meanwhile the wave vectors $\mathbf{q}_j$ and phases φ_j are considered (in our model) statistically independent random quantities.

For two-photon absorption of recording pattern of interference we take

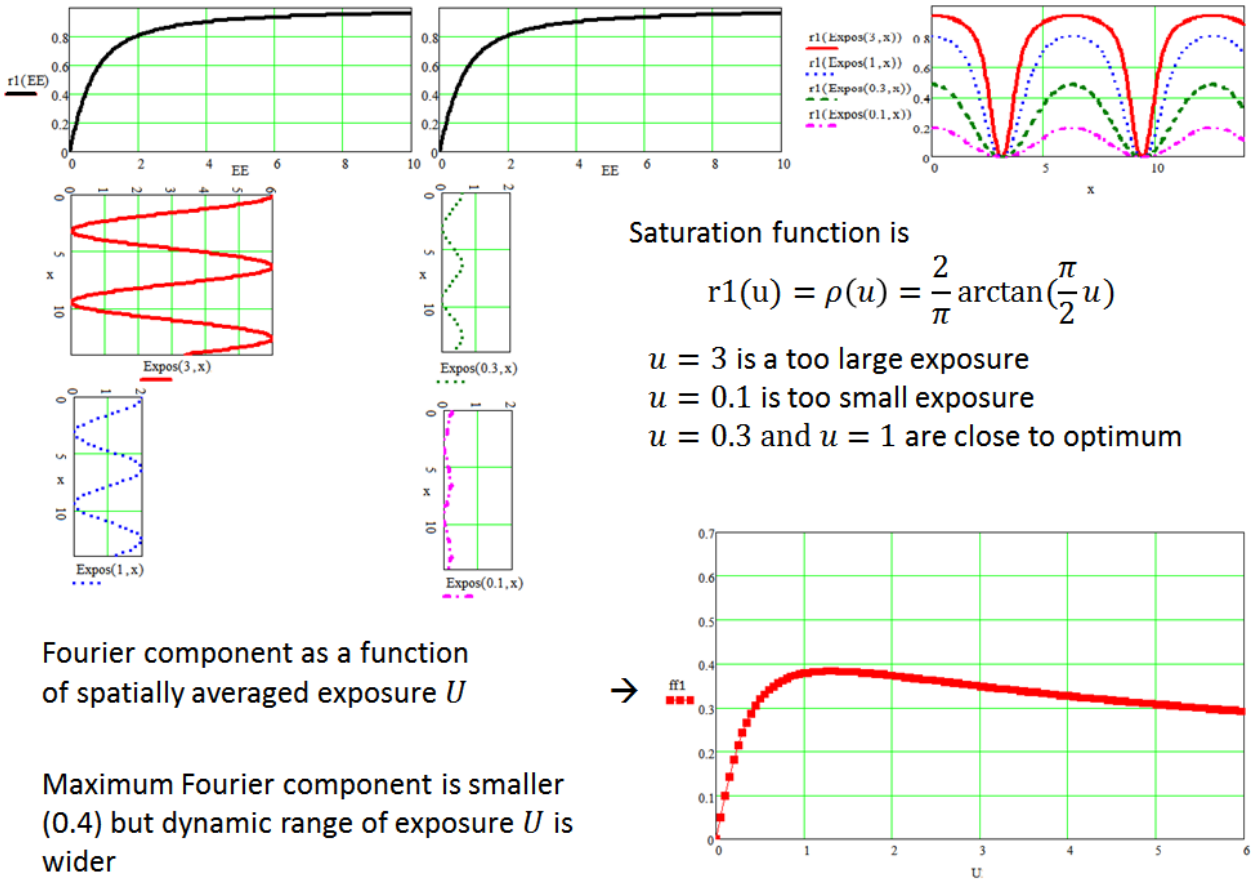

Fig. 84. Recording of single interference pattern $U[1+\cos(qx)]$ at different levels of U.

$$U_j{}^2\left[1+\cos\left(\mathbf{q}_j\mathbf{r}+\varphi_j\right)\right]^2 \equiv U_j{}^2\left[1+2\cos\left(\mathbf{q}_j\mathbf{r}+\varphi_j\right)+\frac{1}{2}+\frac{1}{2}\cos\left(2\mathbf{q}_j\mathbf{r}+2\varphi_j\right)\right] \equiv$$
$$\equiv \frac{3}{2}U_j{}^2\left[1+\frac{4}{3}\cos\left(\mathbf{q}_j\mathbf{r}+\varphi_j\right)+\frac{1}{3}\cos\left(2\mathbf{q}_j\mathbf{r}+2\varphi_j\right)\right]. \qquad (3.11)$$

Note that relative modulation term at "right" spatial frequency has increased by factor $4/3$. Besides that, second spatial harmonic appears in $U(\mathbf{r})$ for two-photon recording.

By Fourier component of VBG we denote the quantity

$$F_j = \frac{2}{V}\iiint d^3\mathbf{r}\rho\left(U(\mathbf{r})\right)\cos\left(\mathbf{q}_j\mathbf{r}+\varphi_j\right). \qquad (3.12)$$

Here trivial factor $\Delta n_{\max}$ is omitted. Normalization coefficient $2/V$, with V being integration volume, is chosen in such a way, that for first 5 curves of saturation $\rho_\alpha(U)$ the value of F_j is equal to U_j at $NU_1 \ll 1$. In actual calculations we used 1-dimentional integral over the interval length L, with normalization coefficient $2/L$:

$$F_j = \frac{2}{L}\int_{\rho}^{L} dx\,\rho\big(U(x)\big)\cos\big(q_j x + \varphi_j\big). \qquad (3.13)$$

The values of $q_j L$ were around 100 radian and more, q_j were chosen mutually non-commensurate, and phases φ_j were random within interval $(0, 2\pi)$. We successfully checked that if some particular component $U_k[1+\cos(q_k x+\varphi_k)]$ was absent during recording then, the Fourier-component F_k calculated by eq. (13) was much smaller than those F_j, whose $U_j\big[1+\cos\big(q_j x+\varphi_j\big)\big]$ were actually present at recording.

Table 6. Peak Fourier amplitudes for all seven functions for $N=1$ grating in case of one-photon absorption.

Curve type	tanh	arctan	power	exp	line (0,0) (1,1)	line (0.5,0) (1,1)	Heaviside at x=0.5
F_1 peak	0.472	0.382	0.343	0.438	0.536	0.625	0.637
$N\cdot U_1$ $(N=1)$ for peak value	1.05	1.3	2.45	1.55	0.65	0.8	1

The first step was to find the dependence of Fourier component of $\delta n(\mathbf{r})$ for recording of a single grating: $N=1$, on the value of exposure $NU_1 \equiv U_1$. Figure 4 shows the dependence of F_j on U_1 for 7 studied curves of saturation. All 7 laws of saturation demonstrated peak of F_1 around $U_1 \sim 1$, and decrease of F_1 for large U_1. The peak values of F_1 peak and corresponding exposure U_1 delivering that F_1 peak are presented in Table 6.

Qualitative conclusion is that sharper $\rho(U)$ curves yield larger values of $F_{1,\ \mathrm{peak}}$. However,

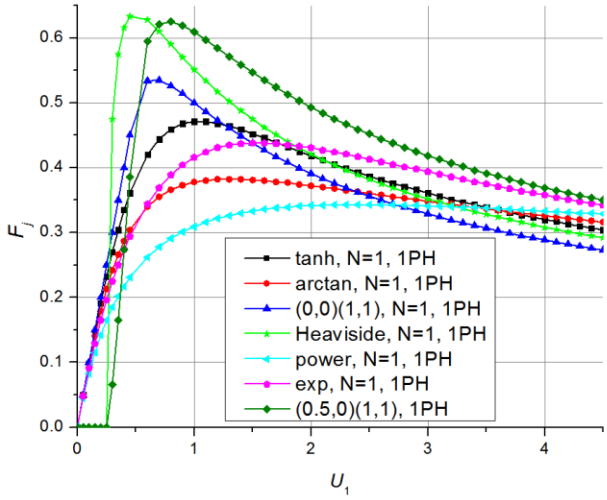

Fig. 85. Dependence of Fourier amplitude F_j of a single recorded grating on spatially average exposure U_1 for different laws of saturation in case of one-photon absorption, denoted by 1PH.

difference between largest $F_{1,\ \mathrm{peak}}$ (for step $\rho(U)$) and smallest $F_{1,\ \mathrm{peak}}$ peak (for power law saturation) constitute only factor around 1.85. Curves in Fig. 85 and data at Table 6 were produced for single-photon absorption model of recording.

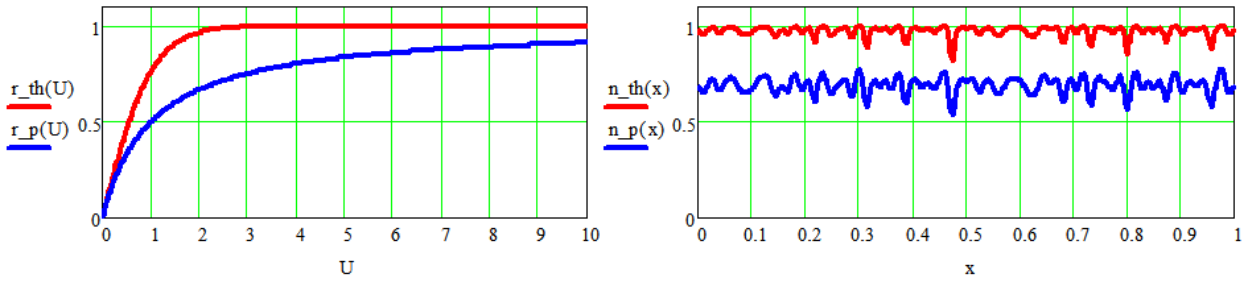

Fig. 86. Two curves of saturation: hyperbolic tangent ($\tanh(U)$) and hyperbola ($U/(1+U)$); and corresponding profile of refractive index change under recording by multiplexed illumination of 16 interference patterns. Spatially average dose $U_{\mathrm{average}} = 2.25$. Curve $\tanh(U)$ demonstrates much stronger saturation at positive peaks of local dose, while hyperbola curve yields much less saturation and as a result, much less suppression of positive peaks.

In Fig. 86 we depict two curves of saturation: hyperbolic tangent ($\tanh(U)$) and hyperbola ($U/(1+U)$); and corresponding profile of refractive index change under recording by multiplexed illumination of 16 interference patterns. Spatially average dose is $U_{\mathrm{average}} = 2.25$. Curve $\tanh(U)$ demonstrates much stronger saturation at positive peaks of local dose, while hyperbola curve yields much less saturation and as a result, much less suppression of positive peaks.

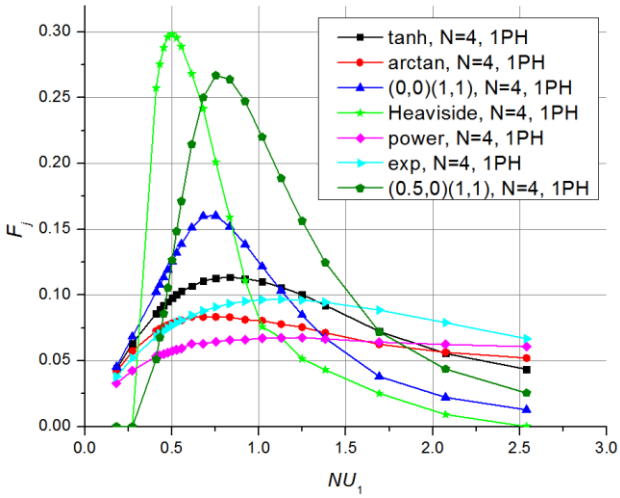

Fig. 87. Dependence of Fourier amplitude F_j of $N = 4$ grating on average exposure NU_1 for various laws of saturation in case of one-photon absorption.

Figure 87 shows the average Fourier component $\langle F_j \rangle$ $(j = 1,2,3,4)$ at single-photon recording of $N = 4$ independent gratings. Again, as in Fig. 27, we tried not to overburden the graph keeping

the curves for 4 laws of saturation only. Argument on horizontal axis is spatially-averaged exposure $U_{\mathrm{av}} = NU_1$ (reminder: $N = 4$).

Analytic calculations for a large number of individually recorded gratings may be done via decomposition $U(\mathbf{r}) = NU_1 + U_1 \cos(\mathbf{q}_j \mathbf{r} + \varphi_j)$ (for single-photon case), so that

$$n(x) = \Delta n_{\max}\left[\rho(\xi) + \frac{\partial \rho}{\partial \xi} U_1 \cos(q_j \mathbf{r} + \varphi_j)\right] = NU_1\,,$$
$$F_j = \Delta n_{\max} \frac{\partial \rho}{\partial \xi} U_j \equiv \frac{1}{N}\left(\xi \frac{\partial \rho}{\partial \xi}\right)\Big|_{\xi = NU_1}. \quad (3.14)$$

The values of maximum of functions $\xi\, \partial\rho/\partial\xi$ are $[\xi\, \partial\rho_{\mathrm{th}}/\partial\xi]_{\max} = 0.448$, $[\xi\, \partial\rho_{\mathrm{at}}/\partial\xi]_{\max} = 1/\pi = 0.38$, $\left[\xi\, \partial\rho_{\mathrm{pw}}/\partial\xi\right]_{\max} = 1/4 = 0.25$, $[\xi\, \partial\rho_{\mathrm{ex}}/\partial\xi]_{\max} = e^{-1} = 0.368$, $[\xi\, \partial\rho_{45}/\partial\xi]_{\max} = 1$, $[\xi\, \partial\rho_{60}/\partial\xi]_{\max} = 2$ at $\xi_{\mathrm{th}} = 0.776$, $\xi_{\mathrm{at}} = 2/\pi = 0.637$, $\xi_{\mathrm{pw}} = 1$, $\xi_{\mathrm{ex}} = 1$, $\xi_{45} = 1$, $\xi_{60} = 1$, respectively.

Results of numerical modeling yield (at least for $N \geq 4$) reasonable agreement with Eq. (3.14).

Special attention should be paid to the case of Heaviside function, $\rho_{\mathrm{st}}(\xi)$ at $\xi = 1$. The optimal value of $NU_1 = \xi_{\mathrm{opt}}$ is evidently $\xi_{\mathrm{opt,\ st}} = 1$, so that $U_{1\,opt,\ st} = 1/N$.
After that one should calculate integral

$$F_j = \frac{2}{L}\int \frac{U_1 \cos(qx + \varphi)}{|\cos(qx + \varphi)|}\cos(qx + \varphi)\, dx,$$

since the periods $\Lambda_j = 2\pi/q_j$ and phases of different gratings are statistically independent. As a result,

$$\left(F_j\right)_{\mathrm{max,\ st}} = 4U_{j\ \mathrm{opt,\ st}}/\pi = 4/\pi N = 1.27/N. \quad (3.15)$$

This result is also in reasonable agreement with numerical modelling at $N \gg 1$.
The value of optimum ξ for two-photon recording (for different $\rho(U)$ curves) should be equalized to $N \cdot \left(3{U_1}^2/2\right)$ and

$$F_j = 2{U_1}^2\left(\xi \frac{d\rho}{d\xi}\right)_{\mathrm{opt}} = \frac{4}{3}\left(\xi_{\mathrm{opt}} \frac{d\rho}{d\xi}\right)\frac{1}{N}, \qquad {U_1}^2 = \frac{2\xi_{\mathrm{opt}}}{3N_1}. \quad (3.16)$$

And again, numerical modeling at $N \gg 1$ is in a reasonable agreement with this extra factor (4/3) for two-photon recording.

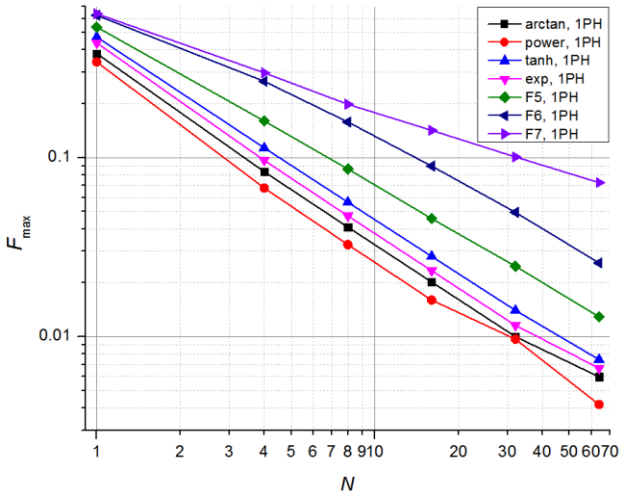

Fig. 88. Dependence of $F_j \sim 1/N$ on the number N of independently recorded gratings; spatially average dose was chosen to produce maximum Fourier amplitude F_j for each of the points of those 7 gratings.

The results of numerical modeling are summarized in the Fig. 88 which shows the dependence of $F_j \sim 1/N$ on the number N of independently recorded gratings.

Quite interesting is the problem of cross-modulation gratings. Namely, if recording profile contains, among others, the terms $U_j\big(1+\cos\big(q_j x+\varphi_j\big)\big)$ and $U_k(1+\cos(q_k x+\varphi_k))$, then a grating $\delta n(x)=\Delta n_{\max}\cdot F_{jk}\big\{\cos\big[\big(q_j+q_k\big)x+\varphi_j+\varphi_k\big]+\cos\big[\big(q_j-q_k\big)x+\varphi_j-\varphi_k\big]\big\}$ is recorded. Again, at $N \gtrsim 4$ analytic expansion of $r(U)$ around $\langle U\rangle = NU_1$ allows predicting

$$F_{jk} \approx \frac{1}{2N^2}\left[U^2\frac{d^2 r(U)}{dU^2}\right]_{U=\langle U\rangle=NU_1}. \qquad (3.17)$$

Our numerical modelling with random phases φ_j and φ_k is in a good agreement with analytical expression (17).

We have studied theoretically recording of multiplexed Volume Bragg Gratings with account of seven possible shapes of saturation curves. Optimum values of spatially averaged total exposure were found for each of those saturation curves, and the corresponding Fourier amplitudes of individual gratings. For relatively large multiplicity (number of gratings $N \gtrsim 4$) analytical formulae (3.14), (3.15), (3.16) derived by us, are in a good correspondence with the results of numerical modeling. In particular, best amplitude of individual Fourier component goes down as $const/N$, and values of that $const$ are determined for each saturation curve $\rho(U)$.

Qualitative conclusion is that sharper profiles of saturation curve $\rho(U)$ yield larger Fourier amplitudes at optimum exposure. Especially good would be threshold-like profile $\rho(U)$ (Heaviside function). Similar beneficial effect shows at sharper saturation due to two-photon recording. However, the price one should pay for this sharpness-provided advantage is the necessity of more precise adjustment of spatially-averaged exposure/development.

3.1.8. Metric for the measurement of the quality of complex beams

Problem of characterizing and measuring transverse quality of a laser beam has long history of studies. It is worth mentioning specifically monograph[65] and papers, *e.g.*[66]. Most laser beams have very small angular divergence θ_x ($\leq 10^{-2}$ rad). Transformation of such beams by lenses without aberrations may separately change $\delta\theta_x$ and the waist radius Δx. However, the product $\Delta x \cdot \Delta\theta_x$ (of dimension meters) is not changed by such transformation, and for almost-diffraction-quality beams is of the order of wavelength λ. Particular dimensionless quantity $\Delta x \cdot \Delta\theta_x/\lambda$ depends on the formal definition of Δx and $\Delta\theta_x$ in theoretical discussions of the problem, and depends on the measuring procedures in experiment. One possible definition of Δx and $\Delta\theta_x$ is root-mean-square and related to it dimensionless parameter ${M_x}^2$, adopted as ISO standard[67]:

$$\Delta x_{rms} = \sqrt{\langle (x - \langle x \rangle)^2 \rangle}, \quad \Delta\theta_{rms} = \sqrt{\langle (\theta_x - \langle \theta_x \rangle)^2 \rangle}, {M_x}^2 = (4\pi/\lambda) \cdot \Delta x_{rms} \cdot \Delta\theta_{rms} \qquad (1)$$

Separate measurement of ${M_x}^2$ and ${M_y}^2$ is often necessitated by not quite axially-symmetric character of the beam, including possible astigmatism. Particular coefficient, 4π, is chosen in such a manner, that minimum value of ${M_x}^2$ equals 1, and is achieved for ideal beam with perfect Gaussian profile.

It is assumed in (1) that Δx_{rms} is measured at the z-position of its minimum (in focal waist in the case of focused beam), while $\Delta\theta_{\mathrm{rms}}$ is measured in the far field zone of the beam. Quite often in experiment the far-field zone with its angular distribution of intensity $I(\theta_x)$ is substituted by the profile $I_{\mathrm{waist}}(x = F \cdot \theta_x)$ in the focal plane of a positive lens with focal distance F. This often leads to confusion, which parameter, Δx_{rms} or $\Delta\theta_{\mathrm{rms}}$ corresponds to near-field, and which one is related to the far-field. Luckily, this modest confusion in terminology does not result in the change of ${M_x}^2$, because as we have already mentioned, the product $\Delta x \cdot \Delta\theta_x$ is invariant under transformation by paraxial optical elements without aberrations.
Many researchers have noted that the quantities Δx_{rms} , $\Delta\theta_{\mathrm{rms}}$ and therefore ${M_x}^2 = 4\pi \cdot \Delta x_{\mathrm{rms}} \cdot \Delta\theta_{\mathrm{rms}}/\lambda$ put too much emphasis upon distant wings of distributions $I_0(x)$ and $I_1(\theta_x)$, e.g.[68, 69, 70].

---

[65] A. E. Siegman, Lasers (University Science Books, 1986).
[66] A. E. Siegman, "How to (maybe) measure laser beam quality," in DPSS (Diode Pumped Solid State) Lasers: Applications and Issues, M. Dowley, ed., 17, OSA Trends in Optics and Photonics (OSA, 1998), paper MQ1.
[67] ISO Standard 11146, "Lasers and laser-related equipment – Test methods for laser beam widths, divergence angles and beam propagation ratios" (2005)
[68] J. M. Slater, B. Edwards. "Characterization of high-power lasers." Laser Technology for Defense and Security VI. Ed. Mark Dubinskii & Stephen G. Post. Orlando, Florida, USA: SPIE, 2010. 76860W-12.
[69] S. Ruschin, E. Yaakobi, E. Shekel, Gaussian content as a laser beam quality parameter, Appl. Opt., August 1 2011, ; 50(22), pp. 4376-81.
[70] H. C. Miller, A laser beam quality definition based on induced temperature rise, Optics Express, Vol. 20, Issue 27, pp. 28819-28828 (2012)

Our personal preference is the use of criterion "width of the slit, containing 85% of total power", and ratio of Beam Propagation Product to the BPP for ideal Gaussian beam by the same criterion. The chosen fraction 85%, seems to be reasonable for energy-delivering applications of laser beams. Meanwhile the slit technology is relatively easy in implementation of field devices.

Given field $E_0(x,y)$ in the near-field zone, one finds intensity profile there $I_0(x,y) = |E_0(x,y)|^2$. Besides that, angular amplitude profile, *i.e.* amplitude profile in the far-field zone is proportional to

$$G_2(\theta_x, \theta_y) = \frac{1}{2\pi}\iint E_0(x,y)e^{-ik(x\cdot\theta_x + y\cdot\theta_y)}dxdy. \quad (2)$$

The resultant angular intensity profile is $I_2(\theta_x, \theta_y) = \left|G_2(\theta_x, \theta_y)\right|^2$. In $(1\mathrm{D}+z)$ case $E_0(x,y) \equiv E_0(x)$, and

$$G_1(\theta_x) = \frac{1}{\sqrt{2\pi}}\int E_0(x)\, exp(-ikx\cdot\theta_x)\, dx, \quad (3)$$

and $I_1(\theta_x) = |G_1(\theta_x)|^2$. Here and below wave number $k = 2\pi/\lambda$, and λ is wavelength in the medium of propagation path (typically in vacuum).

We start with Fourier Transform (FT) as it is used in Physics (PFT). Consider the function $f(x)$ of real variable x (for example, of dimensions of Cartesian coordinate, $[x] = [\mathrm{meter}]$). This function may have real or complex values. We define new function $G(q)$ of new real argument q (of dimensions $[q] = [\mathrm{radian/meter}]$) by

$$G(q) = \frac{A}{\sqrt{2\pi}}\int_{-\infty}^{+\infty} exp(iqx)\, f(x)dx, \quad (4)$$

where $A \neq 0$ is some constant. Then, as it is well known in mathematics, under certain (not very restrictive) conditions, original function $f(x)$ may be found by inverse Fourier transformation,

$$f(x) = \frac{1}{A\sqrt{2\pi}}\int_{-\infty}^{+\infty} exp(-iqx)\, G(q)dq. \quad (5)$$

Traditional choices of constant A are, for example $= 1$, $A = \sqrt{2\pi}$, $A = 1/\sqrt{2\pi}$, but any $A \neq 0$, even a complex number, does the job. Formula (4) defines linear operator of Physical FT; its maps space of functions $f(x)$ of argument x onto the space of functions $G(q)$ of a different argument q, dimensions of q being inverse to the dimensions of x: $[q] = [1/x]$. Parseval's theorem claims that

$$|A|^2 \cdot \int_{-\infty}^{+\infty} |f(x)|^2 dx = \int_{-\infty}^{+\infty} |G(q)|^2 dq. \qquad (6)$$

It looks especially elegant for $A = 1$.

If one wants to discuss eigenfunctions of FT, then FT operator must map space functions $f(y)$ onto itself, $G(y)$. In that case dimensions $[q \equiv y]$ coincides with dimensions $[1/y]$. In other words, argument x of functions $f(x)$ for Mathematical FT (MFT) should be dimensionless. All this gives the justification to the following definition of MFT operator as

$$MFT\{f\}(x) = h(x) = \frac{1}{\sqrt{2\pi}} \int_{-\infty}^{+\infty} exp(ixx')\, f(x')dx'. \quad (7)$$

Parseval's theorem shows that MFT operator is unitary:

$$\int |h(x)|^2\, dx = \int |f(x')|^2\, dx'. \qquad (8)$$

Inverse PFT (5) differs (at $A = 1$) from original PFT (4) only by the sign of phase in the exponential. It allows to conclude that application of MFT operator to a function $f(x)$ two times returns $f(-x)$:

$$(MFT)^2\{f\}(x) = f(-x). \qquad (9)$$

From that one gets

$$(MFT)^4\{f\}(x) = f(x), \quad or \quad (MFT)^4 = \hat{1}, \qquad (10)$$

i.e. 4-th power of MFT operator is unit operator. As a result, eigenvalues Λ of MFT operator satisfy condition $\Lambda^4 = 1$,

$$MFT\{h\}(x) = \Lambda \cdot h(x), \;\; \Lambda^4 = 1. \qquad (11)$$

Thus there are only 4 possible eigenvalues of MFT: $\Lambda_0 = 1,\ \Lambda_1 = i,\ \Lambda_2 = -1,\ \Lambda_3 = -i$ (or $\Lambda_n = i^n, n = 0, 1, 2, 3$). Differentiation and integration by parts in MFT Eq. (7) allows to show that if $f(x)$ is an eigenfunction of MFT with eigenvalue Λ_f, i.e. if

$$\mathrm{MFT}\{f\}(x) = \Lambda_f \cdot f(x), \qquad (12)$$

then functions

$$g(x) = \left(x - \frac{d}{dx}\right) f(x), \qquad h(x) = \left(x + \frac{d}{dx}\right) f(x) \qquad (13)$$

are also eigenfunctions of MFT, and

$$\Lambda_g = i \cdot \Lambda_f, \quad \Lambda_h = -i \cdot \Lambda_f \,. \qquad (14)$$

Function $g_0(x) = \exp(-x^2/2)$ is a well-known eigenfunction of MFT, with eigenvalue $\Lambda_0 = +1$. Moreover, Hermite polynomials $H_n(x)$ multiplied by $g_0(x)$, *i.e.*

$$H_n(x)\, exp(-x^2/2), \qquad (15)$$

up to constant factors, can be produced from $g_0(x)$ by application of "creation operator" $(x - d/dx)$ sequentially n times. Therefore they are eigenfunctions of MFT, with eigenvalues $\Lambda_n = i^n$.
Another function,

$$c_0(x) = \left[cosh\left(x\sqrt{\pi/2}\right)\right]^{-1}, \qquad (16)$$

is also an eigenfunction of MFT, with eigenvalue $\Lambda_0 = +1$. Main difference between $g_0(x)$ and $c_0(x)$ is in their asymptotic behavior at $|x| \to \infty$: $g_0(x) = \exp(-x^2/2)$ (exact); meanwhile $c_0(x) \doteq 2 \cdot \exp\left(-|x|\sqrt{\pi/2}\right)$. Functions $\text{const}_g \cdot g_0(x)$ and $\text{const}_c \cdot c_0(x)$, normalized to $\int |f(x)|^2 dx = 1$, have almost 100% overlapping integral:

$$\|g_0 c_0\|^2 \equiv \frac{\left[\int_{-\infty}^{+\infty} g_0(x) c_0(x) dx\right]^2}{\left[\int_{-\infty}^{+\infty} |g_0(y)|^2 dy\right] \cdot \left[\int_{-\infty}^{+\infty} |c_0(z)|^2 dz\right]} = 0.994 \quad (17)$$

Property $(\text{MFT})^4 = \hat{1}$ allows to construct eigenfunctions of MFT out of an arbitrary function $f(x)$ of dimensionless argument. For example,

$$f_\beta(x) = f(x) + i^\beta MFT\{f\}(x) + i^{2\beta}(MFT)^2\{f\}(x) + +i^{3\beta}(MFT)^3\{f\}(x) \qquad (18)$$

is an eigenfunction of MFT with eigenvalue $\Lambda = i^\beta$, where β is any integer number from 0 to 3. For the case with $\Lambda = +1$, *i.e.* when $\beta = 0$ is considered, formula of the type Eq. (18) was suggested in Ref.[71, 72]. Curious examples of MFT eigenfunctions are

$$r_{even}(x) = \frac{1}{\sqrt{|x|}}, \quad r_{odd}(x) = \frac{x}{|x|} \cdot \frac{1}{\sqrt{|x|}}, \qquad (19)$$

with respective eigenvalues $\Lambda_{\text{even}} = +1,\ \Lambda_{\text{odd}} = +i$. However, each of them has logarithmically divergent normalization integral (both at $|x| \to 0$ and at $|x| \to \infty$).

---

[71] A. Lohmann, D. Mendlovic, Self-Fourier objects and other self-transform objects J. Opt.. Socs. Am. A, 9, pp. 2009-2012.
[72] M. J. Caola, Self-Fourier functions, J. Phys. A: Math. Gen. 24 (1991) L1143-L1144.

Discrete Fourier Transform is usually introduced as an approximation for Physical FT. Consider function $f(x)$ at the interval $a \le x < a + L$, and for definiteness let dimensions of x be $[x] = [\text{meters}]$. Let us characterize this function by its values at the set of N equidistant points $n = 0, 1, \dots, N-1$,

$$x_0 = a, x_1 = a + s_x, \dots, x_n = a + n s_x, \dots, x_{N-1} = a + (N-1)s_x \; ; \;\; s_x = L/N . \qquad (20)$$

Here s_x is step of x-coordinate. It is convenient to assume that function $f(x)$ is continued outside the interval $a \le x < a + L$ in a periodic manner with period L, so that $f(x) = f(x + L)$. Then one can consider extra point $x_{\text{extra}} = a + s_x N \equiv a + L$ with the value $f(a + L) = f(a) \equiv f_0$, which is already accounted for by f_0. Corresponding vector $\vec{f}$ of N-dimensional linear space has components

$$\vec{f} = [f_0 = f(x_0), f_1 = f(x_1), \dots, f_{N-1} = f(x_{N-1})]. \qquad (21)$$

Function $G(q)$ (*i.e.* PFT from (4)) may be approximated by trapezoid formula

$$G(q) \approx \frac{A}{\sqrt{2\pi}} s_x \big[0.5 f_0 e^{iqx_0} + f_1 e^{iqx_1} + f_2 e^{iqx_2} + \cdots + + f_{N-1} e^{iqx_{N-1}} + 0.5 f(x_{extra}) e^{iqx_{extra}}\big]. \qquad (22)$$

Periodicity assumption yields $f(x_{\text{extra}}) \equiv f_0$. Evidently, there are only N linear independent values of function $G(q)$ defined by (22). To express this idea, we can choose to consider N discrete values of argument q:

$$q_0 = 0, q_1 = s_q, q_2 = 2s_q, \dots, q_{N-1} = (N-1)s_q. \quad (23)$$

Periodicity condition in x-coordinate with period L may be satisfied, if the value of step s_q in q-space is chosen as $s_q = 2\pi/L$ (of dimensions [radian/meter]). In that case $f(x_{\text{extra}}) e^{iq_m \cdot x_{\text{extra}}} = = f_0 e^{iq_m \cdot x_0}$, and trapezoid approximation for $G(q)$ becomes

$$G_m \equiv G\big(m \cdot s_q\big) \equiv G\left(m \cdot \frac{2\pi}{L}\right) \approx\approx \frac{L \cdot A}{N\sqrt{2\pi}} exp\left(2\pi i \frac{ma}{L}\right) \sum_{n=0}^{N-1} f_n \, exp\left(2\pi i \frac{n \cdot m}{N}\right). \qquad (24)$$

Vector $\vec{g}$ of N-dimensional linear space is called Discrete Fourier Transform (DFT) of vector $\vec{f}$ from the same space, if its components are defined by

$$g_m = (DFT\{f\})_m = \frac{1}{\sqrt{N}} \sum_{n=0}^{N-1} f_n \, exp\left(2\pi i \frac{n \cdot m}{N}\right). \quad (25)$$

Operator of DFT is implemented in every widely used mathematical software package like Mathcad, MatLab, Maple, Mathematica etc. What we were able to formulate here is that Physical FT $G(q)$ from Eq. (4) may be approximated by

$$G\left(q_m \equiv \frac{2\pi m}{L}\right) \approx exp\left(2\pi i \frac{ma}{L}\right) \frac{L \cdot A}{\sqrt{2\pi N}} (DFT\{f\})_m \,. \quad (26)$$

Intuitively it is clear that Discrete FT Eq. (25) is a certain approximation of Physical FT. What is important is the particular q_m-dependent coefficient in Eq. (26) expressing PFT via DFT. Remarkable mathematical facts about operator DFT defined by (25), are the following: 1) DFT is unitary operator in N-dimensional linear space; 2) Inverse DFT operator (IDFT) looks also as approximation of Eq. (5) of inverse PFT, but is actually exact inverse operator with respect to DFT:

$$f_n = (IDFT\{\vec{g}\})_n = \frac{1}{\sqrt{N}} \sum_{m=0}^{N-1} g_m \, exp\left(-2\pi i \frac{n \cdot m}{N}\right). \qquad (27)$$

The proof of this fact uses formula for the sum of geometrical progression:

$$\sum_{k=0}^{N-1} \eta^k = [N, if\ \eta = 1;\ (1-\eta^N)/(1-\eta)\ \ otherwise], \quad (28)$$

with account of $\eta = \exp[2\pi i(n-m)/N]$.

Additional problem to be covered is that physically both positive and negative values of $q[\mathrm{rad/meter}]$ in (4), (5) are important. At first glance, $q_m = s_q \cdot m = 2\pi m/L$ with $m = 0, 1, \ldots, N-1$, cover positive values of q only. This difficulty is resolved rather simply. For values $q_{N/2} = N\pi/L$ exponential factors $\exp(iq_m \cdot x_n) = \exp(iq_m \cdot a) \cdot \exp(i\pi n)$ oscillate versus n as $\exp(i\pi n) \equiv (-1)^n$. This is a manifestation of the failure of discretization of $f(x)$ into $f_n = f(x_n)$. In other words, we expect PFT of our function $f(x)$ to be negligibly small at q_m with $m \approx N/2$. On the other hand, subtracting $Q = 2\pi N/L$ from any of q_m does not change exponential factors in DFT. Indeed, $exp[i(q_m - Q)x_n] = exp[i(q_m - Q)a] \cdot exp[iq_m s_x n] \cdot\cdot exp[-iQs_x n]$. But $exp[-iQns_x] = exp(-2\pi in) \equiv 1$. Therefore one can subtract $Q = 2\pi N/L$ from any q_m without changing the resultant DFT. We can introduce function

$$phys(m) = \begin{cases} m, & if \quad m < N/2 \\ -N + m, & otherwise \end{cases}, \qquad (29)$$

so that $q_m(\mathrm{physical}) = s_q \cdot \mathrm{phys}(m)$ represent positive q in the range $0 \le m < N/2$ and negative $q = -Q + q_m$ in the range $N/2 \le m \le N-1$.

The definition of Mathematical Fourier Transform for functions of two dimensionless variables x, y is a trivial generalization of 1D case

$$2D\ MFT\{f\}(x,y) = \frac{1}{2\pi}\iint_{-\infty}^{\infty} e^{i(xx'+yy')} f(x',y')dx'dy'. \quad (30)$$

Consider two eigenfunctions of 1D MFT: $f_1(x)$ and $f_2(x)$, with eigenvalues $\Lambda_1 = (i)^{\beta_1}$ and $\Lambda_2 = (i)^{\beta_2}$, respectively. Functions $f_1(x)$ and $f_2(x)$ may be identical; in that case $\Lambda_1 \equiv \Lambda_2$. Besides that $f_1(x)$ and $f_2(x)$ may be different eigenfunctions of MFT with the same or with different eigenvalues Λ_1 and Λ_2 . In any of these cases factorized function of two dimensionless variables

$$F_{factor}(x,y) = f_1(x)f_2(y), \;\; \Lambda_{factor} = \Lambda_1 \cdot \Lambda_2 \qquad (31)$$

is an eigenfunction of unitary 2D MFT operator (30), and $\Lambda_{\text{factor}} = \Lambda_1 \cdot \Lambda_2$. The proof of this simple statement is based on factorization of exponential kernel in 2D MFT (30):

$$e^{ix\cdot x'+iy\cdot y'} = e^{ix\cdot x'} \cdot e^{iy\cdot y'}. \qquad (32)$$

Besides that the scalar product $(\mathbf{r}\cdot\mathbf{r}') \equiv xx' + yy'$ in that kernel is invariant with respect to simultaneous rotation of coordinates by arbitrary angle ψ:

$$(x,y)_{new} = (x,y)\hat{R}, \quad (x',y')_{new} = (x',y')\hat{R}, \hat{R} = \begin{pmatrix} cos\,\psi & sin\,\psi \\ -sin\,\psi & cos\,\psi \end{pmatrix}. \qquad (33)$$

Therefore another function,

$$F_{new,\psi}(x,y) = f_1(x_{new})f_2(y_{new}) == f_1(x\,cos\,\psi + y\,sin\,\psi)\cdot f_2(-x\,sin\,\psi + y\,cos\,\psi), \quad (34)$$

which generally is not factorized into $h_1(x)\cdot h_2(y)$, is still an eigenfunction of 2D MFT with $\Lambda_{\text{new}} = \Lambda_1 \cdot \Lambda_2$. Linearity of 2D MFT operator guarantees that any superposition of such functions with ψ-dependent weight $W(\psi)$,

$$F_{superp}(x,y) == \int_0^{2\pi} W(\psi)\, f_1(x\,cos\,\psi + y\,sin\,\psi)f_2(-x\,sin\,\psi + y\,cos\,\psi)d\psi, (35)$$

is still an eigenfunction of 2D MFT. Using polar coordinates $x = \rho\cos\varphi$, $y = \rho\sin\varphi$ in x,y-plane, one can transform this superposition to

$$F_{superp}(x,y) = F_{new}(\rho,\varphi) == \int_0^{2\pi} W(\psi)f_1(\rho\,cos(\varphi-\psi))f_2(\rho\,sin(\varphi-\psi))d\psi \quad (36)$$

Let us assume that function $W(\psi)$ is periodic with period 2π, *i.e.* $W(\psi+2\pi) = W(\psi)$. Introducing new variable $\alpha = \varphi - \psi$, one transforms integral (36) up to a factor (-1) into

$$F_{new}(\rho,\varphi) = -\int_0^{2\pi} W(\varphi+\alpha)\cdot f_1(\rho\cos\alpha)\cdot f_2(\rho\sin\alpha)d\alpha \quad (37)$$

A minor problem may arise, if the integral in the right-hand-side of Eq. (37) turns out, for some or other symmetry reason, to be exactly zero. Then one gets function equal to zero identically, which is not interesting, albeit may formally be considered as an eigenfunction of any linear operator.

Special interest is presented by the case when $W(\psi) == (-1/2\pi)\exp(im\psi)$, to elucidate the rotation symmetry in (x,y)-plane. Then

$$F_{new}(\rho,\varphi) = e^{im\varphi}R_m(\rho), \qquad R_m(\rho) = \frac{1}{2\pi}\int_0^{2\pi} e^{im\alpha} f_1(\rho\cos\alpha)\, f_2(\rho\sin\alpha)d\alpha. \quad (38)$$

We are especially interested in the case of completely axially-symmetric $(m = 0)$ self 2D MFT functions

$$R_0(\rho) = \frac{1}{2\pi}\int_0^{2\pi} f_1(\rho\cos\alpha)\, f_2(\rho\sin\alpha)d\alpha. \qquad (39)$$

If $f_1(x) = f_2(x) = \exp(-x^2/2)$, then axially symmetric result is trivial, $R_0(\rho) = \exp(-\rho^2/2)$. We were lucky to find another example of completely symmetric self 2D MFT function, with eigenvalue $\Lambda = +1$:

$$C_{00}(\rho) = \frac{1}{2\pi}\int_0^{2\pi} c_0(\rho\cos\alpha)\, c_0(\rho\sin\alpha)d\alpha, \;\; \Lambda = 1, \qquad (40)$$

where $c_0(x) = 1/\cosh\left(x\sqrt{\pi/2}\right)$. Graph of this new function is presented on Fig 77.

Behavior of this function at small and large ρ (remember that ρ is dimensionless) is as follows:

$$C_{00}(\rho) = 1 - \frac{\pi}{4}\rho^2 + O(\rho^4) \;\; at\ \rho \to 0, \qquad (41)$$

$$C_{00}(\rho) \doteq \left[4/\left(\rho\cdot\sqrt{\pi/2}\right)\right] exp\left(-\rho\sqrt{\pi/2}\right) \;\; at\ \rho \to \infty. \quad (42)$$

Normalized (by $\int_0^\infty |f(x)|^2\rho d\rho$) function $C_{00}(\rho)$ is mostly very similar to normalized axially-symmetric function $g_0(\rho) == \exp(-\rho^2/2)$. Indeed,

$$\frac{\left|\int_0^\infty C_{00}(\rho)g_{00}(\rho)\rho d\rho\right|^2}{\int_0^\infty [C_{00}(\rho)]^2\rho d\rho\cdot\int_0^\infty [g_{00}(\rho)]^2\rho d\rho} = 0.992\,. \qquad (43)$$

However, the asymptotic behavior of $C_{00}(\rho)$ at $\rho \to \infty$ is radically different from that of Gaussian function. In this respect $C_{00}(\rho)$ is a better approximation of the radial profile of a single-mode step-profile dielectric fiber with low V-number. In particular, consider the axially symmetric mode $LP_{01}(r)$ of a single-mode fiber with core radius a and V-number

$$V = (2\pi a/\lambda)\left({n_{core}}^2 - {n_{cladding}}^2\right)^{1/2}$$

being $V = 1.7$: well below the threshold $V < 2.4$ of single-mode operation. Our new 2D SMFT function $C_{00}(\rho = r/u)$ has the best overlapping with $V = 1.7$ normalized mode $LP_{01}(r)$ at $u = 1.077 \cdot a$ and is equal to

$$F_C = \frac{\left|\int_0^\infty C_{00}(\rho = r/u) LP_{01}(r) r dr\right|^2}{\int_0^\infty [C_{00}(\rho = r/u)]^2 r dr \cdot \int_0^\infty [LP_{01}(r)]^2 r dr} = 0.9986$$
$$= 1 - 1.14 \cdot 10^{-3}. \qquad (44)$$

Meanwhile the same mode has optimum overlapping integral with Gaussian function $g_{00}(\rho) = \exp[-(\rho = r/u)^2/2]$ at $u = 1.076 \cdot a$; that square of overlapping equals

$$F_g = \frac{\left|\int_0^\infty g_{00}(\rho = r/u) LP_{01}(r) r dr\right|^2}{\int_0^\infty [g_{00}(\rho = r/u)]^2 r dr \cdot \int_0^\infty [LP_{01}(r)]^2 r dr} = 0.9855$$
$$\equiv 1 - 1.45 \cdot 10^{-2}. \qquad (45)$$

At $V = 2.4$ (threshold value of V, below which single mode exists only) Gaussian function $g_{00}(\rho)$ has some advantage over $C_{00}(\rho)$: $F_{g,\ optimum} = 1 - 3.3 \cdot 10^{-3}$, $F_{C,\ optimum} = 1 - 5.0 \cdot 10^{-3}$. However, both approximations are pretty good. Detailed study of approximation for fundamental modes of a fiber by Gaussian function was done by D. Marcuse in Ref.[73], where he considered a variety of smoothed profiles of fiber refractive index.

We consider numerous possible criteria of the beam width, be it in the near field waist (in units of meters), or in the far field (in units of radians). Here is the list of 21 criteria covered, formulated for quantity of dimensions [meters]. Similar definitions are to be taken for θ_x or for $\theta = \left(\theta_x^2 + \theta_y^2\right)^{1/2}$ of dimensions [radian].

1. Δx (HWHIM): Half Width at the level Half of the Intensity at Maximum.
2. Δx (HWe^{-1}IM): Half Width at the level $e^{-1} \equiv 0.368$ of the Intensity at Maximum.
3. Δx (HWe^{-2}IM): Half Width at the level $e^{-2} \equiv 0.135$ of the Intensity at Maximum
4. Δx (HW10^{-2}IM): Half Width at the level 10^{-2} of the Intensity at Maximum
5. r (PIB $f = 0.5$): radius of a circle containing fraction $f = 0.5$ of total Power In the Bucket of that radius.

[73] D. Marcuse, Gaussian approximation of the fundamental modes of graded-index fiber, J. Opt. Soc. Am., Vol. 68, No. 1, January 1978, pp. 103-109.

6. r (PIB $f = 0.75$): radius of a circle containing fraction $f = 0.75$ of total Power In the Bucket of that radius.
7. r (PIB $f = 0.865$): radius of a circle containing fraction $f = 0.865 = 1 - e^{-2}$ of total Power In the Bucket of that radius.
8. r (PIB $f = 0.9$): radius of a circle containing fraction $f = 0.9$ of total Power In the Bucket of that radius.
9. r (PIB $f = 0.95$): radius of a circle containing fraction $f = 0.95$ of total Power In the Bucket of that radius.
10. r (PIB $f = 0.975$): radius of a circle containing fraction $f = 0.975$ of total Power In the Bucket of that radius.
11. r (PIB $f = 0.99$): radius of a circle containing fraction $f = 0.99$ of total Power In the Bucket of that radius.
12. s (PIS $f = 0.5$): half width of the minimum width of the slit, containing fraction $f = 0.5$ of total Power In that Slit of total width $2s$.
13. s (PIS $f = 0.75$): half width of the minimum width of the slit, containing fraction $f = 0.75$ of total Power In that Slit of total width $2s$.
14. s (PIS $f = 0.865$): half width of the minimum width of the slit, containing fraction $f = 0.865$ of total Power In that Slit of total width $2s$.
15. s (PIS $f = 0.9$): half width of the minimum width of the slit, containing fraction $f = 0.9$ of total Power In that Slit of total width $2s$.
16. s (PIS $f = 0.95$): half width of the minimum width of the slit, containing fraction $f = 0.95$ of total Power In that Slit of total width $2s$.
17. s (PIS $f = 0.975$): half width of the minimum width of the slit, containing fraction $f = 0.975$ of total Power In that Slit of total width $2s$.
18. s (PIS $f = 0.99$): half width of the minimum width of the slit, containing fraction $f = 0.99$ of total Power In that Slit of total width $2s$.
19. $x_{\text{rms}} = \sqrt{\langle (x - \bar{x})^2 \rangle}$, root mean square of variation of x-coordinate.
20. $x_1 = \langle |x - \bar{x}| \rangle$, average modulus of variation of x-coordinate.
21. $x_{0.5} = \left(\langle |x - \bar{x}|^{1/2} \rangle \right)^2$, square of average of square root of the modulus of coordinate variation.

We calculated the data for six different profiles of the field in the near-field zone: 1) Gaussian $E(x, y) = \exp[-(x^2 + y^2)/w^2]$, 2) Super-Gaussian $E(x, y) = \exp[-(x^2 + y^2)^2/w^4]$, 3) axially-symmetric 2D sech profile: Self-Fourier Transform profile found in this work, $E(x, y) = C_{00}\left(\rho = \sqrt{x^2 + y^2}/u\right)$; 4) profile of axially-symmetric mode of a single-mode fiber with $V = 2.4$ and of core radius a, $E(x, y) = LP_{01}\left(r = \sqrt{x^2 + y^2}\right)$; 5) Round Top Hat profile $E(x, y) = 1$ at $\sqrt{x^2 + y^2} \leq w$, $E(x, y) = 0$ otherwise; 6) Factorized Hyperbolic secant profile, $E(x, y) = c_0(X = x/u)c_0(Y = y/u)$, $c_0(t) = 1/\cosh\left(t\sqrt{\pi/2}\right)$. They are presented in Table 7.

Since the table contains dimensionless numbers, clarification should be made, in what units of dimensions of meters those data are given. For Gaussian and Super-Gaussian beams, 1 and 2, the data are given in units of traditional notations of w, where $w = \Delta x(\text{HW}e^{-2}\text{IM})$. For new self-Fourier-Transform function $E(x, y) = C_{00}\left(\rho = \sqrt{x^2 + y^2}/u\right)$, defined by eq. (40), coordinate

Table 7: Calculation of individual widths of various beams according to various criteria

	Gauss, $E(r) = \exp[-(r/w)^2]$	Super Gauss, $E(r) = \exp[-(r/w)^4]$	2D sech $C_{00}(r/w = u)$	Fiber mode $LP_{01}(r), V = 2.4$	Round Top Hat of radius w	Factorized 1D hyperbolic secant $c_0(x/w = u)$
Δx HWHIM, [width/w]	0.5887	0.7677	0.6930	0.6840	1	0.7032
Δx HWe^{-1}IM, [width/w]	0.7070	0.8409	0.8476	0.8052	1	0.8657
Δx HWe^{-2}IM, [width/w]	1	1	1.2685	1.0699	1	1.3225
Δx HW10^{-2}IM, [width/w]	1.5170	1.2318	2.1956	1.6923	1	2.3882
θ_x HWHIM, $angle \cdot (w/\lambda)$	0.1874	0.2447	0.1099	0.1493	0.2572	0.1119
θ_x HWe^{-1}IM, $angle \cdot (w/\lambda)$	0.2250	0.2913	0.1345	0.1825	0.3048	0.1378
θ_x HWe^{-2}IM, $angle \cdot (w/\lambda)$	0.3183	0.3993	0.2012	0.2724	0.4112	0.2105
θ_x HW10^{-2}IM, $angle \cdot (w/\lambda)$	0.4829	0.5499	0.3483	0.4518	0.5442	0.3801
r PIB f=0.5, [width/w]	0.5887	0.5807	0.7830	0.6394	0.7070	0.7848
r PIB f=0.75, [width/w]	0.8326	0.7584	1.1551	0.8893	0.8660	1.1591
r PIB f=0.865, [width/w]	1.0006	0.8641	1.4370	1.0699	0.9299	1.4450
r PIB f=0.9, [width/w]	1.0730	0.9069	1.5677	1.1574	0.9487	1.5765
r PIB f=0.95, [width/w]	1.2239	0.99	1.8547	1.3573	0.9747	1.8686
r PIB f=0.975, [width/w]	1.3581	1.0586	2.1304	1.5559	0.9874	2.1509
r PIB f=0.99, [width/w]	1.5174	1.1349	2.4842	1.8161	0.9950	2.5158
θ PIB f=0.5, $angle \cdot (w/\lambda)$	0.1874	0.2327	0.1246	0.1654	0.2654	0.1249
θ PIB f=0.75, $angle \cdot (w/\lambda)$	0.2650	0.3237	0.1838	0.2414	0.3917	0.1845
θ PIB f=0.865, $angle \cdot (w/\lambda)$	0.3185	0.3838	0.2287	0.2963	0.7766	0.2300
θ PIB f=0.9, $angle \cdot (w/\lambda)$	0.3415	0.4095	0.2495	0.3208	0.9063	0.2509
θ PIB f=0.95, $angle \cdot (w/\lambda)$	0.3896	0.4638	0.2952	0.3720	1.7802	0.2974
θ PIB f=0.975, $angle \cdot (w/\lambda)$	0.4323	0.5203	0.3391	0.4175	2.9031	0.3423
θ PIB f=0.99, $angle \cdot (w/\lambda)$	0.4830	0.8080	0.3954	0.4705	5.1887	0.4004
s PIS f=0.5, [width/w]	0.3372	0.3357	0.4488	0.3684	0.4040	0.4383
s PIS f=0.75, [width/w]	0.5752	0.5423	0.7864	0.6220	0.6347	0.7763
s PIS f=0.865, [width/w]	0.7467	0.6727	1.0498	0.8031	0.7607	1.0465
s PIS f=0.9, [width/w]	0.8224	0.7257	1.1724	0.8845	0.8054	1.1747
s PIS f=0.95, [width/w]	0.9800	0.8283	1.4425	1.0652	0.8783	1.4615
s PIS f=0.975, [width/w]	1.1207	0.9121	1.7024	1.2463	0.9237	1.7431
s PIS f=0.99, [width/w]	1.2880	1.0037	2.0371	1.4860	0.9587	2.1117
θ_s PIS f=0.5, $angle \cdot (w/\lambda)$	0.1073	0.1335	0.0714	0.0946	0.1590	0.0697
θ_s PIS f=0.75, $angle \cdot (w/\lambda)$	0.1831	0.2257	0.1252	0.1647	0.2838	0.1235
θ_s PIS f=0.865, $angle \cdot (w/\lambda)$	0.2377	0.2907	0.1671	0.2179	0.4194	0.1665
θ_s PIS f=0.9, $angle \cdot (w/\lambda)$	0.2618	0.3190	0.1866	0.2420	0.6093	0.1869
θ_s PIS f=0.95, $angle \cdot (w/\lambda)$	0.3119	0.3782	0.2296	0.2935	1.1172	0.2326
θ_s PIS f=0.975, $angle \cdot (w/\lambda)$	0.3567	0.4343	0.2709	0.3403	1.9249	0.2774
θ_s PIS f=0.99, $angle \cdot (w/\lambda)$	0.4100	0.5308	0.3242	0.3966	3.7706	0.3361
$\langle x^2 \rangle^{\frac{1}{2}}$, meter/$w$	0.5	0.4465	0.7193	0.5509	0.5	0.7236
$\langle \lvert x \rvert \rangle$, meter/$w$	0.3989	0.3701	0.5564	0.4363	0.4244	0.5530
$\left(\langle \sqrt{\lvert x \rvert} \rangle\right)^2$, meter/$w$	0.3380	0.3205	0.4641	0.3693	0.3723	0.4586
$\langle {\theta_x}^2 \rangle^{\frac{1}{2}}, angle \cdot (w/\lambda)$	0.1591	0.2011	0.1145	0.1474	0.7182	0.1152
$\langle \lvert \theta_x \rvert \rangle, angle \cdot (w/\lambda)$	0.1270	0.1581	0.0885	0.1154	0.3148	0.0880
$\left(\langle \sqrt{\lvert \theta_x \rvert} \rangle\right)^2, angle \cdot (w/\lambda)$	0.1076	0.1336	0.0739	0.0968	0.2093	0.0730

width is given units u. The parameter u in $C_{00}\left(\rho = \sqrt{x^2 + y^2}/u\right)$ coincides with the Δx(HW0.2622IM) of the said beam, so that $|C_{00}(\rho = 1)|^2 = 0.2622$, while $|C_{00}(\rho = 0)|^2 = 1$.

For the mode of step-profile fiber with V-number $V = 2.4$ the data are given in units of core radius a. Finally, for factorized hyperbolic-secant $E(x,y) = c_0(X = x/u)c_0(Y = y/u)$, $c_0(t) = 1/\cosh\left(t\sqrt{\pi/2}\right)$ parameter u may be considered as Δx(HW0.2788IM). As for the angular profile corresponding to those beams, their parameters, like $\delta\theta$[radians] are expressed in units (λ/w) for 1) Gaussian, 2) Super-Gaussian and 5) Round Top Hat beams; in units (λ/u) for 3) axially-symmetric sech-beam and for 6) factorized sech-beam; for 4) LP_{01}-mode of a fiber with V-nubmer $V = 2.4$ angular width is expressed in units λ/a.
Round top Hat beam #5 has well-known angular distribution of amplitude and intensity:

$$\left|G\left(\theta_x,\theta_y\right)\right|^2 = const\left(\frac{J_1(v)}{v}\right)^2, v = \frac{2\pi w}{\lambda}\cdot\sqrt{\theta_x^2+\theta_y^2} \quad (46)$$

so that 1-st zero of intensity of so-called "Airy disk" corresponds to $\left(\theta_x^2+\theta_y^2\right)^{0.5} = 1.22\lambda/2w$.
Power-in-the-bucket fraction for the intensities profile (46) is given by:

$$f(\theta) = 1 - \left[J_0\left(\frac{2\pi w\theta}{\lambda}\right)\right]^2 - \left[J_1\left(\frac{2\pi w\theta}{\lambda}\right)\right]. \quad (47)$$

Here and in Eq. (46) J_0 and J_1 are Bessel functions. Fraction of power in the bucket of the radius

Table 8. Beam propagation products for various near-field profiles $\boldsymbol{E(x,y)}$

$r\cdot\theta/\lambda$, $s\cdot\theta_x/\lambda$, M	Gauss, $E(r) = \exp[-(r/w)^2]$	Super Gauss, $E(r) = \exp[-(r/w)^4]$	2D sech $C_{00}(r)$	Fiber mode $LP_{01}(r), V = 2.4$	Round Top Hat	Factorized 1D hyperbolic secant
HWHIM	0.1103	0.1878	0.0764	0.1021	0.2572	0.0787
HWe^{-1}IM	0.1591	0.2450	0.1143	0.1469	0.3048	0.1193
HWe^{-2}IM	0.3183	0.3993	0.2561	0.2915	0.4112	0.2783
HW10^{-2}IM	0.7329	0.6774	0.7672	0.7645	0.5443	0.9078
PIB $f = 0.5$	0.1103	0.1351	0.0976	0.1058	0.1877	0.0980
PIB $f = 0.75$	0.2206	0.2455	0.2123	0.2147	0.3392	0.2138
PIB $f = 0.865$	0.3183	0.3316	0.3286	0.3170	0.7221	0.3323
PIB $f = 0.9$	0.3665	0.3714	0.3911	0.3713	0.8598	0.3955
PIB $f = 0.95$	0.4768	0.4591	0.5475	0.505	1.7352	0.5557
PIB $f = 0.975$	0.5871	0.5508	0.7223	0.6496	2.8666	0.7363
PIB $f = 0.99$	0.7329	0.9169	0.9822	0.8544	5.1627	1.0073
PIS $f = 0.5$	0.0362	0.0448	0.0320	0.0348	0.0642	0.0306
PIS $f = 0.75$	0.1053	0.1224	0.0985	0.1025	0.1801	0.0959
PIS $f = 0.865$	0.1775	0.1955	0.1754	0.1750	0.3191	0.1743
PIS $f = 0.9$	0.2153	0.2315	0.2188	0.2141	0.4907	0.2196
PIS $f = 0.95$	0.3057	0.3133	0.3312	0.3126	0.9812	0.3400
PIS $f = 0.975$	0.3998	0.3962	0.4613	0.4241	1.7781	0.4836
PIS $f = 0.99$	0.5280	0.5327	0.6605	0.5893	3.6150	0.7097
$M_x^2 = (4\pi/\lambda)\cdot\sqrt{\langle x^2\rangle\langle\theta_x^2\rangle}$	1	$2/\sqrt{\pi} =$ $=1.1281$	1.0349	1.0182	4.5771 (∞)	1.0472
$M_1 = (4\pi/\lambda)\cdot\langle\lvert x\rvert\rangle\langle\lvert\theta_x\rvert\rangle$	0.6366	0.7349	0.6192	0.6326	1.6784	0.6117
$M_{0.5}$ $= (4\pi/\lambda)\,\langle\sqrt{\lvert x\rvert}\rangle^2\,\langle\sqrt{\lvert\theta_x\rvert}\rangle^2$	0.4569	0.5381	0.4308	0.4493	0.9787	0.4206

$\theta_{\text{Airy}} = 1.22\,\lambda/(2w)$ is $f(\text{PIB}\ \theta = 1.22\,\lambda/(2w))$; numerically it is equal to $f = 1 - \left(J_0(3.8317)\right)^2 = 0.8378$. Intensity wings of this angular distribution yield logarithmically divergent $\langle\theta_x^2\rangle$. Finite value of the $\langle\theta_x^2\rangle$ for that table is calculated by truncation of integral for $\langle\theta_x^2\rangle$ at value $\theta_{\max} = 10\,\lambda/w$.

Table 8 contains the values of Beam Propagation Products (BPP) for those 6 beams: $\Delta\theta \cdot \Delta x/\lambda$ or $\delta\theta \cdot r/\lambda$. In these BPP we assumed one and the same criterion (out of 21) for coordinate size (Δx or r) and for angular size ($\Delta\theta_x$ or θ). In principle one can compile 21x21x6=2646 products, if different criteria are used for near field and for far field; Table 9 contains all the necessary data. The results depicted in Table 6 disprove a deeply entrenched myth that Gaussian field profile has the best BPP. This myth is definitely valid for r.m.s. criterion (i.e. M_x^2 criterion), but not necessarily for other criteria. Particular boxes where other beams show BPP smaller than Gaussian are highlighted. However that "advantage" of other beams is not very strong. Observing the data from Tables 4, 5 and 6, we see that 6 beams of essentially diffraction quality all have BPP about 1. Therefore particular choice of criteria should depend on the task for which the beam is intended in a particular application.

We discussed 21 different criteria of width of the laser beam. Those criteria are applicable both for near-field waist, where the width Δx or r has dimensions [meters], and for far field zone,

Table 9. The ratios of beam propagation products for the beams under study to those of Gaussian beam. We have highlighted the particular cells of that table where those ratios are smaller than 1. We see that completely symmetric self-Fourier-Transformed beam $\boldsymbol{C_{00}(\rho)}$ based on hyperbolic secant functions (Eq. (40)) yields certain advantage over the Gaussian beam, albeit for a limited number of criteria. Actually, that advantage is rather modest, about 4% to 30%, depending on particular criterion.

$r \cdot \theta/\lambda$, $s \cdot \theta_x/\lambda$, M	Gauss, $E(r) = \exp[-(r/w)^2]$	Super Gauss, $E(r) = \exp[-(r/w)^4]$	2D sech $C_{00}(r)$	Fiber mode $LP_{01}(r)$, $V = 2.4$	Round Top Hat	Factorized 1D hyperbolic secant
HWHIM	1	1.7026	0.6927	0.9257	2.3318	0.7135
HWe^{-1}IM	1	1.5399	0.7184	0.9233	1.9158	0.7497
HWe^{-2}IM	1	1.2545	0.8046	0.9158	1.2919	0.8744
HW10^{-2}IM	1	0.9243	1.0468	1.0431	0.7427	1.2392
PIB $f = 0.5$	1	1.2248	0.8849	0.9592	1.7017	0.8887
PIB $f = 0.75$	1	1.1129	0.9624	0.9733	1.5376	0.9693
PIB $f = 0.865$	1	1.0418	1.0324	0.9959	2.2686	1.0440
PIB $f = 0.9$	1	1.0134	1.0671	1.0131	2.346	1.0793
PIB $f = 0.95$	1	0.9629	1.1483	1.0591	3.6393	1.1655
PIB $f = 0.975$	1	0.9382	1.2303	1.1065	4.8826	1.2541
PIB $f = 0.99$	1	1.2511	1.3402	1.1658	7.0442	1.3744
PIS $f = 0.5$	1	1.2376	0.884	0.9613	1.7735	0.8445
PIS $f = 0.75$	1	1.1624	0.9354	0.9734	1.7104	0.9108
PIS $f = 0.865$	1	1.1014	0.9882	0.9859	1.7977	0.9820
PIS $f = 0.9$	1	1.0752	1.0163	0.9944	2.2791	1.0200
PIS $f = 0.95$	1	1.0249	1.0834	1.0226	3.2097	1.1121
PIS $f = 0.975$	1	0.991	1.1538	1.0608	4.4475	1.2095
PIS $f = 0.99$	1	1.0089	1.2509	1.1161	6.8466	1.3440
$M_x^2 = (4\pi/\lambda) \cdot \sqrt{\langle x^2\rangle\langle\theta_x^2\rangle}$	1	1.1281	1.0349	1.0182	4.5771 (∞)	1.0472
$M_1 = (4\pi/\lambda) \cdot \langle\|x\|\rangle\langle\|\theta_x\|\rangle$	1	1.1544	0.9727	0.9937	2.6365	0.9609
$M_{0.5} = (4\pi/\lambda)\,\langle\sqrt{\|x\|}\rangle^2\,\langle\sqrt{\|\theta_x\|}\rangle^2$	1	1.1777	0.9429	0.9834	2.142	0.9205

where width $\Delta\theta_x$ or θ has dimensions of [radians]. Since field amplitude in the far-field zone is a Fourier Transform (FT) (2) or (3) of the profile of the field in the waist, we provide the necessary information about properties of FT in Physical approach (PFT), Eq. (4), in Mathematical one (MFT), Eq. (7) and computationally convenient Discrete Fourier Transform (DFT), Eq. (25). We established simple quantitative relationships between PFT, MFT and DFT.

That information has allowed us to find axially-symmetric eigenfunction of MFT Eq. (40). Using Fourier Transformation, we were able to find the values of Δx and $\Delta\theta_x$ (or r and θ) according to 21 criteria for slightly different beams of almost diffraction quality.
In our opinion, the use of particular criterion "width of the slit, containing 85% of total power", constitutes a reasonable compromise between following the energy budget of the beam, on one hand, and suppression of unimportant wings of intensity distribution and measurement noise, on the other hand. Such technique has been demonstrated in recent physical experiments. Dividing beam propagation product to that of ideal Gaussian beam provides, quality parameter, which is close to well-known M_x^2-criterion, but without the drawbacks of the latter.

Results of our theoretical work show that taking some other diffraction-quality beam as etalon for comparison (instead of Gaussian) does not introduce much of a change.
In Appendices A and B we further illustrate important properties of PFT, and connection between DFT and MFT.

3.2. Aberrations and hologram recording setup

3.2.1. Design and assembly of aberration free stable recording setup

The use of volume holographic elements for high-power laser applications places stringent requirements on their performance. The angular and spectral selectivity of such elements and their diffraction efficiency are directly related to the uniformity of the hologram recorded inside the photosensitive material. The perfect case is when for the recording provides two beams with uniform intensity and phase distribution. In reality, this is hardly the case and the main effort in any holographic recording setup is to be as close as possible to the perfect case.

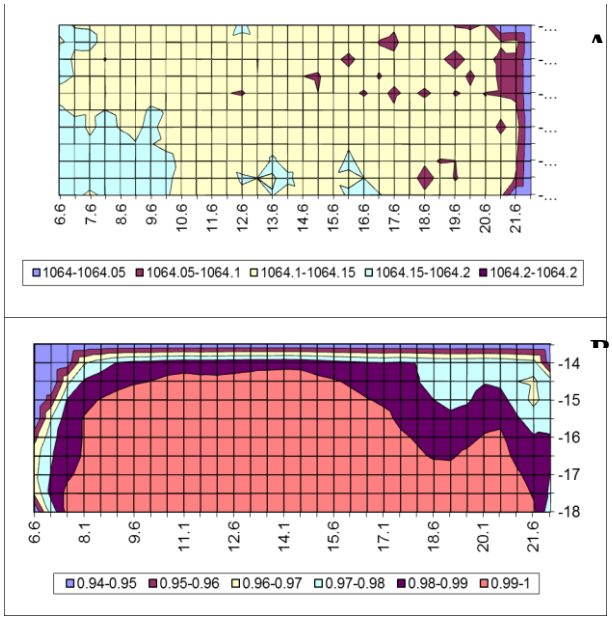

Fig. 89. Resonance wavelength (A) and diffraction efficiency (B) plots for a reflective Bragg grating designed to work at 1064.1 nm.

The first main issue that needed to be addressed was the minimization of the aberrations in the recording setup. For this purpose we implemented an approach where first, the number of complex optical elements is reduced and second, wherever needed the lenses used are so called "best-form" lenses with minimized aberrations. After the

changes, by using a shearing interferometer technique we were able to see a significant improvement in the phase quality of the final beam used for recording. We are still working on quantitative measurement of the improvement. The best current result is shown in Fig. 89 for a very uniform reflective VBG with thickness of 5.6 mm, 100% diffraction efficiency and less than 50 pm deviation in the central targeted wavelength of 1064.1 nm.

Another very important factor that affects the performance of any holographic recording setup is the presence of vibrations and air fluctuations. Both of these lead to smearing of the interference pattern that is being recorded in the photosensitive medium and correspondingly the quality of the optical element decreases. Even though, the setup we use is set on a thick air suspended optical table, there are vibrations that are not canceled by it and of course the air flows are present at all time.

First, we mounted one of the two mirrors that reflect the beams towards their interfering point on a piezo driven stage and if we manage to have a feedback that tells us how much the phase of this beam has shifted due to vibrations and/or air flow we can adjust in real time its phase and

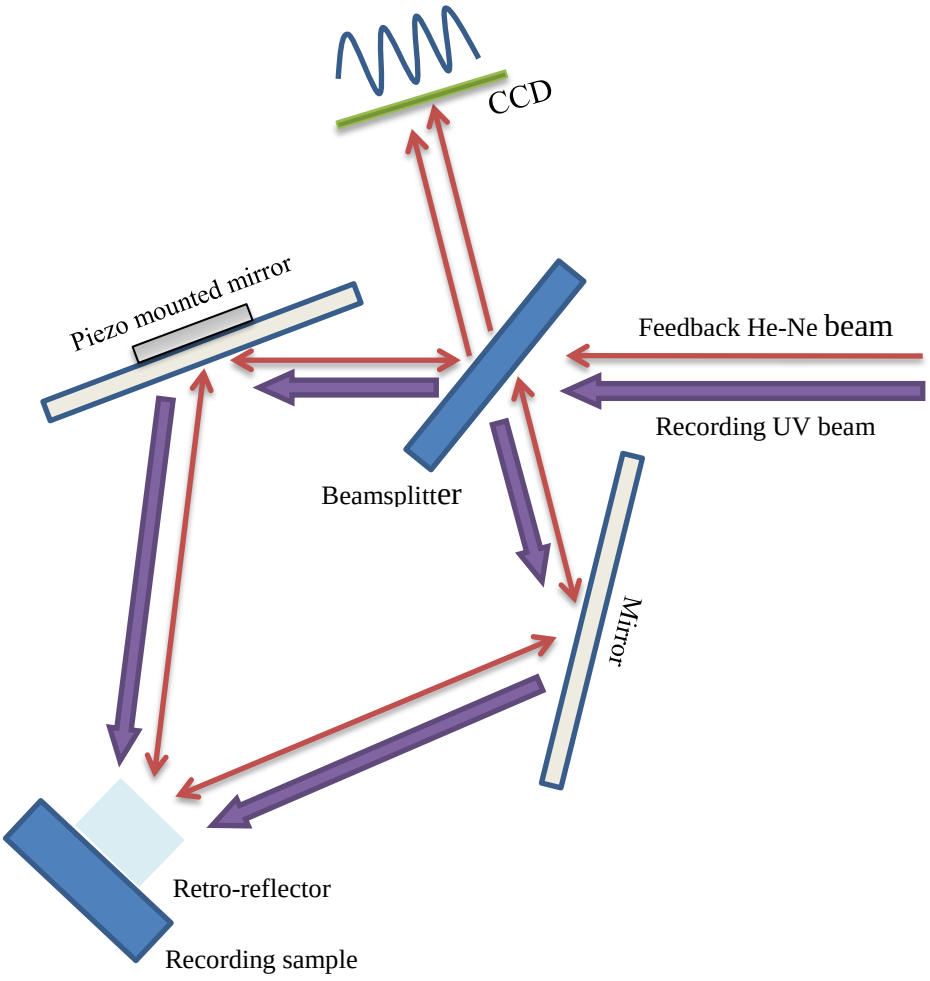

Fig. 90. Principle of operation for active phase stabilized setup. A He-Ne laser beam is used to trace the UV-recording beam and give information about any phase changes through an interference pattern observed on a CCD camera.

compensate for the changes. In such active stabilization schemes the main problem is how and from where to get the feedback information. What we propose is to mount a retro-reflector below the sample that is used for recording the hologram and with the use of a small test He-Ne laser beam that traces the path of the UV recording beam get interference pattern that can inform us of any phase changes. Figure 90 demonstrates the basic principle behind this idea. The interference pattern created by the He-Ne beam is registered on a CCD camera and any fluctuations in its position will trigger a compensation introduced by the piezo mounted mirror. The initial tests we performed proved that we can monitor in real time any changes between the phases of the two recording beams which demonstrated the viability of the approach.

3.2.2. Phase stabilization technique for holographic recording

A new method for phase stabilization of VBGs recording setup is proposed and demonstrated. The method is simple to implement and flexible so that VBGs with arbitrary tilt and resonant wavelength can be recorded. A method for analyzing the effectiveness of this phase stabilization approach is also introduced and successfully demonstrates its benefits.

VBGs are created by recording a spatially varying sinusoidal pattern inside a medium and are typically produced using holographic exposure, lithography, phase masks, or point by point inscription. These methods apply most readily to VBGs written into optical fibers, but for VBGs in a bulk medium with apertures on the order of several millimeters, holographic recording of a two beam interference pattern as shown in Fig. 91 is the most suitable approach. This method can be used to create both reflecting and transmitting type VBGs of different spatial frequencies by adjusting the recording angle of interference. To achieve high quality volume gratings with high-efficiency and periods as low as 200 nm, it is necessary to be able to generate a uniform recording beam intensity modulation period throughout the volume of the medium that would result in high contrast refractive index modulation (RIM). As an example, for gratings being designed as output couplers for laser systems, it is usually necessary to achieve very specific

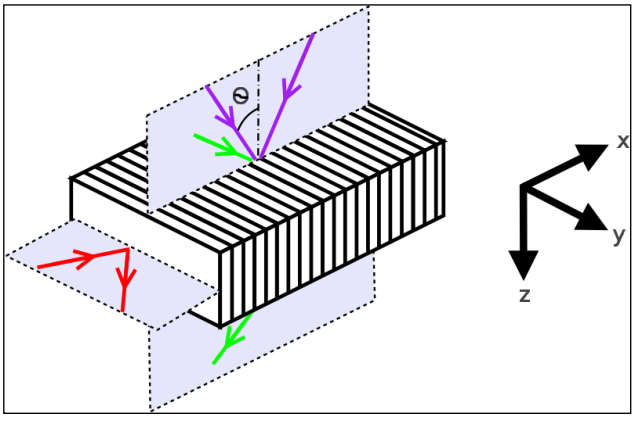

Fig. 91. The general recording and read out for a VBG. Purple rays indicate the recording wavelength which generates the interference pattern. After recording and development, the grating can be used as a transmitting grating at a different wavelength shown in green or at yet another wavelength the grating can be used as a reflecting grating indicated by the red rays.

spectral widths and angular selectivity in addition to precise diffraction efficiencies, making it critical to have exact control over the RIM. The primary detriment to obtaining consistent fringe visibility, and therefore high-quality VBGs, is shifting of the interference fringes during the recording process. Such fringe movement could be due to vibrations of beam delivery optics or the sample as well as localized changes in the relative density of air between the paths of the recording beams.

To control the phase of the interference pattern a number of different methods have been proposed. The most common is the use of the grating being recorded, or through the use of an auxiliary grating, to diffract a portion of each recording beam into the other recording beam to generate an interference pattern. This allows for direct monitoring of the relative shift of the interference pattern and the current grating structure. The drawbacks of this method include the possible recording beam reflections from the back surface of the medium which can only be avoided by specific interference setups or involved processes like AR coating of surfaces prior to recording. This also places the requirement that a weak grating is being formed during the recording process. This may not always be the case when a latent image is formed and further development is necessary or where size constraints of the recording substrate are not able to produce the required diffraction pattern. So, while the use of a grating to diffract the recording beams into each other is applicable to some holographic recording setups, it lacks the flexibility necessary for recording gratings in a variety of ways. To address this issue, we propose a simple, flexible method for phase stabilization that can be applied to most common holographic recording setups with the potential for a factor of two increasing sensitivity. The method shares the same path as the recording beam but does not place any requirements on how the sample should be placed in the setup.

The setup which is proposed to stabilize fringes relies on a propagating a probe beam along the same path as the recording beam but shifted slightly in height. At the recording plane, a corner cube retroreflector is placed above the sample. The probe and recording beams trace along the same path to reach the recording plane and the probe beam is then reflected back over the same path to double the relative phase deviations which is incurred. At the detector plane, the back-reflected probe light forms an interference pattern and the corner cube is adjusted in position to

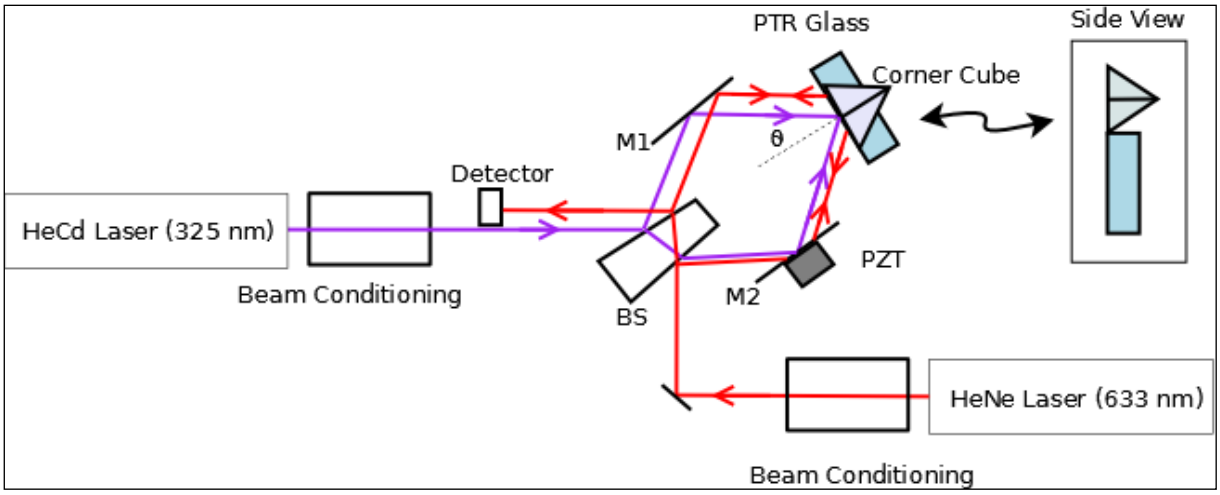

Fig. 92. The VBG recording setup showing the paths of the recording beams (purple) and the probe beam for phase stabilization (red).

achieve perfect overlap of the two collinear probe beams so that the entire beam diameter gives a zero fringe interference pattern. The setup is shown in Fig. 92. By using a retroreflector, the system can be easily moved and realigned for recording gratings of different period. A piezo-electric transducer (PZT) is placed beneath one of the mirrors to correct for measured phase fluctuations.

The sensitivity of the system is also determined by the ratio of probe wavelength to recording wavelength and the number of passes the probe beam makes through the reference arm. In the recording setup presented here, a probe beam from a He-Ne laser at 633 nm and a recording beam from a He-Cd laser at 325 nm are used and the probe beam makes a double pass through the interferometer. Therefore the phase fluctuations at the recording plane for the recording beams are 0.5×633/325 times the phase fluctuations measured in the probe beam. It is important to note that there is a factor of two increasing sensitivity to phase variation over methods of phase stabilization which rely on grating diffraction due to the double pass through the system. It is also important to note that a system relying on a plane mirror (or, if applicable, front surface reflections from the sample) in place of the corner cube would form a Sagnac interferometer which is relatively insensitive to air fluctuations, because both beams would counter-propagate along a shared path. Further improvements in sensitivity can be made by using a probe beam with a shorter wavelength than the recording beam, though the 1:1 scaling that is demonstrated here is sufficient to achieve improved fringe visibility.

The phase difference in the recording beam can be calculated from the measured variations in the detector voltage. In order to determine the conversion factor between the detector's voltage and the probe beam phase difference, the PZT was driven with a ramp function to generate a sinusoidal variation in the detector voltage with a period corresponding to a phase difference in the probe beam of 2π as shown in Fig 93. By fitting a sinusoid to this curve a conversion function was calculated which also accounted for the scaling factor for wavelength and double pass mentioned above.

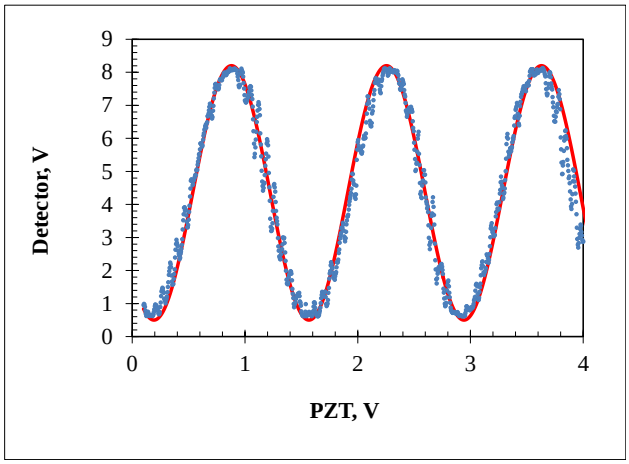

Fig. 93. Ramping of the PZT voltage allows a shift in the detector voltage, centered about the DC level, to be converted to a fraction of a phase shift once the period is determined. Red line shows a fit to the experimental data in blue.

The metrics for analysis of the system is the monitoring of the detector's voltage over time with and without active stabilization. The voltage acquired without any stabilization is shown in the beginning of Fig. 94. Measurement of the RMSE of the detector signal is used to calculate the phase error (σ) in the recording beam to be 0.07λ. This value was determined by calculating the variance of the unregulated signal over a typical recording time period of 200 seconds. The phase stabilization is turned on for the second half of Fig. 94, and the phase variation in the recording beam is calculated to give $\sigma=0.008\ \lambda$. The target value for the phase stabilization is the DC level of the detector signal in Fig. 93 because this region of the curve has highest sensitivity in detecting phase shifts.

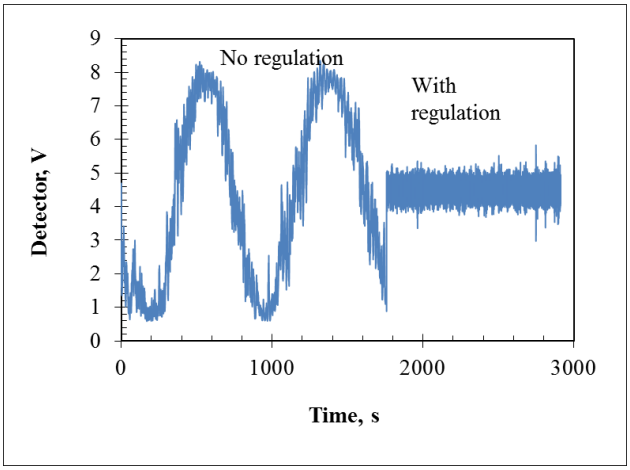

Fig. 94. The zero fringe signal from the retroreflected beams was measured on the detector and the variation in the voltage was monitored. The RMSE of the signal, centered about 4.5 V during a 200 second exposure is 1.9 V without regulation and 0.2 V with regulation. Long term stability without regulation varies over the full range of the fringe pattern.

In conclusion, a demonstration of a new method for phase stabilization is shown to be a flexible method for stabilizing the relative phases of a two beam interference pattern. The method can be applied to the recording of VBGs of arbitrary period without the need for specialized components or difficult alignment procedures. This phase control setup provides the ability to create repeatable VBGs with maximum refractive index modulation by ensuring fringe visibility of close to 100%.

3.2.3. The effect of aberrated recording beams on VBGs

Reflecting Bragg gratings (RBGs) are used as elements in a variety of applications including spectral beam combining, laser mode locking, longitudinal and transverse mode selection in lasers, and sensing. For applications requiring narrow spectral selectivity, or large apertures, these gratings must have a uniform period throughout the length of the recording medium, which may be on the order of millimeters. However, when using typical recording techniques such as two-beam interference for large aperture gratings and phase-mask recording of fiber gratings, aberrations from the optical elements in the system result in an imperfect grating structure.

We studied the effects of aberrations on large aperture gratings recorded in thick media using the two-beam interference technique in order to evaluate their influence on the quality of the VBGs. Previous works in analyzing the effects of aberrations have considered the effects of aberrations in a single recording plane where the beams perfectly overlap. Such an approach is valid for thin media (on the order of tens of microns), but for thick recording media (on the order of several millimeters) there will be a significant shift in the positions of the beams relative to each other as they traverse the recording medium. Therefore, the fringe pattern produced will not be constant throughout the grating if one or both beams have a non-uniform wavefront. Such non-uniform gratings may have a wider spectral width, a shifted resonant wavelength, or other problems. It is imperative therefore to know what the effects of aberrations will have on the properties of the RBGs. Here we consider the spatially dependent change in period and its effect on the reflectance spectrum induced by this imperfect fringe pattern.

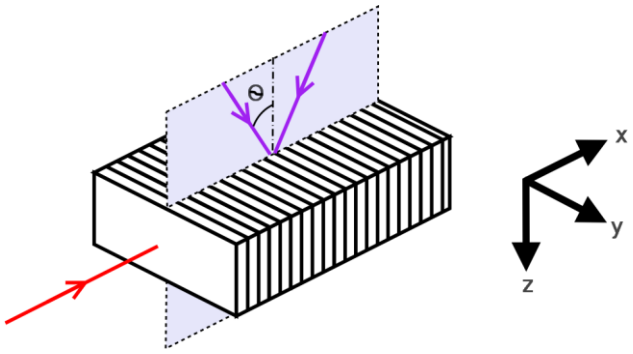

Fig. 95. Grating formed by two-beam interference at an interference angle θ and a probe beam incident upon the grating face.

Let us consider two aberrated beams which interfere at a recording medium as shown in Fig. 95. The intensity profile is given by the well-known two-beam interference equation

$$I(x,y) = I_1(x,y) + I_2(x,y) + 2\sqrt{I_1(x,y)I_2(x,y)}\cos\left(\left(\vec{k}_1 - \vec{k}_2\right)\cdot\vec{r} + \varphi_1(x,y) - \varphi_2(x,y)\right), \quad (5)$$

where I_j, k_j, and φ_j are the intensity, wave vector, and aberration contribution of each beam, respectively. In a typical recording geometry, a single beam is split into the two recording beams and each beam is reflected towards the recording medium, which bisects the angle between the mirrors. As high quality beamsplitters and mirrors are commercially available we will assume that any aberrations are produced prior to the beamsplitter, during beam shaping or resizing. In this case $\varphi_2(x,y) = \varphi_1(-x,y)$ and Eq. (5) can be rewritten as

$$I(x,y) = I_1(x,y) + I_2(x,y) + 2\sqrt{I_1(x,y)I_2(x,y)}\cos\left(2kx\sin\theta + \varphi_1(x,y) - \varphi_1(-x,y)\right). \quad (6)$$

Here k is the wavenumber and θ is the angle of incidence in the medium. To determine the effects of a shifting fringe pattern, consider the case of a uniform beam of radius r, split as described previously, with each of the split beams interfering in a thick recording medium.

Generally the centers of the beams will not overlap (except in one particular *z*-plane) but will have some separation distance d_s between them. The interference equation then becomes

$$I(x,y;d_s) = I_1(x+\tfrac{d_s}{2},y) + I_2(x-\tfrac{d_s}{2},y) + 2\sqrt{I_1(x+\tfrac{d_s}{2},y)I_2(x-\tfrac{d_s}{2},y)}\bullet \cos\left(2kx\sin\theta + \varphi_1(x+\tfrac{d_s}{2},y) - \varphi_1(-x+\tfrac{d_s}{2},y)\right) \quad (7)$$

In the case where perfect overlap is aligned to the center of the recording medium to minimize the maximum overlap mismatch, the separation distance can be written as $d_s = 2\ell\tan\theta$, where ℓ is the distance along the z-axis from the plane of perfect overlap.

In order to properly describe the aberrations in this system, we will write the aberrations in terms of Zernike polynomials, which will allow us to characterize the aberrations of the recording beam with a unique, orthogonal expansion. As the Zernike polynomials are normalized to the radius of the aperture of interest, *r*, we will denote the normalized dimensions as follows:

$$x' = \frac{x}{r} \qquad y' = \frac{y}{r} \qquad \ell' = \frac{\ell}{r}. \quad (8)$$

Table 10. Zernike polynomials, their Cartesian form, and their effect on the wavefront.

Zernike Polynomial	Aberration	Cartesian Form of Z_n	Z_n^*
0	Piston	1	0
1	Tilt *x*	x'	$2x'$
2	Tilt *y*	y'	0
3	Defocus	$2(x'^2+y'^2)-1$	$8x'\ell'\tan\theta$
4	0^o Astigmatism	$x'^2-y'^2$	$4x'\ell'\tan\theta$
5	45^o Astigmatism	$2x'y'$	$4x'y'$
6	Coma *x*	$3x'^3+3x'y'^2-2x'$	$2x'\left(9\ell'^2\tan^2\theta+3x'^2+3y'^2-2\right)$
7	Coma *y*	$3x'^2y'+3y'^3-2y'$	$12x'y'\ell'\tan\theta$
8	30^o Trefoil	$x'^3-3x'y'^2$	$2x'\left(3\ell'^2\tan^2\theta+x'^2-3y'^2\right)$
9	0^o Trefoil	$3x'^2y'-y'^3$	$12x'y'\ell'\tan\theta$
10	Spherical	$6(x'^4+y'^4-x'^2-y'^2)+12x'^2y'^2+1$	$24x'\ell'\tan\theta\left(2\ell'^2\tan^2\theta+2x'^2+2y'^2-1\right)$

The first few Zernike polynomials are listed in Table 10. The effect of aberrations on the wavefront is thus

$$\varphi_1\left(x'+\ell'\tan\theta,y'\right)-\varphi_1\left(\ell'\tan\theta-x',y'\right)=2\pi\sum_n c_n Z_n^*\left(x',y';\ell'\right), \quad (9)$$

where

$$Z_n^*(x', y'; \ell') = Z_n(x' + \ell' \tan\theta, y') - Z_n(\ell' \tan\theta - x', y'),$$

Z_n is the nth Zernike polynomial and c_n is the coefficient of the nth polynomial, chosen to give units of waves inside the recording medium. The contributions of each individual aberration are listed in Table 10. Note that while there is a contribution to the wavefront due to tilt, we will ignore it here as any tilt in the beam can be compensated by adjusting the angle of interference.

By grouping terms in Eq. 9 that have the same dependence on x we can rewrite the modulation term of Eq. 7 as follows:

$$\cos\left(2kx\sin\theta + 2\pi\sum_n c_n Z_n^*(x', y'; \ell')\right) = \cos\left(\sum_{n=1,3,\ldots} p_n(y', \ell') x^n\right) = \cos\left(\frac{2\pi}{\Lambda} x\right). \quad (10)$$

Here $p_1(y', \ell')$ is the sum of all terms with a linear dependence on x (including the term forming the original, unaberrated grating), $p_3(y', \ell')$ is the sum of all terms with a cubic dependence on x, etc. (from the symmetry of the system all terms with even powers of x will be canceled). The grating period Λ is thus equal to

$$\Lambda(x, y, \ell) = \frac{2\pi}{\sum_{n=1,3,\ldots} p_n(y', \ell') x^{n-1}}. \quad (11)$$

To determine the reflection spectrum of the grating for a probe beam propagating along the x-axis we may first determine the reflection spectrum at a single point and then convolve all spectra over the grating aperture (defined as the y-z plane for the probe beam):

$$R(\lambda) = \frac{\iint R(y, \ell, \lambda) I_p(y, \ell, \lambda) dy d\ell}{\iint I_p(y, \ell, \lambda) dy d\ell}. \quad (12)$$

Here R is the reflectance and I_p is the intensity of the probe beam being reflecting by the volume grating. It is important to note that in the absence of spherical, coma x, and 30° trefoil aberrations, (and assuming that all aberrations of higher order than spherical are negligible) the grating period is constant for a given y and ℓ; i.e. there is no chirp of the period along the depth of the grating at a given point along the face.

Due to the spatially varying nature of the grating one may reasonably conclude that several factors will influence the reflectance spectrum, including the length and strength of the grating, the position of the probe beam along the grating face, and the size of the probe beam. To determine the influence of these effects we simulate two gratings: a high efficiency, relatively thin grating (Grating A), useful in applications such as spectral beam combining, and a thick

grating with moderate diffraction efficiency (Grating B), which may be used in applications requiring narrow spectral widths. Grating A is designed such that it ideally has a 1064 nm resonant wavelength with δn = 200 ppm, and t = 5.5 mm. From Eqs. 10-12, this should give a diffraction efficiency of 99.4% and a spectral width of 178 pm. Grating B is designed for the same resonant wavelength, with δn = 20 ppm, and t = 20 mm, corresponding to a diffraction efficiency of 68.5% and a spectral width of 24 pm. To account for beam size and position, we use a 5 mm diameter Gaussian probe beam (a common size that is nevertheless large enough to have potentially significant differences in reflectance over the illuminated region) at normal incidence and examine three locations along the grating face: the center of the grating where the effects of aberrations are expected to be minimal, and halfway between the grating edge and center along the y and z axes. For 25 mm diameter recording beams interfering through a 10 mm recording medium the three probe locations correspond to: (a) $y = \ell = 0$, (b) y = 6.25 mm (y' = 0.5), $\ell = 0$, and (c) $y = 0$, ℓ = 2.5 mm (ℓ' = 0.2).

Figure 96 shows the effects of one wave of a given aberration on the reflectance spectrum for both gratings. As expected, these aberrations have the least effect at the center of the grating, where the resonant wavelength is unchanged in all cases. However, the side lobes become at least partially washed out for both gratings and Grating B shows a reduction in peak diffraction efficiency as well as spectral broadening, with 45^o astigmatism having the largest effect. The change in peak diffraction efficiency and spectral broadening are not noticeable in Grating A due to the wide initial spectral width, in which small changes at a given point are lost in the convolution of Eq. 12. When the probe beam is off-center, there is also a change in resonant

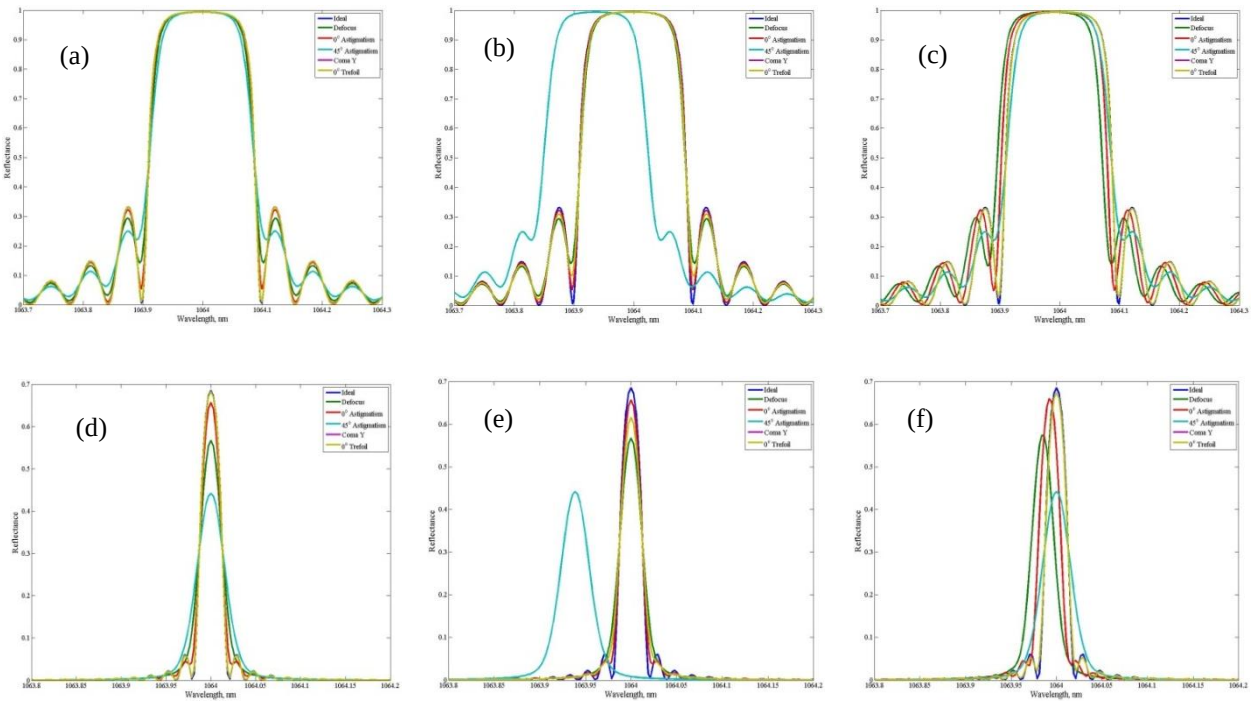

Fig. 96: Reflection spectrum of a 5 mm Gaussian beam in the presence of one wave of the indicated aberration for Grating A [(a), (b), (c)] and Grating B [(d), (e), (f)]. The location of the probe beam along the grating face is [(a), (d)]: y' = ℓ' = 0, [(b), (e)]: y' = 0.5, ℓ' = 0, and [(c), (f)]: y' = 0, ℓ' = 0.2.

wavelength, equal in both gratings, by up to several tens of picometers, with 45^o astigmatism having the largest effect when the beam is shifted on the *y*-axis and defocus having the largest effect when shifted on the *z*-axis.

In the case where spherical, coma *x*, and/or 30^o trefoil aberrations are present, there will be a parabolic chirp to the grating period at a given point along the face. To observe the effects of these chirp-inducing aberrations we have calculated the transfer matrix by dividing Grating A into 100 segments along the *x*-axis and Grating B into 500 segments so that each segment is approximately 50 μm. The probe beam and grating parameters are the same as previously, and to ensure that the chirp was symmetric about the center of the gratings, Grating A was analyzed over the region x = -2.75 mm to x = 2.75 mm and Grating B was analyzed over the region x = -10 mm to x = 10 mm. Figure 97 shows that even at the center of the grating there are significant deviations from the ideal spectrum for both gratings, with spherical aberration completely washing out the side lobes and coma *x* shifting the resonant wavelength by more than 100 pm. In addition, the differences between the two gratings become much more pronounced. Grating B shows large spectral broadening in the presence of spherical aberration, both coma *x* and 30^o trefoil display large asymmetries in their spectra, and all of the aberrations reduce the peak diffraction efficiency. In Grating A the wide initial spectral width again acts as a buffer to these effects, and the broadening, asymmetry, and efficiency reduction are far less noticeable. Also as in Fig. 96 when the beam is off-center there is a shift from the ideal resonant wavelength and in Grating B there is a noticeable change in the broadening and peak efficiency reduction for each aberration.

In conclusion, we have determined that aberrations in recording beams can have potentially

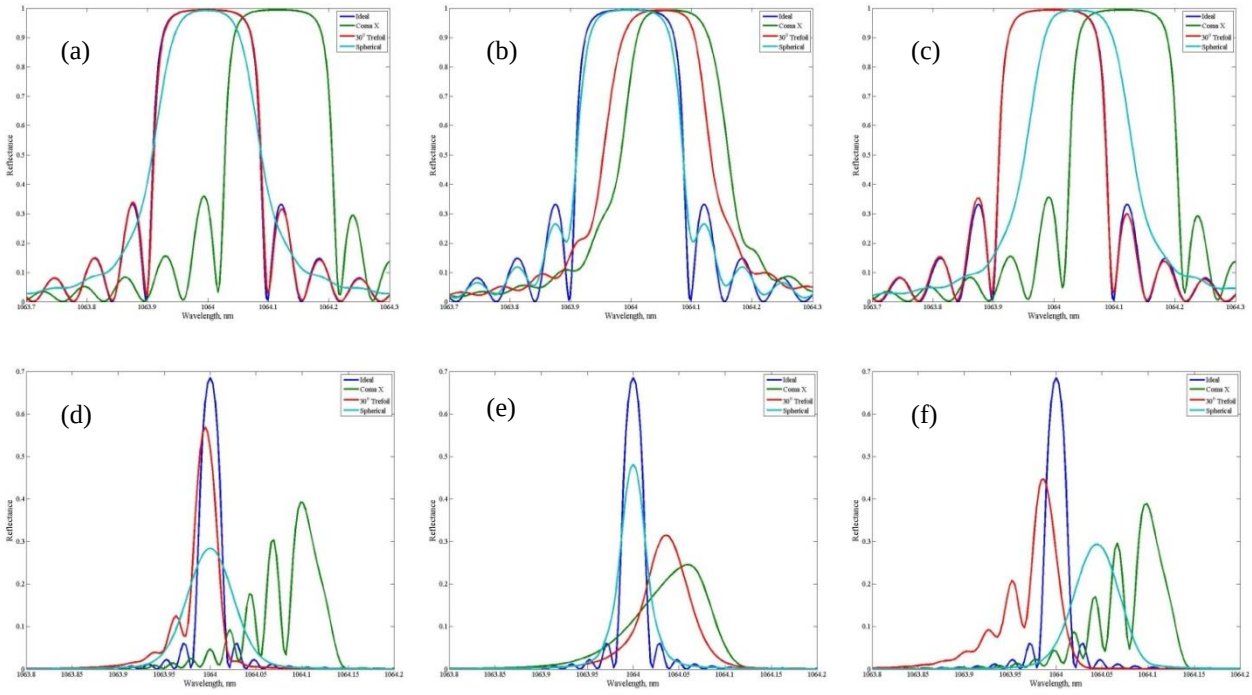

Fig. 97: Reflection spectrum of a 5 mm Gaussian beam in the presence of one wave of the indicated aberration for Grating A [(a), (b), (c)] and Grating B [(d), (e), (f)]. The location of the probe beam along the grating face is [(a), (d)]: $y' = \ell' = 0$, [(b), (e)]: $y' = 0.5$, $\ell' = 0$, and [(c), (f)]: $y' = 0$, $\ell' = 0.2$.

significant adverse effects on an RBG due to the spatial dependence of the overlapped wavefronts. This results in a spatially varying resonant wavelength, which is problematic for spectral filtering, and the sides lobes of the reflection spectrum are washed out, which reduces the efficiency of spectral beam combining. Asymmetrical spectra, spectral broadening, and a reduction in peak diffraction efficiency may also be present, though the wider the initial spectral width, the less noticeable these effects will be. The wavefront of the recording beams can be measured with a standard wavefront sensor and the impact of the measured aberrations calculated. If the aberrations reduce the spectral response beyond a desired tolerance, all optics should be aligned for on-axis use, and specialized optics such as aspherical or astigmatic lenses may be used as necessary to achieve the desired response.

3.2.4. Holographic recording stabilization system

Volume Bragg gratings (VBGs) are a widely used optical component for applications such as spectral shaping, communications, and sensing due to their ability to generate diffraction into a single order with high efficiency when the Bragg condition is met. VBGs are created by recording a spatially varying sinusoidal pattern inside a medium and are typically produced using holographic exposure, lithography, phase masks, or point by point inscription. These methods apply most readily to VBGs written into optical fibers. For VBGs in a bulk medium with apertures on the order of several millimeters, holographic recording of a two beam interference pattern (Fig. 98) is the most suitable approach. This method can be used to create both reflecting and transmitting type VBGs of different spatial frequencies by adjusting the recording angle of interference. To achieve high quality volume gratings with high-efficiency and periods as low as 200 nm, it is necessary to be able to generate a uniform modulation period throughout the volume of the medium together with high contrast of an interference pattern and corresponding magnitude of refractive index modulation (RIM). As an example, for gratings being designed as output couplers for laser systems, it is usually necessary to achieve very specific values of

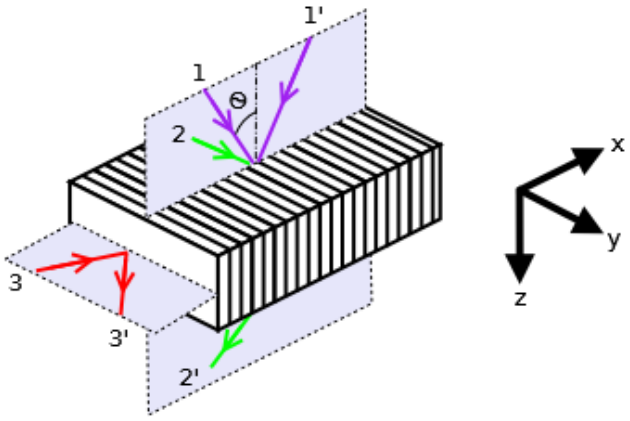

Fig. 98. The general recording and read out for a VBG. Rays marked 1 (purple) indicate the recording wavelength which generates the interference pattern. After recording and development, the grating can be used as a transmitting grating at a different wavelength marked with 2 (green) or at yet another wavelength the grating can be used as a reflecting grating indicated by 3 (red).

spectral width and angular selectivity in addition to precise diffraction efficiencies, making it critical to have exact control over the RIM. The primary detriment in obtaining consistent fringe visibility, and therefore high-quality VBGs, is shifting of the interference fringes during the recording process. Such fringe movement could be due to vibrations of beam delivery optics or the sample, as well as localized changes in the relative density of air along the paths of the recording beams.

By measuring and controlling the relative phases in the recording beams, high visibility fringes can be maintained throughout the recording. The resulting VBG will have a consistent index modulation with efficient use of the material's dynamic range. We developed a simple, flexible method for phase stabilization that can be applied to most common holographic recording setups with doubled sensitivity. The method shares the same path as the recording beam but does not place any requirements on the recording medium.

The entire recording setup which we propose is shown in Fig. 99. At the recording plane, a small portion of the recording beam is used to measure the relative phases of the beams while the rest is used to expose the photosensitive material. The portion of the beam used for phase measurement will be called the probe beam. The phase measurement is achieved through a corner cube retroreflector which is placed above the sample. The probe and recording beams trace along the same path to reach the recording plane and the probe beam is then reflected back along this path to double the relative phase deviations which are incurred. At the detector plane, the back-reflected probe light forms an interference pattern and the corner cube is adjusted in position to achieve overlap of the two collinear probe beams so that the entire probe beam diameter gives a zero fringe interference pattern. One of the primary benefits of this method is that the precision of this alignment can be very coarse. The retroreflector guarantees angular alignment and beam overlap can be achieved without the use of precision stages.

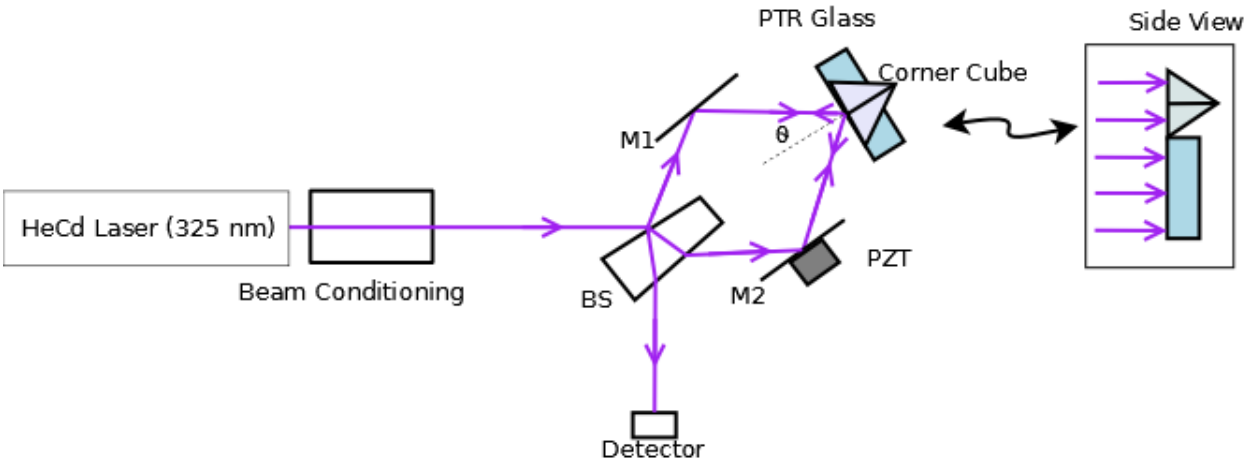

Fig. 99. The VBG recording setup showing the paths of the recording/probe beam. The side view shows how the beam is split between a recording portion and a probe portion for measuring phase.

By using a retroreflector, the system can be easily moved and realigned for recording gratings of different period and arbitrary grating tilt angles. The detector signal is used as feedback and a

piezo-electric transducer (PZT) is placed beneath one of the mirrors (M2 in Fig. 99) to correct for measured phase fluctuations by maintaining a constant detector signal. The feedback control is extremely simple and, in control language, consists of only a proportional gain. Again, introducing other signal processing techniques can be used to improve the performance of the system, but for what we demonstrate here only a simple control system is necessary.

The phase difference in the recording beam can be extracted from the measured variations in the detector voltage. In order to determine the conversion factor between the detector's voltage and the probe beam phase difference, a calibration of the system was performed prior to any measurement of phase. The calibration was accomplished by driving the PZT with a ramp function, generating a sinusoidal variation in the detector voltage with a period corresponding to a phase difference in the probe beams of 2π as shown in Fig. 100. By fitting a sinusoid to this curve, a conversion function was calculated to convert a detector voltage to a phase difference between the beams.

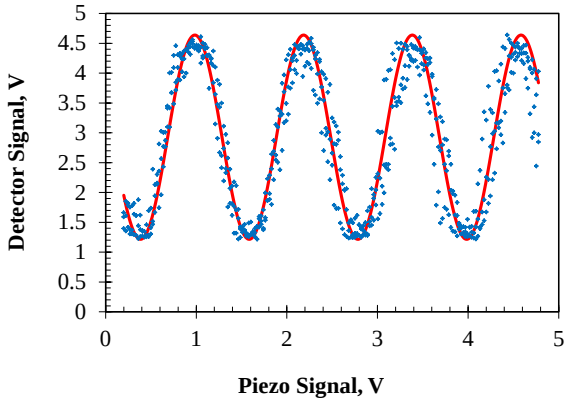

Fig. 100. Ramping of the PZT voltage allows a shift in the detector voltage to be converted to a fraction of a phase shift once the period is determined. Red line shows a fit to the experimental data in blue dots.

In order to demonstrate the performance of a phase stabilization system, it is customary to demonstrate detected feedback signal with the system operating in an open feedback loop and then close the loop and compare the relative amplitudes of fluctuations between the stabilized and unstabilized system. While this demonstrates the effectiveness of the feedback system, it does not directly show the effect that this has on the quality of the recording. If no change in the grating performance is achieved, the system is either measuring incorrectly or phase stabilization is not necessary. We can expect that by demonstrating an improvement of the grating's refractive index modulation we can conclude that phase stabilization is successful. This was conducted using the setup in Fig. 99 to record reflecting VBGs with a resonant wavelength of 978 nm and the time for each recording of 22 min. The recording material for these experiments is photo-thermo-refractive glass, which has proven in recent years to be an excellent material for recording high quality VBGs. This material is photosensitive to UV radiation and develops a permanent refractive index modulation after thermal development.

From these recordings, we expect to see an increased RIM due to increased fringe visibility in the phase stabilized recordings. In a reflecting VBG with high diffraction efficiency, an increased RIM will correspond with a higher bandwidth. The RIM can be calculated by matching measured spectral response to those calculated by theory using measured parameters for thickness and resonant wavelength. Before the exposure of each grating, the feedback signal was monitored so that the phase noise present in the recording environment could be determined. After exposure and development, the gratings were cut to a thickness of 3.75 mm and measured using a wavelength tunable laser. The transmission spectrum of each grating was used to determine the RIM induced in each recording.

The first grating was recorded with no stabilization present. Figure 101 shows the measured feedback signal before and during the recording, converted to phase difference using Fig 100. The relative phase of the beams has both high frequency noise and a slow drift in one direction. Because the detector is measuring the sinusoid of a phase term, the slow drift manifests itself as a periodic oscillation in phase. Unwrapping this phase would give a signal progressing in one direction, but for the current application phase unwrapping is unnecessary and difficult to achieve in the presence of noise levels presented here.

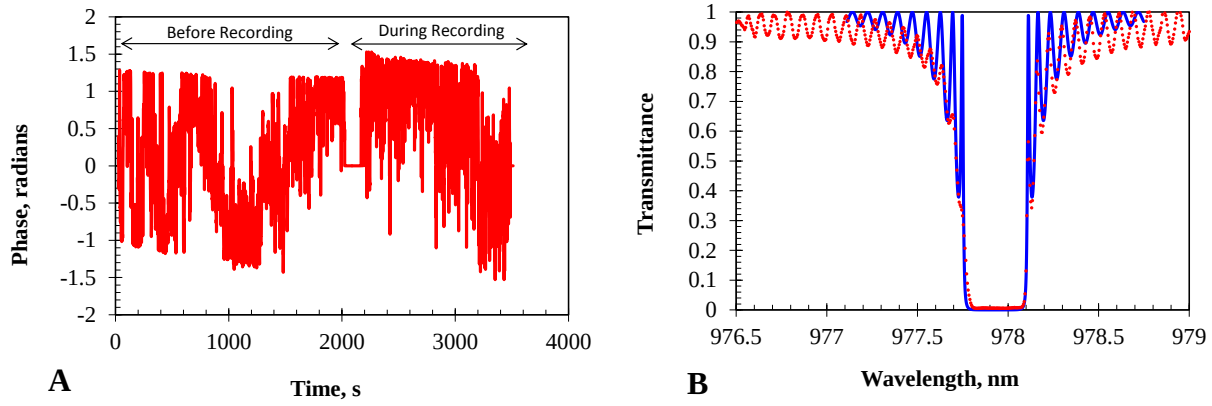

Fig. 101. The recording of an unstabilized grating as a baseline. The relative phase of the recording beams (A) shows both high frequency noise and long term variations. The resulting transmission spectrum (B) of a 3.75 mm thick grating has a bandwidth of 430 pm FWHM. Matching a theoretical spectrum (solid blue) to the measured data (red dots) allows the refractive index modulation to be calculated.

The phase during recording of Fig. 101 was analyzed to determine the best fringe visibility that can be achieved by recording in this condition. The measured data predicts that the RIM will be 76%±5% of a perfect recording. Uncertainty in this measurement is due to changes in the average intensity in the recording beam and is evident only when observing a change in the inflection points of the signal in the region near $\pm\pi/2$. This indicates an area for improvement in managing these changes in power. This also affects the stabilized phase and can be avoided in future work by maintaining a minimum signal at the detector. The measured transmission spectrum is shown in Fig. 101. The refractive index modulation was calculated by matching the measured spectrum to a theoretical spectrum using the resonant wavelength and thickness to give an excellent agreement of spectral shape as shown in the figure. For a 3.75 mm thick RBG with resonant wavelength of 978, a 430 pm bandwidth corresponds to 490 ppm index modulation.

A second RBG was recorded using the same parameters. During the recording process, the PZT was used to maintain a constant relative phase of the recording beams. Figure 102 shows the phase variations immediately before recording and during. The remaining noise during stabilization has RMSE of 0.0052λ and the expected visibility of this recording is 99.8%. The signal sent to the PZT during the recording is shown on the same plot to demonstrate how it was used to counteract the phase noise. The spectral response of this grating was also measured and fit to theory. At a thickness of 3.75 mm the bandwidth of 660 pm corresponds to an index modulation of 740 ppm.

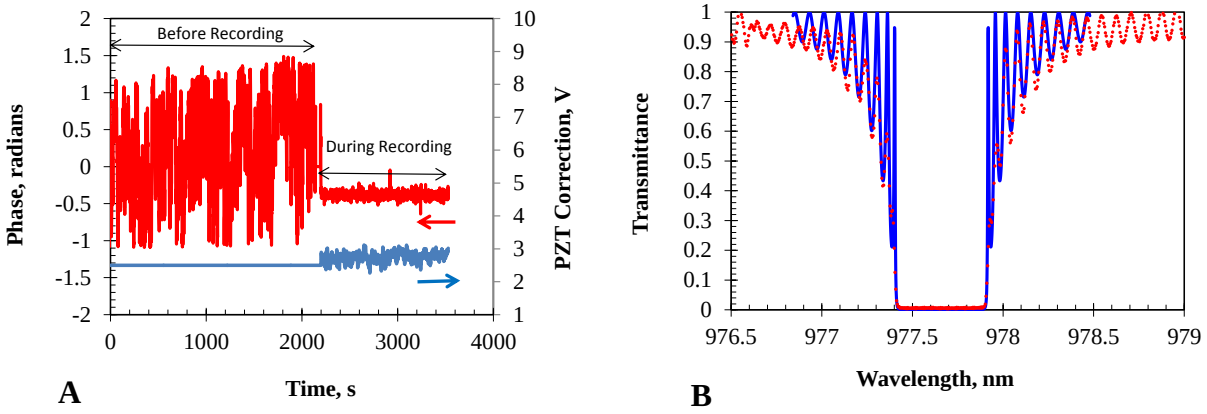

Fig. 102. The recording of a stabilized grating. The relative phase of the recording beams (A) shows high frequency noise. The correction applied to the PZT is shown at left in blue. The resulting transmission spectrum (B) of a 3.75 mm thick grating has a bandwidth of 660 pm FWHM. Matching a theoretical spectrum (solid blue) to the measured data (red dots) allows the refractive index modulation to be calculated.

Before implementing this control system in an actual recording setup, a calculation of the effect of phase noise on the recorded grating showed that, to maintain fringe visibility above 95%, random noise variations have to be maintained below 0.05λ. The proposed system is shown to produce phase stabilization well below this level by using a corner cube retroreflector to sample the recording beams and measure relative phase. The lateral sensitivity of the retroreflector system was verified experimentally to show that it is comparable to other common methods of phase stabilization. The effectiveness of using this system was verified by recording reflecting Bragg gratings both with and without phase stabilization and demonstrating a factor of 1.5 increase in the refractive index modulation. This matches well with predicted results, though improvements in the signal processing can help to eliminate any errors resulting from changes in incident irradiance. The primary benefits of the system presented here are that it can be used to ensure fringe visibility of >99% in a holographic recording, independent of the recording media and is applicable for any grating period or tilt.

3.2.5. The effect of aberrations in a holographic system on reflecting VBGs

Reflecting Bragg gratings (RBGs) are used as spectrally selective elements in a variety of applications including spectral beam combining, mode selection in lasers, and spectral filtering. For applications requiring narrow spectral selectivity, or large apertures, these gratings must

have a uniform period throughout the thickness of the recording medium, which may be on the order of millimeters, two orders of magnitude thicker than typical film gratings. In addition, this homogeneity in period must also exist over an aperture of several millimeters, which is one to two orders of magnitude larger than typical fibers. It has been shown that typical recording techniques such as holographic recording and recording through a phase mask can create an imperfect grating structure due to aberrations induced by the optics in the system. However, to the best of our knowledge no one has characterized the deterioration in spectral response of such larger aperture, thick gratings.

We developed a method for determining the effects of aberrations on large aperture gratings recorded in thick media. This method may be used in any two-beam recording system and can be easily generalized to systems with three or more beams, though here we will focus on single-sided two-beam recording. Previous works have considered the effects of aberrations in a single recording plane where the beams perfectly overlap. Such an approach is valid for thin media (on the order of tens of microns), but for thick recording media (on the order of several millimeters) there will be a significant shift in the positions of the recording beams relative to each other as they traverse the recording medium. Therefore, the fringe pattern produced will not be constant throughout the grating if one or both beams have a non-uniform wavefront. Such non-uniform gratings may have a wider spectral width, a shifted resonant wavelength, or other problems. It is imperative therefore to know what the effects of aberrations will have on the properties of the RBGs. Here we consider the spatially dependent change in period and its effect on the reflection spectra induced by this imperfect fringe pattern.

Let us consider two aberrated beams which interfere at a recording medium as shown in Fig. 6. The beams will create a grating structure with a periodicity determined by the standard two-beam interference equation:

$$I(x,y,z) = I_1 + I_2 + 2\sqrt{I_1 I_2}\cos\left(\left(\vec{k}_1 - \vec{k}_2\right)\cdot\vec{r}\right), \qquad (14)$$

where I is the intensity and $\vec{k}$ is the wavevector. In general the wavevector for each beam is not a constant in the presence of aberrations. Therefore the wavevector at any given point must be determined from the local wavefront. To calculate the beam wavefront let us consider one of the aberrated beams in the shifted coordinate system $(\bar{x},\bar{y},\bar{z})$, where the beam propagates along the $\bar{z}$ axis. (Note that this coordinate system is beam-specific.) In order to properly describe the aberrations of this beam, the aberrations at the $\bar{z}=0$ plane are written in terms of Zernike polynomials, which allow characterization the aberrations of the recording beam with a unique, orthogonal expansion. As the Zernike polynomials are normalized to the radius r of the aperture of interest, the normalized dimensions are denoted as $(\bar{x}',\bar{y}') = (\bar{x},\bar{y})/r$. The electric field of the beam may then be written as:

$$E(\bar{x},\bar{y},0) = E_0(\bar{x},\bar{y},0)\exp\left(ik\sum_n Z_n(\bar{x}',\bar{y}')\right), \qquad (15)$$

where Z_n is the nth Zernike polynomial in Noll notation. While this characterization is sufficient for thin gratings, the beam must be propagated through the depth of the recording medium for

thick gratings. Therefore the three-dimensional distribution of the electric field is calculated using the beam propagation method:

$$E(\bar{x},\bar{y},\bar{z}) = \mathrm{F}^{-1}\left\{\mathrm{F}\left\{E(\bar{x},\bar{y},0)\right\} e^{\frac{-\left(f_x^2+f_y^2\right)\bar{z}}{2k}}\right\} e^{ik\bar{z}} \quad . \qquad (16)$$

As the local phase incursion φ of the electric field at a given $\bar{z}$-plane is related to the wavefront by $\varphi = k(\bar{z}+W)$, the wavefront at a given $\bar{z}$-plane may be calculated by

$$W(\bar{x},\bar{y},\bar{z}) = \frac{1}{k}\arctan\left(\frac{\mathrm{Im}\left[E(\bar{x},\bar{y},\bar{z})\right]}{\mathrm{Re}\left[E(\bar{x},\bar{y},\bar{z})\right]}\right) - \bar{z} \quad . \qquad (17)$$

The local wavevector is then given by the gradient of the wavefront:

$$\vec{k}(\bar{x},\bar{y},\bar{z}) = \frac{k}{\sqrt{1+\left(\frac{\partial W}{\partial \bar{x}}\right)^2+\left(\frac{\partial W}{\partial \bar{y}}\right)^2}}\begin{pmatrix} -\frac{\partial W}{\partial \bar{x}} \\ -\frac{\partial W}{\partial \bar{y}} \\ 1 \end{pmatrix} . \qquad (18)$$

In order to calculate the wavevector in the grating-centered coordinate system we must convert the local wavevector from the beam-centered coordinate system to the grating-centered coordinate system by rotating by the half angle of interference θ:

$$\vec{k}_g(\bar{x},\bar{y},\bar{z}) = \begin{pmatrix} \cos\theta & 0 & \sin\theta \\ 0 & 1 & 0 \\ -\sin\theta & 0 & \cos\theta \end{pmatrix} \vec{k}(\bar{x},\bar{y},\bar{z}) \quad . \qquad (19)$$

Finally, the position of the local wavevector along the wavefront in the (x,y,z) coordinate system is given by converting the $(\bar{x},\bar{y},\bar{z})$ coordinates to (x,y,z) coordinates, giving

$$\vec{k}_g(x\cos\theta - z\sin\theta, y, -x\sin\theta + z\cos\theta) = \vec{k}_g(\bar{x},\bar{y},\bar{z}) \quad . \qquad (20)$$

In situations where the intensity distribution of a recording beam is altered due to aberrations such as strong defocus, the fact that a particular wavefront in the $(\bar{x},\bar{y},\bar{z})$ coordinate system does not cross a given z-plane all at once must be considered. To take this into account it is necessary in general to propagate the beam until all of the local wavevectors are known at a given plane. However, this is an atypical case and the aberrations in a typical recording beam are expected to be small enough that the beam should still behave similar to a plane wave. Therefore the amount of spatial deviation of the wavefront after propagating a few millimeters is expected to be negligible and a local wavevector will therefore travel parallel to the tilt angle of the recording beam. In this case the wavevector at the z = 0 plane can be written as

$$\vec{k}_g(x,y,0) = \vec{k}_g(\bar{x}/\cos\theta_{eff,x}, \bar{y}/\sin\theta_{eff,y}, 0), \quad (21)$$

and the wavevector at an arbitrary z-plane can be written as

$$\vec{k}_g(x,y,z) = \vec{k}_g(x + z\tan\theta_{eff,x}, y + z\cot\theta_{eff,y}, 0). \quad (22)$$

Here the effective angles are given by

$$\theta_{eff,x} = \arctan\left(\frac{\vec{k}_{g,x}(0,0,0)}{\vec{k}_{g,z}(0,0,0)}\right)$$
$$\theta_{eff,y} = \arccos\left(\frac{\vec{k}_{g,y}(0,0,0)}{k}\right), \quad (23)$$

where it should be noted that $\theta_{eff,y}$ is given using the standard notation for spherical coordinates. The effective angles take into account the half angle of rotation as well as any alterations to the half angle caused by tilt.

If the probe beam were incident on the same face as the recording beams the grating would act as a transmitting grating, with a local grating vector of

$$\vec{K}_{TBG}(x,y,z) = \vec{k}_{g,1}(x,y,z) - \vec{k}_{g,2}(x,y,z). \quad (24)$$

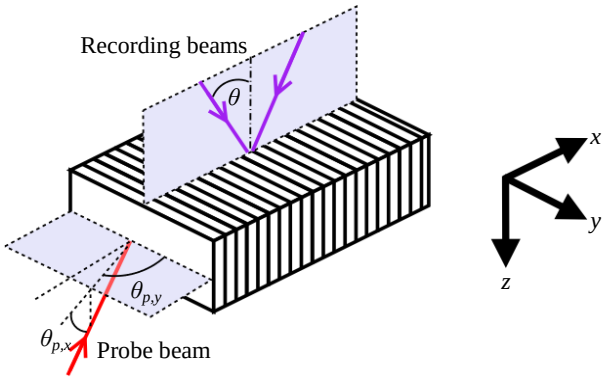

Fig. 103. Geometry of a grating recorded by two-beam interference where the nominal half angle of interference is θ. This grating acts as a reflecting grating for a probe beam incident in the plane orthogonal to the recording plane. All angles are angles inside the medium.

However, to use the grating as a reflecting grating the probe beam must be incident from a perpendicular plane as shown in Fig. 103, which requires an additional 90º rotation:

$$\vec{K}_{RBG} = \begin{pmatrix} 0 & 0 & -1 \\ 0 & 1 & 0 \\ 1 & 0 & 0 \end{pmatrix} \vec{K}_{TBG}, \qquad (25)$$

for a probe beam incident along the x-axis. The local grating tilt is then $\tan\phi_x = K_x/K_z$ and $\cos\phi_y = K_y/K$.

To determine the reflection spectrum of the grating for a probe beam propagating along the x-axis we may first determine the reflection spectrum at a single point and then integrate all spectra over the grating aperture (defined as the y-z plane for the probe beam):

$$R(\lambda) = \frac{\iint R(y,z,\lambda) I_p(y,z,\lambda) dydz}{\iint I_p(y,z,\lambda) dydz}. \qquad (26)$$

Here R is the reflectance and I_p is the intensity of the probe beam being reflected by the volume grating. However, because the grating has a spatially dependent period and inclination factor we utilize the coupled-wave theory transfer matrix technique to calculate the reflection at a given wavelength.

Coupled-wave theory dictates that the fields of forward and backward propagating waves in a uniform grating can be written as follows:

$$\begin{pmatrix} E_+(0) \\ E_-(0) \end{pmatrix} = \mathbf{T} \begin{pmatrix} E_+(t) \\ E_-(t) \end{pmatrix}. \qquad (27)$$

Here E+ and E- are the forward and backward propagating waves, respectively, and **T** is a transfer matrix with elements

$$\begin{aligned} T_{11} &= \left[\cosh(\gamma t) + i\Delta k \sinh(\gamma t)/\gamma\right] \exp\left(ik_{Bragg} t\right) \\ T_{12} &= -\kappa t \sinh(\gamma t) \exp\left(-i\left(k_{Bragg} t + \varphi\right)\right)/(\gamma t) \\ T_{21} &= -\kappa t \sinh(\gamma t) \exp\left(i\left(k_{Bragg} t + \varphi\right)\right)/(\gamma t) \\ T_{22} &= \left[\cosh(\gamma t) - i\Delta k \sinh(\gamma t)/\gamma\right] \exp\left(-ik_{Bragg} t\right). \end{aligned} \qquad (28)$$

Here $\Delta k = k_p - k_{Bragg}$ is the difference between the propagation constant of the probe beam and the propagation constant for a wave satisfying the Bragg condition, φ is the grating phase factor, $\kappa = \pi\delta n/\lambda$ is the coupling coefficient between the forward and backward-propagating waves (assuming TE polarization), $\gamma^2 = \kappa^2 - (\Delta k)^2$, and δn is the refractive index modulation.

In order to determine the k_{Bragg} term, the general case of grating tilt must be considered in which there is a y-component to the grating tilt as well as an x-component. It is therefore necessary to generalize Kogelnik's coupled-wave equations to cases where the grating vector does not lie in

the x-z plane. Assuming that the y-component of the grating and probe beam vectors are non-zero, we find that the Bragg condition becomes

$$K = 2k_{Bragg}\left(\sin\theta_y \sin\phi_y \cos\left(\phi_x - \theta_x\right) + \cos\theta_y \cos\phi_y\right), \quad (29)$$

where θ_x and ϕ_x are the angles of the probe beam and grating vectors, respectively, relative to the x-axis (as the x-axis is the axis for which the probe beam nominally propagates along), and θ_y and ϕ_y are the angles of the probe beam and grating vectors, respectively, relative to the y-axis. Note that in this formulation we use the standard spherical coordinate definitions for the angles, so a grating vector which lies in the x-z plane has an inclination angle of $\phi_y = \pi/2$, reducing Eq. 29 to the Bragg condition described by Kogelnik.

Note also that each of the terms in Eq. 28 is assumed to be constant. To allow for a varying period and grating tilt we will assume the slowly-varying envelope approximation, permitting us to divide the grating into N segments and write **T** as

$$\mathbf{T} = \prod_{i=1}^{N} \mathbf{T}_i, \quad (30)$$

where T_i is a function of a local (constant) κ_i, Δk_i, t_i, and φ_i. In order to match the phases between the segments, φ_i must satisfy the relationship $\varphi_i = \varphi_i + 2t_{i-1}\pi/\Lambda_{i-1}$. The reflectance at a given point is then given by

$$R(y,z,\lambda) = \left|\frac{T_{21}}{T_{11}}\right|^2. \quad (31)$$

Inserting Eq. 31 into Eq. 26 provides the reflection spectrum for a probe beam incident upon the front facet of a grating.

Due to the spatially varying nature of the grating one may reasonably conclude that several factors will influence the reflection spectrum, including the thickness and refractive index modulation of the grating, the position of the probe beam along the grating face, and the size of the probe beam. The combination of grating and beam parameters provides a plethora of possible deteriorated profiles. To demonstrate the influence of these effects we simulate two gratings representing different applications for lasers emitting in the vicinity of 1064 nm. The first one is a high efficiency, relatively thin grating (Grating A), useful in applications such as spectral beam combining, and the second one is a thick grating with moderate diffraction efficiency (Grating B), which may be used in applications requiring narrow spectral widths. A recording medium which is capable of recording such large aperture, thick gratings is photo-thermo-refractive glass, which has been demonstrated in a variety of applications. This glass is transparent in the visible and NIR range and photosensitive in the near UV region. One of the most common recording wavelengths for this glass is the emission wavelength 325 nm, the emission wavelength of a He-Cd laser.

Grating A is designed such that it ideally has a 1064 nm resonant wavelength with δn = 200 ppm, and t = 5.5 mm. From Eqs. 26-31 this should give a peak diffraction efficiency of 99.4% and a spectral width of 178 pm (FWHM). Grating B is designed for the same resonant wavelength, with δn = 20 ppm, and t = 20 mm, corresponding to a diffraction efficiency of 68.5% and a spectral width of 24 pm. To account for beam size and position, a 3 mm diameter Gaussian probe beam at normal incidence is used for modeling. Two locations along the grating aperture are examined: the center of the grating where the effects of aberrations are expected to be minimal, and halfway between the grating edge and center along the y axis. For 25 mm diameter recording beams interfering through a 6 mm deep recording medium (z-axis dimension) the probe locations correspond to: y = 0 and y = 6.25 mm with z = 0 in the y-z plane.

To observe the effects of one wave (peak-to-valley) of a given aberration we have calculated the transfer matrix by dividing Grating A into 100 segments along the x-axis and Grating B into 500 segments so that each segment is approximately 50 μm. To minimize the effects of any possible grating chirp, Grating A was analyzed over the region x = -2.75 mm to x = 2.75 mm and Grating B was analyzed over the region x = -10 mm to x = 10 mm. Figs. 104a, and 104b show the effects of one wave of a given aberration at the recording wavelength of 325 nm on the

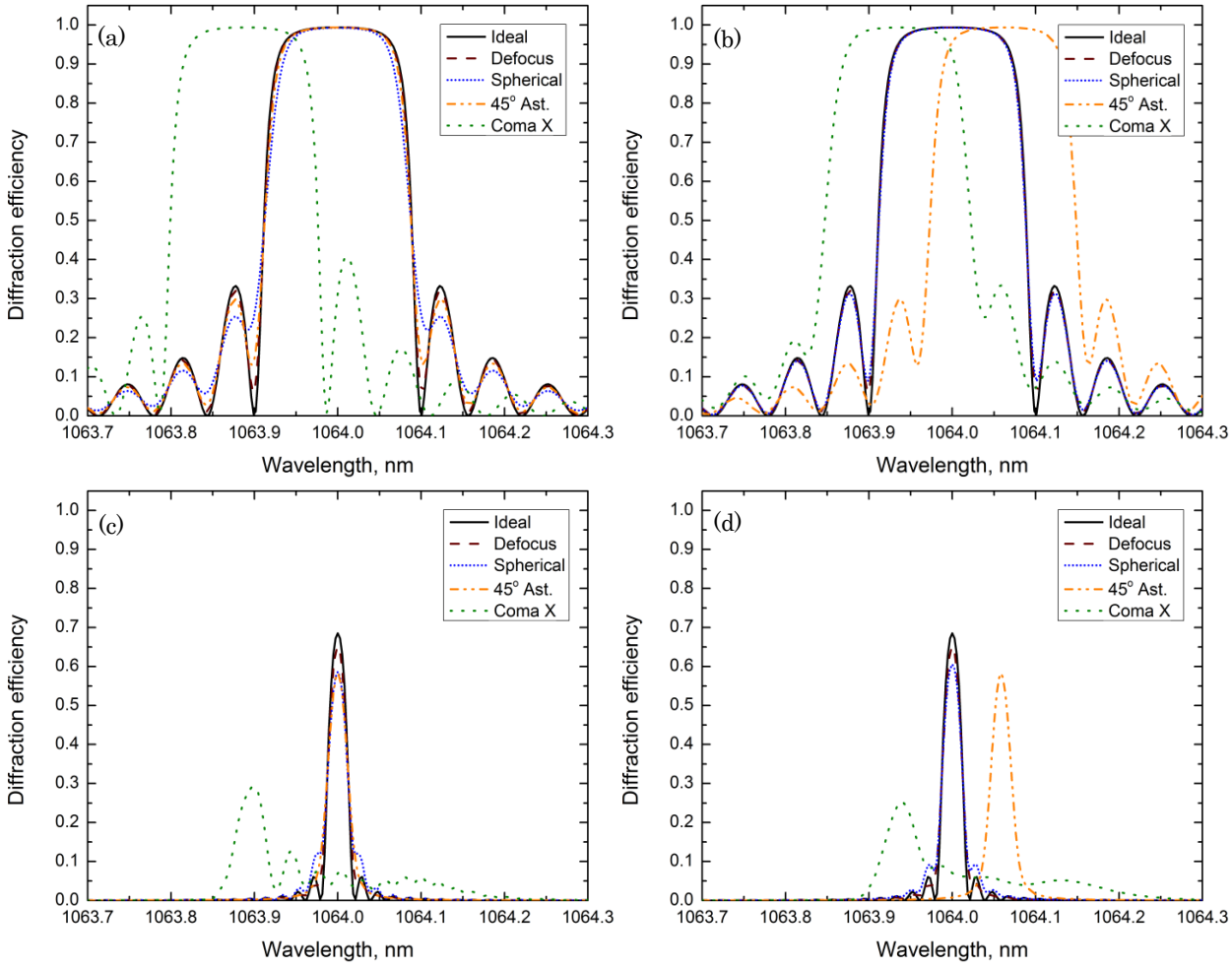

Fig. 104. Reflection spectra in the presence of one wave of a given aberration at the center of the grating {(a),(c)} and halfway between the center and the edge of the grating {(b),(d)}.

reflectance spectrum at 1064 nm for Grating A and Figs. 104c and 104d show the effects for Grating B in the presence of the first several terms of the wavefront expansion.

A comparison of these figures shows four commonly occurring effects: a shift in resonant wavelength, side lobes becoming at least partially washed out, a reduction of peak diffraction efficiency, and spectral broadening. Defocus and spherical aberrations show similar behavior for both gratings simulated, with the resonant wavelength being unaffected but the side lobes becoming washed out and the peak diffraction efficiency being reduced, with Grating B showing a far more pronounced reduction than Grating A. This difference in peak diffraction efficiency reduction between the two gratings can be attributed to the difference in the initial spectral widths of the gratings. Because Grating A has a wide initial spectral width, small deviations in the reflectance spectra at individual points are masked, whereas in Grating B these deviations constitute a significant shift relative the spectral acceptance of the grating and therefore have a more noticeable effect in the integrated spectrum, resulting in reduced peak diffraction efficiency and spectral broadening.

45º astigmatism shows behavior similar to defocus and spherical when the probe beam is centered on the grating, but when it is moved off-center there is a change in resonant wavelength as well. This shift in resonant wavelength is identical for both gratings, but since Grating B has a narrower spectral acceptance, the shifted spectrum falls almost entirely outside of the desired spectral region, whereas there is still a region of overlap in Grating A. Coma x likewise displays a shifted resonant wavelength, even when the probe beam is centered on the grating, and in addition the spectra are asymmetrical, similar to chirped gratings. The effects of coma x are most noticeable however in Grating B, where spectral broadening has completely deformed the reflectance spectrum.

As mentioned previously, the degradation in spectral profiles is a combination of local differences in resonant wavelength as well as the local differences in grating tilt at individual points, which when integrated into the full spectrum result in the above effects. We would like to stress here that both the differences in grating tilt and resonant wavelength must be considered in order to properly characterize the deteriorated spectra. If for instance the deviations in local grating tilt are ignored the deteriorated spectra will still show spectral broadening, a shift of resonant wavelength, etc., but the overall profile will be significantly different from the profiles calculated by taking both effects into account. Thus in order to properly characterize the effects of aberrations on the reflectance spectra of a volume Bragg grating, the above methodology should be used.

We have developed a numerical method to characterize the effects of aberrations in a holographic recording system on reflecting Bragg gratings, which can be used in any recording geometry and for any combination of aberrations and grating parameters. Aberrations in recording beams can have potentially significant adverse effects on properties of thick reflecting Bragg gratings due to the spatial dependence of the overlapped wavefronts. This results local deviations in the grating vector, causing effects such as a spatially varying resonant wavelength, which is problematic for spectral filtering, and washed out sides lobes of the reflection spectrum, which reduces the combining efficiency of spectral beam combining using dense channel spacing. Asymmetrical spectra, spectral broadening, and a reduction in peak diffraction

efficiency may also be present, though the wider the initial spectral width, the less noticeable these effects will be.

3.3. Multiplexed reflecting gratings

3.3.1. Multiplexed volume Bragg gratings for spectral beam combining

The recent development of kW fiber laser sources makes the concept of laser systems operating at power levels from tens of kilowatts up to 100-kilowatt levels a reality. The use of volume Bragg gratings for spectral beam combining (SBC) is one approach to achieve that goal. To make such systems compact, lower the complexity and minimize the induced thermal distortions we propose and demonstrate the use of special volume Bragg elements which have several Bragg gratings written inside as combining optical components. Reflecting Bragg gratings used in a beam combining system are frequency (or wavelength) selective filters. They are not angularly dispersive, but reflect a beam at some angle for only a narrow range of wavelengths. This eliminates the added beam dispersion usually associated with SBC by surface gratings. The properties of these gratings, such as reflection spectrum bandwidth, angle, and wavelength, can be tailored to fit the desired system and diffraction efficiency of VBGs close to 100% has been demonstrated. When using VBGs for spectral beam combining, it is important to ensure high diffraction efficiency for the diffracted beam and low diffraction efficiency for the transmitted beams simultaneously.

One year ago, we reported the development of a five-channel SBC system using reflective VBGs. The system had channel separation of 0.25 nm between adjacent wavelengths with a total combined power of 0.75 kW within a 1 nm spectral range and used 4 VBGs to combine all five beams. To make systems such as the one just described compact, lower its complexity and minimize the induced thermal distortions, we propose the use of special volume Bragg elements which have several Bragg gratings written inside as combining optical components. The

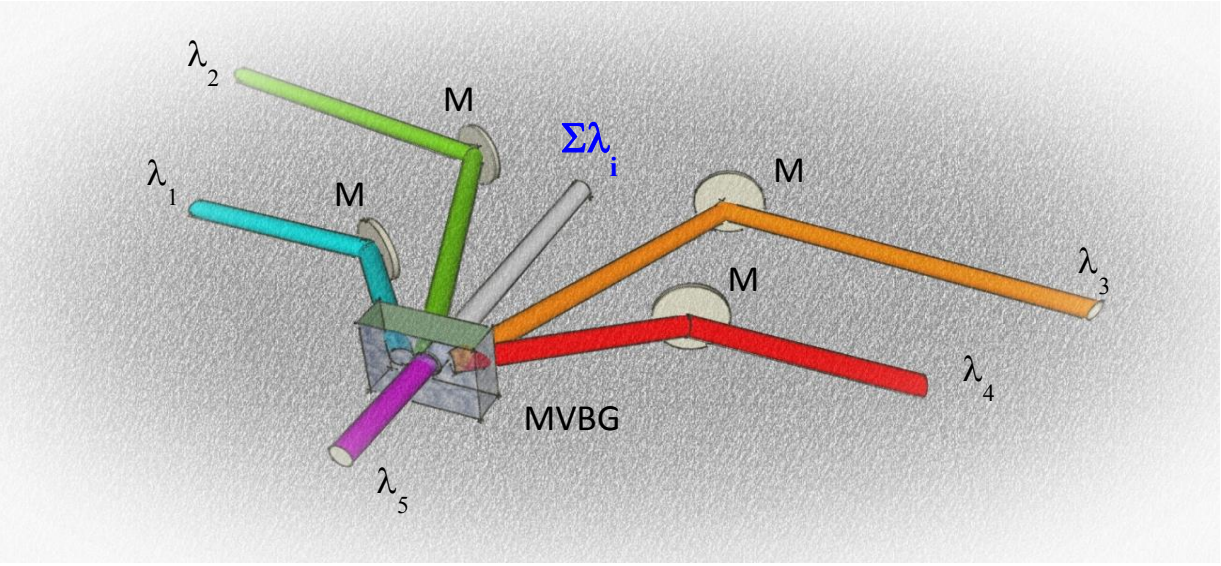

Fig. 105. Five-channel spectral beam combining scheme implemented by using a multiplexed reflecting M_4-VBG.

properties of the PTR glass allow recording of several VBGs in a single piece and therefore the complexity of the setup could be decreased proportional to the number of gratings recorded together. Figure 105 shows a spectral beam combining system capable of combining 5 laser beams which uses one PTR optical element containing four VBGs (M_4-VBG). This system is fully analogous to the one using 4 VBGs but with the benefit of being more compact and simpler to align. To show the feasibility of this approach, we first designed and fabricated a double-multiplexed M_2-VBG, which can combine up to three beams as shown in Fig. 106.

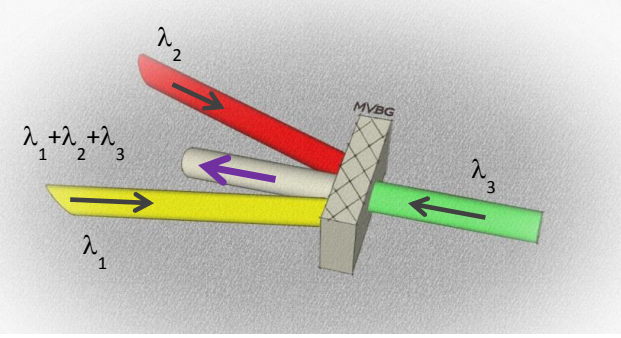

Fig. 106: Three-channel spectral beam combining scheme implemented by using a single reflecting M_2-VBG

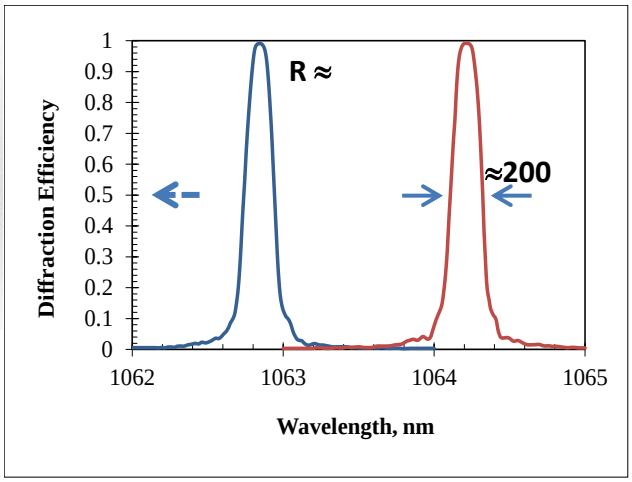

Fig. 107. Diffraction efficiency spectrum of M_2-VBG.

The first experiments were done by combining two low-power fiber lasers using a M_2-VBG. Both laser beams were reflected by the volume gratings inside the PTR glass and correspond to λ_1 and λ_2 as shown in Fig. 106. The initial beam quality parameter M^2 for both lasers was 1.05 and after the spectral combining, the M^2 of the output beam was 1.07. This promising result allowed us to move towards the design and fabrication of a M_2-VBG suitable for use at power levels on the order of hundreds of watts. Such an optical element required high-optical quality glass that will introduce no beam distortions and has very low absorption coefficient. Using the already well-developed PTR glass technology, several M_2-VBGs were recorded with suitable high-power parameters. Figure 107 shows the diffraction efficiency spectrum of a high-power M_2-VBG recorded in PTR glass used in the experiments described below. The two volume gratings had resonance frequencies approximately 1.4 nm apart and had spectral widths of about 200 pm. Their diffraction efficiency was 99% and matched well the initial design. We also performed a full efficiency characterization for each of gratings across their working aperture. The uniformity for aperture size of 13 x 17 mm was within 1%, which together with the measured absorption of 2×10^{-4} cm^{-1} made these gratings suitable for high power spectral beam combining.

The initial high-power experiments were done in "reflection only" configuration where two beams 3 - 4 mm in diameter (see Fig. 106 - λ_1 and λ_2) were reflected by the corresponding VBGs. A total combined power of 282 W was achieved with combining efficiency of 99%. The M^2 of the combined beam was measured to be 1.15 in the 'X' and 1.08 in the 'Y' direction, which did not deviate substantially from the lasers' original M^2 of 1.05 for both lasers in each direction.

Throughout the experiment, the MVBG was kept at a constant temperature using a thermo-electric element and copper housing around the glass (Fig. 108). This approach allowed for retuning the VBGs into resonance in case there was any heating due to the lasers' radiation being absorbed. Any heating would cause the grating period to change and therefore go out of resonance for the operating wavelengths. We did not observe any heating issues and the M_2-VBG temperature stayed constant. In conclusion, in this pure reflection configuration, where the power density on the M_2-VBG was approximately 3 kW/cm^2, no beam quality degradation was observed.

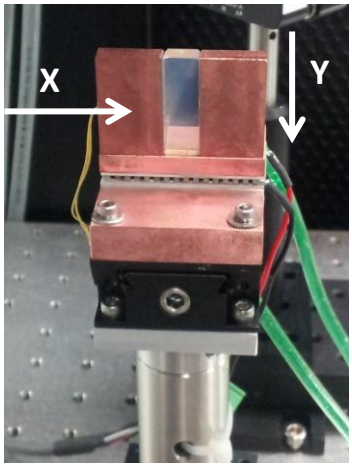

Fig. 108. M_2-VBG thermal stability control mounting.

As a next step, we added a third laser beam to the combining setup. The wavelength of this laser was chosen to be out of resonance with the two gratings so it could be transmitted through the glass in order to be combined with the two reflected beams (see Fig. 106 - λ_3). With three incoming beams, the total combined power was 420 W, achieved with 96.5% combining efficiency. The M^2 of the combined beam was measured to be 1.38 in the 'X' and 1.20 in the 'Y' direction. It is evident, that there is a substantial deviation from the lasers' original M^2 of 1.05 for both reflected lasers (in both directions) and 1.13 and 1.16 for the X- and Y-directions of the transmitted laser. In order to keep the two gratings in resonance, the temperature of the M_2-VBG was lowered by approximately 8°K. In the previous configuration, where only two reflected beams were combined, such thermal issue was not present. We can say with confidence that the worse M^2 and the change of the M_2-VBG temperature set point are due to heating of the glass introduced by the transmitted laser beam. This conclusion is also supported by the difference in the combined beam M^2 in X- and Y- directions for the three-beam configuration. The laser beams' Gaussian power distribution centered in the middle of the MVBG and the different temperature at which the edges of the glass are kept to counteract the glass heating, creates a thermal gradient that is more pronounced in the X-direction due to the specifics of the VBG mounting. In the X-direction the glass is only 10 mm wide and the gradient is much higher when compared with the 25 mm size of the glass in the Y-direction and the lack of copper at the top of the glass. This leads to the definite conclusion, that the presence of a transmitted beam introduces extra heat into the glass via an absorption process, at levels sufficient to degrade the quality of the combined beam.

Fig. 109. Dependence of VBG reflectivity on thickness.

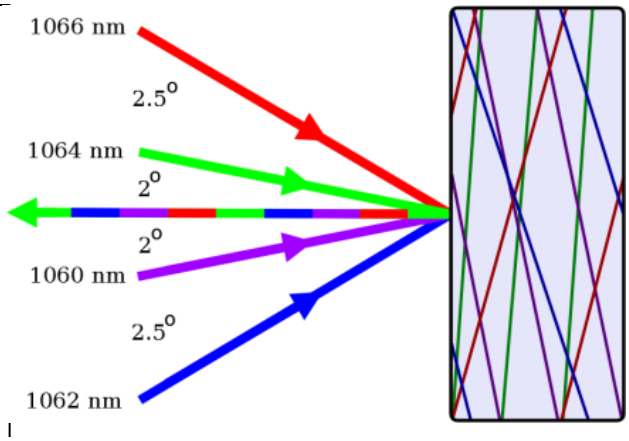

Fig. 110. A 4x multiplexed reflecting grating for spectral beam combining with of four laser channels with wavelength separation of 2 nm.

To explain why the two reflected beams did not follow the same law and deposit similar amounts of heat inside the glass we need to look at how the reflectivity of a VBG depends upon the thickness of the volume grating. Figure 109 shows a simulation of the dependence of reflectivity on the VBG thickness for a VBG with parameters matching the grating used in our experiments. The simulation shows that a VBG with 99 % reflectivity has thickness of approximately 6 mm but 90% of power is reflected within 50% of the volume grating thickness. This explains why in the case of combining two reflected beams no heating or any substantial M^2 degradation were observed. The reflected beams penetrated significantly less into the MVBG when compared to the case where the transmitted beam was also present and therefore much less of their power was absorbed and deposited as heat into the glass.

With successful demonstration of beam combining with a 2x multiplexed grating at high power levels, the next step is to demonstrate scalability of such a system. A new multiplexed grating was designed to combine four laser channels in reflection geometry. The device and design angles are shown in Fig. 110. The performance was tested by probing the common arm with a tunable laser and measuring the splitting efficiency in each of the input arms. The relative diffraction efficiency spectra of each grating are shown in Fig. 111. This characterization shows that scaling of the number of multiplexed gratings recorded in PTR glass to four can occur while maintaining high efficiency.

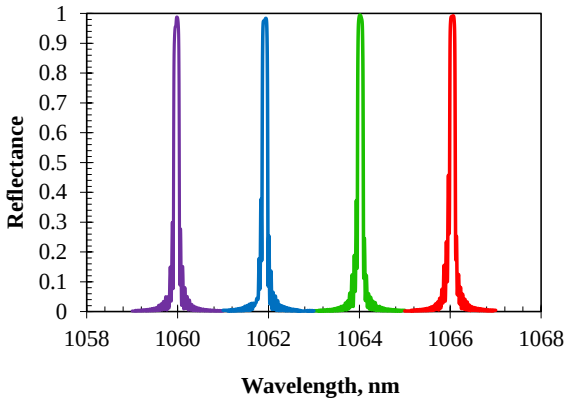

Fig. 111. The reflection spectra of the 4x multiplexed volume reflecting Bragg grating. Measurement is obtained by illumination by a tunable laser source along the direction of the central arrow in Fig. 32 and power meters placed in input arms (arrows marked with wavelengths in Fig. 110).

The quality of beams reflected from the 4x multiplexed RBG was characterized by M^2 measurements at low power to demonstrate that there are no inherent deformations being caused by increasing the number of gratings

within the PTR glass sample. Using the same testing configuration that was used to measure the reflectance spectrum, the M^2 of each of the reflected beams was measured as the wavelength of the incident beam in the common arm was tuned to each of the reflection peaks shown in Fig. 110. The results are summarized in Table 11. Again, the x axis in these results refers to the plane of diffraction. No degradation of the beam quality is observed after reflection from the 4x RBG. These results show that homogeneity of the grating and subsequently the reflected beam quality is preserved in a multiplexed grating with an increased number of combining channels.

Table 11. M^2 of beams reflected from a 4x multiplexed RBG

	Wavelength, nm	**M^2, x**	**M^2, y**
Incident Beam	1064	1.13	1.20
Reflection from	1060	1.10	1.19
Multiplexed	1062	1.12	1.19
RBG	1064	1.07	1.22
	1066	1.10	1.23

From these low power tests, the scalability of multiplexed volume Bragg gratings recorded in PTR glass for applications in beam combining has been verified. Combined with results of high power combining with a 2x multiplexed grating, the pathway to combining more laser systems to achieve higher power beam combining with high efficiency is established.

A 4x multiplexed monolithic grating was shown to maintain high efficiency exceeding 98% and caused no degradation of the incident beam's M^2 value. These positive results pave a way for further power scaling with spectral beam combining using volume Bragg gratings recorded in PTR glass.

In conclusion, the approach of using multiplexed volume Bragg gratings for spectral beam combining is an excellent extension to the current state of the art combining techniques and especially valuable is its capability to reduce the number of optical elements in the system while being able to manage the expected thermal load when kilowatt level sources are used for beam combining.

3.3.2. Forced air cooling effect on VBGs

Volume Bragg gratings have been successfully used in spectral beam combining of high power fiber lasers with narrow channel separation and in four channel passive coherent beam combining of fiber lasers. For a reflecting volume Bragg grating, heat is deposited on the surface and through the volume of the glass. To properly cool the grating, both surfaces must be cooled. Forced air cooling blown across both surfaces of the grating is both easy and cheap, but has been avoided in the past due to concerns of how the air density fluctuations will hurt beam quality.

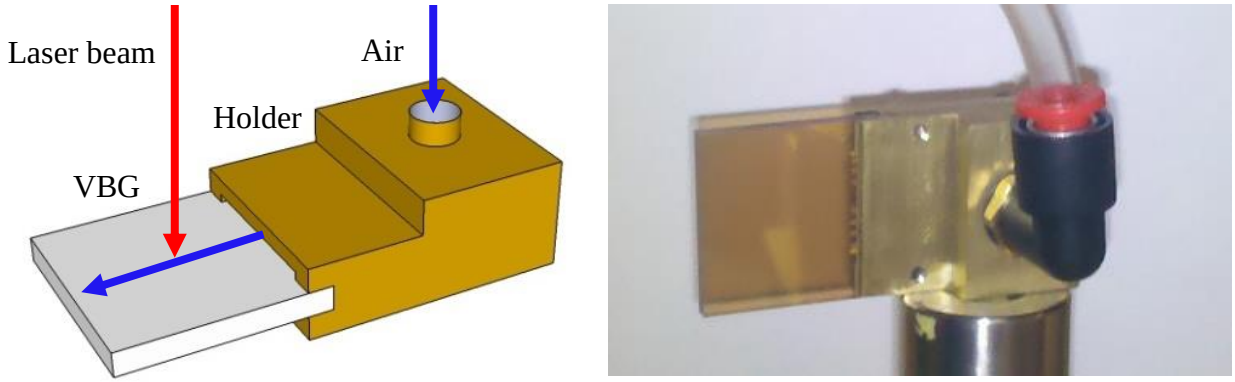

Fig. 112. Schematic and image of the air cooling system with a high absorption VBG attached. Normal VBG's have an absorption of approximately 10^{-4} cm^{-1} and are clear. The absorption of this VBG was artificially increased by 140 times to allow for the simulation of 11 kW beams.

To test the effects of heating and air cooling on the M^2 parameter, a reflecting Bragg grating was recorded with 95% diffraction efficiency and a FWHM of 140 pm. To simulate a higher power beam incident on a grating with absorption of 10^{-4} cm^{-1}, the grating was further exposed to UV-radiation and developed at low temperature to artificially increase the absorption by 140 times. In this manner, a 10 kW imitating beam was produced by the use of a 150 W CW fiber laser. For a power level of 48, 64, and 77 W, incident power at the grating, the illumination is equivalent to a power level of 6.7, 8.9, and 11 kW respectively. To cool the grating, a special brass holder was constructed to fix the grating in the air flow and prevent additional stresses (Fig. 112).

Temperature is measured using a small probe beam to detect the shift in the Bragg wavelength. A shift of 10 pm corresponds to 1°K of heating in the grating. Temperatures were measured and compared to theoretical modeling in Comsol software. Agreement between modeling and measurements was within 10°K. Calculations of temperature distribution in air and in the VBG show small heating and only a small effect on the beam quality could be expected (Fig. 113).

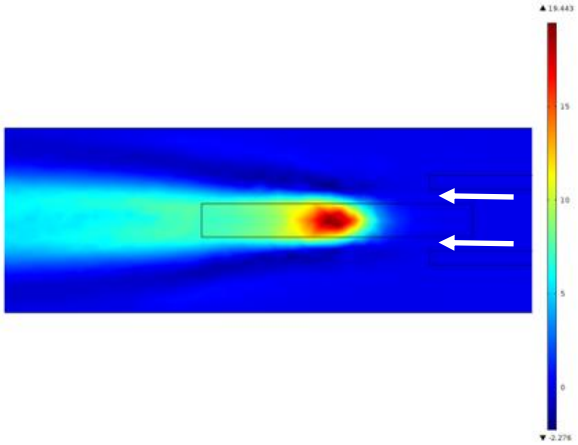

Fig. 113. Modeling of temperature distribution in air flow (white arrows) and grating exposed to laser beam (calculated with Comsol software). The grating temperature growth is 19°K in the center of the laser spot, while the air is heated for 5°K.

Beam quality of a beam diffracted or transmitted by the VBG exposed to the high power beam was tested in two conditions. In the transmitted condition, the grating is tuned out of resonance such that only defocusing in the glass and density fluctuations in the air flow affect the beam quality. In the reflected condition, the grating is turned into resonance such that the effect of the grating on the diffracted beam quality can be measured.

At low power in the transmitted condition, air flow did not change the M^2 parameter of the beam. For a high power simulating of 6.7 kW beam without air flow, the temperature increases for 97°K and the M^2 increases to 1.3 (Fig. 114). Increasing the air flow to 6SCFM decreases the M^2 down to 1.14 and the temperature increment decreases down to 21°K. To within the accuracy of the beam quality measurement, this is the nominal beam quality of the laser, showing the air cooling has no effect on the beam quality.

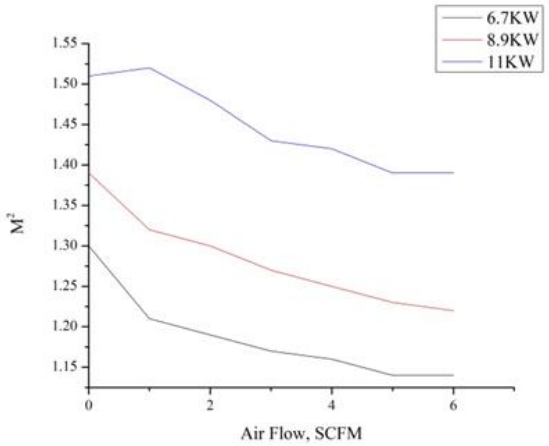

Fig. 114. Effect of air flow on M^2 of the beam transmitted through the grating for different equivalent powers.

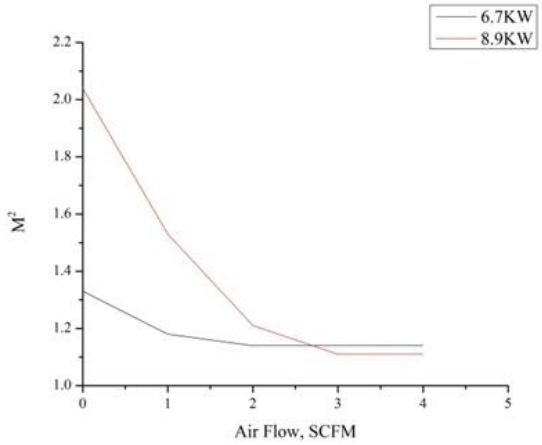

Fig. 115. Effect of air flow on M^2 of the beam diffracted by the grating for different equivalent powers.

When the grating is tuned into resonance with the high power beam, diffraction efficiency greatly suffers from the heating effects, and the beam quality is significantly hurt (Fig. 115). However, increasing the air flow quickly improves the M^2 parameter to the nominal value and restores the diffraction efficiency.

To test the effectiveness of VBGs, a series of experiments were performed in collaboration with Nufern. A low absorption VBG was recorded to be characterized in a high power laser and compare the performance with and without the air cooling. To fully understand the limits of the air cooling, the VBG was tested in two configurations: the reflecting and the transmitting configuration. The reflecting configuration is designed to show how much power can be diffracted by the VBG, while the transmitting configuration is designed to show the limits of SBC using a transmitted beam through the VBG. In the reflecting configuration, the VBG is tuned to be in resonance with the laser, diffracting all of the power.

The VBG was recorded with 99% diffraction efficiency, a normal incidence resonance centered at 1065nm and a spectral bandwidth (FWHM) of 300 pm. The performance of the VBG was characterized in a 1 kW fiber amplifier and compared to the performance using the air cooling system. The wavelength of the fiber amplifier was centered at 1064 nm and was resolution limited to have a spectral bandwidth of less than 50 pm, significantly less than that of the VBG. The beam was fiber delivered and collimated to a diameter of approximately 3.5 mm. The nominal M^2 parameter of the beam was measured to be <1.1 through the full power range of the amplifier.

In the reflecting configuration, it was found that maintaining an air flow of 1.8 SCFM (standard cubic feet per minute) allowed the beam to maintain an M^2 of less than 1.1 through the full power range (**Error! Reference source not found.**). No degradation in beam quality was seen due to the turbulence of the air flow, and minimal heating of the VBG was seen at full power. At 907 W incident on the VBG, the temperature of the VBG was seen to be 22°C, near room

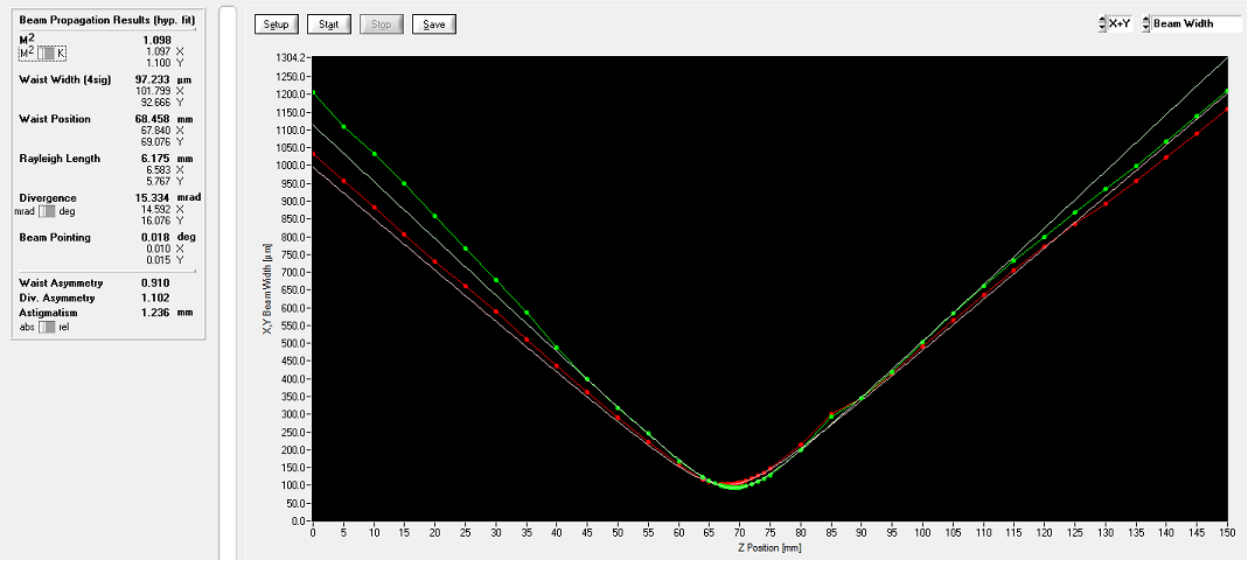

Fig. 116. Caustic profiles of the 907 W beam after diffraction by the VBG air cooled with a 1.8 SCFM flow rate. M^2 parameter remains nominal and below 1.1.

temperature.

The air flow was then modulated to understand the minimum necessary to maintain high performance of the VBG. Reduction of the air flow showed higher temperatures in the VBG, but the temperatures were not high enough to hurt the M^2 of the beam. However, as the temperature of the VBG increased, thermal expansion inside the VBG caused the Bragg period to change and shifted the resonance of the VBG. This effect was seen at 0.6 SCFM, where the resonance conditions changed, resulting in a reduction of diffraction efficiency for the used alignment.

In the transmitting geometry, the beam interacts with a larger volume of the VBG, and more absorption is expected, leading to more thermal distortions. However, high beam quality could similarly be maintained at maximum power with only 1.8 SCFM of air flow. A higher temperature was observed, but at only 28°C, the VBG temperature was still very close to room

temperature. Again, the air flow was modulated. Through the full range of the modulation, no reduction of M^2 was seen. Reducing the air flow to 0.6 SCFM showed the temperature increase to 36°C, which was not enough significantly distort the beam.

Results using the low-absorption VBG in the 1 kW amplifier were promising, and showed that air cooling was an efficient method of managing small thermal effects in high power beams. However, there was not enough data to understand the limits of such cooling methods for more drastic thermal effects in higher power beams. Without access to higher power lasers, a VBG with 140 times larger absorption was recorded to simulate the effects of high power beams using only 80 W lasers. Such experiments allow simulation of power levels up to 11 kW.

Air cooling is shown to efficiently cool VBG's without adverse effects on beam quality caused by the air turbulence. At 8.9kW diffracted by the grating, forced air cooling restores the M^2 parameter from 2.0 to a nominal value of 1.1 while mitigating heating of the grating from 71 to 14 K above room temperature. These experiments show that current technology of PTR VBGs enables the use of these elements in 10 kW class lasers while keeping the beam quality close to the diffraction limit.

3.3.3. Multiplexed volume Bragg gratings for coherent beam combining

Multiplexed VBGs with different inclinations and periods to provide a common Bragg angle for several beams with the same wavelength launched from different directions were holographically recorded in a single PTR glass substrate. They are key elements in multichannel coherent beam combiners which provide efficient radiation exchange between different channels in a multichannel laser system.

As a first step during the reported period, two symmetric VBGs were recorded in a single PTR glass sample at an angle of ±3.3° with respect to the sample surface. Each VBG has high peak diffraction efficiency (~ 99%) and a FWHM bandwidth of 210 pm around the 1065.7 nm at normal incidence (incidence along the grating vector of the respective VBG). We studied the properties of the M_2-VBG in detail to understand the complexity of the alignment and its performance as a coherent combiner. In particular, we presented theoretical and experimental results for the spectral properties of this novel optical element under three specific cases of

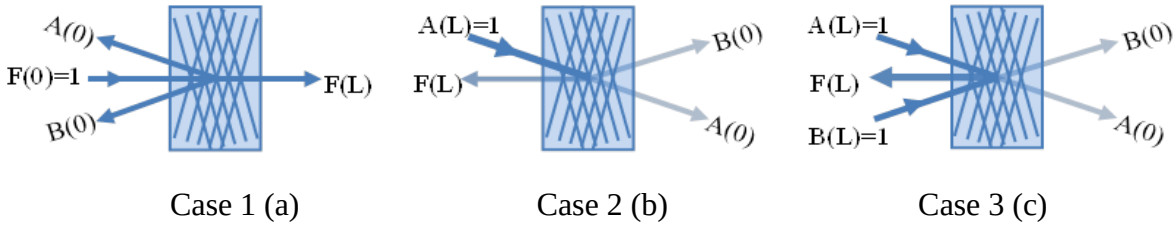

Fig. 117. Multiplexed VBG splitter considered for the 3 cases of incidence along (a) the bisector of the two grating normal (wave F), (b) the conjugate angle for one of the gratings (wave A), and (c) conjugate angle for both gratings (in-phase waves A and B).

incident beams relevant to CBC experiments as shown in Fig. 117.

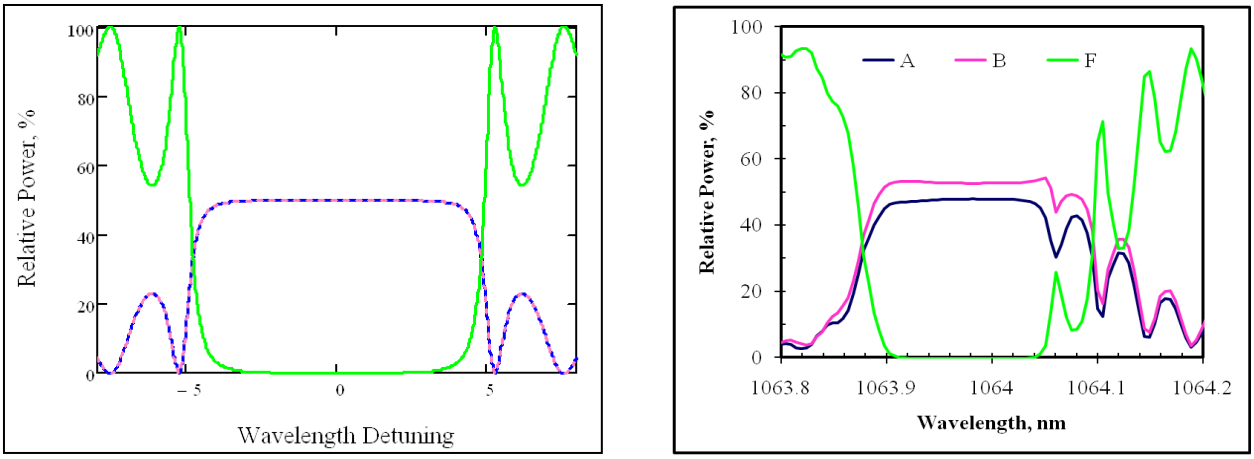

Fig. 118. Simulated (left) and measured (right) spectral response of M-VBG for configuration depicted in Fig. 114(a).

For incidence along the axis bisecting the two VBGs, this M_2-VBG acts as a 50:50 beam splitter for a narrow spectral band around the degenerate Bragg wavelength of 1064.0 nm, Fig. 117(a), and is transparent at wavelengths outside of the grating bandwidth. Figure 118 shows the simulated and measured spectral response for this case. The splitting is almost 50:50 but not exact probably due to small fluctuations in the recording process for the two VBGs. The two beams reflected by the M_2-VBG make angles of $\pm$ 9.6^o relative to the input beam. The asymmetry in the measured response could be explained by the 2nd order inhomogeneity in background refractive index of the glass wafer along the recording direction. Angular detuning of the M_2-VBG around this angle shifts the spectral response of the two individual VBGs in opposite directions. As the angular detuning is increased, the two VBGs become more and more independent of each other and finally act as single VBGs at their respective Bragg angles.

For incidence at the conjugate angle of ±9.6° and the same degenerate Bragg wavelength of 1064.0 nm, the M_2-VBG acts as a three-way splitter, Fig. 117(b). The incident wave is diffracted by its respective VBG (and does not interact with the other VBG for which Bragg condition is

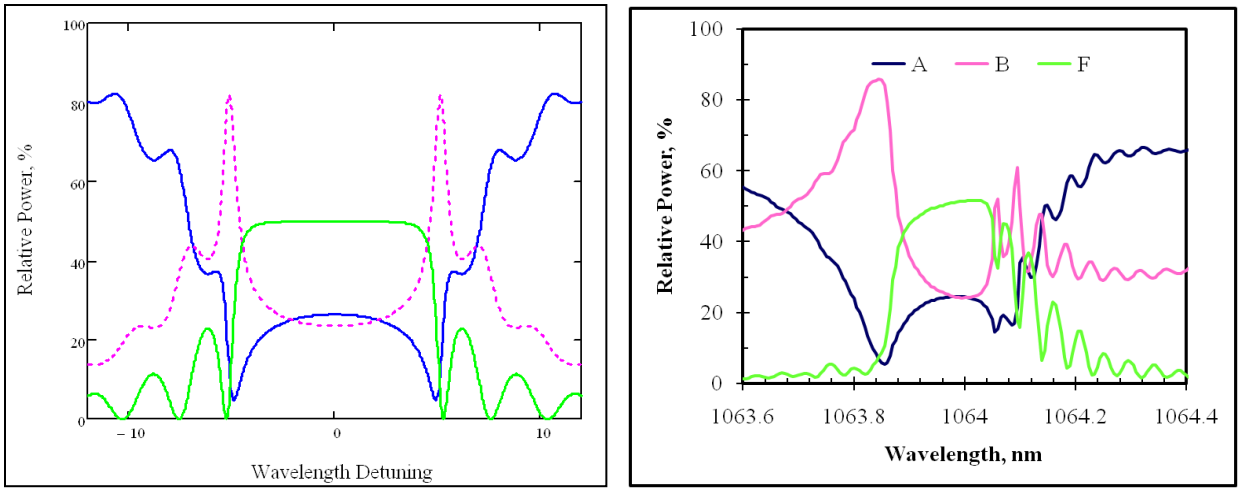

Fig. 119. Simulated (left) and measured (right) spectral response of M_2-VBG in configuration depicted in Fig. 114(b).

not satisfied at this angle of incidence). The diffracted wave is along the bisector of the two VBG vectors and, as it propagates through the sample, it is partially re-diffracted by both gratings. Note that the beams split in the ratio F:A:B = 50:25:25 near the degenerate wavelength. The simulated and measured spectral response for this case is shown in Fig. 119. It is important to note that in spite of complex spectral response depicted in Figs 118 and 119, this multiplexed

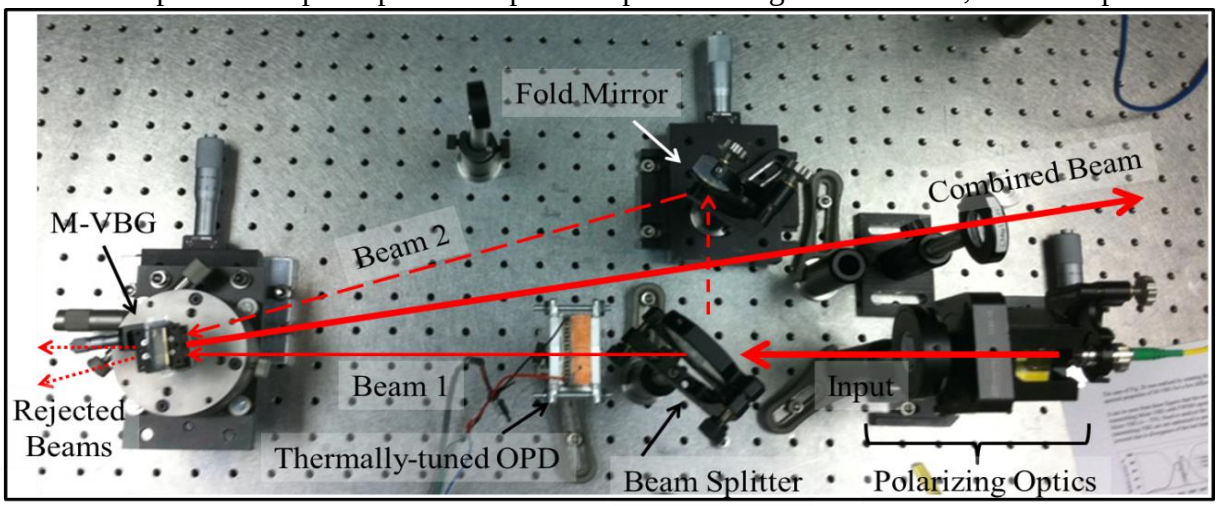

Fig. 120. Experimental setup to test M_2-VBG as a coherent beam combiner depicted in Fig. 38(c).

grating works perfect as a beam splitter at the designed wavelength and incident angle and could be used at a multichannel semitransparent mirror for different interferometers design.

It is intuitive that the M_2-VBG, being an efficient splitter, should act as an efficient beam combiner if the beams in Fig. 117(a) are reversed as shown in Fig. 117(c). To measure the response of this case and evaluate the performance of the M_2-VBG as a beam combiner, we tested the M_2-VBG in a Michelson interferometer like setup. Figure 120 shows the interferometric setup built for this study.

The output from a tunable laser is linearly polarized and split equally using a beam splitter. The two split beams are combined again at the M_2-VBG, and the combined beam is observed in the far field using an IR camera to ensure perfect overlap of the diffracted beams from the two gratings. A 5-mm-thick piece of silica glass is inserted in one of the arms. Thermal tuning of this glass provides relative phase change between the two arms. The tunable laser was set to the degenerate wavelength of 1064.0 nm and had a maximum output power of 4 mW. After the beam splitter, beam 1 and beam 2 (Fig. 120) had 2.04 mW and 1.94 mW respectively. The M_2-VBG is first aligned with respect to beam 1 so that the split beams correspond closely to the

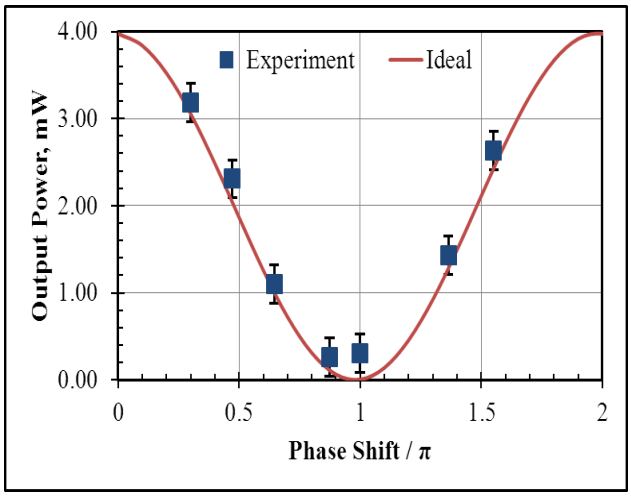

Fig. 121. Measured and calculated power in the combined beam as a function of relative phase difference.

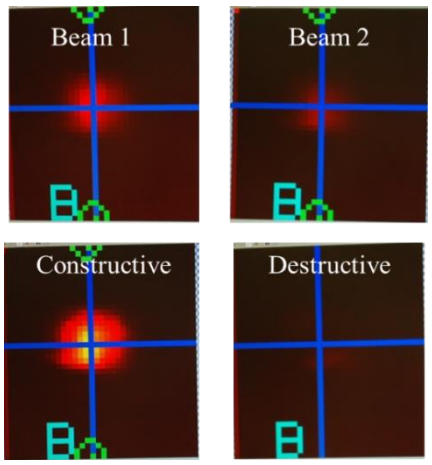

Fig. 122. The individual beams (top) and the combined beams (bottom) for constructive and destructive interference at the M_2-VBG

ratio at 1064 nm in Fig. 117(b); i.e. 50:25:25. Beam 2 is then aligned so that the diffracted beams are in perfect overlap.

The two beams are combined along the bisector of the two gratings. Figure 121 shows the power in the combined beam as a function of relative phase change. The silica glass was heated from 29.9°C to 32.6°C to provide a π phase change. Figure 122 shows the pictures as seen from the IR camera of the two individual beams, the combined beam corresponding to constructive interference, and the combined beam corresponding to destructive interference. Figure 123 shows the simulated and measured spectral response (averaged over several scans) measured

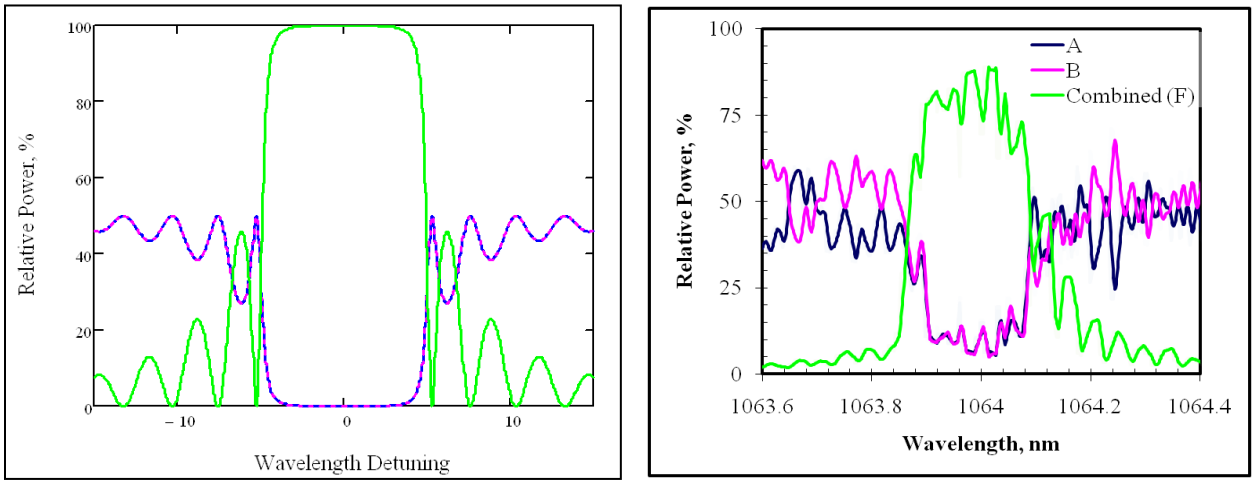

Fig. 123. Simulated (left) and measured (right) spectral response for M_2-VBG depicted in Fig. 114 (c).

when the combined power was close to maximum, i.e. the two beams were almost in-phase. The fluctuation in the measured signals is attributed to the random atmospheric and thermal perturbations in the interferometric system over the course of the scan.

The theoretical model is generalized to N-th order M-VBGs, i.e. N VBGs multiplexed in the same volume, to investigate the potential scalability of this approach. In general, for N multiplexed gratings with the same period, (N+1) coupled differential equations are solved for the specific boundary conditions of case 3 in Fig. 117 (c). It is found that the diffraction efficiency of individual VBGs required for 99% combining efficiency decreases as the order of M-VBG increases (Fig. 124). This property makes this technique very practical to scale, as more low efficiency gratings can be recorded in the same volume than high efficiency gratings.

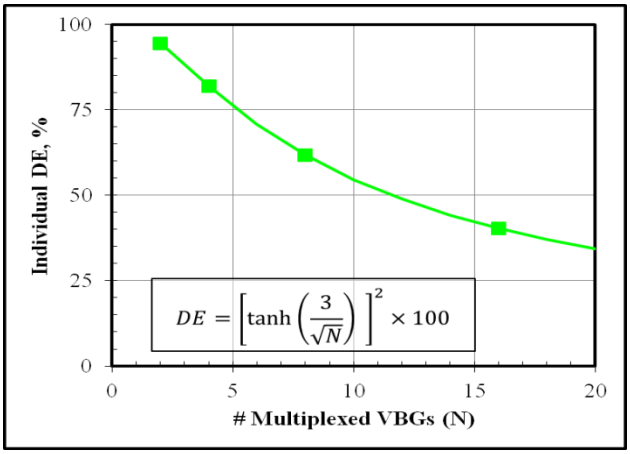

Fig. 124. Required DE of each VBG to achieve 99% combining efficiency as a function of the number of individual gratings in a reflecting M-VBG.

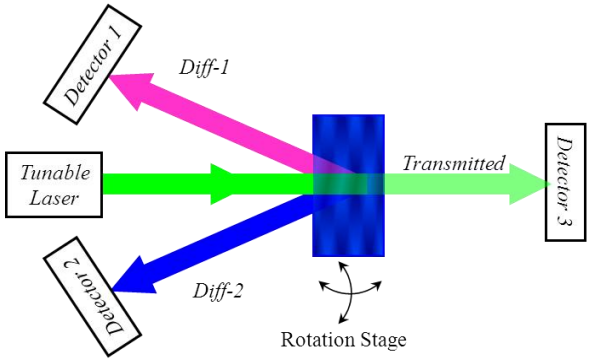

Fig.125. Setup for M-VBG alignment using a tunable laser.

The M-VBG is first aligned using a tunable laser and three detectors in a setup shown in Fig. 125. For rough alignment, the tunable laser is first set to the degenerate wavelength of 1064.25 nm and the M_2-VBG angularly aligned so that two diffracted beams are observed. Precise alignment is achieved by scanning the wavelength of the tunable laser about the degenerate wavelength (1064 nm – 1064.35 nm) while making small adjustments to the M_2-VBG angular alignment. Figure 126a shows the case of near-perfect overlap of the two gratings (degenerate angle) and Fig. 126b shows the case when the M-VBG is angularly detuned by 135 arc seconds

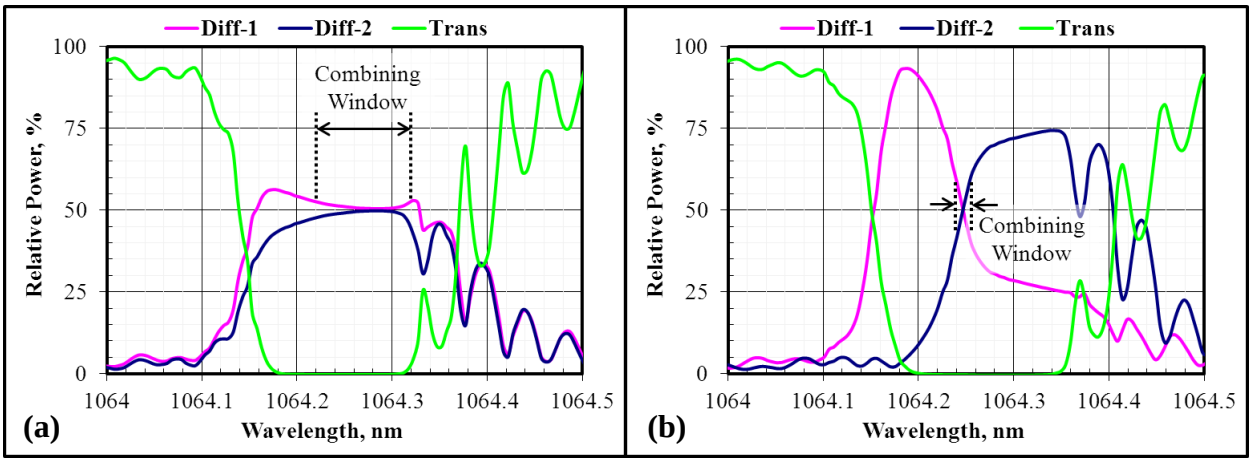

Fig. 126. (a) Spectral response of M-VBG corresponding to near-perfect overlap of the two gratings, and (b) spectral response of M-VBG angularly detuned by 135 arc sec (0.65 mrad)

(0.65 mrad) from the degenerate angle. An interesting observation is that even for a slight angular detuning as in Fig. 126b, there exists a degenerate wavelength where perfect 50:50 splitting is observed. However, in this case the "*combining window*" (bandwidth over which MVBG performs as a ~50:50 splitter) is narrowed by almost an order of magnitude from ~100 pm to ~10 pm. Angular detuning of the M_2-VBG to drastically reduce the combining window can lead to important insights in understanding the passive CBC process in broadband versus narrowband couplers and in understanding the scalability of this approach to larger number of channels (where the occurrence of common-cavity supermodes will be less frequent).

3.3.4. Highly multiplexed reflecting gratings

While fiber based VBGs are appealing for many applications, the large aperture that can be created using bulk photosensitive glass such as PTR does afford unique design opportunities. For example, the bulk glass can be used to record different gratings in different areas of the sample that can be accessed by translation[74], [75] or used to angle multiplex many gratings within the volume, each of which is only accessible at particular angle of incidence[76, 77]. The recent work of combining high power laser beams using multiplexed VBGs recorded in PTR glass has prompted interest in the number of high-efficiency multiplexed gratings that can be recorded into a single device.

As a whole, the use of multiplexed volume Bragg gratings is not new but the investigation of multiplexing gratings in PTR is of interest due to the unique filtering properties that the recording media provides. Multiplexed VBGs have been recorded in many of the common holographic recording materials and for numerous applications. Applications include wavelength division multiplexing/demultiplexing (i.e. combining and splitting), spectral filters, optical logic, and optical data storage[78, 79, 80, 81, 82]. In these applications gratings can be multiplexed in angle, wavelength or a combination of both. Certain designs only require a set number of multiplexed gratings such as a one-to-two beamsplitter. Other applications such as data storage benefit from multiplexing as many gratings as possible. The question of how many gratings can be multiplexed depends on the required efficiency of each grating, the geometry of the device, and

---

[74] D. Ott, S. Mokhov, I. Divliansky, and L. Glebov, "Narrowband Filtering by a Volume Bragg Grating with a Tunable Spectral Transmission Bandwidth," Frontiers in Optics 2013, OSA Technical Digest, paper FTh3F.7 (2013).

[75] D. Ott, M. SeGall, I. Divliansky, G. Venus, L Glebov, "High spectral contrast filtering produced by multiple reflections from paired Bragg gratings in PTR glass," in Proc. SPIE 8982, paper 8982-36, 2014.

[76] D. Ott, I. Divliansky, B. Anderson, G. Venus, and L. Glebov, "Scaling the spectral beam combining channels in a multiplexed volume Bragg grating," Opt. Express, 21, 29620-29627 (2013).

[77] A. Jain, O. Andrusyak, G. Venus, V. Smirnov, and L. Glebov, "Passive coherent locking of fiber lasers using volume Bragg gratings," in Proc. SPIE 7580, vol. 7580, p. 75801S, 2010.

[78] G. J. Steckman, a Pu, and D. Psaltis, "Storage density of shift-multiplexed holographic memory.," Appl. Opt., vol. 40, no. 20, pp. 3387–94, 2001.

[79] G. B. Ingersoll and J. R. Leger, "Theoretical analysis of multiplexed volume holograms for spectral beam combining," Proc. SPIE, vol. 7195, 71951P, 2009.

[80] B. Moslehi, P. Harvey, J. Ng, and T. Jannson, "Fiber-optic wavelength-division multiplexing and demultiplexing using volume holographic gratings," Opt. Lett., vol. 14, no. 19, pp. 1088–1090, 1989.

[81] L. Cao, X. Ma, Q. He, H. Long, M. Wu, and G. Jin, "Imaging spectral device based on multiple volume holographic gratings," Opt. Eng., vol. 43, no. 9, p. 2009, 2004.

[82] R. Kowarschik, "Diffraction efficiency of sequentially stored gratings in reflection volume holograms," Opt. Quantum Electron., vol. 10, no. 2, pp. 171–178, 1978.

the dynamic range of the material. For example, data storage applications often require only 1% efficiency for each stored hologram for a positive detection, whereas high power beam combining attempts to reach efficiencies as close to 100% as possible. The design of the grating for a particular application can also play a role. For example, when degenerate gratings exist, they can work together to achieve 100% efficiency even though each individual grating cannot diffract at high efficiency[83, 84].

The final determining factor for the number of multiplexed gratings is the dynamic range of the material. This material property defines the amount of total change in refractive index that can be achieved in a material. If the superposition of the RIM of each grating creates a change in the refractive index that exceeds the material dynamic range the sum total grating structure will be clipped. This can reduce the efficiency of the device or change the diffraction characteristics. Materials such as photopolymers and dichromated gelatin have extremely high dynamic range. Indeed this is necessary for thin media since the coupling parameter which determines the VBG efficiency depends on the product of RIM and thickness[85]. Despite being thin, these materials have enough dynamic range to multiplex many gratings within a volume and retain close to maximum efficiencies. Photosensitive glass (fiber and bulk) on the other hand has relatively low dynamic range. The RIM modulation for a typical PTR VBG is below 1000 ppm (change in n of $<10^{-3}$). For single VBGs this is sufficient to create reflection gratings with efficiency >99% due to the homogeneity and thickness of the material. In terms of the number of multiplexed VBGs that can be recorded in photosensitive glass the dynamic range does provide a limitation. The focus of this section will be investigating the number of reflection gratings that can be recorded into the volume of PTR glass. Recording extremely thick reflecting VBGs is simpler than recording equivalent transmitting VBGs. The large thickness of the reflecting VBG will allow us to make the most efficient use of the PTR dynamic range in order to achieve high efficiency device performance with many multiplexed channels.

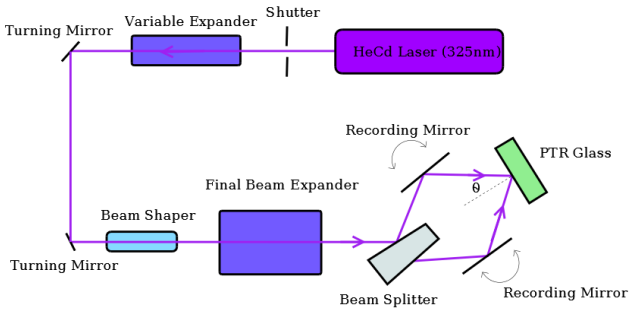

Fig. 127. The holographic recording setup for VBGs in PTR glass. Rotating mirrors allow the recording period to be changed for every recording.

[83] S. Mokhov, A. Jain, C. Spiegelberg, V. Smirnov, O. Andrusyak, G. Venus, B. Zeldovich, and L. Glebov, "Multiplexed Reflective Volume Bragg Grating for Passive Coherent Beam Combining," Laser Science XXVI, LWG2, 2010.
[84] C. Moser, L. Ho, E. Maye, and F. Havermeyer, "Fabrication and applications of volume holographic optical filters in glass," J. Phys. D. Appl. Phys., vol. 41, no. 22, 2008.
[85] H. Kogelnik, "Coupled Wave Theory for Thick Hologram Grating," Bell Syst. Tech. J., vol. 48, no. 9, pp. 2909–2945, 1969.

The setup for recording VBGs in PTR glass is shown in Fig. 127. Since PTR glass is sensitive to UV radiation, a He-Cd laser at 325 nm was used for exposure. Beam conditioning optics created an expanded flat top beam profile with a diameter approximately 3 cm. A beamsplitter and two rotating mirrors are used to create a two beam interference pattern at the recording plane. The PTR glass is mounted on a motorized stage to precisely control the tilt of the PTR plate with respect to the bisecting angle of the recording beams for recording tilted VBGs. Changing the angle of the two mirrors allows the period of the VBG to be controlled. This setup allows either transmitting or reflecting VBGs to be recorded with periods ranging from 200 nm to 1 μm. Small modifications to the recording geometry and setup can be used to record gratings with longer periods, larger aperture reflecting VBGs, and chirped VBGs. Typical dimensions for PTR substrates are 25×25×(1-15) mm^3. Larger samples are possible, but these initial demonstrations were conducted with 25×25 mm^2 samples. The use of larger samples will allow for larger multiplexing numbers in the future since thicker media requires lower refractive index modulation in order to achieve high efficiency. After photo-exposure, the PTR is thermally developed to induce permanent refractive index change. It is important to note that, unlike many other holographic materials, the induced RIM is not controlled by the applied recording dosage only. Rather the dosage is a fixed value and the thermal cycle used for development controls the induced RIM. For multiplexed gratings discussed here, this means that the relative strength of gratings can be controlled using the applied dosages of each sequential recording. The thermal development will be used to achieve the appropriate total RIM. For the gratings discussed here, the goal was to create a multiplexed device where each grating has the same efficiency, but this can be modified if necessary.

The first type of a multiplexed VBG with many channels that will be discussed is a type of beam splitter. The general operation of this type of device is shown in Fig. 128. In Fig. 128a there is one degenerate arm for each grating. When light is incident at this degenerate arm, it will be split into as many output channels as there are gratings. If the system is reversed with beams incident along the arms that are fanning out as shown in Fig. 128b, they can be combined if the optical phase of each beam is matched. Such a device can be utilized for coherent beam combining, as it was shown in Ref.[34]. The multiplexed VBG can also be designed to work at different wavelengths but still have a common output such as shown in Fig. 128c[33]. This device can be used as a wavelength division de/multiplexer or a spectral beam combiner. The coherent multiplexed grating of Figs 128a and 128b is designed for a single wavelength and will be used as a first example of many channel multiplexing. The advantage of this coherent design is that all gratings effectively act in concert. Light incident at one of the designated angles of incidence that

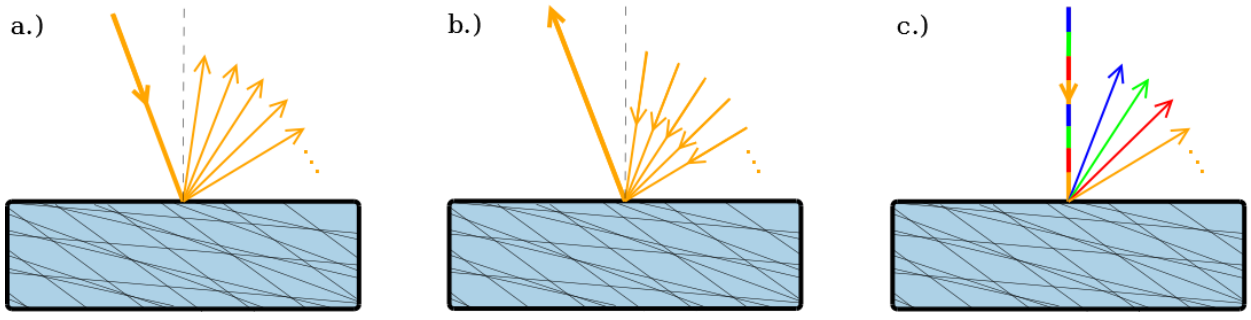

Fig. 128. Various alignment configurations for the 20 channel coherent multiplexed filter. a.) the use as a 1:N splitter for a single wavelength; b.) a coherent N:1 beam combiner; c.) a wavelength division demultiplexer.

corresponds to the Bragg condition of a particular grating will be simultaneously interacting with all of the multiplexed gratings as they exchange energy between the degenerate arm and the inputs. Therefore, the dynamic range of the material is utilized more efficiently since each individual grating is not the only grating responsible for generating high efficiency within the given device thickness. Using coupled wave theory to describe the coherent system of multiple gratings shows that the required efficiency of each grating in a coherent combiner needs to only operate individually with an efficiency shown in Eq. 3.1.1[40]. This will produce 99% theoretical combining efficiency for a device with *N* gratings.

$$\mathrm{DE}_{\min} = \tanh^2\left(\frac{3}{\sqrt{N}}\right) \qquad (1)$$

To demonstrate a proof of concept of this type of grating, 20 exposures, each with a dosage of 0.035 J/cm^2, were recorded into a piece of PTR glass. The targeted resonant wavelength was in the vicinity of 1064 nm. The design uses angles of incidence in air with respect to the surface normal of 10° for the common degenerate arm and the individual split arms range from -2° to -12.25° in steps of 0.75°. The grating was cut to a thickness of 10.4 mm after photo-exposure and thermal development. The aperture of the device is 25 mm by 6 mm. The device was tested by probing at 10° angle of incidence using a tunable laser source to measure the transmitted irradiance as the wavelength of the laser was swept to generate the spectral response of the device. The transmittance through the sample at the design angle of incidence is shown in Fig. 129. When the reflected light is observed on a card within this spectral bandwidth, 20 spots separated by 0.75° are visible. At this particular angle of incidence all gratings are being addressed simultaneously and effectively acting as a 20 way splitter with 90% of the light going into the split arms. At this particular alignment the device is operating as a multiplexed RBG for coherent combining of 20 channels.

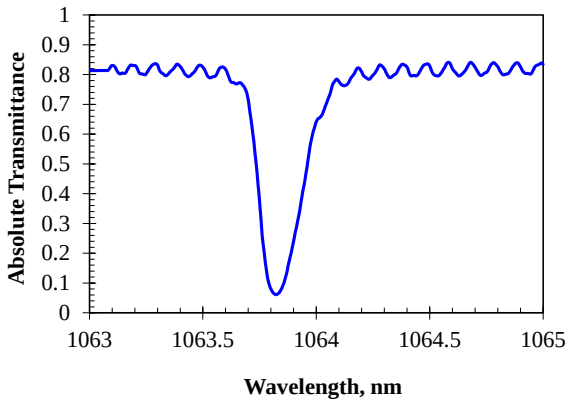

Fig. 129. The transmission spectrum of a coherent splitter as measured with a tunable laser. Diffracted light is split into 20 channels separated by 0.75°.

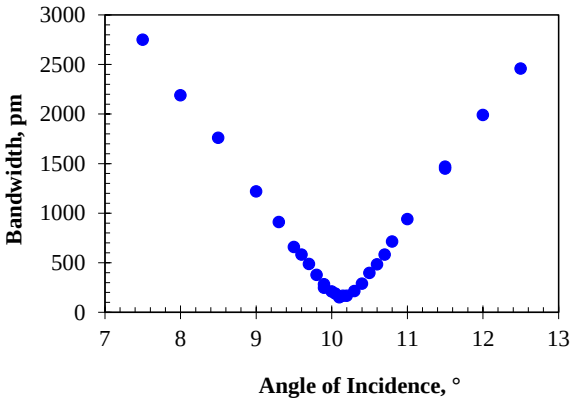

Fig. 130. The reflection bandwidth of the 20 channel multiplexed VBG depends on alignment of the angle of incidence to the grating structure. Incidence at 10° gives a coherent beam combiner. At angles far from normal, the device can be used as a wavelength division de/multiplexer.

It is also interesting to look at the behavior of this grating at angles of incidence that differ from the design. By completing spectral transmission scans at various angles of incidence, an

interesting pattern in the bandwidth of the spectrum is observed as shown in Fig. 130. At a particular angle, all of the grating spectra start to converge and the bandwidth finds a minimum value. This location corresponds to the alignment for coherent splitting or combining. At angles far from this location, the individual gratings become resonant at different wavelengths. When the spectra split far enough, the device can be used for spectral beam combining or wavelength division de/multiplexing as shown in Ref.[33].

Unique performance is achieved at an angle of 7°. At this alignment the spectra are fully decoupled and act as individual gratings. The spectral transmission at this angle of incidence is shown in Fig. 131. The device operates over a 3.2 nm range. It is important to note that the device was not designed to produce 100% diffraction efficiency for the individual gratings. Rather they are intended to operate coherently. So this particular device produces only approximately 30% efficiency as a demultiplexer at this alignment. The efficiency of 30% corresponds to the individual efficiency of the gratings. Such a device can be used as a splitter/demultiplexing with 30% being de-multiplexed and 70% being transmitted. As the incident wavelength is tuned over this range, the reflected light is deviated in steps of 0.75° as the light becomes resonant with each subsequent grating giving an angular dispersion is 4.4 °/nm. Therefore, at this particular alignment, the angle of reflection can be selected by changing the incident wavelength. At angles of incidence within ±1° of 10°, multiple adjacent reflected spots can be addressed by a single wavelength until the alignment reaches 10° in which all of the reflected spots are illuminated with a single wavelength. This tunable switching function is another interesting potential use of this device.

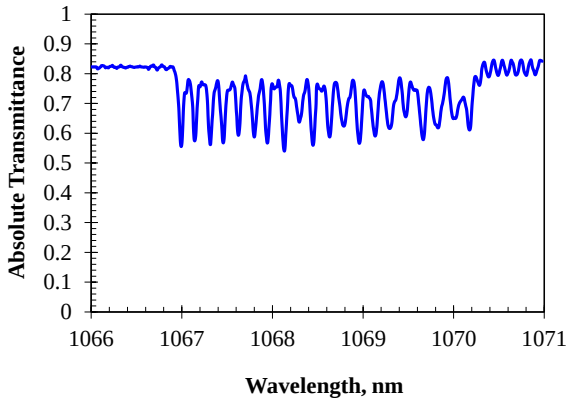

Fig. 131. At an angle of incidence of 7°, the individual gratings start to decouple. The spectra start to shift away from each other. At this alignment, the gratings acting independently with an efficiency of about 30%.

Recording multiple reflection gratings with the same tilt angle but different periods can be used to create multi-notch filters. Notch filters can be useful for applications such as spectroscopy or astronomy where there are unwanted atmospheric noise signals[86]. The use of a filter to reject these signals can be multiplexed into a signal device that will transmit all light except for the

[86] C. Moser, L. Ho, E. Maye, and F. Havermeyer, "Fabrication and applications of volume holographic optical filters in glass," J. Phys. D. Appl. Phys., vol. 41, no. 22, 2008.

select noise signatures. This type of device poses challenges for the dynamic range of PTR because all gratings are operating independently. Therefore, the multiplexed notch filter demonstrated here gives an indication of the practical level of independently multiplexed gratings that are possible in PTR glass and allows the performance of each grating to be observed individually.

A multiplexed notch filter was recorded to produce spectral filtering of 18 spectral lines in the vicinity of 1064 nm, each separated by 0.5 nm. This particular design is arbitrary in that it was not designed for a particular application, rather as a proof of concept of many channel multiplexing. The device was recorded using 18 sequential exposures of a sample of PTR glass. After thermal development the grating was processed to produce a thickness of 20 mm with an aperture of 25×12.5 mm^2. The transmission spectrum was measured by sweeping the wavelength of a tunable laser and monitoring the transmitted irradiance on a photodetector. The transmission spectrum is shown in Fig. 132. The light that is rejected by each of the notch filters is reflected back along the incident path. The filter produces 18 notches with a rejection greater than 10 dB with respect to the out of band transmitted light and a bandwidth of around 50 pm.

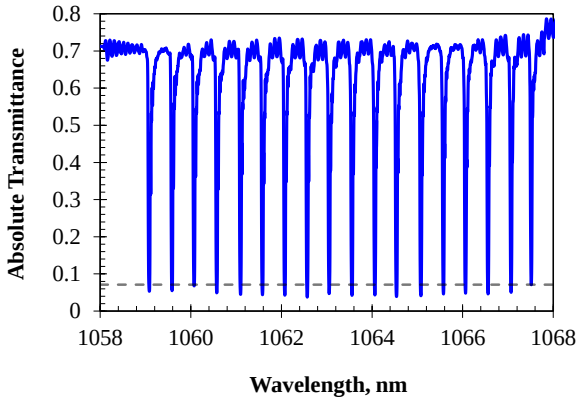

Fig. 132. The transmittance spectrum of a multiplex notch filter. The 18 spectral notches are separated by 0.5 nm and all exhibit efficiency above 90% with respect to the out of resonance transmission as indicated by the dashed line.

Thus, the examples of many channel multiplexed devices that have been presented here demonstrate potential for expanding the functionality of PTR based VBGs. The number of multiplexed gratings depends on numerous design and application parameters. The focus of the work is on generating devices with efficiencies in the range of 90%. The examples shown in this paper address two particular types of multiplexed gratings. The first type relies on the interaction of many individual gratings to function. In this case, the necessary individual strength of each grating will depend on the design of the device and its intended application. The second device is multiplexed such that each individual grating operates independently. This is a more general device and it is a good indication of the level of expected multiplexing that can be expected. We have demonstrated up to 18 independent gratings multiplexed into the same PTR glass volume, each demonstrating efficiency above 90%. Further improvements to the multiplexing number can be achieved by advances in material science, modification of thermal development and the use of

thicker VBGs. Practically speaking the number of high efficiency gratings that can be multiplexed independently in PTR glass will be on the order of 20 gratings due to the dynamic range of the material. By investigating the level of multiplexing that can be achieved in PTR, we have developed an understanding of the scalability of previously demonstrated devices. With this work established, new types of multiplexed VBGs can be pursued that utilize the increased functionality inherent to the increased number of grating channels.

3.4. Moiré gratings

A Fabry-Perot etalon, consisting of two π phase shifted reflecting volume Bragg gratings, is presented. These gratings are obtained as a moiré pattern resulting from sequential recording of interference patterns with different periods in photo-thermo-refractive glass and called moiré volume Bragg gratings (MVBGs). Experimental results demonstrating a MVBG with a 15 pm bandwidth and 90% transmission at resonance are presented. The use of the MVBG for longitudinal mode selection in a laser resonator is shown.

Narrow bandwidth sources find many applications in the fields of spectroscopy, metrology, WDM communication systems and optical sensor networks. Thin film filters and Fabry-Perot etalons are commonly used to create narrow bandwidth filters with large apertures. Bragg gratings and Moiré volume Bragg gratings or known as well as phase-shifted gratings (PSGs) are employed for fiber based filters, most prominently appearing in Distributed Bragg Reflector and Distributed Feedback lasers. However, until recently, no experimental demonstrations of PSGs were performed outside of fibers due to the unavailability of bulk photosensitive materials with high optical homogeneity. Recent development in the use of photo-thermo-refractive (PTR) glass for recording volume holographic elements has led to the production of high efficiency volume Bragg gratings. The main advantage of such elements is that they allow for narrowband filters in both spectral and angular spaces and are suitable for high power laser applications. This allows high efficiency reflecting Bragg gratings (RBG) to be recorded in several millimeter thick pieces of glass with losses below 1%.

Recording a PSG into a bulk medium can be achieved most efficiently by using a sequential recording of two volume Bragg gratings with grating vectors of different magnitude, but otherwise collinear. The two gratings of different spatial frequency produce a moiré pattern which consists of a high spatial frequency refractive index modulation and a slowly varying envelope. The location of zero envelope amplitude induces a π phase shift in the rapidly varying refractive index modulation. When this phase shift is located in the center of a grating with a total thickness of two moiré semi-periods, a Fabry-Perot etalon resonance condition is produced. The result is a narrow bandwidth transmission peak in the center of the RBG spectrum.

The most common method for modeling the spectral and angular response of a volume Bragg grating element is coupled wave theory (CWT) developed by Kogelnik. This method predicts results closely matched to experiment with low computational effort. In the present work, only unslanted reflecting Bragg grating (RBG) geometry is of concern. In order to accurately describe the spectral response of the grating with non-uniform refractive index modulation, the slowly varying envelope approximation (SVEA) was employed. In this approximation, the low frequency envelope must have a frequency many times less than the resonant frequency of the

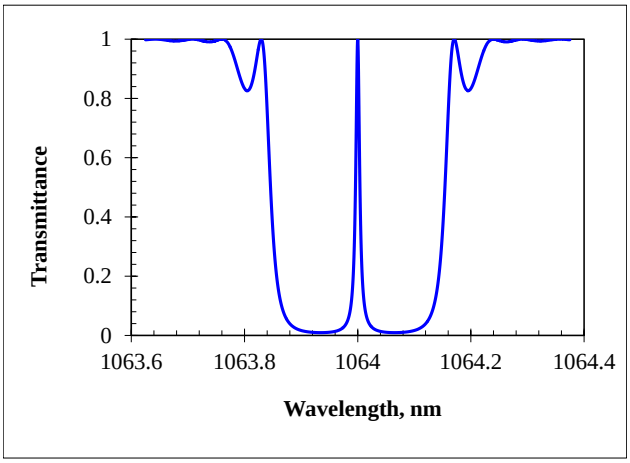

Fig. 133. Theoretical transmission spectrum of a MVBG with transmission bandwidth of 10 pm. Parameters are n1=n2=180 ppm and grating thickness of 5.5 mm.

grating. For gratings discussed here the ratio is on the order of 100 making SVEA valid. Therefore, the grating can be described using a successive application of the results of CWT. The grating is divided into equal sections and the average refractive index modulation (n1) is used in determining the response for each section of grating. As an example, Fig. 133 demonstrates a simulation of a MVBG with the following parameters: λ_0 =1064 nm, $\Delta\lambda$= 135 pm, n_1= 180 ppm, n_2=130 ppm and grating total length of 5.5 mm. The full width at half maximum (FWHM) of the resulting resonance is 8 pm. We also made design curves for the spectral width of an MVBG and they demonstrate that it is possible to achieve spectral widths even well below 10 pm using parameters typical for volume Bragg gratings in PTR glass. With the capability of designing MVBGs we moved towards their recording and implementation as narrow band transmitting filters.

The recording setup for an MVBG is essentially the same as for a uniform VBG. A single grating is recorded into the media, then the resonant wavelength is changed by modifying the angle of convergence between the recording beams and a second grating is recorded into the same depth. The source for our recording setup is a single frequency He-Cd laser, hence the period of the recording pattern is changed by adjusting the angles of convergence while keeping the direction of bisector constant. To record a resonant wavelength shift of 100 pm at 1064 nm, a shift in angle

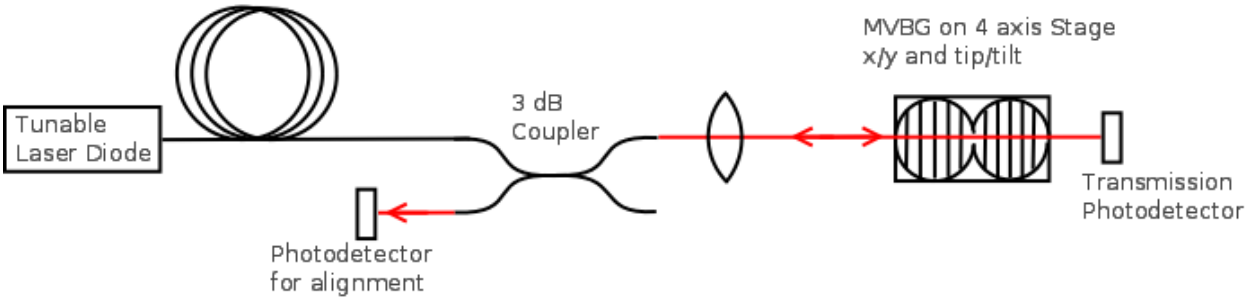

Fig. 134. The setup for characterization of the spectral transmission of an MVBG with a high resolution tunable laser. A 3 dB coupler is used to determine alignment by monitoring the intensity of back reflection from the gratings rejection band.

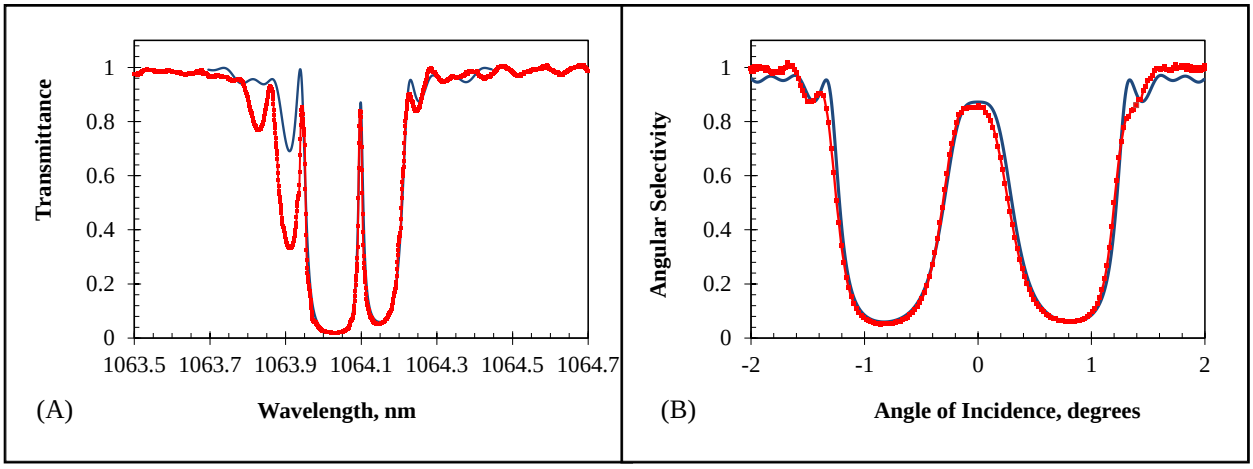

Fig. 135. Transmission spectra (A) and angular selectivity (B) of a moiré Bragg grating in PTR glass. Length = 5.3 mm, refractive index modulation n1=126 ppm, n2=234 ppm. Blue – theory, red – experiment.

of 9.4 arc seconds is required. The recorded grating contains the envelope in an undefined state. It is necessary to process the grating after recording to accurately determine the location of the zeros in the envelope pattern. This is accomplished by scanning the transverse axis (z axis) of the grating with a probe beam such that the grating acts as a transmission Bragg grating. The dips in the diffraction efficiency at these locations can be correlated to the points of zero envelope magnitude. From identifying these locations, the grating can be cut and polished such that the final grating contains a single envelope zero located in the center of the grating.

The transmission spectrum of the grating was measured using a tunable laser diode with sub-picometer resolution. The experimental setup is shown in Fig. 134. A fiber coupled tunable laser was sent through a 3 dB coupler. One arm probed the grating with a collimated beam, while a power detector measured the transmission through the grating. The unused arm of the coupler was used to monitor back reflection from the sample to ensure that the grating is characterized at normal incidence. The resultant transmission spectrum of the MVBG is shown in Fig. 135. It shows experimental data as well as a theoretical fit using matrix CWT. The width of the transmission peak is 15 pm FWHM and rejection band is 254 pm FWHM. The filter has a rejection ratio of -13 dB and the spectrum shows a distinct asymmetry about the resonant peak. It was found that this asymmetry is primarily due to a mismatch in the recording dosages. By inducing a mismatch in the strength of the refractive index modulation (RIM) we are able to

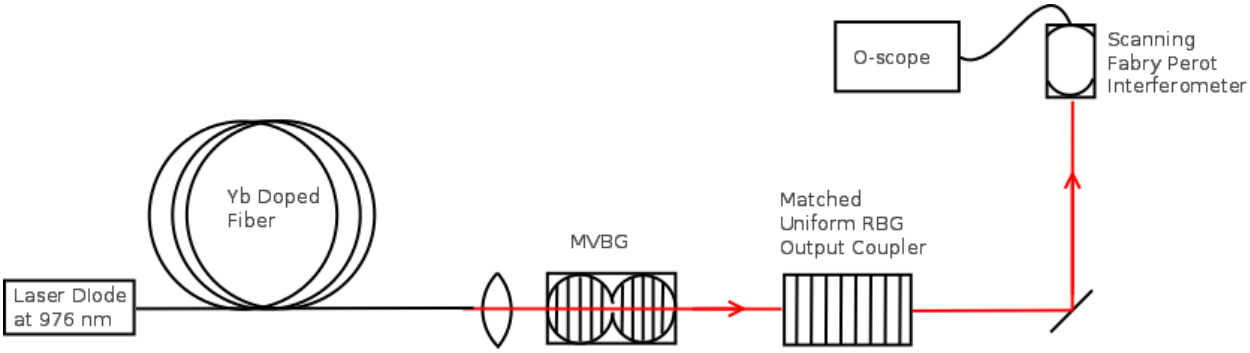

Fig. 136. A fiber laser with free space section of cavity incorporating a MVBG for mode selection. A scanning Fabry Perot interferometer is used to determine the longitudinal modes present in the laser.

predict the level of error in our exposure and model the results. The mismatch in RIM is 50 ppm from the specified value. Excellent coincidence between experimental results and the theory can be seen in the region of the pass band and rejection band of our filter.

The narrow band transmission of a MVBG can be used for the generation of single frequency laser using an intracavity MVBG (Fig. 136). We implemented a laser cavity consisting of an Yb doped fiber as the gain medium. The output was coupled into the free space cavity where the MVBG was placed to achieve longitudinal mode selection. A uniform RBG with 30% reflectance was used as an output coupler. The spectral width of the output coupler was selected to match the spectral width of the MVBG such that only the modes within the resonance peak of the MVBG were allowed to resonate in the cavity. The longitudinal mode structure of the laser was characterized using a scanning Fabry Perot interferometer (SFPI). The cavity length of the laser was approximately 1.5 m resulting in a longitudinal mode spacing of 120 MHz (0.5 pm). The spectral output of the laser with an intracavity MVBG was measured using an SFPI with a resolution of 7.5 MHz and a free spectral range of 1.5 GHz. Figure 137 shows the spectrum with and without the MVBG placed in the cavity. Without the filter in place, the modes fill the FSR of the etalon. The 15 pm bandwidth of the filter effectively acts as a filter with bandwidth around 2 pm due to only a very narrow region in the transmission peak of Fig. 135 being above lasing threshold. The filter thus allows selection of three longitudinal modes from the spectrum.

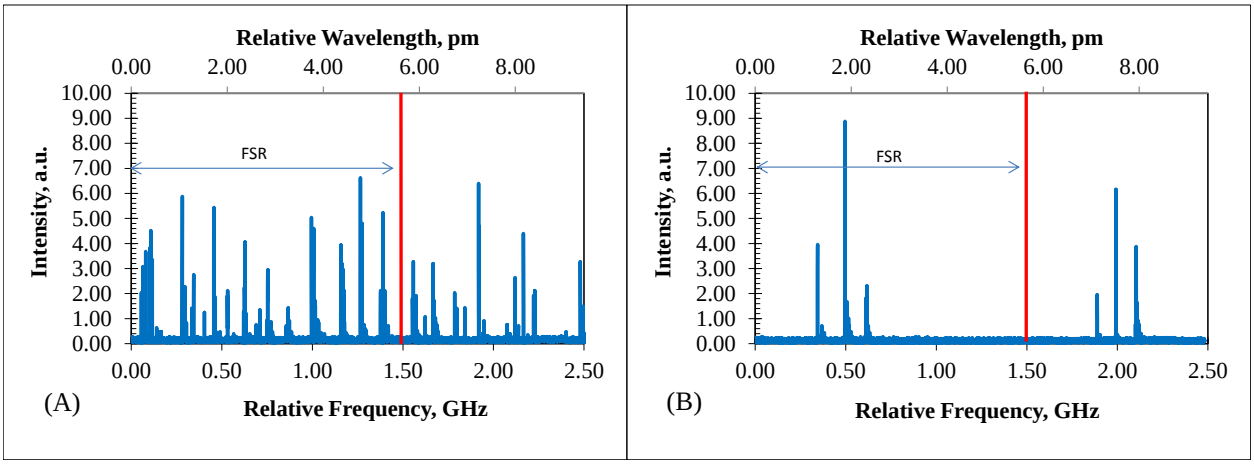

Fig. 137. The spectrum of the laser depicted in Fig. 136 as measured by scanning Fabry-Perot etalon. (A) - no MVBG; (B) - MVBG in the cavity.

In conclusion, a moiré volume Bragg grating with spectral FWHM of 15 pm is demonstrated with good correspondence to theory. The application of the MVBG into a laser cavity shows the potential for generating high power single frequency output. Given the current laser configuration, the number or resonating longitudinal modes is reduced to three. The primary benefit of this mode selection device is the simple alignment procedure for free space laser cavity systems. Further work will focus on fabrication of MVBG grating devices with higher transmission throughput.

3.5. Multipass gratings

Reflecting volume Bragg gratings (VBGs) in photo-thermo-refractive (PTR) glass have been used extensively in laser development and applications in recent years. One of the reasons for the success of these devices is excellent homogeneity of PTR which allows fabrication of VBGs with thicknesses on the order of centimeters. Utilizing coupled wave theory to predict the performance of both reflecting and transmitting volume Bragg gratings shows that the spectral acceptance is inversely proportional to the material thickness. Therefore, excellent narrow band filtering can be achieved using a highly homogeneous holographic recording material such as PTR glass. These thick gratings are capable of narrowband spectral filtering with bandwidths as narrow as tens of picometers in the near IR. The narrowband filtering that is produced by a reflecting VBG is a notch filter with resonant light being reflected and light outside of the resonance band being transmitted. For filter applications that require high levels of isolation between wavelengths, it is necessary to have steep roll-off at the filter edge. Examples of such filters include multiple micro-ring cavities which produce filter roll-offs of around 50-100 dB/nm for optical communications. These filters are able to create a high signal-to-noise (SNR) between the resonant light and the out-of-band light. So while VBGs are capable of excellent narrowband filtering, the spectral sidelobes that are inherent to the device do not provide steep filter roll-off. We present several methods for increasing the roll-off of a narrowband reflecting VBG filter within a monolithic device to produce roll-off slopes >100 dB/nm.

The proposed devices will produce very low levels of reflection outside of the reflection band due to the suppression of RBG sidelobes. In order to measure these low power levels, the measurement system depicted in Fig. 138 was used. A tunable laser is sent to the device under test (black box). The filtered light is coupled into a fiber and send to an optical spectrum analyzer (OSA) which acts as a power detector. The OSA is synced to the tunable laser source such that it only measures optical power at the appropriate incident wavelength. This system was chosen because of the good low level detection of the optical spectrum analyzer (Ando AQ6317B). Incorporating a synced tunable laser source allowed us to produce higher incident signal per data point compared to using a broadband source resulting in a significantly higher the SNR for the measurement. Sweeping the tunable laser in discrete steps and measuring the power at the appropriate wavelength on the OSA generates the spectral response of the device under test. This combination was found to produce the best SNR for low level detection given our available equipment.

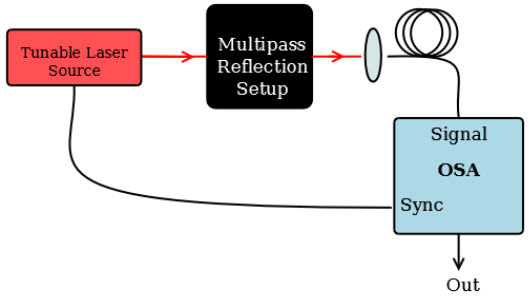

Fig. 138. Measurement system for the detection of low optical powers.

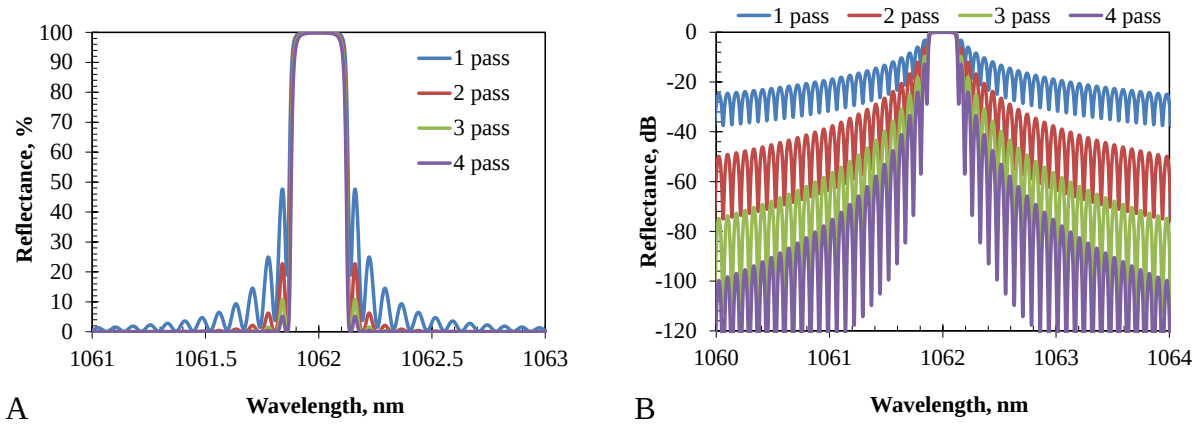

Fig. 139. The reflection spectrum of an RBG after successive reflections. A – reflection coefficient; B - reflectance on a logarithmic scale to show detail of the out-of-band sidelobes.

One usual method for reducing the sidelobes of an RBG is by producing an apodization profile in the grating. To reduce sidelobes further requires more complex apodization profiles than the raised cosine. We propose a simple modification to the two beam holographic recording set up to achieve similar performance without introducing these different types of apodization. This modification creates a wavelength tunable filter with sharp spectral roll off. The fundamental concept of this filter is that by filtering a signal by the same spectral filter multiple times, the sidelobes are decreased dramatically while the reflectance in the resonant bandwidth remains high as demonstrated in Fig. 139. This figure shows the reflection spectrum of a typical RBG with 5 mm thickness and refractive index modulation n_1=320 ppm, designed for a resonant reflection at 1062 nm for 5° angle of incidence. If the incident light is repeatedly reflected from the same RBG, the sidelobes in the spectrum will decrease but the reflectance of the light within the resonant pass band (reflection band) will maintain high efficiency. This effect is more clearly illustrated by looking at the same spectrum on a logarithmic scale. It is clear that the reflection sidelobes extend to wavelengths far outside the reflection band. The use of multiple reflections from the RBG severely lowers the reflectance of this off resonance light and increases the filter roll-off.

In order to generate multiple reflections from an RBG, we propose several schemes shown in Fig. 140. The first scheme employs a single RBG with a mirror to generate multiple passes. A similar scheme uses a second RBG with identical parameters in place of the mirror. Recording matched RBGs can easily be achieved in PTR since the size of the recording substrate is typically large enough to cut multiple RBGs with thickness of ~5 mm out of the same volume. This type of setup has a benefit of adjusting the number of reflections that occur by a relative translation of the two grating as illustrated in Fig. 140c. The final system is a monolithic multipass reflector, shown in Fig. 140d. Two matched gratings are recorded within the PTR glass, spatially separated by a gap and containing entrance/exit windows. Incident light will be reflected between the two gratings multiple times before exiting the device. Because each RBG is identical in period and tilt, the exiting light will be parallel to the incident beam, but shifted in lateral position. The monolithic nature of this device allows the resonant wavelength to be tuned by rotating the device without inducing any angular deviation in the outgoing beam.

The first system that was tested is the RBG/mirror combination shown in Fig. 140a with two reflections from the RBG. The measurement system depicted in Fig. 139 was used to measure the reflection spectrum. The results are shown in Fig. 141 along with the theoretical spectrum from coupled wave theory. The reflection spectra of single pass reflections from two points on the RBG where actual reflections occur are included for reference. The insertion loss is low at 0.1 dB. The dashed line follows a slope of -65 dB/nm.

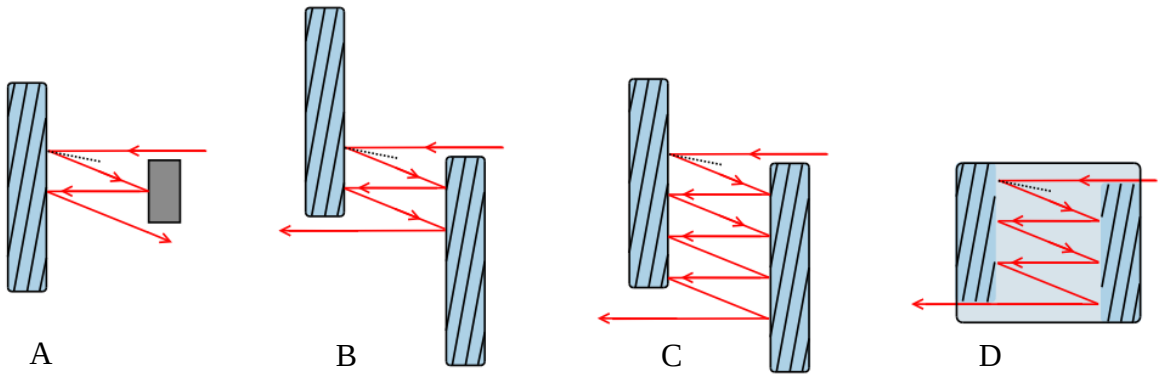

Fig. 140. Schemes for achieving multiple reflections from an RBG. A - a single RBG and a folding mirror; B- double pass matched RBGs whose relative positions controls the number of reflections; C - quadruple pass matched RBGs; D - a monolithic implementation.

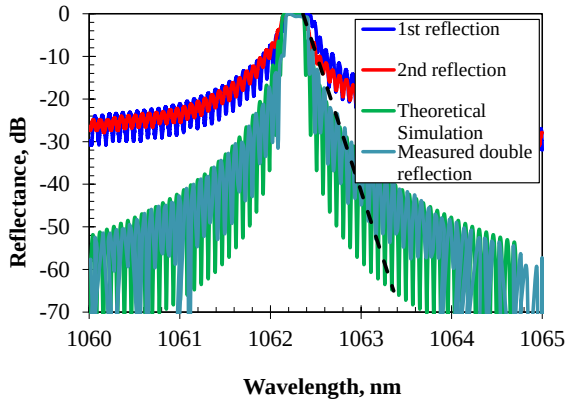

Fig. 141. The double pass reflection spectra of the multipass scheme in Fig. 37a. Theoretical simulation is produced using coupled wave theory. The single pass reflection spectra measured at two locations on the RBG (red and dark blue) are shown for reference.

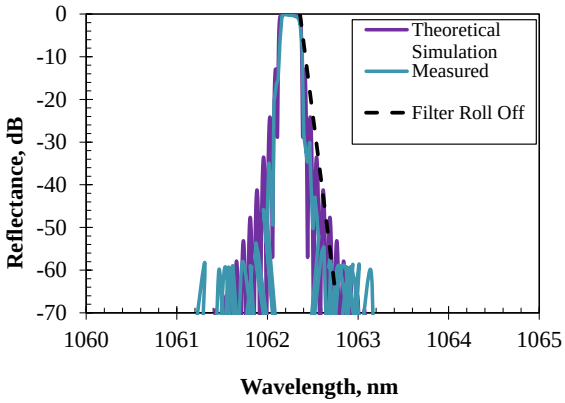

Fig. 142. The reflection spectrum (blue) of the multipass scheme in Fig. 37c with four reflections. Theoretical simulation (purple) is produced using coupled wave theory. The dashed line following the filter roll-off has a slope of -167 dB/nm.

To increase the number of reflections and further reduce the sidelobes, the mirror was replaced with a matching grating, creating the system in Fig. 140b. The reflection spectrum after four passes is shown in Fig. 142 along with the expected spectrum from theory. The out-of-band sidelobes have been suppressed further. The detection limit of the measurement system is reached at approximately -60 dB. While the oscillations of the sidelobes do not show up well in the measured data, the trend of the spectral response follows the simulated spectrum well. The dashed line shows a slope of -167 dB/nm and the system has an insertion loss of 0.2 dB.

In order to produce the monolithic multipass filters in Fig. 37d, a sample of 50×25 mm^2 PTR glass was masked with a piece of aluminum affixed to the surface in order to selectively prevent exposure of the sample at desired locations. The recording beam has diameter of 30 mm and therefore the entire sample was not able to be illuminated by a single exposure. Due to the limitations of the current recording beam size, two separate exposures of the PTR glass with a translation of the sample between exposures were required. Reliable realignment of the sample is difficult and small changes in the period and tilt of the recorded gratings results in small mismatch between the two gratings that will be demonstrated here. Future work into improving the recording system will focus on expanding the recording beam in order to be able to expose an entire 50 mm substrate. The use of an amplitude mask in one of the arms of the recording system would allow interference in only select regions as shown in Fig. 143. The proposed recording method for generating two identical, spatially separated Bragg gratings in the same piece of PTR glass. This requires a sufficiently large beam in order to expose an entire mask. The two gratings would be the part of the same exposure and therefore have identical parameters. This method would remove any relative misalignments of the two RBGs within the device. In lieu of a large aperture recording beams, the current devices are fabricated by using two separate exposures. The PTR sample is masked and translated between exposures to record two separate gratings with similar parameters.

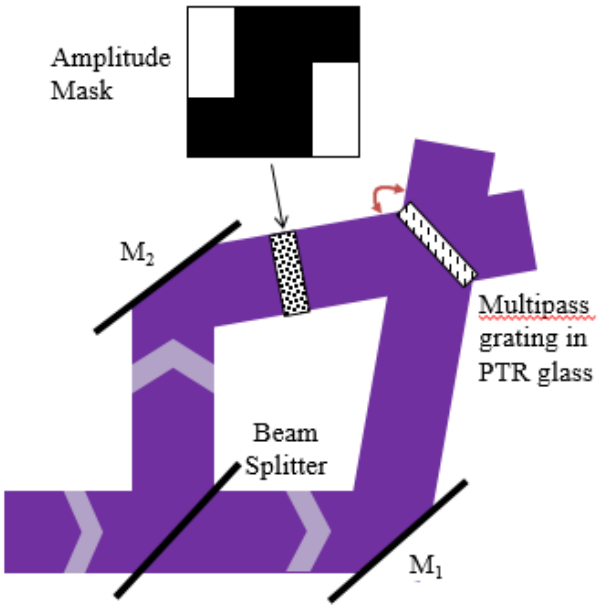

Fig. 143. Recording method for generating two identical, spatially separated Bragg gratings in the same piece of PTR glass.

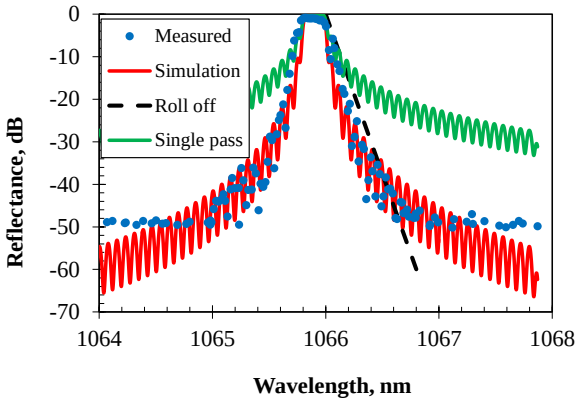

Fig. 144. The reflection spectrum (blue) of the multipass scheme in Fig. 37d with two reflections. Theoretical simulation (red) is produced using coupled wave theory and the effects of a 3 mm Gaussian incident beam. The dashed line following the filter roll-off has a slope of -75 dB/nm.

The first multipass filter is designed to produce two reflections and contains two gratings, each with thickness of 5 mm and a tilt angle of 10° with respect the entrance surface. The spectrum of the double pass device is shown in Fig. 144. The measured data matche well with simulation for a refractive index modulation of 250 ppm. This is compared with a simulation of a single grating of the same parameters. The simulations include the effects of a 3 mm diffraction limited beam.

In order to demonstrate the concept of angle tuning of this monolithic multipass filter device, the setup depicted in Fig. 145 was used. This setup uses a collimated tunable laser source incident on the filter. The transmitted light is analyzed by a photodetector as the wavelength of the source is swept to determine the wavelength of peak transmission. At this resonant wavelength an autocollimator is used to determine angular changes in the transmitted beam. The autocollimator consists of a CCD placed at the focus of a 280 mm focal length lens. This system transforms angular spectrum into linear translation and is insensitive to lateral shifts of the output beam.

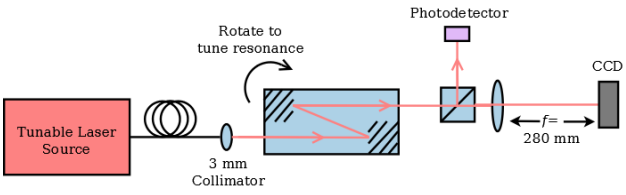

Fig. 145. Testing setup for simultaneous measurements of the resonant wavelength and the output angle from a monolithic double pass grating.

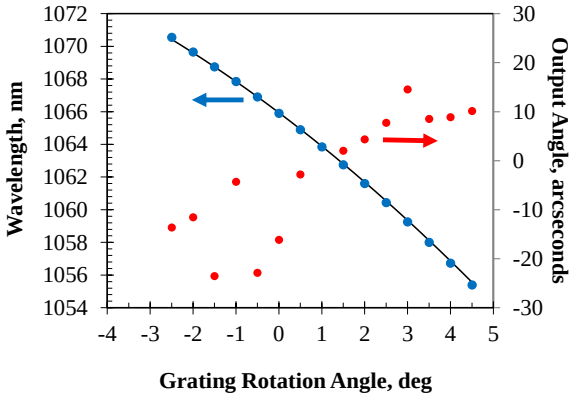

Fig. 146. The effect of angle tuning of the two pass monolithic filter. Wavelength is shown as blue dots and a theoretical fit with solid line. The red dots show the output angle as measured by the autocollimator.

This allows the shift of resonant wavelength to be determined while monitoring any angle shifts that the beam encounters.

The two pass monolithic filter was tested at several different rotation angles to generate the results shown in Fig. 146. The nominal zero angle indicates the angle at which the front facet of the filter is normal to the incident light. The blue dots indicate the shift of the resonant wavelength as a function of angle tuning. The theoretical curve fit to this data follows the expected resonant wavelength of a Bragg grating according to the Bragg condition: $\lambda=2n_0\Lambda\cos\theta$. Where n_0 is the background refractive index (1.489), Λ is the period of the grating (362.4 nm), and θ is the angle within the glass between the incident light and the grating vector (9° for light incident at 0° with respect to the entrance facet). The red dots indicate the shift in angle that occurs to the output light as the device is rotated in angle space. Ideally no shift of the beam would exist, but distortions of the angular spectrum do occur as a result of grating rotation, this causes the distortions of the focused beam at the CCD, resulting in motion of the centroid. The shift of the angle remains within ~30 arc seconds though a 7° angular tuning range of the device, while the resonant wavelength is shifted by 15.2 nm.

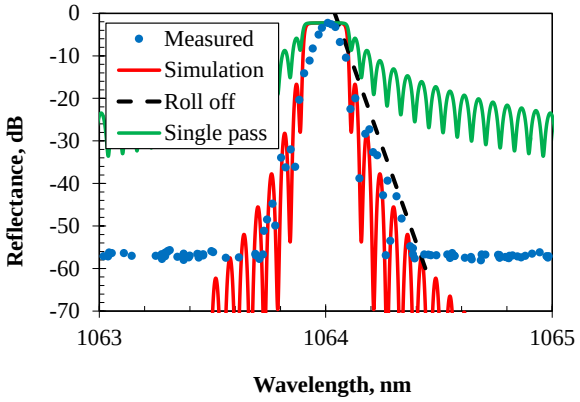

Fig. 147. The reflection spectrum (blue) of the multipass scheme in Fig. 37d with four reflections. Theoretical simulation (red) is produced using coupled wave theory and the effects of a 3 mm Gaussian incident beam. The dashed line following the filter roll-off has a slope of -150 dB/nm.

Along with the ability to reduce sidelobes of the reflection band, these filters are capable of tuning the resonant wavelength of a filter without inducing an angular deviation in the filtered light. This feature is particularly useful for laser application, where the multipass filter can be introduced within the laser cavity. Angular rotation of the filter will tune the wavelength of the output radiation, but will not destroy the alignment of the cavity since the filtered beam is not deviated in angle. In general, this feature is extremely useful for alignment purposes as tuning the filter only introduces a small translation on the order of a few millimeters (depending on design parameters of the multipass grating).

Finally, a four pass monolithic grating was recorded and measured to demonstrate scaling the number of reflections using this method. Each grating has a thickness of 6 mm and a tilt of 5° with respect to the entrance aperture. The spectrum is shown in Fig. 147 along with simulation of the gratings using a refractive index modulation of 250 ppm for each grating and using a Gaussian beam with a 3 mm diameter. The measured results match well with theory, though they do not exhibit the intensity oscillations expected in the sidelobes. The insertion loss of this device is high at -2.2 dB. The roll-off of the filter is -150 dB/nm.

The same concept of multiple sequential diffractions can be applied to transmitting Bragg gratings (TBGs). Compared to RBGs of similar thickness, these filters have roughly order of magnitude broader spectral selectivity. Therefore, TBGs find more application as filters for angular spectra such as in transverse mode selection for laser resonators. For this type of application, it is necessary to match the angular selectivity of the TBG to the zeroth order mode of the resonator. By removing the sidelobes of the TBG through multipass diffraction, the angular selectivity of a TBG can match the fundamental mode more closely. To achieve multipass diffraction with TBGs, the system in Fig. 148 is used. A single TBG was recorded and diced into two pieces to create two identical TBG angular filters. The filters are designed to diffract 1064 nm light by 14° when it is incident normal to the surface. The thickness of the filters is 1.45 mm and the refractive index modulation is 380 ppm to give a diffraction efficiency of 95% for a single TBG. These TBGs are aligned parallel to each other such that light resonant with the first grating will also be resonant with the second grating as indicated by the blue ray path. Light that is not diffracted by gratings will follow the red and green arrows with the associated efficiency shown in the angular transmission spectra shown in Fig. 45 (right) for each beam. In comparison to the multipass reflection gratings, this system requires additional TBGs to be introduced in order to scale the number of diffraction passes. The measured angular response is shown in Fig. 149 on a log scale. The measured results from a single diffraction and double diffraction are shown together along with theoretical calculations. The sidelobes are significantly reduced by passing through multiple gratings.

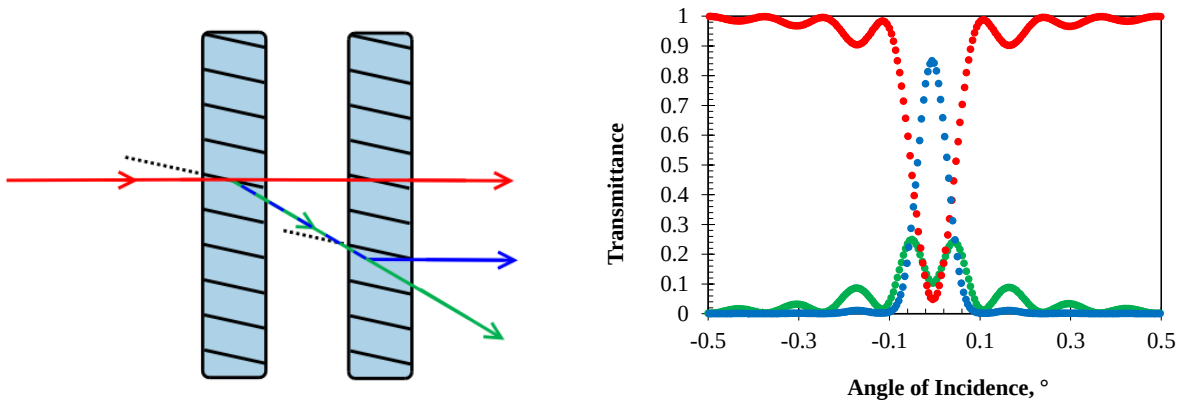

Fig. 148. Angular selector including two matched transmitting Bragg gratings aligned to produce two sequential diffractions of incident light (left). The angular transmission spectra the selector (right). The red arrow and dots – radiation transmitted through both gratings; the green arrow and dots – radiation diffracted by the first TBG and transmitted by the second one; the blue arrow and dots– radiation diffracted by both TBGs. Each grating is 1.45 mm thick with 380 ppm refractive index modulation; for 1064 nm, angle of incidence - 0°, exit angle - 14°.

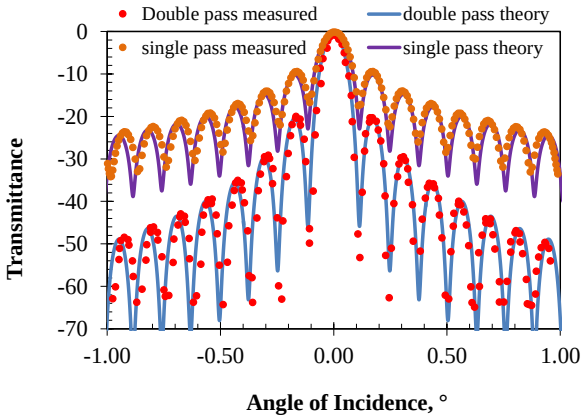

Fig. 149. The angular transmission spectra for single and two sequential TBGs in a log scale.

In conclusion, we present three different geometries for producing multiple reflections from reflecting volume Bragg gratings as well as a multipass diffraction through two matched transmitting volume Bragg gratings. The measurement system used to obtain reflection spectra of each device is sensitive to -60 dB. The various multipass devices are demonstrated producing two or four successive reflections and effectively suppress the spectral sidelobes well below the level of a single reflection from an RBG. The multipass configuration that utilizes two matched RBGs is able to tune the number of reflections by a simple translation of the gratings with respect to each other. This setup produced a filter roll-off of -167 dB/nm with insertion loss of only 0.2 dB. The final type of device that was demonstrated is a monolithic implementation of the two RBG configurations. All alignment of the device is produced during recording; therefore there is no alignment necessary when such a filter is used in practice. Rotation of the filter allows the resonant wavelength to be tuned while the reflections exit the filter parallel to the incident light within 30 arc seconds. This device has been shown with up to four passes and produced a filter roll-off of -150 dB/nm. Finally, the use of multiple filtering was applied to angular filtering using two transmission gratings to reduce the sidelobes of an angular filter. These schemes for producing multiple reflections from a PTR volume Bragg grating allow for narrowband spectral filtering with sharp filter roll-offs, giving a filter with excellent resolution and SNR.

3.6. Holographic phase masks

3.6.1. Encoding phase masks inside of transmitting volume Bragg gratings

Phase masks are important optical elements that have been utilized in a large variety of application areas from imaging to encryption for several decades. While traditional methods of producing phase masks provide elements which are inherently monochromatic, it was previously found that the use of birefringence in subwavelength diffraction gratings enables their partial achromatization. We present here a new method which by encoding phase profiles into volume Bragg gratings, allows these holographic elements to be used as phase masks at any wavelength capable of satisfying the Bragg condition of the hologram. Moreover, this approach enables completely new capabilities, as several encoded phase masks may be multiplexed into a single holographic element without cross-talk while maintaining high diffraction efficiency.

To simplify fabrication and to provide a clear demonstration of the phenomenon we chose to use binary phase profiles, but the approach is fully applicable for multi-level phase masks as well. The holographic phase mask (HPM) utilizes the diffraction characteristics of TBGs, which can diffract up to 100% of a beam into a single order, and can diffract over a broad range of wavelengths by changing the angle of incidence (with the diffraction efficiency depending on the wavelength and strength of the grating). The high angular selectivity of a TBG also allows for several TBGs to be multiplexed into the same element with little to no cross-talk between gratings; each grating is accessed by altering the beam's angle of incidence onto the element. In order to explain the unique properties of the HPMs we note that a Bragg grating is the simplest volume hologram, which, unlike more complex holograms, can diffract multiple wavelengths without distorting the beam profile. By encoding phase levels which cover a macroscopic area, the HPM acts locally as a standard TBG with a given phase shift. Thus the HPM will diffract in the same manner as a standard TBG except at the relatively small number of phase discontinuities, and the diffracted beam's phase profile will match the encoded phase level profile regardless of incident wavelength.

We demonstrate HPMs that, though recorded at 325 nm, preserve a binary phase profile in the diffracted beam at wavelengths beyond 1 μm and can operate over a bandwidth larger than 500 nm. These elements are used to perform fiber mode conversion and simultaneous TEM mode conversion and spectral beam combining.

To encode the phase profile into a TBG, consider the holographic recording setup in Fig. 150. Here a multi-level phase mask has been placed into one arm of a two-beam interference system (the object beam), where the two beams interfere at an angle θ relative to the normal of the holographic sample. The

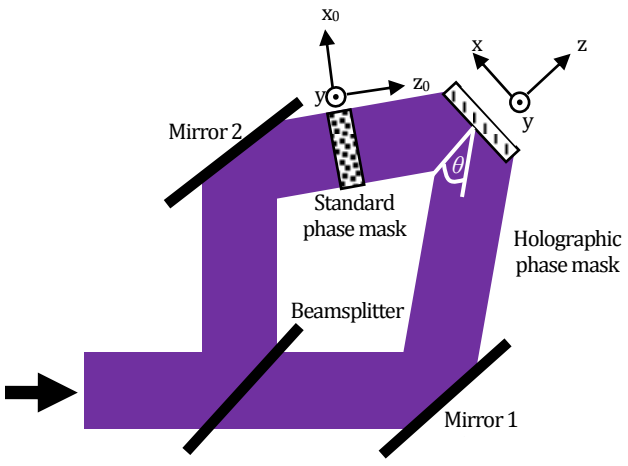

Fig. 150. Experimental setup for holographic phase masks recording. Recording wavelength - 325 nm.

two-beam interference equation describing the fringe pattern in the sample is then

$$I = I_1 + I_2 + 2\sqrt{I_1 I_2}\cos\left(\left(\vec{k}_1 - \vec{k}_2\right)\cdot\vec{r} + \varphi(x,y,z)\right) \qquad (1)$$

where I is the intensity, $\vec{k}_i$ is the wavevector for each beam, and φ is the phase variation introduced by the phase mask after the object beam has propagated to the sample. Since the phase mask's profile is located in the x_0-y plane, which is rotated with respect to the sample plane, the recorded phase profile will generally be different than the phase mask. However, if the thickness of the sample, the axial distance between the phase mask and the sample, and θ are small then $\varphi(x,y,z) \approx \varphi(x,y) \approx \varphi(x_0,y)$ so the recorded phase profile will be approximately the same as that of the original phase mask. The recorded hologram will have a refractive index profile of

$$n(x,y,z) = n_0 + n_1\cos\left(\vec{K}\cdot\vec{r} + \varphi(x,y)\right), \qquad (2)$$

where n_0 is the background refractive index, n_1 is the refractive index modulation, and $\vec{K} = \vec{k}_1 - \vec{k}_2$ is the grating vector.

Once the hologram is recorded, it is placed in a system with some probe beam to be diffracted, which may or may not have the same wavelength as the recording beams. If the probe beam is incident at or near the Bragg condition [87], the total electric field will satisfy the scalar Helmholtz wave equation,

$$\nabla^2 E - k_p^2 n^2 E = 0 \quad . \qquad (3)$$

Here k_p is the wavenumber of the probe beam. The Helmholtz equation has a general solution of the form:

$$E(x,y,z) = A(x,y,z)e^{\left(-i\vec{k}_p\cdot\vec{r}\right)} + B(x,y,z)e^{\left(-i\vec{k}_d\cdot\vec{r}\right)}, \qquad (4)$$

where A and B are the complex amplitudes of the transmitted and diffracted waves, respectively, and $\vec{k}_d = \vec{k}_p - \vec{K}$ is the wavevector of the diffracted beam. Inserting Eq. (4) into Eq. (3) results in a set of coupled wave equations between the amplitudes A and B. Kogelnik [20] has solved these equations when A and B depend solely on the axial distance z (homogenous gratings). However, when a phase mask is placed in the recording system, the phase term is not a constant across the entire hologram aperture and consequently it cannot be assumed that this one-dimensional dependence will still hold. In this particular study we are only interested in probe beams that exactly satisfy the Bragg condition. In this case, the coupled wave equations become

[87] H. Kogelnik, "Coupled wave theory for thick hologram gratings," Bell Syst. Tech. J. 48(9), 2909–2945 (1969).

$$\frac{1}{k_p}\left(k_{p,x}\frac{\partial A}{\partial x}+k_{p,y}\frac{\partial A}{\partial y}+k_{p,z}\frac{\partial A}{\partial z}\right)=-i\kappa e^{-i\varphi(x,y)}B$$
$$\frac{1}{k_p}\left(k_{d,x}\frac{\partial B}{\partial x}+k_{d,y}\frac{\partial B}{\partial y}+k_{d,z}\frac{\partial B}{\partial z}\right)=-i\kappa e^{i\varphi(x,y)}A \quad . \quad (5)$$

Here $\kappa=\pi n_1/\lambda_0$ is the coupling coefficient of the grating. Note that we have assumed that the second derivatives are negligibly small in the same manner as Kogelnik [87], as we still expect the transfer of energy between the transmitted and diffracted waves to be slow.

We solve the coupled equations numerically by converting Eq. (4) into Fourier space along the transverse dimensions x and y, giving

$$\frac{2\pi i}{k_p}\left(f_x k_{p,x}+f_y k_{p,y}\right)\tilde{A}+\frac{k_{p,z}}{k_p}\frac{\partial\tilde{A}}{\partial z}=\mathcal{F}\left\{-i\kappa e^{-i\varphi(x,y)}B\right\}$$
$$\frac{2\pi i}{k_p}\left(f_x k_{d,x}+f_y k_{d,y}\right)\tilde{B}+\frac{k_{d,z}}{k_p}\frac{\partial\tilde{B}}{\partial z}=\mathcal{F}\left\{-i\kappa e^{i\varphi(x,y)}A\right\} \quad . \quad (6)$$

where $\tilde{A}$ and $\tilde{B}$ are the Fourier transforms of A and B, respectively, and f_x and f_y are the spatial frequencies along the x and y axes, respectively. To solve these equations we split the propagation and energy transfer between the waves into two discrete steps and successively propagate and transfer energy between waves over several small propagation steps. To calculate the propagation of the beam, the right side of Eq. (6) is assumed to be zero. In this case the Fourier amplitudes will have a solution of the form:

$$\tilde{A}\left(f_x, f_y, z+\Delta z\right)=\tilde{A}\left(f_x, f_y, z\right)e^{\left(-i\frac{2\pi}{k_{p,z}}\left(f_x k_{p,x}+f_y k_{p,y}\right)\Delta z\right)}$$
$$\tilde{B}\left(f_x, f_y, z+\Delta z\right)=\tilde{B}\left(f_x, f_y, z\right)e^{\left(-i\frac{2\pi}{k_{d,z}}\left(f_x k_{d,x}+f_y k_{d,y}\right)\Delta z\right)} \quad . \quad (7)$$

Note that this only exact in the case where the right side of Eq. (6) truly equals zero but for small (~100 nm) propagation steps this is a reasonable approximation. To account for energy transfer we piecewise integrate the right side of Eq. (5) with the Euler method and add it to the inverse Fourier transform of Eq. (7):

$$\begin{aligned}A(x,y,z+\Delta z)&=\mathcal{F}^{-1}\left\{\tilde{A}\left(f_x, f_y, z+\Delta z\right)\right\}\\&\quad -i\kappa e^{-i\varphi(x,y)}B(x,y,z)\Delta z\\B(x,y,z+\Delta z)&=\mathcal{F}^{-1}\left\{\tilde{B}\left(f_x, f_y, z+\Delta z\right)\right\}\\&\quad -i\kappa e^{i\varphi(x,y)}A(x,y,z)\Delta z\end{aligned} \quad . \quad (8)$$

Calculations indicate that for a propagation step size of 100 nm our numerical method conserves energy to within 0.01% after propagating the coupled waves through the entire system, which is sufficient for the phase profiles discussed here.

Numerical simulations were performed to determine the diffracted beam phase profile and diffraction efficiency of an HPM in the case where a binary phase profile is encoded. The numerical method described previously was first applied to simulate a standard TBG with an 8 μm period, a refractive index modulation of 250 ppm, and a thickness of 2 mm. The probe beam with a wavelength of 1064 nm is incident at the Bragg angle and propagates in the *x*-*z* plane (Fig. 151(a)). Using a propagation step size of 100 nm, the simulated diffraction efficiency of this TBG is 99.13%, which is consistent with the peak diffraction efficiency of a homogenous TBG described by Kogelnik theory. A π phase step was then introduced to the grating at a recording wavelength of 325 nm. This binary step was first introduced along the x-axis and then along the *y*-axis to determine if there would be any orientation-dependent variations in diffraction efficiency or phase profile.

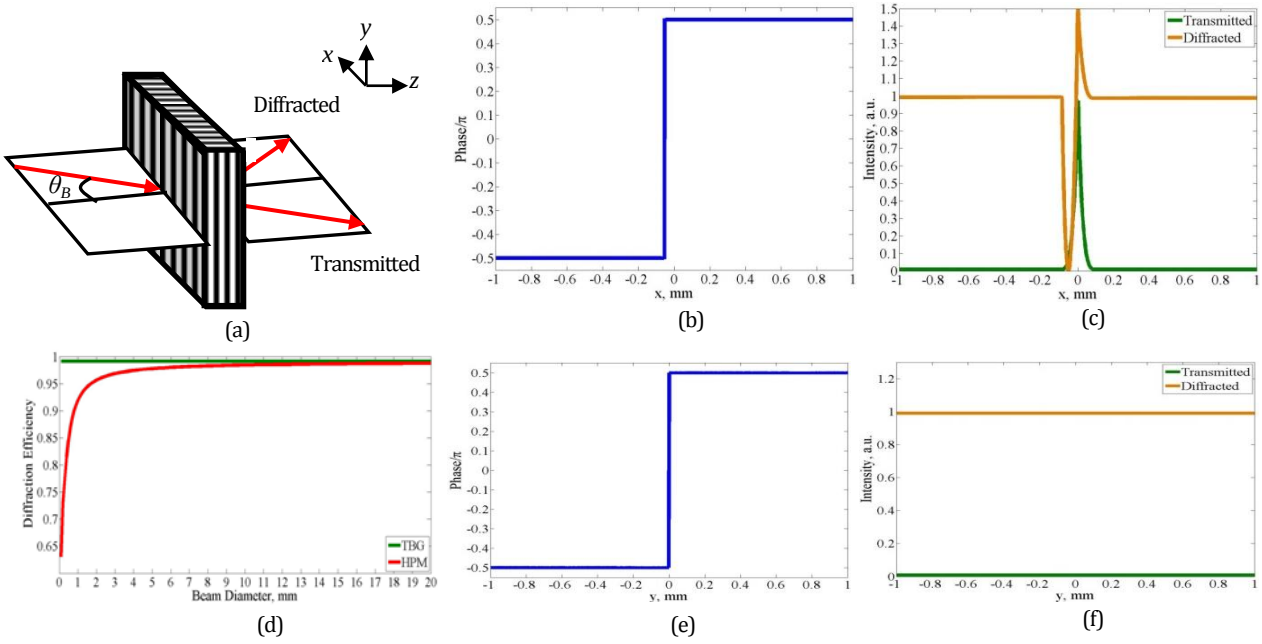

Fig. 151. (a) A probe beam incident at the Bragg angle is diffracted by an HPM. (b) The diffracted beam phase profile, (c) the local transmitted and diffracted intensity of a plane wave, and (d) the diffraction efficiency of an HPM as a function of beam diameter when a binary phase dislocation is encoded along the *x*-axis. Here the coordinate origin is the center of the front surface of the HPM. (e) The diffracted beam phase profile and (f) the local transmitted and diffracted intensity when a binary phase dislocation is encoded along the *y*-axis.

As shown in Fig. 151(b), the diffracted beam contains a π phase shift when the phase step is introduced along the *x*-axis. The location of the phase step is slightly offset from the origin due to the propagation of the beam through the sample. For the local intensities of the transmitted and diffracted waves, shown in Fig. 151(c) for a plane wave, an increase in transmitted energy and a general decrease in diffracted energy is observed at the phase discontinuity. This is unsurprising, as any region of the probe beam crossing the phase discontinuity will not be able to satisfy the Bragg condition at that point. This inability to satisfy the Bragg condition locally will result in a decrease in diffraction efficiency (which is the total energy in the diffracted beam divided by the total energy in the incident beam) that is dependent on the fraction of the beam energy which crosses the phase discontinuity. However, as shown in Fig. 151(d), this loss in

efficiency becomes very small with increasing beam size and the diffraction efficiency of an HPM will asymptotically approach the diffraction efficiency of a standard TBG as the beam diameter approaches infinity.

When the phase discontinuity is oriented along the y-axis, the phase profile of the diffracted beam will also have a π phase shift, as shown in Fig. 151(e). Here the phase discontinuity is located at the origin because the probe beam has no component propagating along the *y*-axis. This zero *y*-axis component also results in only a single infinitesimal fraction of the beam ever encountering the phase discontinuity, giving constant local intensities for the transmitted and diffracted waves, as shown in Fig. 151(f). The simulated diffraction efficiency of the HPM in this case is constantly 99.12% regardless of beam diameter, and given that there is a 0.01% uncertainty in energy conservation in the numerical method we conclude that the diffraction efficiency is identical to a standard TBG. These two cases indicate that the diffracted beam from an HPM will always inherit the phase profile of the original phase mask, and will have some orientation-specific decrease in diffraction efficiency that is dependent on beam size and largely negligible for most typical beam diameters. Repeating these cases for other wavelengths at their respective Bragg angles show similar results, with the diffraction efficiency of both the TBG and HPM changing with respect to wavelength. Thus the HPM will maintain the diffraction characteristics of a TBG while preserving the desired phase profile over the whole bandwidth of possible Bragg wavelengths, a remarkable feature in striking contrast to the monochromatic operation of conventional phase masks.

A complete set of experiments have been performed using a HPM recorded in a 1.97 mm-thick photo-thermo-refractive (PTR) glass sample as illustrated in Fig. 150. To fabricate the HPM a four-sector binary phase mask designed for the recording wavelength of 325 nm was placed in one arm of the setup and the interference angle was chosen to give an 8 μm grating period.

In order to directly and accurately compare the diffraction efficiency of the HPM with that of a standard TBG, we fabricated a sample containing both an HPM and a homogeneous TBG in the same volume of PTR glass. This was done by recording an HPM and then removing the phase mask from the object beam and rotating the PTR glass sample without lateral shifting to record a tilted TBG with the same recording dosage. Recording both elements in the same volume ensured that the local refractive index change and any sample inhomogeneities would be shared

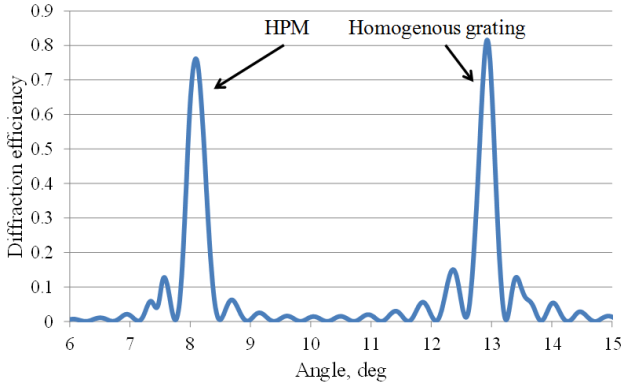

Fig. 152. Diffraction efficiency angular spectrum of an HPM and a homogeneous grating.

between the elements and demonstrated a new opportunity for holographic phase mask multiplexing. As shown in Fig. 152, the diffraction efficiencies of each element are approximately the same, showing good agreement with theoretical predictions. Note also that there is no cross-talk between the two multiplexed holograms, demonstrating that the HPM preserves the narrow angular acceptance of standard TBGs.

3.6.2. Mode conversion by holographic volume phase masks

As demonstrated previously, a four-sector binary phase mask can itself be used as an optical mode converter when the probe beam center is properly aligned with respect to the phase steps. As shown in Fig. 153(a), the expected far field intensity profile for a beam passing through the center of a four-sector binary mask consists of a four-lobed clover pattern. However, effective mode conversion only occurs at the design wavelength, which for our mask is 325 nm. Here, we report a series of experiments to test the theoretical predictions of HPM multi-wavelength operation presented above. If the encoded binary phase steps are indeed transferred to the probe beams diffracted from the HPM at their respective Bragg wavelengths, the HPM should simultaneously act as a diffraction element and a mode converter when the beams are correctly aligned to the phase steps. To perform this investigation we recorded the far field intensity distributions of diffracted beams at multiple wavelengths by imaging them onto a CCD camera using a 500 mm lens.

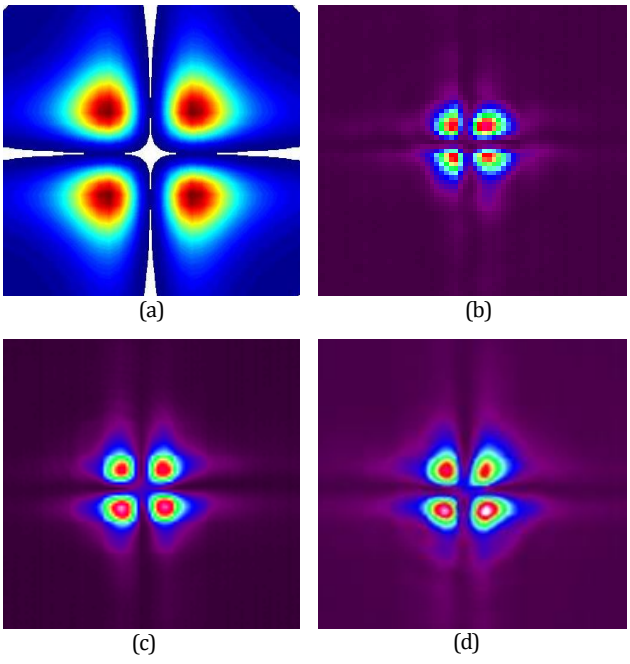

Fig. 153. (a) Simulated far field profile of a beam after passing through an ideal four-sector binary mask and the diffracted beam from a four-sector HPM at (b) 632.8 nm, (c) 975 nm, and (d) 1064 nm. The sizes are not to scale.

Three beams (3 mm in diameter at $1/e^2$) at wavelengths in the visible and the infrared regions were applied to study the wavelength dependence of diffraction and mode conversion using the

HPM. As shown in Fig. 50(b-d), for the three very different Bragg wavelengths (632.8 nm, 975 nm, and 1064 nm), the diffracted beam profiles exhibited the predicted four-lobed pattern. This clearly confirms our initial thesis that the binary phase profile is being preserved in the diffracted order for an extremely broad range of wavelengths.

To further verify the binary phase step in the diffracted beam, an interferometric experiment was developed and is presented in Fig. 154(a). A 1064 nm laser was collimated and split into two arms of a Mach-Zehnder interferometer. The HPM was placed in one arm, rotated so that the beam incident on the HPM was at the Bragg angle, and the two beams were recombined and imaged onto a camera. In this experiment, the beam incident on the HPM was horizontally offset from the center so that the HPM acted as a two-sector binary mask. As shown in Figs. 51(b) and 51(c), the interference fringes of the upper and lower lobes produced by the HPM have a relative π phase shift, confirming that the encoded phase profile is preserved in the diffracted beam at wavelengths far from the recording wavelength.

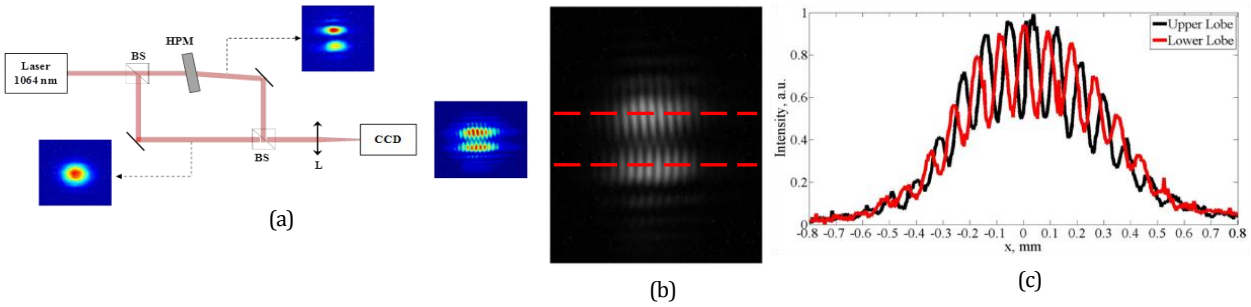

Fig. 154. (a) Mach-Zehnder interferometer measuring the relative phase between the upper and lower lobes of the diffracted beam from the HPM. (b) The resulting interferogram with markers indicating two line cuts, and (c) the line cuts of the two lobes compared to each other, showing a relative π phase difference. Note that the line cuts do not appear to be completely out of phase due to the slight tilt of the fringes, which can be seen in (b).

Beam combining offers the potential to scale the power of laser systems beyond the limits of individual lasers. Currently, spectral beam combining and coherent beam combining are the two dominant methods in the effort to reach multi-kilowatt diffraction-limited beams. In parallel, as discussed above, fibers that support high order modes (HOMs) are considered to overcome power limitations of fiber lasers and amplifiers. Therefore, the combination of several HOM beams from different lasers into one high-power fundamental mode beam suggests itself as a power scaling approach. Here we describe a method to accomplish this task by taking advantage of the mode-converting capabilities of HPMs.

While the ability of HPM elements to perform mode conversion is not unique, what is unique is the ability to simultaneously convert multiple beams into different modes while combining them into a single beam. As previously demonstrated it is possible to angularly multiplex several HPMs or gratings into a single element. To perform beam combining, we utilize the same approach used in multiplexed volume gratings, where the periods and tilts of each grating are adjusted so that probe beams of different wavelengths and angles of incidence will diffract into the same channel. Here we encode each grating with the appropriate phase profile so that each grating will also simultaneously perform mode conversion. To demonstrate this we created two

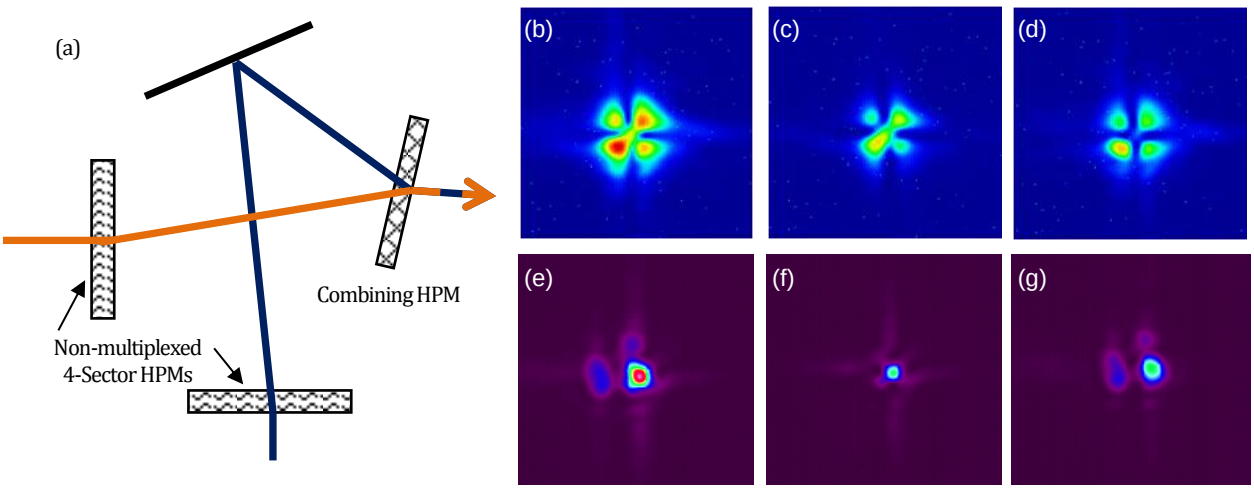

Fig. 155. (a) A multiplexed four-sector HPM spectrally combines two beams at 1061 and 1064 nm. (b) If the initial four-sector HPMs are removed from the system it combines two Gaussian beams while simultaneously converting them to the TEM_{11} mode. The 1064 nm beam (c) and 1061 nm beam (d) can also be converted separately. (e) If the initial four-sector HPMs are included in the system then the Gaussian beams are converted to the TEM_{11} mode and then reconverted back to a Gaussian beam. The reconverted beam profile closely matches the sum of the individual profiles at (f) 1064 and (g) 1061 nm.

free-space converting/combining systems, illustrated in Fig. 155(a), where 1061 and 1064 nm beams are incident upon a multiplexed four-sector HPM. In the first combining/converting system the original Gaussian beams were incident on the combining HPM without any additional phase elements added to the system, resulting in spectrally combined TEM_{11} modes. The second system added two four-sector HPMs to each beam, converting each beam to the TEM_{11} mode, and subsequently reconverting them to the fundamental mode while spectrally combining them.

The far field intensity profile of the combined TEM_{11} beam in the first setup, shown in Fig. 155(b), shows good beam combination and conversion from the Gaussian mode. Note that the differences between the 1064 and 1061 nm far field profiles in Fig. 155(c-d) are due to different collimations between the beams rather than to a poor HPM conversion efficiency. The conversion from the TEM_{11} mode to the fundamental mode in the second setup, shown in Fig. 155(e), is likewise demonstrated. While there are some wings remaining in the combined beam this is predominately a limitation imposed by using HPMs as the initial converters, which creates increased alignment challenges, as seen in the individual beam profiles (Fig. 155(f-g)). Nevertheless, we have demonstrated that HPMs may be used for complex beam transformation-combination schemes.

Thus, we have successfully demonstrated that binary phase profiles may be encoded into transmitting volume Bragg gratings (TBGs) to form holographic phase masks (HPMs), and that for any probe beam capable of satisfying the Bragg condition of the hologram the binary phase profile will be present in the diffracted beam. These holographic phase masks may be used to simultaneously diffract and convert both free space and fiber modes. They can also be multiplexed for beam combining in the same manner as homogenous multiplexed TBGs are used while simultaneously converting the incident beams into a desired mode. This integration of beam combining and mode conversion at multiple wavelengths opens new optical design spaces

in application areas such as high power beam combining or mode multiplexing in optical communication systems.

3.6.3. Achromatic phase masks

Optical phase masks have been used for various applications like encryption, beam shaping, mode conversion, and imaging based on the physical phenomenon of interference. The most common approach of making phase masks is based on varying the optical path length in certain areas of the phase mask. In order to produce the changes in path length, manufactures would generate a contoured surface in an optical material or generate a change in refractive index in photosensitive material. Consequently, since these phase shifts are based on changing optical path length the elements are only effective for a specifically designed wavelength. Previously we showed that it was possible and effective to encode stepped phase masks into transmitting Bragg gratings in photo-thermo-refractive (PTR) glass[88]. These holographic phase masks (HPMs) can successfully give a phase shift and achieve high diffraction efficiency (based on wavelength and the grating strength) for a broad range of wavelengths by tuning the element to the grating's Bragg condition for each discrete wavelength. In order to truly achromatize the HPM we present here an approach using the combination of surface diffraction gratings with a HPM to dispose of the need for angle tuning. In this paper we demonstrate the performance of a HPM paired with surface gratings as achromatic phase element for successful mode conversion over a range of 300 nm.

The holographic phase mask proof of concept was presented described above, where holograms of a four-sector mode converting mask (chosen to give a binary phase shift along the horizontal and vertical axes in a single element) were recorded using a Mach-Zehnder-type recording system in a 1.97 mm-thick photo-thermo-refractive (PTR) glass plate (Fig. 150). The holographic phase mask was examined in the far field (achieved by focusing the beam with a 500 mm lens) at multiple wavelengths in the visible and the infrared regions using a 3 mm in diameter probe beam to determine the wavelength dependence of mode conversion. In all cases the diffracted profile exhibited the same four-lobed pattern.

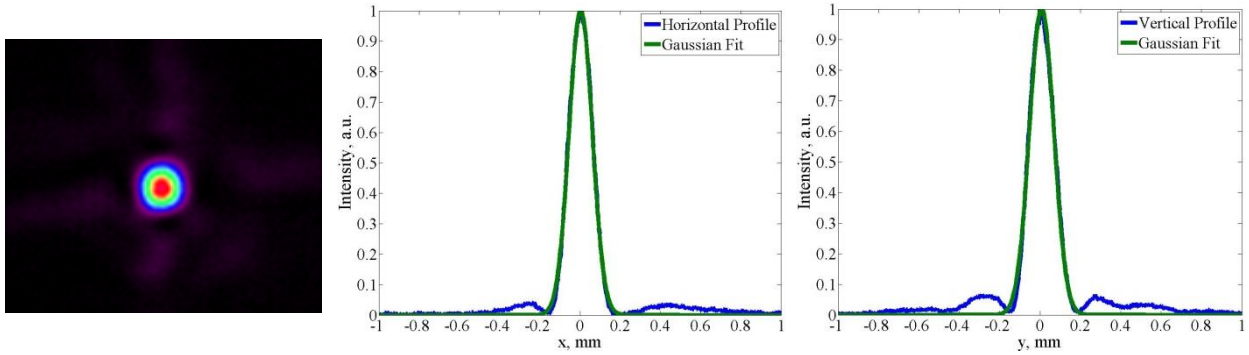

(a) (b) (c)

Fig. 156: (a) Far field pattern of a beam converted from a higher order mode to a Gaussian profile. (b) Horizontal and (c) vertical cross sections of the beam indicate that the central spot is nearly diffraction limited.

[88] SeGall, M., Divliansky, I., Jollivet, C., Schülzgen, A., Glebov, L., "Simultaneous laser beam combining and mode conversion using multiple volume phase elements," Proceedings of SPIE 896050 (2013).

The mode converting ability of the phase masks is of course not limited to converting a Gaussian beam to a higher order mode; it is also possible to convert from a higher order mode to a Gaussian profile. To demonstrate this, two 4-sector mode converting holographic phase masks were aligned so that a 3 mm Gaussian beam at 1064 nm was incident on the first mask and the diffracted (converted) beam from this mask was incident on the second converter. This doubly converted beam was then focused by a 500 mm lens to achieve the far field profile. As shown in Fig. 156a, the far field profile is a Gaussian spot with some low-energy side lobes. Cross sections of the beam, shown in Fig. 156b and 156c, were fitted with Gaussian functions to determine the size of the main spot relative to a diffraction-limited spot. The fits indicate that the spot size along the horizontal axis is 228 μm, nearly identical to the diffraction-limited spot size of 226 μm, while the spot size along the vertical axis is 240 μm, which is close to diffraction-limited. The wings are caused by the finite transition regions at the boundary between the different grating phases and can be reduced by reducing the size of the transition regions in the original phase mask used for recording as well as placing the phase mask closer to the sample during recording.

True achromatization of HPMs can be achieved with the concept of pairing the Bragg grating with two surface gratings[89]. According to the grating dispersion equation (Eq. 1), a surface grating with a given period (Λ_{SG}) will diffract normally incident light an angle (θ) in different orders as a function of wavelength (λ).

$$\Lambda_{SG} \sin\theta = m\lambda \quad (1)$$

As well, based on coupled wave theory[42], a VBG will diffract light highly efficient at the Bragg condition Eq. 2. Under this condition light is incident and diffracted at the Bragg angle (θB), and diffraction efficiencies for these gratings can be as efficient as 100%.

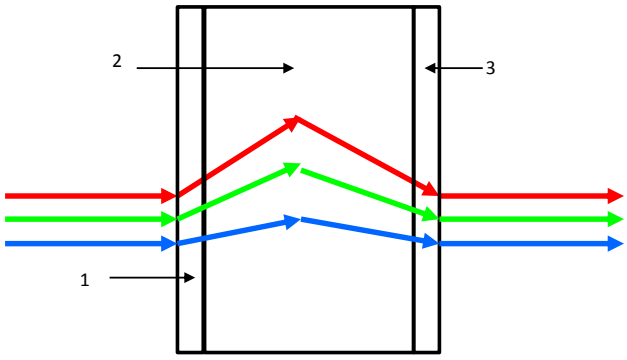

Fig. 157. Concept of using surface gratings pairs to meet the Bragg condition for various wavelengths regardless of angle tuning. 1 – entrance surface grating, 2 – volume Bragg grating, exit surface grating.

[89] L. Glebov, V. Smirnov, N. Tabirian and B. Zeldovich, "Implementation of 3D Angular Selective Achromatic Diffraction Optical Grating device", Frontiers in Optics 2003, Talk WW3.

$$2\Lambda_{VBG}\sin\theta_B = \lambda \quad (2)$$

$$2\Lambda_{VBG} = \Lambda_{SG} \quad (3)$$

Since both of these diffraction angles are dependent on the grating period, theoretically if the surface grating period is double the period (Eq. 3) of the volume Bragg grating then any first order diffraction by normally incident light will be at the corresponding Bragg condition of the volume Bragg grating and that will hold for any wavelength[46]. If we add an identical surface grating in a mirror orientation to the transmitting volume Bragg grating like shown in Fig. 157, we can completely cancel out the dispersion and re-collimate the outgoing beam. Applying this concept to our holographic phase mask the need for angle tuning to the Bragg condition can be disregarded, making it a fully achromatic phase element.

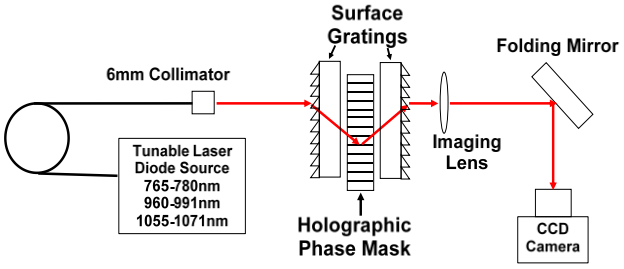

Fig. 158. Experimental setup for observing Gaussian to TEM_{11} conversion of the HPM surface grating system with three different diode sources.

As proof of concept, two surface gratings with a grove spacing of 150 lines/mm (a period of 6.66 µm) were aligned to a HPM with a period of 3.4 µm in our experimental setup shown in Fig. 158. The goal of our experiment was to achieve successful broadband mode conversion from a Gaussian to a TEM11 mode without the need to angularly tune the HPM. In our experiment three different tunable diode laser sources were used in order to get a wavelength range of over 300 nm (765-1071 nm). The lasers were collimated individually with a 6 mm collimator in order to unsure full illumination of the HPM. The first surface grating was aligned so that the HPM's Bragg condition would be met for all wavelengths, and then the second grating was placed to nullify the beam deviation and dispersion. Surface gratings with a blaze wavelength of 725 nm were chosen with diffraction efficiencies in the range of 50% to 70% for the corresponding 765-1071 nm spectral range. To achieve far field imaging, the beam was

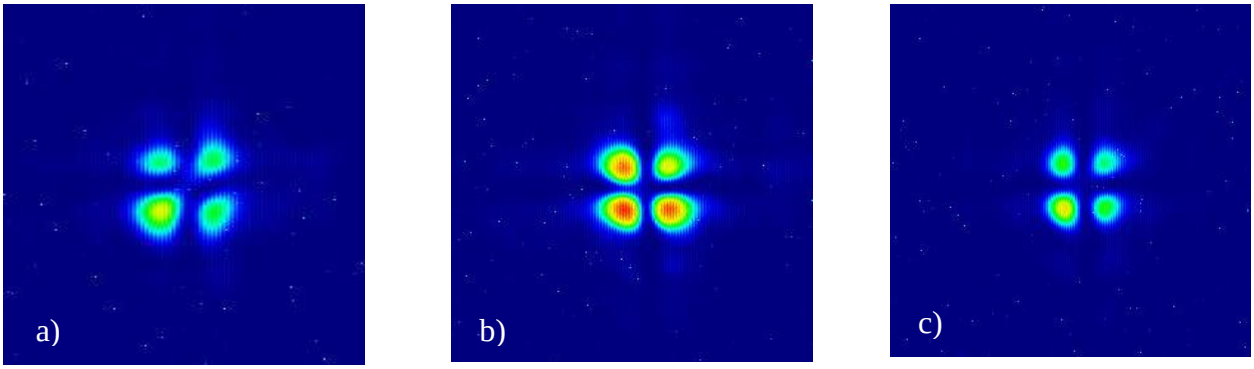

Fig. 159: Far field pattern of the diffracted beam after propagating through a holographic four-sector mode converting mask aligned to two surface gratings at (a) 765 nm, (b) 978 nm, and (c) 1071 nm. The sizes shown here are not to scale.

focused on a CCD camera with an achromatic lens (f=500 mm).

Figure 159 demonstrates the TEM11 mode profile for a single wavelength for each one of the three laser sources. The differences in the intensities are due to the difference in output power for each of the diode sources. Figure 159 also demonstrates that HPMs can provide the same quality phase transformation as regular phase masks with the main difference being that one HPM works

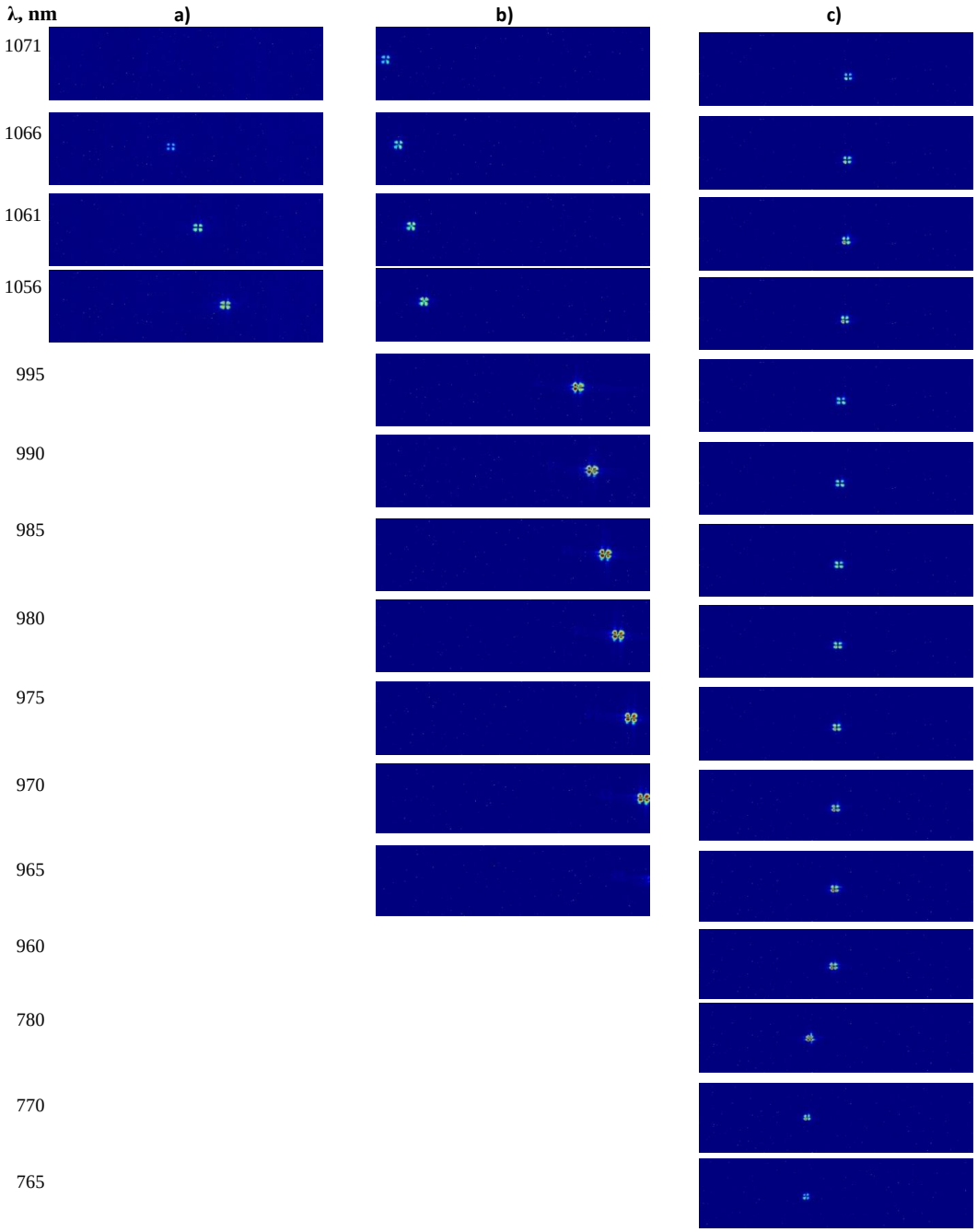

Fig. 160: Far field profiles of the diffracted beam after propagating through: a) a holographic four-sector mode converting mask, b) one surface grating aligned to the Bragg angle of a holographic mask, and c) two surface gratings aligned to the Bragg angle of a holographic phase mask.

for very broad spectral range, as demonstrated.

Three different experiments were done based on the combination of the gratings used and are presented in Fig. 160. The first experiment had the two surface gratings removed, and Fig. 160a shows only images of the beam after the HPM (no surface diffraction gratings present on its sides). The wavelength bandwidth of the HPM is limited to the bandwidth of a transmission Bragg grating and therefore it can only diffract in this particular case approximately 12 nm without angular adjustment. Because of this the top picture in Fig. 160a does not show any signal after for wavelengths less than 1056 nm and larger than 1066 nm. In the second experiment (Fig. 160b) we introduced the one surface diffraction grating on the entrance side of the HPM. For this configuration, the bandwidth of the system is dramatically increased and maximum diffraction efficiency (and therefore mode conversion) is being achieved for wider spectral region. However, due to the wavelength dispersion of the surface grating the signal walks off the camera. To nullify the lateral movement of the beam present in this second experiment, a second surface grating was added and the images for a scan of over 300 nm are shown in Fig. 160c. It clearly proves that the combination of two surface gratings and a holographic phase mask with accordingly matched periods works as achromatic phase element over very wide wavelength region. Since we used three different tunable laser sources and for each one the 6 mm collimator had to be realigned a beam hopping is observed when switching between the three spectral regions covered in column (c). Some small beam shifting is also present while sweeping each of the individual sources. We attribute this effect to the non-exact ratio between the TBG and the surface gratings periods.

We have successfully demonstrated that full achromatization of a holographic phase mask can be achieved with the combination of surface gratings and phase encoded transmitting volume Bragg grating. An experimental mode conversion from a Gaussian to a TEM11 mode for a range of more than 300 nm was successfully achieved with a single phase element and without any angular adjustments. It should be emphasized that this device enable the use of phase masks for femtosecond lasers and, therefore, provide a new tool for spectral and temporal shaping of ultrashort pulses.